Mathematical modelling of human sperm motility

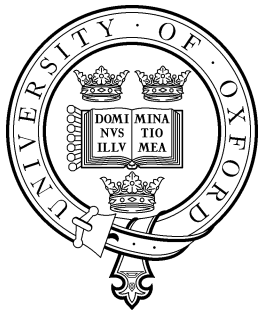

Hermes Gadêlha

St John's College

University of Oxford

A thesis submitted for the degree of

Doctor of Philosophy

Hilary 2012

To my loving wife,

my parents,

my little sister &

my future children.

Acknowledgements

Firstly, I would like to thank God for the miracle of our existence, the gift of life.

I would like to acknowledge and extend my deepest gratitude to my supervisor, Eamonn Gaffney, who has encouraged and challenged me through my DPhil program. Our long hour discussions proved to be very inspirational (I would go further and even describe our meetings as therapeutic), always motivating me to give my best in every part of this journey. I will be always in debited for his unconditional support, encouragement, guidance and contagious excitement. I was very lucky to have him during this wonderful journey, and I hope I will honour his mathematical rigor and critical perspective. Thank you so much!

I will be always indebted to Philip Maini for his unconditional support during my DPhil. He has made available his assistance in a number of ways.

I would like to express my especial gratitude to my collaborators in Birmingham Dave Smith, Jackson Kirkman-Brown and John Blake who have immensely contribute to my knowledge in this field.

It is a pleasure to thank Alain Goriely for further inspiring me to different aspects in elasticity. Also for the great fun playing Foosball (of course, I always let you win on purpose).

I am especially grateful to the Brazilian government, through Capes foundation scholarship for had funded my DPhil program. And also, all academic grants and financial support from St. John's College and the Mathematical Institute. Their contributions were of extreme important for my accomplishments during the period as a DPhil candidate.

During my Oxford years I had the opportunity to meet very especial people. The friendship I had developed with my office mates Henry Shum, Ornella Cominetti, James MacLaurin and Guido Klingbeil will last for life. I would like to thank all of them for their sincere companionship and support.

I also would like to thank my examiners Dr. Jonathan Whiteley and Prof. Raymond Goldstein for critically reading this thesis.

Finally, and most especially, I would like to thank my whole family who supports goes beyond love.

Mathematical modelling of human sperm motility

Hermes Gadêlha, St John's College

A thesis submitted for the degree of Doctor of Philosophy

Hilary term 2012

The propulsion mechanics driving the movement of living cells constitutes one of the most incredible engineering works of nature. Active cell motility via the controlled movement of a flagellum beating is among the phylogentically oldest forms of motility, and has been retained in higher level organisms for spermatozoa transport. Despite this ubiquity and importance, the details of how each structural component within the flagellum is orchestrated to generate bending waves, or even the elastic material response from the sperm flagellum, is far from fully understood.

By using microbiomechanical modelling and simulation, we develop bio-inspired mathematical models to allow the exploration of sperm motility and the material response of the sperm flagellum. We successfully construct a simple biomathematical model for the human sperm movement by taking into account the sperm cell and its interaction with surrounding fluid, through resistive-force theory, in addition to the geometrically non-linear response of the flagellum elastic structure. When the surrounding fluid is viscous enough, the model predicts that the sperm flagellum may buckle, leading to profound changes in both the waveforms and the swimming cell trajectories. Furthermore, we show that the tapering of the ultrastructural components found in mammalian spermatozoa is essential for sperm migration in high viscosity medium. By reinforcing the flagellum in regions where high tension is expected this flagellar accessory complex is able to prevent tension-driven elastic instabilities that compromise the spermatozoa progressive motility.

We equally construct a mathematical model to describe the structural effect of passive link proteins found in flagellar axonemes, providing, for the first time, an explicit mathematical demonstration of the counterbend phenomenon as a generic property of the axoneme, or any cross-linked filament bundle. Furthermore, we analyse the differences between the elastic cross-link shear and pure material shear resistance. We show that pure material shearing effects from Cosserat rod theory or, equivalently, Timoshenko beam theory or are fundamentally different from elastic cross-link induced shear found in filament bundles, such as the axoneme. Finally, we demonstrate that mechanics and modelling can be utilised to evaluate bulk material properties, such as bending stiffness, shear modulus and interfilament sliding resistance from flagellar axonemes its constituent elements, such as microtubules.

Contents

List of Figures

Chapter 1

Introduction

1.1 Motivation: the human male fertility problem

Ever wondered how sperm know where they are going? Every one of us is the consequence of a sperm cell winning the epic race through the female tract to reach the egg, covering the equivalent distance of climbing Mount Everest. However, despite its phenomenal evolutionary success [96], flagellar motility regularly exposes human reproduction to difficulties arising from sperm dysfunction and sub-motility [1, 2, 6, 59, 74, 123, 127]. In the UK 1:7 couples are classed as sub-fertile [*ibid*], with sperm dysfunction the single most common cause, affecting approximately 1:15 men, in addition to an alarming proportion of the 18-years-old male population, 20%, also classed as sub-fertile [6, 59, 74, 127]. This dramatic scenario places male sub-fertility as a current global health issue [1, 2, 6, 59, 74, 123, 127]. While 'sperm count' is typically used for semen analysis, it is a poor predictor of fertility and fails to account for the functional nature of sperm motility; how to even interpret detailed flagellar waveform information for clinical use is unknown. It is therefore perhaps no surprise that male infertility diagnostics are unreliable; furthermore 'treatment', or rather circumvention, is limited to invasive and expensive procedures that carry significant risk for the healthy female partner [1, 2, 6, 59, 74, 96, 123, 127].

Nevertheless, against this background, our understanding of sperm progression within the female reproductive tract is surprisingly limited [123]. Human spermatozoa

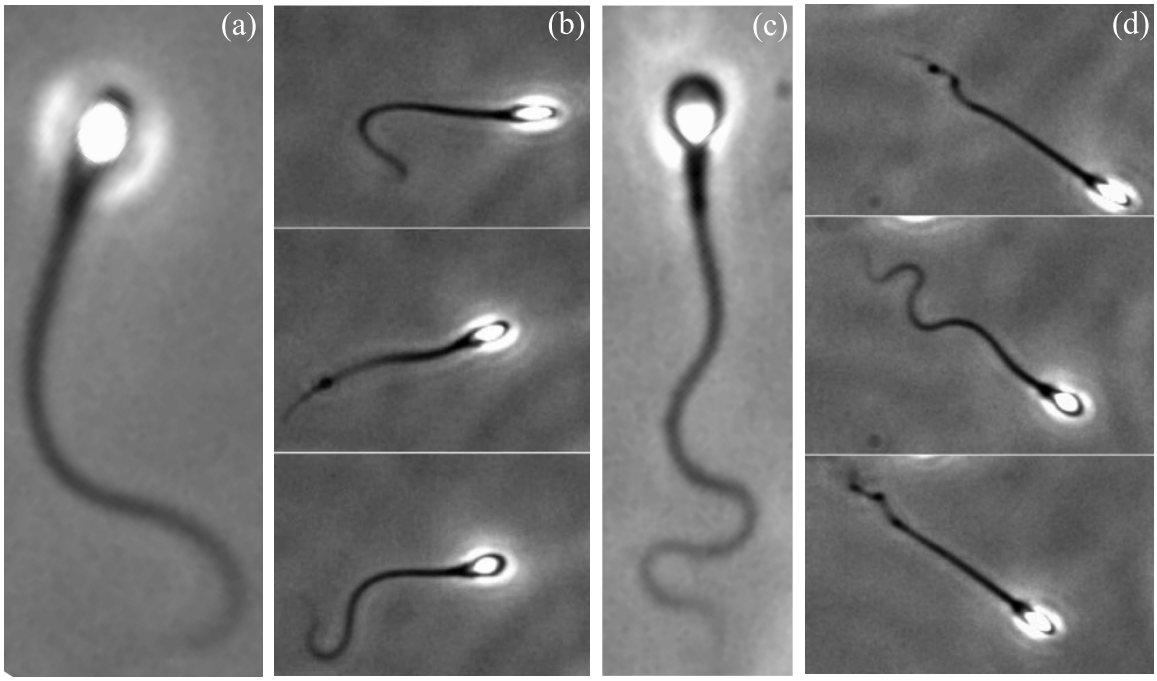

Figure 1.1: Overview of human sperm swimming behaviours: (a,b) human sperm cells migrating in a low viscosity medium, (c,d) in high viscosity medium. In this case, the sperm cells were imaged at $\sim$ 2cm migration distance into a capillary tube that was in contact with a capsule containing raw semen, and therefore they represent a selection of the migrating population. For further details about the microscopy materials and methods, see Appendix A. Figures originally published by Smith, Gaffney, Gadêlha et al. [120], with permission from John Wiley and Sons (2958800134968).

exhibit a bewildering array of morphologies and swimming behaviours [43,83,120,123], as numbers of which are illustrated in Fig. 1.1, and it is a difficult task to isolate which cells might be capable of fertilising within a given sample. In the female reproductive tract, sperm encounter a complex chemical and physical environment [43, 83, 123], see Fig. 1.2: A successful human sperm must generally penetrate cervical mucus, avoid the possibility of prolonged cervical crypt entrapment, endure uterine peristalsis, find the utero-tubal junction and progress in the oviducts despite ciliated flows and convoluted epithelial folds (Fig. 1.2) before penetrating the porous cumulus and a glycoprotein coat surrounding the egg [43,123]. It is unclear what key factors distinguish the few successful sperm in-situ from the many millions which fail during each critical phase of human sperm ascension through the female reproductive tract. Do

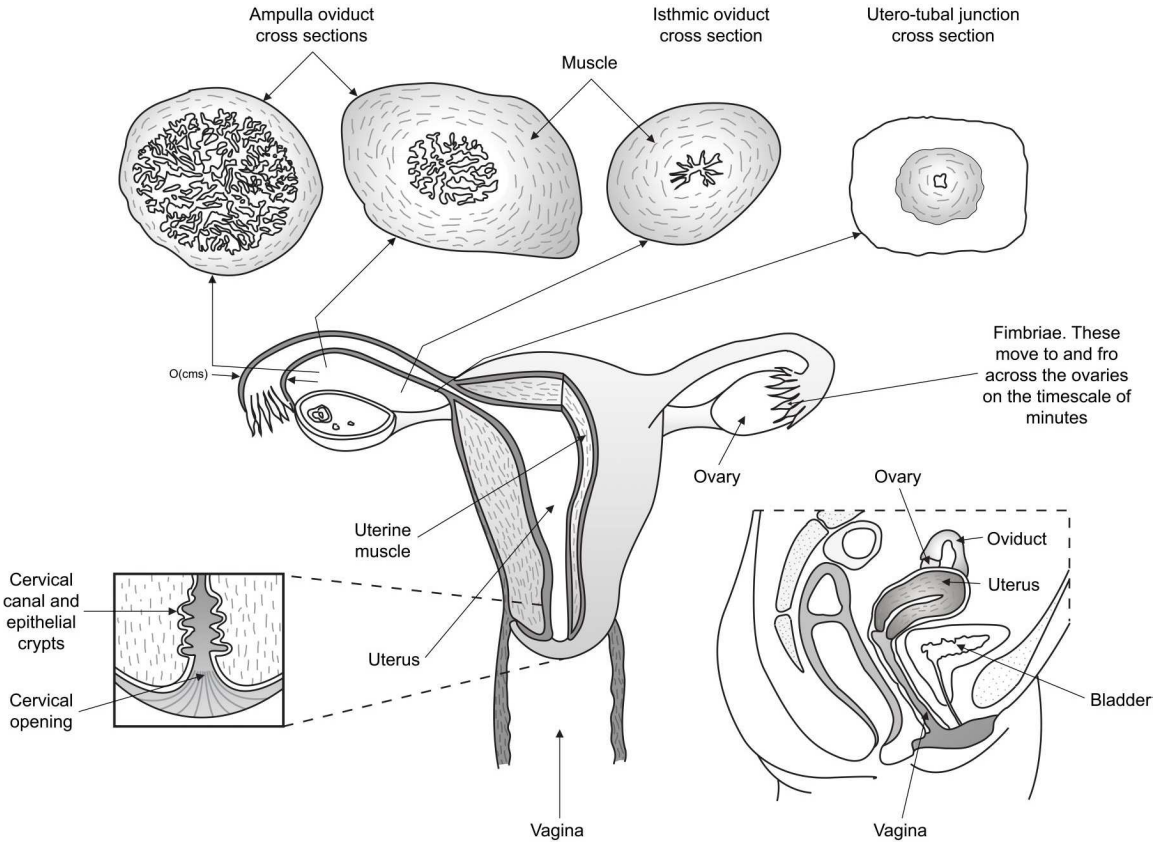

Figure 1.2: Schematic representation of the female reproductive system showing different stages of sperm transport. Human fertilisation requires that a mature sperm reaches the oviducts for a sperm-egg encounter. This is contingent on a combination of several mechanisms including, but not limited to: spermatozoa motility, muscular peristaltic contraction of the uterus and oviduct and oviductal epithelium ciliary beating. In this process, the spermatozoa must travel from the insemination site through the cervix into the uterus, from where it can finally reach the oviduct. The number of sperm cells that can be found in a typical semen sample is between 50 and 400 million, but the number of cells that actually reach the oviduct is incredibly low [37]. It is estimated that 1/10 of the sperm cells initially deposited ever reach the cervix, and only 1/10 of these successfully penetrate the cervical mucus and enter the uterus, which is not the ultimate destination. Only 1/10 of those make it through the uterus to the oviducts [31]. Figure originally published by Gaffney, Gadêlha et al. [43], with permission from Annual Reviews (2958800966317).

certain patients with low motile sperm counts actually have numerous 'good sperm' that could fertilise with, for example, drug treatment or intra-uterine insemination? and how do sperm navigate through the female reproductive tract and locate the egg, given their very limited ability to express protein in response to environmental cues?

All of these questions are receiving more attention as one in six couples now receive fertility treatment in the UK, with one in every hundred children born in the UK, being achieved through in vitro fertilisation (IVF) [1, 74].

Microbiomechanics can provide numerous fundamental insights into sperm progression within the female reproductive tract [42, 43, 49, 83, 120, 123]. By using microbiomechanical modelling and simulation, we aim to develop bio-inspired mathematical models to allow the exploration of sperm motility elucidating, in this manner, the mechanisms behind the flagellar wave modulation and even the intricate elastic response associated with the internal elements of the flagellar structure, as detailed in the next section. With an improved understanding of how the local biophysical environment modulates the sperm flagellar waveform and hence its progression, it may be possible to consider how swimming behaviours in the laboratory may translate to behaviours in-situ, providing novel means of assessing pharmacological screening for sub-fertility interventions. Such studies will also provide valuable insight concerning how mechanical interactions during sperm progression regulate cell function, reflecting a core theme of modern mechano-cellular biology [43, 83, 123].

1.2 The human spermatozoon physiology

The word spermatozoid originates from the ancient Greek and has a beautiful, but peculiar, philosophical meaning: it is translated as a 'living being seed'. The Greeks did not know, however, that the human sperm cell is responsible for carrying the most densely packed genetic material known. The genetic information is condensed as DNA crystals in the sperm head, which also carry the sex chromosome type (XX or XY), ultimately dictating the child gender. The human sperm head has a smooth oval configuration with an average length of $5-6\mu$m and a width of $2.5-3.5\mu$m. The sperm flagellum is $50-60\mu$m long and is often divided in three main regions, which differ in internal structure [38]: (i) the midpiece, (ii) the principal piece and (iii) the

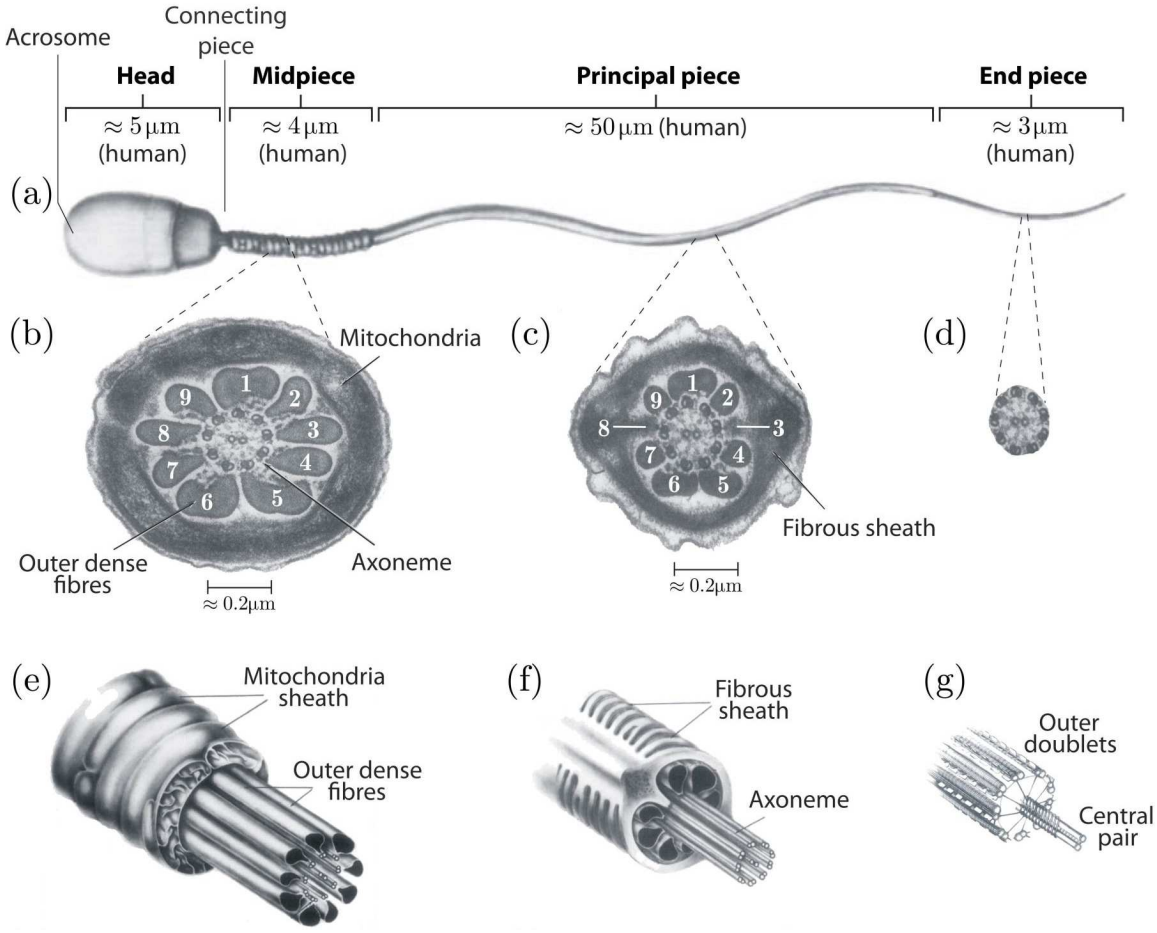

Figure 1.3: Illustration of a mammalian sperm cell and underlying structure: (a) Regions of the sperm flagellum. (b) A cross-section of the mid-piece flagellum, showing the presence of nine outer dense fibres exterior to the microtubule doublets; this structure is also illustrated in (e). All fibres taper and end prior to the distal tip of the sperm, and are also bound to their associated doublet until the distal end along the flagellum. The fibrous sheath is located at the principal piece of the sperm flagellum (a), where it is also found two longitudinal columns attached to fibres 3 and 8. The end of the fibrous sheath delimits the principal piece from the end piece, where only the axoneme structure persists, as depicted in panels (d,g). [38,39]. Figure originally published by Gaffney, Gadêlha et al. [43], with permission from Annual Reviews (2958800966317).

end piece (see Figure 1.3(a)).

The flagellum is attached to the head [113] in the centriole; from this a highly conserved and important cytoskeletal structure, the axoneme (Fig. 1.4), emerges and extends throughout the sperm tail. This is composed of nine cylindrically arranged microtubule doublets (outer doublets) surrounding a central pair, frequently referred

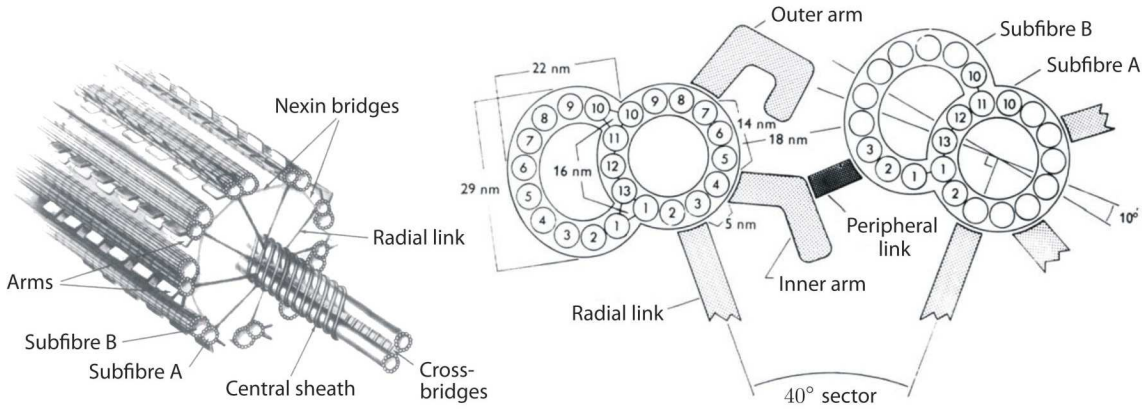

Figure 1.4: Schematic representation of the internal structure of the axoneme, with its nexin bridges and radial links, in addition to the illustration of the inner and outer dynein arms, responsible for producing shearing force between the microtubule doublets that are capable of bending the axonemal scaffolding, driving therefore the flagellar waveform [38,39]. Figure originally published by Gaffney, Gadêlha et al. [43], with permission from Annual Reviews (2958800966317).

to as the 9+2 axoneme, as depicted in Fig. 1.4. This complex structure is held together by stable but flexible nexin links connecting the outer microtubules, together with nine radial spokes, originating from each of the outer doublet pairs, and projecting inward toward the central pair. Additionally, the molecular motors, known as outer and inner dynein arms (Fig. 1.4), are rigidly, and locally, connected with each of the 9 outer doublets, and are responsible for generating the motive force within the flagellum. The dynein's intricate machinery is driven by ATP, and leads to a relative sliding between the microtubules doublets (Fig. 1.4).

The midpiece in Fig. 1.3(a) occupies approximately 1/10 of the flagellum length and is characterised by the presence of a mitochondrial sheath (MS) that encloses nine outer dense fibres (ODFs), which lie outside each of the outer microtubules doublets (Fig. 1.3(b,e)). The mitochondrial sheath is only present in the midpiece, ending at the junction with the principal piece. In this latter region of the flagellum, the ODFs related with the first and fifth outer microtubules doublets have also been replaced by two longitudinal columns of an exterior fibrous sheath (FS) (Fig. 1.3(c,f)). It is

noteworthy that the principal piece constitutes 2/3 of the flagellum length, and is defined by the presence of fibrous sheath and only seven outer dense fibres, rather than nine, surrounding the axoneme (Fig. 1.3(c,f)). Finally, the fibrous sheath and outer dense fibres taper along the flagellum and terminate before the end piece, a small remaining region which only contains the axoneme enclosed by the plasma membrane (Fig. 1.3(d,g)). Curiously, the three additional accessory structures (the MS, ODFs and FS) present in human sperm are found in all mammalian sperm flagella.

1.3 Observations of human sperm flagellar beats in-vitro

Inspired by recent advances in modern microscopy in capturing real-time live human sperm, we briefly illustrate in this section how digital capture and analysis techniques were used to inform our understanding in sperm motility by enabling enhanced experimental measurements [43, 120]. High frame rate digital imaging has been used to measure and characterise the flagellar waveform and kinematics of migrating human spermatozoa [120]. New experimental findings have emerged, unveiling additional gaps in our knowledge that are yet to be explained, further motivating this DPhil work.

Human sperm experiments were carried out using a high-speed, high resolution digital imaging technology, where real-time live human sperm were recorded and the flagellar shape was tracked by an image processing algorithm, generating a precise spatial and temporal description of the flagellar movement, as illustrated in Figs. 1.5 and 1.6. We considered Human sperm cells migrating in a low viscosity medium (LVM), Fig. 1.5, with an effective viscosity 0.02 Pa.s, and a high viscosity medium (HVM), Fig. 1.6, with an effective viscosity 0.14 Pa.s, both liquids generated by dissolving methyl-cellulose in in-vitro fertilisation media (see Ref. [120] for more details on the fluid rheology). In this collaborative effort, the fundamental contribution of

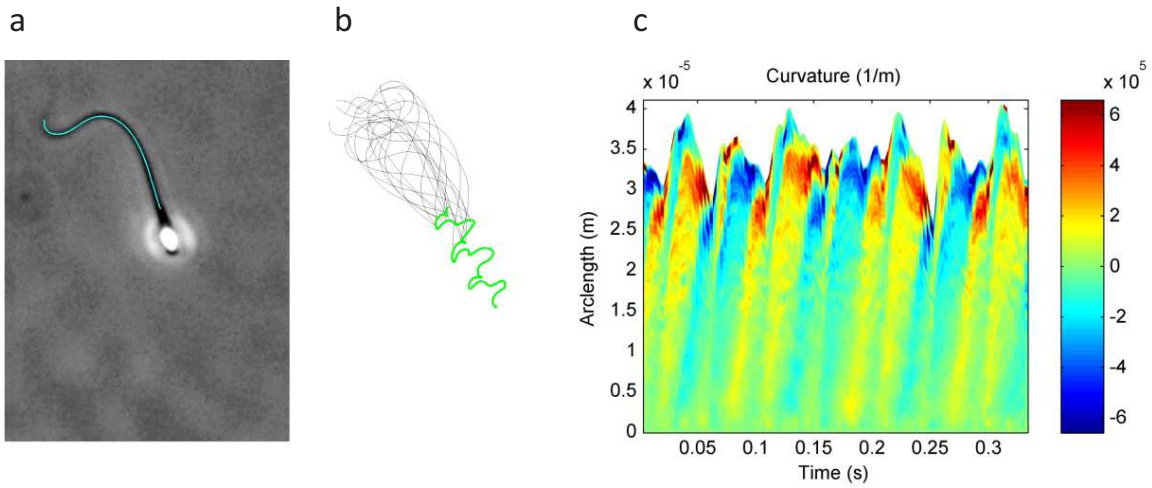

Figure 1.5: Detailed analysis of a cell migrating in low viscosity liquid. (a) Example imaging frame, with the captured flagellar profile indicated in cyan. (b) Montage of flagellar positions (thin black lines, time interval 0.12 s) and the trajectory of the head/neck junction (green line, time interval 0.29 s). (c) Curvature portrait of flagellar movement as a function of time and arclength. Figure originally published by Smith, Gaffney, Gadêlha et al. [120], with permission from John Wiley and Sons (2958800134968).

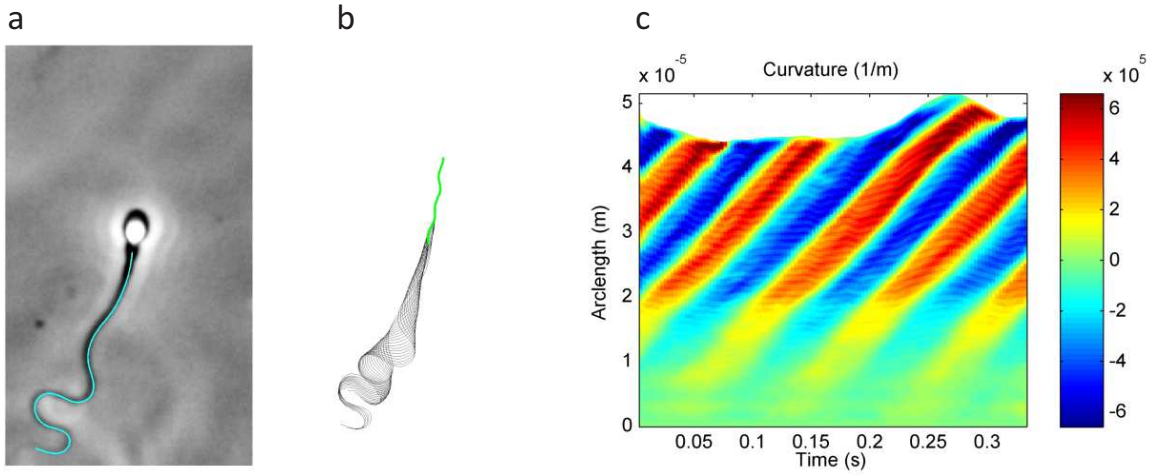

Figure 1.6: Detailed analysis of a cell migrating in high viscosity liquid. (a) Example imaging frame, with the captured flagellar profile indicated in cyan. (b) Montage of flagellar positions (thin black lines, time interval 0.12 s) and the trajectory of the head/neck junction (green line, time interval 0.29 s). (c) Curvature portrait of flagellar movement as a function of time and arclength. Figure originally published by Smith, Gaffney, Gadêlha et al. [120], with permission from John Wiley and Sons (2958800134968).

the author was in the detailed data capture and analysis, as well as contributing to the overall study and experimental design. The experimental work took place in the Centre for Human Reproductive Sciences (ChRS), based at Birmingham Women's Hospital.

We have found that viscosity profoundly alters the cell rolling rate, planarity, torsion, waveform and trajectory, although, surprisingly, not the progressive velocity [120]. Detailed measurements of the flagellar movement for two representative cells in Figs. 1.5 and 1.6 reveal the contrasting behaviour between spermatozoa migrating in low and high viscosity liquids. The trajectory of the proximal end of the flagellum in Fig. 1.5b (green trace), shows a complex but near-periodic nature of the cell trajectory in low viscosity, together with a significant yawing of the head, while for the high viscosity example in Fig. 1.6b, the path of the head/neck junction yaws very little and shows a near linear trajectory. The curvature portraits in Figs. 1.5c and 1.6c illustrates the captured two-dimensional bending wave as it progresses, and despite the complexity associated with each beating pattern, the wavelength and wavespeed are approximately constant along the length of the flagellum. In particular, the lower beat frequency is evident from the reduced number of bending streaks in Fig. 1.6c, and their reduced gradient shows the slower wavespeed characteristic of high viscosity motility. Furthermore, curvature modulation creates the characteristic waveforms of high viscosity swimming, Fig. 1.6, with remarkably effective cell progression against greatly increased resistance, even in high viscosity liquids. While there were considerable differences in the wavespeeds, wavelengths and frequencies of cells in low and high viscosities (see figure caption in Fig. 1.7), the mean progressive velocities were similar, being 62 μm/s and 65 μm/s respectively. This is despite an approximate a hundred times increase in viscosity, recalling that resistance is proportional to the viscosity; a remarkable achievement for sperm swimming that is still to be explained.

The scaling laws relating kinematic parameters to progression are very different

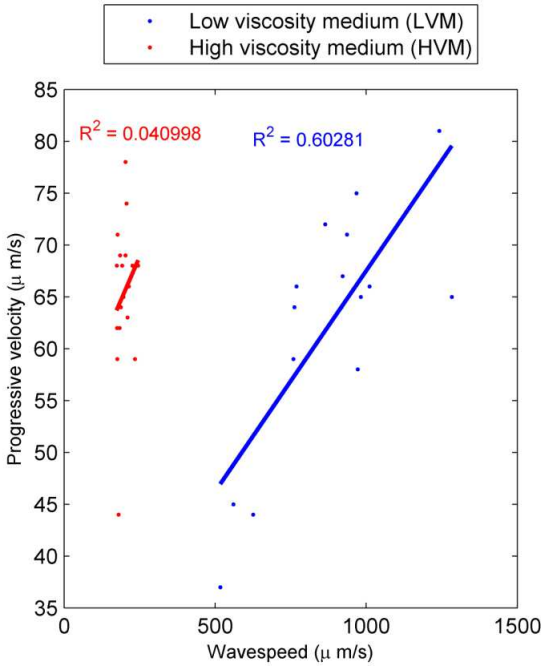

Figure 1.7: Progressive velocity versus flagellar wavespeed, for cells in low viscosity medium (blue) and high viscosity medium (red) at 37°C, lines represent linear regression fits, with R^2 values indicated. In low viscosity medium, the mean value across 16 cells in the migrating population for the progressive velocity was 62 μm/s, the progression per beat was 2.7 μm, frequency 23 Hz, wavelength 39 μm and wavespeed 890 μm/s. In high viscosity medium, the mean value across 19 cells in the migrating population for the progressive velocity was 65 μm/s, the progression per beat was 5.8 μm, frequency 11 Hz, wavelength 18 μm and wavespeed 200 μm/s. In low viscosity, the strongest correlation, $R^2 = 0.60$, is found between wavespeed and progressive velocity, with weaker but significant correlations, $R^2 = 0.39$ and 0.22, respectively, for wavelength and beat frequency. In high viscosity liquid, all correlations were found to be very weak ($R^2 = 0.041, 0.014$, and 0.0003, for wavespeed, wavelength and beat frequency respectively, not statistically significant). Figure originally published by Smith, Gaffney, Gadêlha et al. [120], with permission from John Wiley and Sons (2958800134968).

in low and high viscosities, as exemplified in Fig. 1.7, and in particular there appears to be a constraint on the wavespeeds that may be observed in high viscosity liquids. The correlations observed in low viscosity, shown in blue in Fig. 1.7, were consistent with the characteristic linear dependence on wavespeed and wavelength expected from Newtonian fluid mechanics models and reported previously. However the results for high viscosity did not show any correlation, see red line in Fig. 1.7; this

demonstrates that non-Newtonian effects may play an important role even for weakly non-Newtonian fluids. Furthermore, this evidences that Newtonian fluid mechanics may provide an incredibly poor approximation when considering even very dilute solutions of a common non-Newtonian and cross linked mucus analogue, methyl-cellulose.

The experimental observations presented here readily illustrate the enormous complexity behind the flagellar bending generation. They highlight how human spermatozoa sense and actively respond to changes in the micro-environment via intricate modulation and adjustments of the flagellar wave movement. It equally emphasises the importance of not only the hydrodynamic resistance, but instead the combined effect between the fluid viscous friction and the flagellar flexible structure; a core theme of this DPhil work. Although these empirical observations equally inspired this DPhil study, they are still subject of extensive debate in the literature [43] and, therefore, it is beyond the scope of this thesis the detailed investigation of these findings [43, 120].

1.4 An overview of the relevant mechanics

Human sperm cells are known to endure in a variety of environments (Fig. 1.2), from complex polymeric biological fluids, colloidal dispersions and acidic medium to simple and innocuous watery solutions. A crucial task for these cells is, however, to swim on small, cellular, scales which requires intrinsic microfluidic actuation to achieve locomotion in inertialess environments, due to the excessive hydrodynamic friction. The human gamete ingeniously overcame such difficulty by periodically deforming whip-like, flexible cell appendages, thus inducing propagating bending waves (Fig. 1.1). Although conceptually simple, how each active and structural component within the flagellum (Figs. 1.3 and 1.4), that share different mechanical properties, sizes and functions, are combined, constructively, to execute a harmonic, and rather gracious, self-organized undulatory motion, is perhaps one of the most intriguing question in molecular, cellular and systems biology.

Since the seminal work of Gray and Hancock in the 1950s [49], there have been several attempts to explain the observed flagellar beat via different internal control hypotheses [43, 79, 109, 123]. While each competing hypotheses is capable of successfully generate bending waves that 'resemble' in-vitro observations [109], without a thorough mathematical analysis and experimental validation it is unclear which model, if any, can provide a quantitative understanding of the regulation and nature of the internal mechanics. On the other hand, it is a challenging task to measure experimentally the collective dynamics of the flagellar molecular motors in real time for live cells. Dynein motors are deeply embedded within the flagellar structure, non-trivially connecting and forcing microtubules, spokes and protein links which are organised in a three-dimensional fashion (Figs. 1.3 and 1.4). In addition, molecular motors are characterised by an even smaller length scale (Fig. 1.4), and it would be an impossible task to infer their behaviour via reductionism, without interfering with their motion or chemically changing their own structure or the components around them. While sophisticated theories for the motion of elastic slender objects in Stokes flow may be employed to evaluate accurately the hydrodynamic forces, biomathematical models often neglect the internal elastic response, by prescribing the flagellar wave form instead. Furthermore, even when the elastic contribution is taken into account, this is commonly simplified to the level of Euler-Bernoulli filament theory.

1.4.1 Low Reynolds number hydrodynamics

In order to understand spermatozoa locomotion, we shall consider, for simplicity, the dynamics of a Newtonian, but incompressible, viscous fluid. The fluid flow is governed by the Navier-Stokes equations and the continuity equation [3, 138]

$$\rho\left[\frac{\partial \mathbf{u}}{\partial t} + (\mathbf{u}\cdot\boldsymbol{\nabla})\mathbf{u}\right] = -\boldsymbol{\nabla} p + \eta\nabla^2\mathbf{u}, \tag{1.1}$$

$$\boldsymbol{\nabla}\cdot\mathbf{u} = 0, \tag{1.2}$$

where $\mathbf{u}$ represents the velocity of a fluid element moving relative to an inertial reference frame, ρ is the fluid density and t is time. The first term of the right of Eq. (1.1) is the force generated by the gradients of the hydrodynamic pressure p, while the second term is a consequence of "internal friction" due by the fluid resistance to deformation during the motion, noting that the friction forces between the fluid elements is proportional to the viscosity η for a Newtonian fluid. The inclusion of other forces experienced by the fluid (gravitational, magnetic, centrifugal, etc.) can be incorporated via extra terms on the right hand side of the Eq. (1.1). To fully describe the fluid flow, the Navier-Stokes equations are supplemented by initial and boundary conditions. Typically, no-slip condition is assumed at the fluid-solid interface.

When a rigid body moves relative to the surrounding fluid, the work done is dissipated in two ways. First, it displaces fluid out of its path, imparting energy to the fluid. At the same time, it experiences the internal fluid friction imposed by the viscous forces in Eq. (1.1). The Reynolds number is the ratio of these two effects, and is defined as

$$Re = \frac{\text{inertial force}}{\text{viscous force}} = \frac{|(\mathbf{u}\cdot\boldsymbol{\nabla})\mathbf{u}|}{|\eta\nabla^2\mathbf{u}|} \simeq \frac{\rho U L}{\eta},$$

where U and L are, respectively, the typical velocity magnitude and the typical length-scale of velocity variations. The whole nature of the motion depends crucially on the size of this number, which for a small-scale, slow or highly viscous, flows approaches zero, characterising the low Reynolds number regime.

The typical values for the velocity and length-scale for a human spermatozoa are $U = 10^{-4}$m/s and $L = 5.5 \times 10^{-5}$m, where the "kinematic viscosity" in most naturally aqueous media is $\eta/\rho = 2 \times 10^{-6}\text{m}^2/\text{s}$ [23, 77], giving $Re = 2.75 \times 10^{-3}$. As a consequence, the motion is uninfluenced by the inertia, and thus $[\partial\mathbf{u}/\partial t + (\mathbf{u}\cdot\boldsymbol{\nabla})\mathbf{u}]$ can be neglected in Eq. (1.1), giving the Stokes equation

$$0 = -\boldsymbol{\nabla}p + \eta\nabla^2\mathbf{u}. \tag{1.3}$$

Now, the viscous forces are completely balanced with the fluid pressure p. Taking

the divergence of Eq. (1.3), together with the continuity condition Eq. (1.2) we find that the pressure is a harmonic function, whereas $\mathbf{u}$ satisfies the vectorial biharmonic equation, after taking the Laplacian of Eq. (1.3) [106]. This is supplemented by the boundary condition $\mathbf{u} = \mathbf{U}_\circ$ at the sperm boundary, where $\mathbf{U}_\circ$ denotes the speed of the sperm boundary and thus represents no slip, and that both $\mathbf{u}$ and p vanish as the observation point $||\boldsymbol{r}|| \to \infty$. The fluid flow is instantaneous in time and therefore initial conditions are redundant.

In order to represent the fluid motion induced by a rigid body, let $\mathbf{f}$ be its force acting on the fluid, and because each fluid element must remains in equilibrium under any distribution of external forces, it implies that the modified form of Eq. (1.3), known as forced Stokes equation, takes the form

$$\boldsymbol{\nabla} p - \eta \nabla^2 \mathbf{u} = \mathbf{f}, \tag{1.4}$$

which is valid for the volume of fluid exterior to the rigid body, with $\mathbf{u} = \mathbf{U}_\circ$ at the rigid body surface and $\mathbf{u} \to 0$ for $||\boldsymbol{r}|| \to \infty$. Since Eq. (1.4) does not depend on any time derivatives, the velocity $\mathbf{u}$ responds instantaneously to the boundary motion of the rigid body and the force $\mathbf{f}$ exerted by the body, achieving the terminal velocity at once. Equally, because there is no dependence on $(\mathbf{u}\cdot\boldsymbol{\nabla})\mathbf{u}$ in Eq. (1.4), the velocity and pressure are linear in the body force. Hence, and importantly, the force is proportional to the velocity rather than acceleration. Furthermore, since $-\mathbf{u}$, $-p$ and $-\mathbf{f}$ also satisfy Eq. (1.4), together with symmetric boundary conditions, the reversed flow is a physically possible solution. In this case, the direction of forces and torques are also reversed when the signs of $\mathbf{u}$ and p are switched. This means that if the motion is reversed over time, then each material point retraces its history. This time reversibility leads to the so-called "scallop theorem" [107], which states that no time-reversible motion can result in swimming at low Re in an infinite fluid or near a rigid surface. It follows from the scallop constraint that low Reynolds number swimmers need to undergo a non-reciprocal motion in order to

generate propulsion. Interestingly, the travelling waves propagating down the sperm flagella during locomotion are not reciprocal motions and this mechanism is a very common method of propulsion over a wide range of Reynolds number.

The rigid body motion is specified by the boundary conditions and, in general, subjected to: (i) the no-slip condition at the body surface; and (ii) the fluid velocity far way from the rigid body must be equal to some background velocity, which is also a solution to the Stokes equation. For a rigid body with an arbitrary shape, a full boundary integral formulation for this system would yield non-trivial integral equations on its surface [106]. On the other hand, the sperm flagellum is not a rigid body, since it is composed by a complex elastic structure, and can undergo deformations resulting from the fluid-structure interaction. Even though the inertia is irrelevant for the human gamete locomotion, this system is very difficult to solve accurately with a grid based method. Rigorously, the appropriate elastic equations have to be solved in the regions occupied by the sperm flagellum and, treating the sperm head as a rigid body, the fluid equations are solved in the rest of the domain, coupled to the sperm flagellum via boundary conditions.

Due to above numerical difficulties, several approximate methods have been proposed, but mainly in the context of passive elastic filaments sitting in the fluid. The beads-model [117], for example, describes elastic filaments as a string of spherical beads, to simplify the hydrodynamic interaction, where each bead is linked by inextensible connectors. However, although the beads model accurately represent no-slip condition for each bead, it does not capture detailed elastic contribution from flexible filaments. The immersed boundary method [104] has also been applied to this class of problems, and consists of discretising the elastic structure with connected Lagrangian markers, and tracking their relative displacements by fluid motions, to calculate the elastic response. Nevertheless, the immersed boundary method (IBM) typically accounts for two dimensional flows, while the resulting constitutive relations

of the immersed elastic structure, which is composed by a collection of nodes connected by springs with different strengths, is generally unknown. In the present work, we will consider a very different approach, based on the slender-body hydrodynamics, which exploits the large aspect ratio of slender bodies, as the spermatozoa flagellum, and uses the body slenderness to reduce computationally expensive integral equations at the slender-body surface to just its centreline, by using fundamental solutions to the Stokes equation. The sperm head can also be represented by the dynamics of a simple rigid body in Stokes flow. Furthermore, the slender-body hydrodynamics is not only more accurate than the bead-model, in terms of hydrodynamic interactions, it is also appropriate for describing flexible filaments [131], rather than IBM that describes flexible sheets deforming in a fluid.

1.4.1.1 Slender-body theory

The fundamental solution for the singularly forced Stokes equation

$$\boldsymbol{\nabla} p - \eta \nabla^2 \mathbf{u} = \mathbf{f}\, \delta(\boldsymbol{r} - \boldsymbol{r}'), \tag{1.5}$$

is given by the Green's function, and takes the form

$$\mathrm{u}_i(\boldsymbol{r}) = \frac{1}{8\pi\eta} G_{ij}(\boldsymbol{r}, \boldsymbol{r}')\ \mathrm{f}_j, \tag{1.6}$$

where $\boldsymbol{G}$ is the Green's function, $\boldsymbol{r}'$ is position of the force point, and $\boldsymbol{r}$ is the observation point. Equation (1.6) expresses the velocity field due to a concentrated point force of strength $\mathbf{f}$, and depends on the geometry and topology of the flow domain. For instance, the free-space Green's function represents the solution for a unbounded flow, and the half-space Green's function for a semi-infinite flow bounded by a solid plane surface. As the observation point $\boldsymbol{r}$ approaches the pole $\boldsymbol{r}'$, all Green's function exhibit singular behaviour, and the leading order term acts as a free-space Green's function. In addition, the Green's functions for unbounded flow are required to decay at infinity at a rate equal to (or faster than) the free-space Green's function.

Recalling that the Stokes flow is linear, it is possible to write the associated Green's function for the vorticity, pressure and stress fields, respectively, as

$$w_i(\boldsymbol{r}) = \frac{1}{8\pi\eta}\Omega_{ij}(\boldsymbol{r}, \boldsymbol{r}')\ \mathrm{f}_j, \tag{1.7}$$

$$P(\boldsymbol{r}) = \frac{1}{8\pi}p_j(\boldsymbol{r}, \boldsymbol{r}')\ \mathrm{f}_j, \tag{1.8}$$

$$\sigma_{ik}(\boldsymbol{r}) = \frac{1}{8\pi}T_{ijk}(\boldsymbol{r}, \boldsymbol{r}')\ \mathrm{f}_j, \tag{1.9}$$

where the symmetric stress tensor T is associated with $\boldsymbol{G}$ via

$$T_{ijk}(\boldsymbol{r}, \boldsymbol{r}') = -\delta_{ik}p_j(\boldsymbol{r}, \boldsymbol{r}') + \frac{\partial G_{ij}}{\partial r_k}(\boldsymbol{r}, \boldsymbol{r}') + \frac{\partial G_{kj}}{\partial r_i}(\boldsymbol{r}, \boldsymbol{r}'). \tag{1.10}$$

As a result, if the fluid domain is unbounded, we must have that (1.7), (1.8) and (1.9) vanish as the observation point moves to infinity, since p vanishes as the observation point $||\boldsymbol{r}|| \to \infty$. Moreover, substituting (1.6) into the continuity equation (1.2), we obtain that the Green's function has to satisfy

$$\frac{\partial G_{ij}}{\partial r_i}(\boldsymbol{r}, \boldsymbol{r}') = 0, \tag{1.11}$$

and integrating (1.11) over a fluid volume bounded by a surface S we find

$$\int_S \boldsymbol{G}(\boldsymbol{r}, \boldsymbol{r}')\hat{\boldsymbol{n}}(\boldsymbol{r})dS = 0, \tag{1.12}$$

independently of where the force point $\boldsymbol{r}'$ is located, provided that for the free space stokeslet the integral at infinity vanish.

The so-called *Stokeslet* tensor is the free-space Green's function due to a concentrated external force $\mathbf{f}$ acting at $\mathbf{r}'$, and is given by

$$G_{ij}(\boldsymbol{r} - \boldsymbol{r}') = \left(\frac{\delta_{ij}}{r} + \frac{r_i r_j}{r^3}\right). \tag{1.13}$$

In addition to the Stokeslet, higher order fundamental solutions can be constructed by differentiation. This process gives rise to a sequence of *irrotational* singularities, as the *potential dipole* and the *potential quadrapole*, when applied to the potential

sources. Similarly, the velocity due to a potential dipole is given by $\mathrm{u}_i = D_{ij}\, d_j$, where $\boldsymbol{d}$ is the dipole strength divided by 4π, and

$$D_{ij} = \left(-\frac{\delta_{ij}}{r^3} + 3\frac{r_i r_k}{r^5} \right). \tag{1.14}$$

It is worth noting that the velocity field due to a potential dipole, also known as *source-doublet*, exerts no external force on the fluid.

The linearity of the governing equation in Stokes flow allows the superposition principle by which complex solutions can be constructed from combinations of the above fundamental solutions, and of course, their derivatives which also satisfy Stokes equations Eq. (1.5). Thus detailed flow structures can be determined with minimal analytical effort, allowing a straightforward computation of numerous physical quantities such as, the forces and torques exerted on the fluid.

The slender-body theory describes slender bodies with circular transverse cross-sections, and longitudinal cross-sections which are approximately elliptic close to the body ends, i.e. prolate-ellipsoidal body ends [61, 66, 77]. The slender-body approximation can be derived by using a distribution of singularities (stokeslets and source doublets) at the slender-body centreline, where the singularity strengths are chosen in order to satisfy the non-slip boundary conditions at asymptotic accuracy in the slenderness parameter ε, which is the ratio between the body radius and length. Consistency constraints entail the potential dipole weightings can be expressed in terms of the stokeslet weightings $\mathbf{f}_\mathrm{b}$ (force per unit length on the slender-body) at leading order for a curvilinear prolate ellipsoid. Thus, this yields a non-local integral equation for the slender-body velocity in terms of its centreline $\mathbf{X}(s,t)$, at a given material point $s \in [0, L]$ along a slender-body with length L and time t, as

$$\frac{\partial \mathbf{X}(s,t)}{\partial t} = \boldsymbol{\Lambda}[\mathbf{f}_\mathrm{b}](s) + \boldsymbol{\Gamma}[\mathbf{f}_\mathrm{b}](s), \tag{1.15}$$

where the slender-body radius is given by $b(s) = 2\varepsilon\sqrt{s(L-s)}$, so that $b(L/2) = \varepsilon L$,

and $\mathbf{f}_\mathrm{b}$ is the force per unit length on the slender-body. The local operator $\mathbf{\Lambda}$ reads

$$\mathbf{\Lambda}[\mathbf{f}_\mathrm{b}](s) = \frac{1}{8\pi\eta}\big[\zeta(\mathbf{1}+\hat{\mathbf{s}}\hat{\mathbf{s}}) - 2(\mathbf{1}-\hat{\mathbf{s}}\hat{\mathbf{s}})\big]\mathbf{f}_\mathrm{b}(s), \tag{1.16}$$

where η denotes the fluid viscosity, the constant $\zeta = \log(\varepsilon^2 e)$ and $\hat{\mathbf{s}} = \mathbf{X}_s \equiv \partial\mathbf{X}/\partial s$ is the tangent vector along the slender-body. The integral operator $\mathbf{\Gamma}$ is given by

$$\begin{aligned}\mathbf{\Gamma}[\mathbf{f}_\mathrm{b}](s) = &-\frac{1}{8\pi\eta}\int_0^L \left(\frac{\mathbf{1}+[\mathbf{X}(s)-\mathbf{X}(s')][\mathbf{X}(s)-\mathbf{X}(s')]}{|(\mathbf{X}(s)-\mathbf{X}(s')|}\right)\mathbf{f}_\mathrm{b}(s')\,\mathrm{d}s' \\ &+\frac{1}{8\pi\eta}\int_0^L \frac{\mathbf{1}+\hat{\mathbf{s}}\hat{\mathbf{s}}}{|s-s'|}\,\mathbf{f}_\mathrm{b}(s)\,\mathrm{d}s',\end{aligned} \tag{1.17}$$

and is often called finite part integral, since each term in the integrand is singular at the point force s'. Note that the operators $\mathbf{\Lambda}$ and $\mathbf{\Gamma}$ depend on the slender-body configuration, even though is not explicitly indicated in the notation. In Eq. (1.15), the local hydrodynamic effect is accounted by $\mathbf{\Lambda}$, while $\mathbf{\Gamma}$ includes non-local corrections which capture the global effect on the fluid velocity from the presence of the body. Moreover, Johnson [61] demonstrated that Eq. (1.15) is accurate to $O(\varepsilon^2\log\varepsilon)$, given $b(s) = 2\varepsilon\sqrt{s(L-s)}$, including the slender-body end points [61]. More details about the derivation of Eq. (1.15) can be found in [61, 66], including a generalisation to slender bodies with circular cross sections which asymptote to prolate ellipsoidal caps at their ends.

It is not difficult to understand why the slender-body theory (SBT) is often used to describe the motion of flagellated microorganisms in a Newtonian fluid. By using SBT, it is possible to take full advantage of the fact the flagellum itself has a very small slenderness ratio, as is the case of the human sperm flagellum with $\varepsilon \approx 10^{-3}$. Here, Eq. (1.15) can be used to represent the equation of motion for the flagellar movement, when subjected to some force $\mathbf{f}_b$ acting on the flagellum. Alternatively, the flagellum position $\mathbf{X}(s,t)$ can be extracted from experiments, through image capture analysis [120], and, therefore, Eq. (1.15) provides experimentalists with an accurate means of extracting the hydrodynamic forces acting on the flagellum.

On the other hand, because the internal force $\mathbf{f}_b$ exerted on the flagellum is not known a *priori*, sperm dynamics is often prescribed by some flagellar waveform within the frame of reference of the cell, and then Eq. (1.15) is used to update the spermatozoa position, while the imposed beat pattern is inspired by experimental observation. Although the motion is prescribed in an *ad-hoc* manner, this approach has successfully explained several hydrodynamic effects in flagellar dynamics such as, for example, boundary accumulation of spermatozoa close to surfaces [119]. Nonetheless, in addition to the hydrodynamic drag experienced by the flagellum, Eq. (1.15), there is still a non-trivial coupling between the elastic response of the sperm flagellum and the internal active bending moment. In this case, the slender-body approximation can be numerically very expensive and analytically untractable, since this elastohydrodynamic system is characterised by a highly coupled non-linear integro-differential equations, with stiff fourth-order derivatives, due to the elastic bending moments, and weakly singular integrals, responsible for even more severe numerical instabilities. Because of these difficulties, elastohydrodynamic systems using the slender-body theory has only been employed for the dynamics of passive elastic fibres [131], and a similar study in the context of internally driven flagella, as well as its interaction with the sperm head, is still lacking in the literature. This motivates the consideration of a simpler modelling framework.

1.4.1.2 Resistive-force theory

The pioneering work of Gray and Hancock [49] established a very simple approximation for the hydrodynamic drag force experienced by slender-bodies, the so-called resistive-force theory (RFT). While investigating the sperm locomotion, they argued that as the flagellum undulates, provided its radius of curvature is large compared to its diameter, the normal and tangential drag forces acting on the flagellum would be approximately given by the velocity of each elemental flagellum length and the corresponding resistive coefficients, perpendicular $\xi_\perp$ and parallel $\xi_\parallel$ to straight cylinders,

which are solely determined the geometry and topology of the flow [77, 91]. More specifically, resistive-force theory neglects non-local hydrodynamic interactions, and represents the leading order term of the slender-body hydrodynamics, given by $\mathbf{\Lambda}$ in Eq. (1.15).

In the following, each infinitesimal element ds of the sperm flagellum is considered as a small cylinder, so that the drag force elicited from the fluid opposes the motion of element ds, and is directly proportional to the medium viscosity and the velocities in the direction of (and perpendicular with) the cylinder axis. The viscous frictional forces per unit length on the normal, f^{n}, and tangential, f^{t}, direction, relative to a local orthogonal basis within the flagellum, can be written as

$$\frac{\mathrm{d}\mathbf{F}_{\mathrm{Drag}}}{\mathrm{d}s} \equiv \begin{pmatrix} f^{\mathrm{t}}(s,t) \\ f^{\mathrm{n}}(s,t) \end{pmatrix} = \begin{pmatrix} -\xi_{\parallel} & 0 \\ 0 & -\xi_{\perp} \end{pmatrix} \begin{pmatrix} \mathrm{U}^{\mathrm{t}}(s,t) \\ \mathrm{U}^{\mathrm{n}}(s,t) \end{pmatrix} \tag{1.18}$$

where U^{t} and U^{n} are, respectively, the velocities on the tangential and normal direction, while the parallel and perpendicular resistive-force coefficients are given by, respectively,

$$\begin{aligned} \xi_{\parallel} &= \frac{2\pi\eta}{\log(\lambda/r) - 1/2} \\ \xi_{\perp} &= 2\xi_{\parallel}, \end{aligned} \tag{1.19}$$

where r is the radius of the flagellum and λ is the wavelength of a sine wave [49]. Note that for a swimming spermatozoa, since the friction in the normal direction exceeds the tangential resistance, the normal force, which has a component in the direction of motion, is greater than the tangential force, that has components in the opposite direction, thus generating a net reaction on the flagella to overcome the fluid resistance (see Figure 1.8). Hence, the propulsion of a spermatozoon depends on the fact that hydrodynamic drag effects from tangential forces acting along the flagellum are compensated by propulsive components acting normally to its surface; which is only possible if the viscous friction is anisotropic along the flagellum.

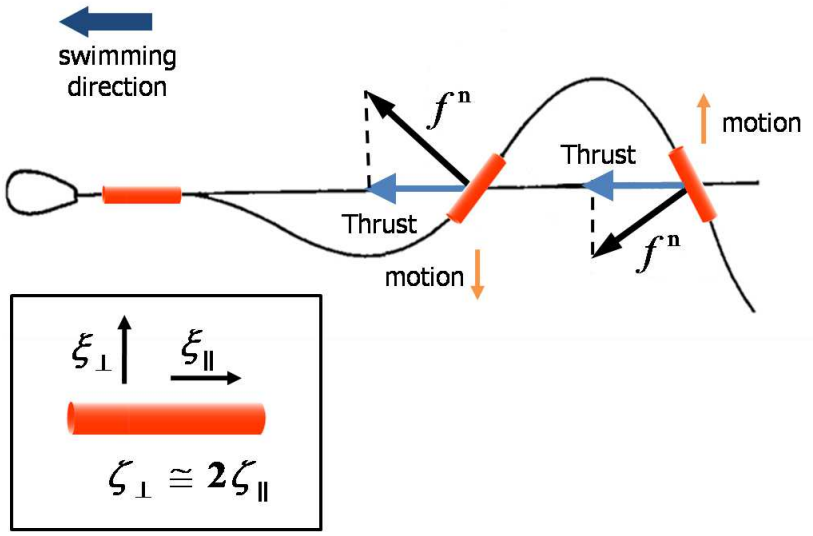

Figure 1.8: Diagram illustrating the resistive-force theory approach showing the forward trust as a result of the normal force component on the swimming direction.

The propulsive force for any element of the flagellum is simply given by the projected viscous friction on the direction of motion, and can be simply evaluated by expressing Eq. (1.18) relative to the laboratory frame

$$\boldsymbol{\varphi}(s,t) \equiv \begin{pmatrix} f^{x}(s,t) \\ f^{y}(s,t) \end{pmatrix} = \boldsymbol{D} \begin{pmatrix} \mathrm{V}^{x}(s,t) \\ \mathrm{V}^{y}(s,t) \end{pmatrix}, \tag{1.20}$$

with

$$\frac{\partial \mathbf{X}(s,t)}{\partial t} = \mathrm{V}^{x}\hat{\mathbf{x}} + \mathrm{V}^{y}\hat{\mathbf{y}},$$

where $\boldsymbol{D}$ is a symmetric matrix defined as

$$\boldsymbol{D} = \boldsymbol{R}^{-1} \begin{pmatrix} -\xi_{\parallel} & 0 \\ 0 & -\xi_{\perp} \end{pmatrix} \boldsymbol{R} = \xi_{\parallel} \begin{pmatrix} -(\gamma-1)\sin^{2}\theta - 1 & -(1-\gamma)\sin\theta\cos\theta \\ (\gamma-1)\sin\theta\cos\theta & (1-\gamma)\cos^{2}\theta - 1 \end{pmatrix}, \tag{1.21}$$

where θ is the angle between the tangent vector along the flagellum length and the horizontal direction. The anisotropic ratio is denoted by $\gamma = \xi_{\perp}/\xi_{\parallel}$, and is always greater than one for a cylinder, while the rotation matrix is represented by $\boldsymbol{R}(s,t)$ and satisfy

$$\begin{pmatrix} \mathrm{U}^{\mathrm{t}}(s,t) \\ \mathrm{U}^{\mathrm{n}}(s,t) \end{pmatrix} = \boldsymbol{R} \begin{pmatrix} \mathrm{V}^{x}(s,t) \\ \mathrm{V}^{y}(s,t) \end{pmatrix}, \tag{1.22}$$

where $\theta(s,t)$ is the angle between the vectors $\hat{\mathbf{s}}$ and $\hat{\mathbf{x}}$. Also note that, as expected from a Stokes flow, there is no preferential direction for the force density in Eq. (1.20).

Moreover, if we assume that the sperm cell is swimming in the $-\hat{\mathbf{x}}$ direction, by generating travelling waves in the opposite direction, the propulsive force per unit length is simply given by

$$\frac{\partial \mathrm{F}_{\mathrm{thrust}}}{\partial s} = \boldsymbol{\varphi} \cdot \hat{\mathbf{x}} = -\xi_{\parallel} \left[\mathrm{V}^{y}(\gamma - 1) \sin\theta \cos\theta + \mathrm{V}^{x}((1-\gamma)\sin^{2}\theta - 1) \right]. \tag{1.23}$$

Eq. (1.23) not only depends on the angle relative to the direction of propulsion, and transverse and parallel velocities, but also on the anisotropic ratio γ. If $0 < \gamma < 1$, meaning that the tangential friction is larger, locomotion is still possible, however, the net force will act on the opposite direction of the wave propagation, causing the cell to swim backwards as, for instance, the ochrophytes. In these algaes, the flagellum is fully covered with mastigonemes, lateral 'hairs', so that the resistive coefficients switch their behaviour $\xi_{\parallel} > \xi_{\perp}$. Most importantly, Eq. (1.23) exemplifies the importance of the anisotropic drag for the flagellar locomotion in low Reynolds number regime, since it would be impossible to generate propulsion if the viscous friction on the flagellum was symmetric ($\gamma = 1$). In this manner, in order to optimise propulsion, one would need to design geometric shapes so that the anisotropic ratio is maximised. Amazingly enough, the highest value for γ is only found for slender cylinders ($\gamma \approx 2$), in contrast to $\gamma \approx 1.5$ for a swimming sheet for example. Alternatively, the drag anisotropy could also be dramatically improved by making the flagellum surface super hydrophobic. Although the latter is not found in biological systems, it may be relevant while designing artificial microswimmers.

1.4.2 Euler-Bernoulli rod theory

1.4.2.1 The Euler-elastica

One way to incorporate the elastic response from the sperm flagellum is to consider the flagellar structure as a simple Euler-Bernoulli filament, i.e. an inextensible and unshearable, slender elastic body that resists bending deformations. If the effect of torsion is neglected, when a elastic slender-body is bent into a curved shape, the

part of body under tension exerts a bending moment on the part of the body under compression, that is linearly related with the slender-body curvature [8, 41, 73, 128],

$$M = E\theta_s, \tag{1.24}$$

where the constant of proportionality is given by the elastic bending modulus E, defined as the product between the Young's modulus and the moment of inertia of the cross-section [73]. If the slender-body is under the action of external, and opposing, forces at the end points, with magnitude Q, in the horizontal direction, the bending moment density along the body is balanced by external load, yielding

$$E\theta_{ss} + Q\sin\theta = 0, \tag{1.25}$$

which describes geometrically exact deformations of an Euler-elastica [8,34,41,73,128], together with the boundary conditions. Typically, it is assumed that the elastic body is free from external moments at the boundaries. In this case, the bending moment is a periodic function of θ, with singular points at $M = 0$ and $\theta = k\pi$ in the $M-\theta$ phase space, where k is an integer. By defining a new variable ϕ, such that $\sin(\theta/2) = \ell\sin\phi$, and $\ell = \sin(\theta_\circ/2)$, Eq. (1.25) can be simplified to

$$\phi_s^2 = r(1 - \ell^2\sin^2\phi), \tag{1.26}$$

where $r = Q/E$ and $\theta_\circ$ is the value of θ at the inflection $s = 0$. In this case, if we define the elliptic function

$$u(\varphi, \ell) = \int_{\varphi_\circ}^{\varphi} \frac{\mathrm{dt}}{\sqrt{1 - \ell^2\sin^2 t}}, \tag{1.27}$$

the exact solution of Eq. (1.26) is reduced to

$$s\sqrt{r} = u(\phi, \ell), \tag{1.28}$$

with boundary conditions given by $\phi_\circ = \pi$ and $\theta(0) = \theta_\circ$, if the slender-body is free from external moments [8, 41, 73, 128]. The solution (1.28) is therefore given by a

(a) Euler's elastica (b) Machin's elastohydrodynamic solutions

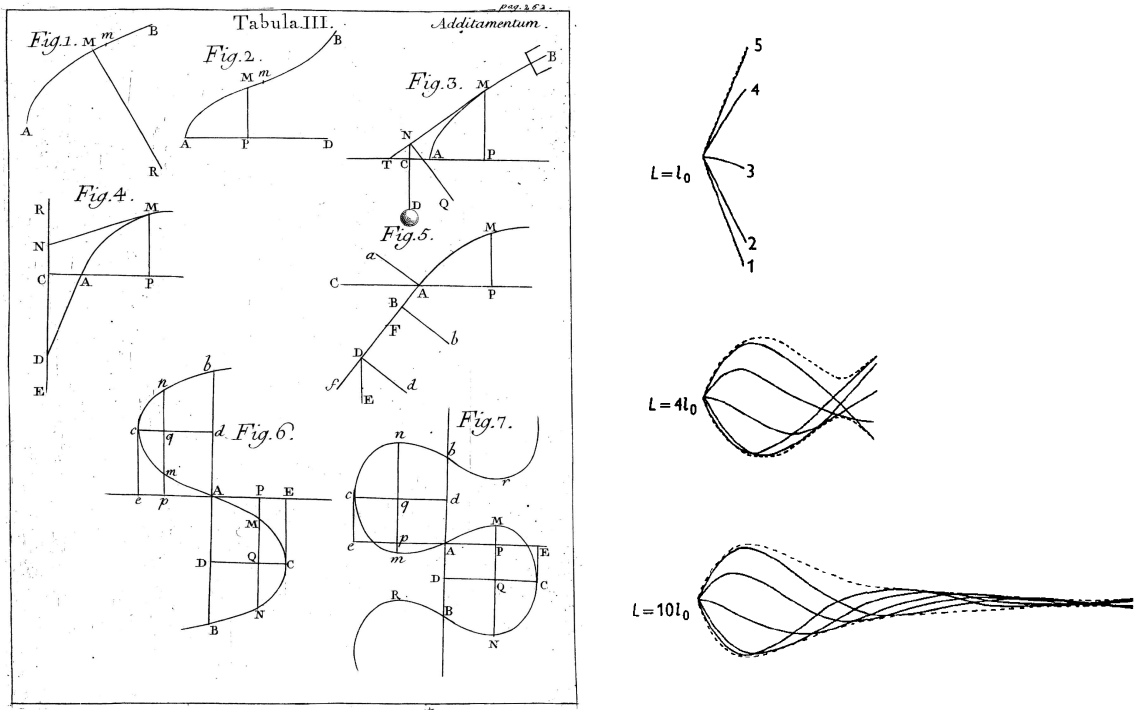

Figure 1.9: Example solutions for (a) the inflectional Euler-elastica [34] (no copyright restriction), and (b) the hyper-diffusion equation, Eq. (1.30), first reported by Machin [88] (reproduced with permission from Journal of Experimental Biology).

Jacobian elliptic integral of 1st kind, and it is a periodic function with a period π, with a maximum of $(1-\ell^2)^{1/2}$ at $\phi = (2p+1)\pi/2$ and minimum of 1 at $\phi = q\pi$, where p, q are integers. The family of solutions for the inflectional elastica was first reported by Euler [34], and is illustrated in Fig. 1.9(a). Furthermore, by linearising Eq. (1.25) it is possible to evaluate the critical load,

$$P_e = \frac{\pi E}{L^2}, \tag{1.29}$$

which is required for the elastic buckling of the rod, also referred as Euler-Buckling.

1.4.2.2 The hyper-diffusion equation

Now, if we consider instead that the elastic slender filament is embedded in a viscous fluid, the total contact forces are balanced by the hydrodynamic drag experienced by each element ds along the filament. Working to first order in deflection

$h(s)$, and balancing this elastic force with the transverse viscous force from resistive force theory, we find the so-called hyper-diffusion equation

$$\xi_{\perp}\, h_t = -E\, h_{xxxx}, \tag{1.30}$$

where the subscript t and x denotes differentiation with respect to time and space, respectively. The shape of the slender body is then given in terms of a linear combination of hyperbolic and trigonometric functions [46, 47, 88, 140], still subjected to appropriate boundary conditions, which are typically assumed to be force free and torque free conditions at the endpoints. Eq. (1.30) describes the linearised elastohydrodynamics of a passive filament in a viscous fluid and has already been studied analytically [15, 36, 40, 46, 47, 63, 88, 140, 141] and experimentally [15, 140, 144]. The historical significance of Eq. (1.30), however, dates back to the pioneering work from Machin [88], who realised, while solving the elastohydrodynamics of angularly actuated filaments, illustrated in Fig. 1.9(b), that actively contractile elements along the flagellum length should be required in order to maintain the flagellar bending observed in spermatozoa experiments. This hypothesis was later validated with the discovery of the axoneme internal structure, revealing that dynein internal bending moments are responsible for actively driving flagellar wave propagation [112].

1.4.2.3 Euler-Bernoulli theory vs. flexible filamentous structures in biology

Due to the simplicity of the Euler-Bernoulli theory [8, 41], the formulation presented here for slender filaments has been applied to several biological systems in order to explain shape deformations of filamentous polymers [29, 30, 45, 60, 67, 71, 84, 95, 97, 98, 103, 126, 133, 134, 139, 140], such as cytoskeletal filaments, and most importantly to extract filament material properties from experiments [*ibid*]. Hence, the elastic bending rigidity that we often find in textbooks [58] and elsewhere in the literature [29, 30, 45, 60, 67, 71, 84, 95, 97, 98, 103, 126, 133, 134, 139, 140], with almost no

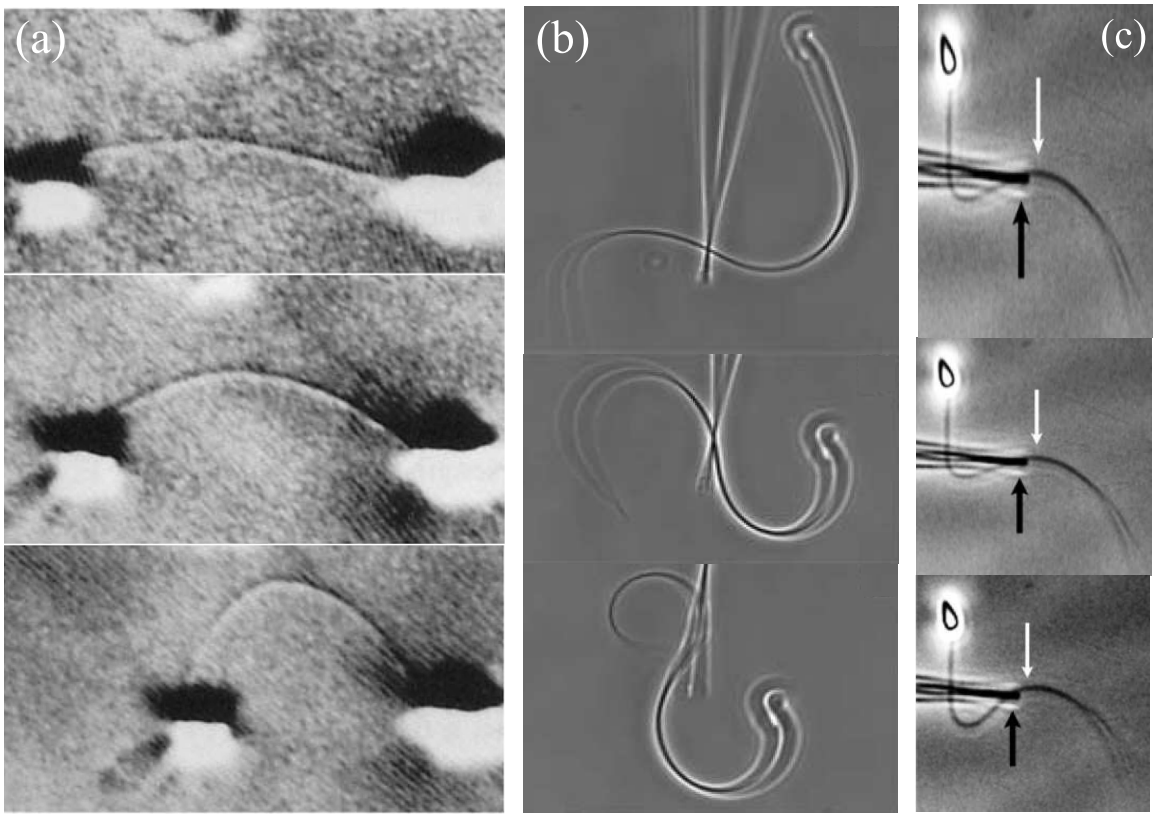

Figure 1.10: Example shape deformation of biological filaments during buckling experiments of: (a) microtubules [71] (b) a rat sperm flagellum [84] and (c) a sea urchin sperm flagellum [103]. Figure reproduced from Kurachi et al. [71], Lindemann et al. [84] and Pelle et al. [103], with permission from John Wiley and Sons (2958780034260), Elsevier (2958780544029) and John Wiley and Sons (2958780742312), respectively.

exception, was measured by employing some form of linear relation between bending moment and curvature, from actin filaments and microtubules [29,30,45,60,67,71,95, 126,133,134,139,140], to the sperm flagellum of different species [82,84,97,98,103], despite the inherent complexity associated with the internal architecture of these flexible bodies. Incidentally, the inadequacy of this theory when applied for complex biological structures often appear in the literature as a paradoxical empirical phenomenon. This was the case, for instance, of the length-dependent bending rigidity in microtubules [64,70,71,76,102] measured from load-displacement experiments [71], as illustrated in Fig. 1.10(a), despite the similarity between the deformed

shapes, Fig. 1.10(a), and the Euler-elastica, Fig. 1.9(a). But most importantly, recent empirical studies revealed the structural significance of the flagellar cross-linked proteins while developing the counterbend phenomenon [84, 103], as illustrated in Figs. 1.10(b,c). This apparent paradoxical effect takes place when a passive flagellum, simply obtained by disabling the dynein molecular motors, is forced under the action of an external load. This phenomenon was first reported during buckling experiments of passive rat sperm flagellum [84], Fig. 1.10(b), however, because in mammals the sperm flagellum is reinforced by additional ultrastructural components (Fig. 1.3), it was not entirely clear which structural interaction was fundamental while instigating the counterbend effect. A few years later, Lindemann and co-workers [103] established the counterbend phenomenon as an intrinsic mechanical effect of the axoneme (Fig. 1.4), during bucking investigations of sea urchin sperm flagellum, Fig. 1.10(c), which is solely composed by the axoneme surrounded by a plasma membrane. In this case, because the axonemal structure is composed of $9 + 2$ microtubules, arranged cylindrically, and each microtubule is interconnected by radial spokes and nexin links, deeply embedded within the flagellum (Fig. 1.4), it is no surprise that the resulting elastic structure do not behave as a simple Euler-Bernoulli filament, contrast for instance Figs. 1.9(a) and 1.10(c). In particular, the inadequacy of the Euler-Bernoulli theory on these systems motivated theoretical investigation presented in Chapters 4 and 5 of this DPhil work.

1.5 Thesis overview

The aim of this DPhil thesis is to explore the internal mechanical response of the sperm flagellum by considering distinct structural interactions via first principle studies. By using microbiomechanical modelling and simulation, we develop bio-inspired mathematical models to allow the exploration of sperm motility and the material response of the sperm flagellum. Using these models to explore the underlying scientific

questions motivating this study will not only provide valuable insights regarding the mechanical function of the constituent elements within a sperm flagellum. It may also assist us in interpreting the acquired data from human sperm experiments, Sec. 1.3, in more detail [43], as well as generating evidence based hypotheses for guiding novel directions of experimental investigation.

All chapters are motivated and organised independently for each system under consideration. In the first half of the thesis, Chapters 2 and 3, we explore spermatozoa dynamics by coupling the internally generated forces with the fluid-structure interactions utilising resistive-force theory, which is logarithmically accurate in the slenderness parameter and does not require computationally costly and numerically difficult integrations, as discussed above. In particular, motivated by the large deformations of the flagellum observed in experiments, as illustrated in Figs. 1.5 and 1.6, we explore how geometrically non-linear elastic effects may influence the flagellar waveform and the consequences for the biophysics of flagellated swimming. In Chapter 3 we extend the biomathematical model developed in Chapter 2 to incorporate the mechanical influence of the accessory structures found in human spermatozoa, i.e. the passive elastic influence of the flagellar ultrastructural tapering along the flagellum length (Fig. 1.3).

The flagellum structural response is the subject of the second half of the thesis, where we study the resulting material shearing response from the passive elastic crosslinking connectors found in flagellar axonemes. The classical Euler-Bernoulli filament theory is generalised in Chapter 4 to include the mechanical influence of shearing deformations, by employing the Cosserat theory of rods. While the mathematical theory described in Chapter 4 can be used for inextensible shearable filaments, such as the microtubules within the flagellum, we show that the pure material shearing effects are fundamentally different from the elastic cross-link induced shear within the axoneme, detailed discussed in Chapter 5. In this instance, we develop a mathemat-

ical model based on the sliding-filament mechanism to elucidate the static scenario of the counterbend phenomenon, Fig. 1.10(c), providing in this way a comparative analysis between the Euler-Bernoulli filament theory, pure material shearing and the axonemal cross-link induced shear. Conclusions and future directions are presented in Chapter 6.

Chapter 2

Non-linear instability in flagellar dynamics

2.1 Introduction

Spermatozoan motility is critical for natural fertilisation and relies on the whip-like beating of a flagellum. This waveform arises through an intricate balance of internally generated shear, flagellar elastic resistance and hydrodynamic viscous drag. Despite complex beat patterns, aspects of the overall swimming trajectories are simply related to properties of flagellar bending. In particular, averaged over a beat cycle, symmetrical flagellar waveforms propel free swimming cells in relatively straight paths [49,65,119,120], while bending asymmetry drives the cell in curved trajectories, as illustrated in Fig. 2.1(b). Furthermore, when the sperm head is pinned to a surface, beat asymmetry induces cell rotation about the point of attachment [48]. Asymmetric bending has also been observed to be important in the chemotactic response of sperm [92, 137] and during hyperactivation [65, 68], a motility change which has been demonstrated to be necessary for successful fertilisation. However, despite the vital role of symmetry breaking phenomena for the flagellar waveform, and consequently for sperm transport, the mechanism by which asymmetric beating is generated is yet to be fully understood.

Domain boundaries can also induce asymmetric dynamics [65]. When sufficiently

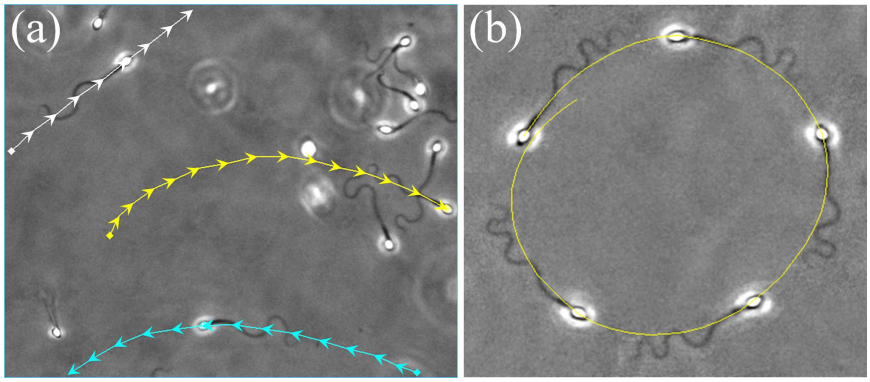

Figure 2.1: Imaging frames for non-rolling human sperm cells migrating within a viscous medium, containing 2% methyl-cellulose, in a capillary chamber of 400μm depth, captured at the same focal plane: (a) Swimming trajectories (*arrows*) for three cells, indicated in white, yellow and cyan and plotted at same time interval, 0.4s. (b) A circularly swimming cell further along the capillary chamber; the imaging sequence is superimposed at equal time intervals of 2 seconds with the swimming trajectory given by the yellow curve. For further details about the microscopy materials and methods, see Appendix A. Figure originally published by Gadêlha et al. [42].

close to a solid boundary, typically at a distance of less than the sperm body length, numerous swimming behaviours have been observed. Rodent sperm with hook-like heads often swim with a planar flagellar waveform and a trajectory curvature of fixed chirality relative to the sperm head. This is considered to arise from the influence of head geometry on stable surface swimming [142]. Similarly, for sperm with more symmetrical heads, non-planar beating can occur with cell rolling during surface swimming, resulting in circular swimming trajectories in the direction of cell rolling, which is always the same within a species [*ibid*].

Surfaces do not always appear to dictate the symmetry breaking of sperm cells. This is illustrated in Fig. 2.1(a), for non-rolling human sperm that have migrated significant distances within a deep chamber (400μm) filled with a physiological high viscosity medium. Here, clockwise (yellow) and counterclockwise (cyan) surface swimmers can be observed together with an approximately straight swimming path (white). In this case no obvious morphological feature, nor presence of a nearby surface, dictates the chirality of path curvature. In Fig. 2.1(b), the manifest asymmetrical bend-

ing associated with circular swimming is also illustrated.

These observations readily establish that symmetry breaking and curved trajectories can occur without cell rolling or asymmetric cell morphology and need not be driven by dominant boundary influences. In such cases it is not clear whether an internal asymmetry of the flagellum is dynamically important and driving symmetry breaking, whether it is due to an asymmetric force generation by the dynein molecular motors, as indicated in hyperactivation arising from elevated intracellular calcium [124], or the subtle heterogeneities of flagellar structure [38]. This is especially the case for species such as human which can also exhibit highly symmetric waveforms. Thus, our aim is to explore whether physical principles support the null hypothesis that asymmetric flagellar waveforms can be generated with no intrinsic asymmetry and without asymmetric internal forces via a dynamical instability, as observed with passive filament bending in viscous shear flows [13]. In the following study, we therefore summarise relevant features of flagellar mechanics, construct a simple elastohydrodynamical model exploring flagella waveform symmetry breaking for sperm motility within viscous, Newtonian, fluids and, finally, place the findings in the context of sperm motility through numerical simulations and a parameter study.

2.2 Flagellar mechanics

The elastohydrodynamic formulation, which couples the structural mechanics of the flagellum with the surrounding fluid, has been extensively studied [17, 18, 21, 22, 40, 55–57, 79, 88, 109], both experimentally and theoretically. The founding study [88] proposed that an internal forcing mechanism was required to maintain the flagellar bending observed in spermatozoa experiments. This hypothesis was later established with the discovery of the axoneme internal structure, revealing that sliding microtubules drive active flagellar bending [112]. Although Brokaw first considered this microtubule sliding mechanism in modelling flagellar locomotion [17, 18],

the non-linear flagellar elastohydrodynamic equations were only derived several years later [57]. Later, analogous, models have also been proposed in the literature, exploring both linear [21, 22, 40, 109] and more recently weakly non-linear dynamics [55].

Despite such progress in modelling the internally driven flagellum, the influence of dynamical non-linear instabilities on the emergent flagellar beat pattern and the consequences for cell swimming have been largely neglected. Nonetheless, non-linear instabilities are well established for the biophysical dynamics of slender body systems, including gliding motility assays of cytoskeletal filaments with flow defects [15], torque-induced writhing of a rotating elastica [141] and the behaviour of passive filaments within shear flows [13, 63]. The latter in particular highlights that instabilities can emerge from filament compression, with a sharp transition to buckling followed by complicated shape perturbations. Recent studies of flagellar waveform mechanics have initiated explorations of internally generated shear between the microtubules via a linear formulation [21, 22, 40, 109], as well as considering the lowest order non-linear effects on the self-organised bending waves [55]. These investigations highlight that the emergent axonemal beat patterns are a good approximation to the weakly non-linear problem [55]. However, except for a brief, perturbative, study on the role of tension due to an external force [21], the possibility that non-linear tension dynamics can induce dynamical symmetry breaking has been widely neglected in active flagellar mechanics. Furthermore, this entails that the range of validity of the linear model is not completely explored.

Thus, in contrast to the vast majority of works on the internally driven filament, we investigate whether flagellar tension can induce symmetry breaking via a buckling mechanism and how it may influence flagellar beating and sperm swimming trajectories. This requires considering geometrical nonlinearities in flagellar models coupling internal shear generation via microtubule sliding, the flagellum elastic response, and viscous drag. In addition, we also explore the agreement between the geometric non-

linear theory and the linear approximation. This will allow us to delimit the region of validity of linear theory in parameter space, further bridging the gap between linear and non-linear regimes. In turn, such studies will be important for the formulation of well-founded models for forced elastohydrodynamic problems in the future.

2.3 Elastohydrodynamic formulation

We consider an internally driven sperm flagellum with a planar waveform, immersed within a viscous fluid. Inertial effects are negligible, due to the very low Reynolds number of sperm swimming, while the hydrodynamic interactions are simplified using resistive-force theory (RFT) [49]. This local drag model is the leading order term of the equations of slender-body hydrodynamics [61], and it is simply specified by a local linear relation between the velocity of the flagellum centreline and the force (per unit length) exerted on the fluid, through the anisotropic drag coefficients. Although resistive-force theory is only valid for very slender filaments, it is widely used for general elastohydrodynamic problems, including relaxational and forced dynamics of stiff polymers [13, 15, 46, 47, 88, 140, 141, 144], as well as flagellar dynamics [17, 21, 22, 40, 55–57, 62, 79, 88, 109], among others. Theoretical predictions using RFT have previously shown a remarkably good agreement with experimental measurements for actuated filaments [140, 144] and the buckling instability exhibited by a single passive filament within a shear flow [13, 63, 131]. In addition, microscopy imaging [109] has also confirmed that RFT is surprisingly accurate when applied to bull sperm flagellar dynamics, while numerical simulations accounting for non-local hydrodynamic effects support the use of RFT for microswimmers with relatively small cell bodies, including human sperm [62].

Sperm flagellar motion is driven by dynein motor proteins exerting a relative shearing force between outer adjacent filaments, or microtubules, of the flagellar axoneme: this is referred to as the sliding filament model [17, 18, 21, 22, 40, 55–57, 109].

For planar flagellar waveforms of mammalian sperm there is a preferred plane of beating imposed by the mammalian flagellar accessory structures [85]. In this context, faithful three-dimensional descriptions of the cylindrical arrangement of microtubule doublets in mammalian sperm have been shown to be equivalent to a simpler two-dimensional representation of the sliding forces within the axoneme, as depicted in Fig. 2.2 [55, 56]. Here, a pair of parallel elastic filaments may slide relative to each other within the beat plane in response to dynein forces. Each sliding filament is assumed to be homogeneous, inextensible and separated by a constant gap spacing b, which corresponds to the axoneme diameter. At the sperm head junction, we assume for simplicity that no interfilament shear is permitted due to structural constraints. The axoneme motor proteins induce active shear stresses along the flagellum, which act in opposite directions and force the filaments to locally slide with respect to each other, inducing flagellar bending (see Fig. 2.2).

2.3.1 Geometrically non-linear theory: equations of motion

It is convenient to describe the flagellum position, relative to the laboratory frame of reference, by its neutral line $\mathbf{X}(s,t)$ (see Fig. 2.2), noting that t is time and s denotes the distance along the flagellum with $0 \leq s \leq L$, where L is the filament length. The local flagellum coordinate system is represented as an orthonormal pair with a positive orientation $(\hat{\mathbf{s}}(s,t), \hat{\mathbf{n}}(s,t))$, where $\hat{\mathbf{s}} = \mathbf{X}_s \equiv \partial\mathbf{X}/\partial s$ is the tangent vector and $\hat{\mathbf{n}}$ is the vector normal to the flagellum centreline (Fig. 2.2). The sperm flagellum local sliding displacement can be expressed in terms of flagellum bending via geometry, and the position vector of the filament above and below the neutral line is given by

$$\mathbf{r}_{\pm} = \mathbf{X}(s,t) \pm \frac{b}{2}\,\hat{\mathbf{n}}(s,t), \tag{2.1}$$

as depicted in Fig. 2.2, where $\hat{\mathbf{n}}(s,t)$ is normal to the flagellum and b is the flagellar axoneme diameter. The filament sliding displacement, at a point $\bar{s}$ along the flagellum,

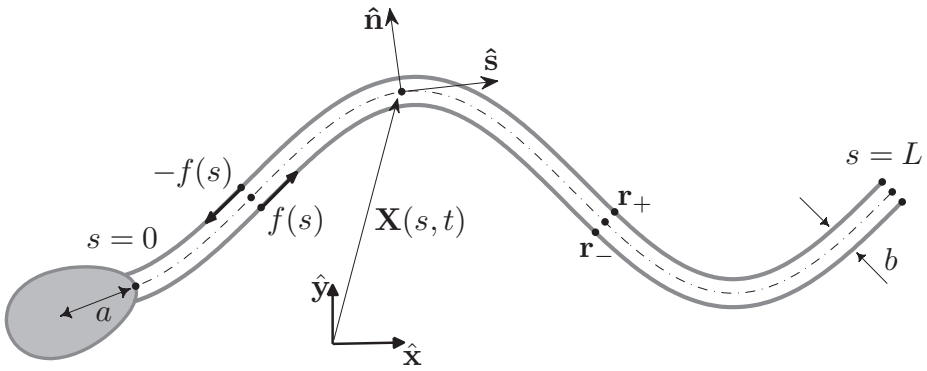

Figure 2.2: A schematic of the sliding filament mechanism. Relative to a laboratory fixed frame $\{\hat{\mathbf{x}}, \hat{\mathbf{y}}\}$, the vector $\mathbf{X}(s,t)$ describes the position of the point which is an arclength s along the flagellum neutral line (dashed curve) at time t. The internal shear force $f(s,t)$ is acting tangentially and in opposite directions on each sliding filament $\boldsymbol{r}_{\pm}(s)$ (solid gray curves) causing the flagellum to bend. The distance between the centre of mass of the sperm head and the flagellum junction is denoted by a and the flagellar axoneme diameter is b. Figure originally published by Gadêlha et al. [42].

can be defined as the total arclength difference between the upper and lower filaments:

$$\Delta(\bar{s}) = \int_0^{\bar{s}} (|\partial_s \mathbf{r}_-| - |\partial_s \mathbf{r}_+|) \, \mathrm{ds}. \tag{2.2}$$

Utilising variational calculus, the internal forces acting on the flagellum, together with the natural boundary conditions, can be easily derived from the principle of minimum potential energy [41]. With this approach and neglecting twist elasticity [47], the energy functional is

$$\nu = \frac{1}{2} \int_0^L \left[E\mathbf{X}_{ss}^2 + 2f\Delta(s) + \tau \left(\mathbf{X}_s^2 - 1 \right) \right] \mathrm{ds}, \tag{2.3}$$

where the first term represents the energy associated with the bending forces, with constant elastic stiffness E, and the last term is the Lagrange multiplier τ acting to reinforce a constant flagellum length. The second term is the work done by the internal shear density $f(s,t)$, which couples the dynein molecular motor activity and the passive cross linking proteins and drives the bending deformations on the sperm flagellum. At equilibrium, the variation of ν with respect to the virtual displacement

$\delta\mathbf{X}$ must vanish; after integrating by parts twice and collecting terms, it is possible to write the internal elastic force per unit length,

$$\mathbf{f}_{\text{int}} = -\partial_s \left[E\mathbf{X}_{sss} - bf\hat{\mathbf{n}} - T\mathbf{X}_s \right], \tag{2.4}$$

in terms of $\mathbf{X}(s,t)$, the internal shear density $f(s,t)$ and the tension $T(s,t)$, which is a combination of the Lagrange multiplier τ and the tangential component of the elastic force. Because the contact forces are not constitutively specified [8], $T(s,t)$ is unknown and determined by the inextensibility condition i.e., the tension acts to preserve the flagellum length by resisting extension or compression during deformation. Note that the calculations required to derive Eq. (2.4) are simplified by working with the total shear stress acting on the flagellum between arclength s and the maximum arclength, L,

$$F(s,t) \equiv -\int_s^L f(s',t)\,\mathrm{d}s', \tag{2.5}$$

as extensively detailed by [21].

Furthermore, deriving the expression for the internal elastic force, Eq. (2.4), also requires boundary terms of the energy functional variation ν to vanish, naturally yielding force and torque balance at the flagellum ends. Also, from Eq. (2.4), the internal force $\mathbf{F}_{\text{int}}$ acting on the flagellum between arclengths s and L is simply

$$\mathbf{F}_{\text{int}} = -E\mathbf{X}_{sss} + bf\hat{\mathbf{n}} + T\mathbf{X}_s. \tag{2.6}$$

By inspecting Eq. (2.6) one can see that the internal shear, originating from sliding forces, is acting purely in the normal direction, and working against the elastic relaxational bending, tensile forces and, as we will see later, viscous drag, in order to deform the flagellum.

2.3.1.1 Fluid-structure coupling

The viscous drag force per unit length experienced by the sperm flagellum, $\mathbf{f}_{\text{vis}}$, is modelled using resistive-force theory [49]. Thus we have

$$\mathbf{f}_{\text{vis}} = -\left[\xi_{\perp}\hat{\mathbf{n}}\hat{\mathbf{n}} + \xi_{\parallel}\hat{\mathbf{s}}\hat{\mathbf{s}}\right]\mathbf{X}_t, \tag{2.7}$$

where the subscript t denotes differentiation with respect to time, $\hat{\mathbf{s}}$ is tangent to the flagellum, and $\xi_{\perp}, \xi_{\parallel}$ represent, respectively, the perpendicular and parallel fluid dynamic resistance coefficients. The dynamics of the sperm flagellum, and hence ultimately the sperm cell, arises via balancing the viscous drag force per unit length of the flagellum with the internal elastic forces; hence $\mathbf{f}_{\text{vis}} + \mathbf{f}_{\text{int}} = 0$ at all points along the flagellum. We nondimensionalise with respect to the length scale L and time scale ω^{-1}, for a given flagellum length L and beating frequency ω, together with a rescaling of the force density by E/L^3, where E is the flagellum bending stiffness. This yields the dimensionless elastohydrodynamic equation of motion for the flagellum neutral line

$$\begin{aligned}\mathrm{Sp}^4\mathbf{X}_t = &-\mathbf{X}_{ssss} - (\gamma - 1)\left(\mathbf{X}_s \cdot \mathbf{X}_{ssss}\right)\mathbf{X}_s \\ &+ \left(T\mathbf{X}_{ss} + \gamma T_s \mathbf{X}_s\right) + \left(f_s\hat{\mathbf{n}} + \gamma f \hat{\mathbf{n}}_s\right),\end{aligned} \tag{2.8}$$

where $\gamma = \xi_{\perp}/\xi_{\parallel}$ is the anisotropic ratio. The important dimensionless number

$$\mathrm{Sp} = L\left(\frac{\xi_{\perp}\omega}{E}\right)^{1/4} \tag{2.9}$$

is the *sperm-compliance parameter* and measures the relative importance of the flagellum elastic rigidity compared to its characteristic viscous drag force [47, 140]. Also, note that Eq. (2.8) can be derived from a full three-dimensional dynamic description of the axoneme, and does not require the introduction of the explicitly two-dimensional axoneme representation shown in Fig. 2.2 [55]. The tensile force along the flagellum $T(s,t)$ is determined by the filament inextensibility constraint $\partial_t(\mathbf{X}_s \cdot \mathbf{X}_s) = 0$;

utilising Eq. (2.8), this can be written in the explicit form:

$$\gamma T_{ss} - (\mathbf{X}_{ss} \cdot \mathbf{X}_{ss})T = -3\gamma(\mathbf{X}_{sss} \cdot \mathbf{X}_{sss}) - \gamma(\hat{\mathbf{n}}_{ss} \cdot \mathbf{X}_s)f$$
$$- (3\gamma + 1)(\mathbf{X}_{ss} \cdot \mathbf{X}_{ssss}) - (\gamma + 1)(\hat{\mathbf{n}}_s \cdot \mathbf{X}_s)f_s. \tag{2.10}$$

However, in practice, numerical instabilities associated with stiff fourth-order derivatives in Eqs. (2.8) and (2.10) may be introduced and exacerbated during the simulations [131], ultimately causing $|\mathbf{X}_s|$ to vary. This is resolved by considering, instead,

$$\frac{1}{2}\partial_t(\mathbf{X}_s \cdot \mathbf{X}_s) = \lambda \mathrm{Sp}^4(1 - \mathbf{X}_s \cdot \mathbf{X}_s),$$

which introduces the term $\lambda \mathrm{Sp}^4(1 - \mathbf{X}_s \cdot \mathbf{X}_s)$ on the right hand side of Eq. (2.10). This term is theoretically zero; however, it dampens length errors as they occur hence improving the performance of the numerical algorithm. Our solutions typically used $\lambda = 40$, but they are insensitive to the details of the choice of λ, as also observed for dynamics of passive elastic filaments in a viscous fluid [131]. We also have verified that under an appropriate variable transformation, the equations of motion presented here agree with previous work [21, 50, 57] for a generic internal shear distribution f.

Although the sliding filament mechanism has been successful in explaining flagellar bending, there is a limited quantitative understanding of the regulation and nature of the internal shear stress f, which represents the coupling between the dynein molecular motor activity and the passive cross linking proteins within the flagellum [20, 94]. There have been several attempts to explain the observed flagellar beat via different shear-control hypotheses dictating the regulation of internal shear f [17, 18, 20–22, 57, 79, 94], though comparison with experiments has only become possible recently [109]. Here, it is beyond the scope of the study to consider detailed assessments of the internal shear regulation and the difficulties associated with dynein control mechanisms, including chemical cues that may influence the axonemal beating clock. Instead, we use a symmetric model, based on observations of shear in-situ, to explore the symmetry breaking event. As detailed in Appendix A, travelling waves of

bending [120], and thus internal shear forces, periodically propagate down the flagellum; given that the dominant mode typically dictates the dynamics [109] we therefore model the internal shear density as a simple travelling wave

$$f(s,t) = A\cos(ks - t), \tag{2.11}$$

with dimensionless force amplitude A and wavenumber k. This particular choice of internal shear will not just isolate the potential for symmetry breaking of a symmetrically driven flagellum, it will also enable us to investigate a wide range of shear distribution k, bringing to light new non-linear effects within a general framework.

2.3.1.2 Boundary and initial conditions

The equations governing the flagellar dynamics (Eqs. (2.8) and (2.10)) are closed by defining the initial flagellum and cell configuration together with the boundary conditions. From the natural boundary conditions of the variational treatment of flagellar dynamics, we are required to specify either the movement of the flagellar endpoints or to impose a balance of forces at the ends. In particular, at the distal boundary of the flagellum, $s = L$, we have no applied torque or force which yields

$$\begin{aligned} 0 = \mathbf{F}_{\text{ext}} &= -\mathbf{X}_{sss} + f\hat{\mathbf{n}} + T\mathbf{X}_s, \\ 0 = \mathbf{M}_{\text{ext}} \times \mathbf{X}_s &= \mathbf{X}_{ss}. \end{aligned} \tag{2.12}$$

At the proximal end of the flagellum, $s = 0$, we consider three boundary conditions motivated by common laboratory examples:

(a) **The clamped head.** The sperm head is strongly adhered, with no rotation about its point of attachment, so that both its position and tangent vectors are fixed at $s = 0$.

(b) **The pivoting head.** The sperm head is adhered at $s = 0$ so that it does not move except for rotation about its attachment, due to the absence of an external moment.

Table 2.1: Summary of the three choices of boundary conditions at the sperm head junction, $s = 0$. The pivoting head conditions are also supplemented by moment balance, Eq. (2.13), while the freely swimming sperm boundary conditions require force and moment balance, Eqs. (2.14)-(2.15).

Boundary Condition	Constraints at $s = 0$
(a) Clamped head	$\mathbf{X}_t = 0$ & $\mathbf{X}_{st} = 0$
(b) Pivoting head	$\mathbf{X}_t = 0$ & $\mathbf{M}_{\text{ext}} = 0$
(c) Free head swimming sperm	$\mathbf{F}_{\text{ext}} = \mathbf{F}_{\text{head}}$ & $\mathbf{M}_{\text{ext}} = \mathbf{M}_{\text{head}}$

(c) **The swimming sperm.** The flagellum is driving a cell body and thus experiences a viscous drag force, $\mathbf{F}_{\text{head}}$, and moment, $\mathbf{M}_{\text{head}}$, due to the sperm head.

The resulting boundary conditions are summarised in Table 1. For the pivoting sperm, the boundary conditions at $s = 0$ requires zero external moment, $\mathbf{M}_{\text{ext}} = \mathbf{0}$. When the angular motion at the boundary is not specified, the natural boundary conditions of the variational formulation require the moment balance [41]

$$\mathbf{M}_{\text{ext}} \times \mathbf{X}_s = -\mathbf{X}_{ss} + F\hat{\mathbf{n}}. \tag{2.13}$$

where F is given by Eq. (2.5) with $s = 0$. Thus the condition for the elastohydrodynamic partial differential equations (Eq. (2.8)) is obtained by imposing $\mathbf{M}_{\text{ext}} = \mathbf{0}|_{s=0}$ in Eq. (2.13) for the pivoting case.

Similar remarks on the moment balance apply for the swimming sperm boundary conditions, case (c). Now, however, $\mathbf{M}_{\text{ext}}$ is given by the viscous torque exerted on the flagellum at $s = 0$ by the cell body, $\mathbf{M}_{\text{head}}$. This can be expressed in terms of the cell body velocity, $\mathbf{U}$, and angular velocity, $\mathbf{\Omega}$, in the laboratory frame as detailed below. In addition, the external force on the sperm at $s = 0$, $\mathbf{F}_{\text{ext}}$, is given by $\mathbf{F}_{\text{head}}$, the viscous drag exerted on the flagellum by the cell body. The natural boundary conditions of the variational formulation impose the force balance at $s = 0$ [41]

$$\mathbf{F}_{\text{ext}} = \mathbf{X}_{sss} - f\hat{\mathbf{n}} - T\mathbf{X}_s \tag{2.14}$$

which in turn gives a boundary condition for the elastohydrodynamic partial differential equations (Eq. (2.8)), once $\mathbf{F}_{\text{ext}} = \mathbf{F}_{\text{head}}$ is known. For the swimming sperm, viscous fluid dynamics yields

$$\begin{pmatrix} \mathbf{F}_{\text{head}} \\ \mathbf{M}_{\text{head}} \end{pmatrix} = L^4 \left(\frac{\eta\omega}{E} \right) \mathcal{R}(a/L, t) \begin{pmatrix} \mathbf{U} \\ \mathbf{\Omega} \end{pmatrix}, \tag{2.15}$$

where η denotes the fluid viscosity and $\mathcal{R}$ represents the dimensionless grand-resistance matrix for the sperm head. This depends on the geometrical properties of the head, as well as the distance between its centre of mass and the sperm junction, represented by the parameter a in Fig. 2.2. Note that the effective load in Eq. (2.15), $L^4(\eta\omega/E)$, scales with the fourth power of the sperm-compliance parameter, Sp, and that the grand-resistance matrix is time dependent since it is relative to the laboratory fixed frame. Closure is therefore finally achieved for Eq. (2.8) by noting that $\mathbf{U} = \mathbf{X}_t|_{s=0}$ and $(\mathbf{X}_{st} \times \mathbf{X}_s)|_{s=0} = -\mathbf{\Omega}$, whence Eqs. (2.15) and (2.14) yield the required boundary condition at $s = 0$ for the neutral line $\mathbf{X}$.

The initial configuration was chosen, without loss of generality, to be a straight line. After evolving in time under the action of a periodic internal shear f, the flagellum reaches a long time asymptote of periodic motion, so that the final solution is independent of initial transients.

2.3.1.3 Parameter estimation

The fluid dynamic resistance coefficient for a translating cylinder in a fluid, with the cylinder axis normal to the flow direction, is proportional to fluid viscosity but depends very weakly on its the aspect ratio [49, 78]. For the low viscosity, watery, in-vitro fertilisation medium used in [120] $\xi_\perp = 1.4 \times 10^{-3}$ Pa.s, rising to $\xi_\perp = 3.2$ Pa.s for the most viscous fluids considered, assuming a Newtonian behaviour. This study also revealed beating frequencies of $\omega = 11$ Hz for the most viscous media considered, while $\omega = 23$ Hz for the in-vitro fertilisation medium. Moreover, the human flagellum length is around 50 μm [2] and its average bending stiffness, E,

is estimated to be 4×10^{-21} Nm^{-2}. The latter merits some attention as it is not based on human data. The average rat flagellum stiffness has been measured as approximately 2.5×10^{-19} Nm^{-2} [84], but its outer dense fibres have eight times the cross sectional area of the human sperm analogue [11]. Furthermore, with the exception of the anomalous bull sperm and guinea pig sperm, cross species mammalian flagellar structural properties are observed to scale approximately with geometry for fixed material properties [*ibid*]. Noting that for a given material, the bending stiffness of a filament scales with the square of its cross sectional area, we estimate the human sperm bending stiffness as 1/64 that of the rat, giving 4×10^{-21} Nm^{-2}. Hence the sperm-compliance parameter $\mathrm{Sp} = L(\xi_\perp \omega/E)^{1/4}$ ranges between $\mathrm{Sp} = 4$ to $\mathrm{Sp} = 24$, working to the nearest integer given the level of approximation used.

While we typically focus on this range in the illustrative examples in Sec. 2.4, values of Sp as low as unity are addressed for completeness when exploring the validity of linear theory. This may be relevant for model construction when simulating aquatic cells with substantially shorter flagella, for example the choanoflagellates [105]. Similarly, these values of Sp are also relevant for recent actuated elastic filament experiments [144]; see Fig. 2.3.

2.3.1.4 Numerical methods

The numerical scheme was based on a combination of second-order finite differences and second-order implicit time-stepping. Eqs. (2.8) and (2.10) are highly-coupled non-linear partial differential equations, mainly characterised by their fourth-order derivatives, yielding severe constraints for the time-stepping size if all terms in Eq. (2.8) are treated explicitly [131]. This is resolved by performing a second-order implicit-explicit method (IMEX) [10], where only the higher-order terms $\mathbf{X}_{ssss}$ are treated implicitly, and before any previous time level is available, we replace the second-order IMEX by the first-order IMEX [10]. The spatial discretization is uniform in arclength with N intervals. Second-order divided differences are used to

approximate spatial derivatives, in which skew operators are applied at the boundaries [131]. As a result of both spatial and temporal discretizations, the timestep can be chosen to be the same order of magnitude as the grid spacing, yielding just a first-order constraint for timestepping. Once the iterations have been initiated via a first order IMEX scheme, which is analogous to the algorithm below, the numerical scheme is summarised as follows:

- The tension equation (Eq. (2.10)) is only a function of $\mathbf{X}$, an active force f, which is given, and other known parameters. Consequently, all coefficients of tension and its derivatives in Eq. (2.10) can be easily evaluated at the n^{th} time point, t^n, as the flagellum positions are known from earlier iterations.

- Natural force boundary conditions, where the forces at the flagellum ends are known, possibly in terms of other modelling variables (e.g. $\mathbf{U}$), are coupled to the tension. The tangential projection of these yield constraints on the tension at the flagellum ends, that is boundary conditions for the tension equation. When the location of a flagellum end is imposed, the natural force boundary conditions do not apply [41] and Eq. (2.8) at the end grid point of the flagellum is not used in the timestepping of $\mathbf{X}$. However, it still constrains the tension, so that the tension equation can be solved.

- Given the tension at the n^{th} time point t^n, Eq. (2.8) can be timestepped using the appropriate boundary conditions to obtain the flagellar position at the next time point. For the free head swimmer case, the time stepping additionally accommodates the net motion of the sperm and utilises a second order Heun's method. Further progress is achieved by iteration.

2.3.1.5 Model validation

Our non-linear second order implicit-explicit (IMEX) numerical scheme has been validated against experiments and numerical solutions for the actuated elastic filament

problem [144]. In this instance, the internal shear f vanishes in Eq. (2.8), where, at $s = 0$, the passive elastic filament is subjected to an angular periodic actuation, with amplitude a_0 and frequency ω, while the distal end of the filament is force and torque free. A comparison of experimental observation (red circle) with the linear (green line) and non-linear (dashed blue line) theories for various filament characteristics and actuations was performed by [144] and illustrated in Fig. 2.3. The original figure taken from [144] was modified to include the non-linear second order IMEX numerical scheme solution, represented by the solid black line displayed in Fig. S2. Note that Ref. [144] considered non-linear equations for the actuated elastic filament in terms of the local angle ϕ of the filament tangent vector $\mathbf{X}_s = (\cos\phi, \sin\phi)$, instead of the filament centreline $\mathbf{X}(s,t)$, as in Eqs. (2.8) and (2.10). Their numerical solution (dashed blue line) used a Newton-Raphson iteration in contrast to our second-order IMEX scheme though the models are equivalent in principle for zero internal shear. There is an excellent agreement between our numerical simulation and experiments [144] (see Fig. 2.3); in particular, our non-linear solution provides a slightly better match to observation than the results presented by [144]. Furthermore, global force and torque balances have been confirmed for the second order IMEX numerical scheme for numerous prototypical background flows and internal shear configurations, including the passive filament case $f = 0$.

2.3.2 Parallels with the linear theory

For small deflections, [21] have shown that the equation of motion (Eq. (2.8)) simplifies to

$$\mathrm{Sp}^4 \mathrm{h}_t = -\mathrm{h}_{ssss} + f_s, \tag{2.16}$$

where $x \approx s$ and $\mathbf{X}(s,t) \approx s\hat{\mathbf{x}} + \mathrm{h}(s,t)\hat{\mathbf{y}}$. The tensile forces only contribute at subleading orders and hence $T(s,t) \approx 0$. In the absence of internal shear, Eqs. (2.8), (2.16) describe the elastohydrodynamics of a passive filament in a viscous fluid and have

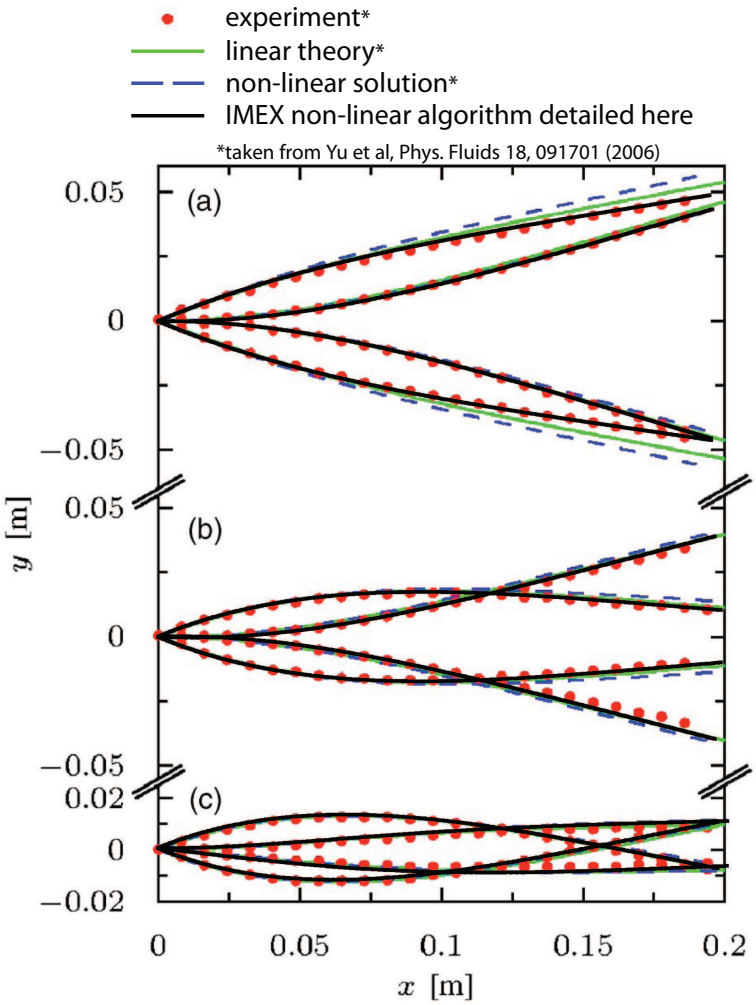

Figure 2.3: Comparison between experiment (red circles), linear (solid green line), and non-linear (dashed blue line) theories of filament shapes for a harmonic angular actuation $\theta = a_0 \sin(\omega t)$ at $s = 0$, taken from Ref. [144]. Snapshots are shown at four points in the cycle for one filament with length $L = 20$ cm, diameter $b = 0.5$ mm, angular amplitude $a_0 = 0.435$ rad, at three different oscillation frequencies: $\omega = 0.50$ rad/s (Sp = 1.73), $\omega = 1.31$ rad/s (Sp = 2.20), and $\omega = 5.24$ rad/s (Sp = 3.11), where Sp is the 'sperm' compliance parameter for the actuated filament. The black solid line correspond to the non-linear solution of Eqs. (2.8) and (2.10) by using the second order IMEX numerical scheme, while the dashed blue line correspond to the non-linear solution using a Newton-Raphson iteration from Ref. [144]. Figure originally published by Gadêlha et al. [42].

already been studied analytically [15, 40, 46, 47, 88, 140, 141] and experimentally [15, 63, 140, 144]. Despite the relative simplicity of the linearised formulation (Eq. (2.16)), there has not been a study of its accuracy compared to the full non-linear framework

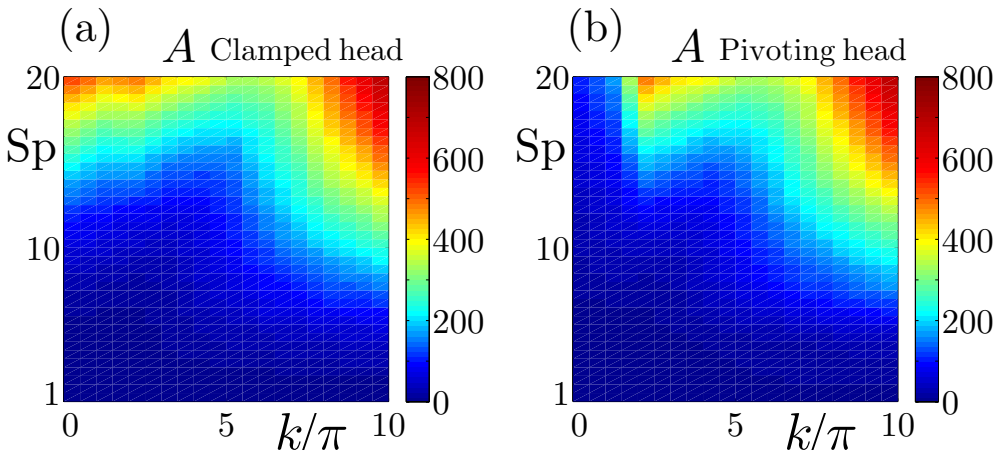

Figure 2.4: The dimensionless shear magnitude A, Eq. (2.11), required to produce flagellar bending waveforms with amplitudes of 10% of the flagellum length, as predicted from the linear theory, Eq. (2.16). This is plotted as an interpolated function of the sperm-compliance parameter, Sp, and the wavenumber, k, for (a) the clamped sperm head and (b) the pivoting sperm head. Figure originally published by Gadêlha et al. [42].

(Eq. (2.8)) given the variation of parameters such as the shear force wavenumber k, shear force amplitude A and the sperm-compliance Sp. This was circumvented in [40] by choosing the sliding force amplitude A, for a given Sp and k, so that the maximum deflection of the filament was no larger than 10% of the total filament length L. More recently, Jülicher and collaborators [55] have considered the role of leading non-linear contributions in a perturbative formulation and demonstrated that the linear theory provided a good estimate, with no evidence of a buckling instability.

2.4 Results

Numerical simulations were carried out assuming a fluid dynamic resistance ratio $\gamma = 2$. Once the boundary conditions are specified, there are two further degrees of freedom: the sperm-compliance parameter Sp and the wavenumber k. Given these, the force amplitude A is fixed by the constraint that the maximum flagellar displacement does not exceed 10% of the flagellar length in the linear theory, that is $\max_{xt} |\mathrm{h}| = 0.1$ in Eq. (2.16), as in Ref. [40]. The force amplitude A is plotted for

the clamped and pivoting boundary conditions in Fig. 2.4 and the parameter regimes considered are consistent with typical physical quantities observed in spermatozoa experiments [11, 84, 120]. As detailed in Sec. 2.3.1.3, estimates for the human sperm-compliance parameter for various media range from $\mathrm{Sp} = 4$ to $\mathrm{Sp} = 24$ which dictates the choice of Sp in the illustrative examples below. We also display results for smaller Sp, as low as unity, for completeness, when assessing the validity of linear theory as other flagellates can operate at smaller compliance numbers.

2.4.1 Clamped Head and Pivoting Head Results

We begin our investigation by contrasting the non-linear flagellar dynamics (Eq. (2.8)) with its linear approximation (Eq.(2.16)), with illustrations of symmetry breaking behaviour, for the clamped and pivoting head boundary conditions. Plots 2.5 (a)-(l) show the time evolution of the linear and non-linear flagellar shapes for both clamped and pivoting boundary conditions, and six different pairs of wavenumber and sperm-compliance parameter (k, Sp). Plots 2.5 (m)-(x) additionally illustrate the time evolution of the non-linear model predictions for the flagellar beat pattern when symmetry breaking occurs for a range of internal shear wavenumbers, k, and sperm-compliance $\mathrm{Sp} = 19$ for the clamped head plus sperm-compliance $\mathrm{Sp} = 15$ for the pivoting head.

The linear theory provides a good agreement with the full non-linear problem for plots 2.5 (a,b,g,h) and (d,e,j,k). In contrast, the linear approximation fails for cases (c,i,f) and (l) in Fig. 2.5 for both the pivoting and clamped boundary conditions, where the non-linear solutions are characterised by condensed or highly asymmetric waveforms, breaking up-down symmetry in the plane. This is despite the constraint on the maximum flagellum amplitude, as illustrated for $k = 5\pi$ and $\mathrm{Sp} = 12$ in Fig. 2.5 (f). The symmetry breaking behaviour within the non-linear model is further highlighted in Fig. 2.5,(m)-(x). In particular, at large values of the sperm-compliance

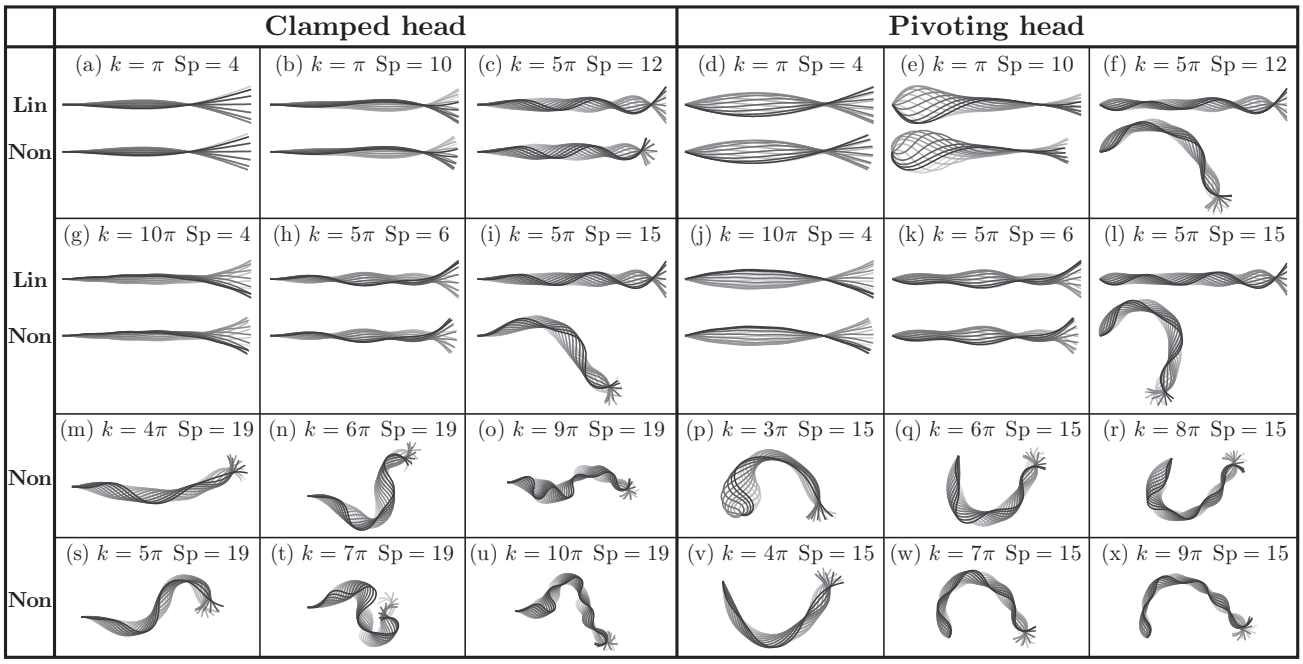

Figure 2.5: Snapshots of the flagellar evolution for the clamped and pivoting head boundary conditions, plotted at equal time intervals (darker curves for later times). The internal sliding force is given by Eq. (2.11) for $\pi \leq k \leq 10\pi$ and $4 \leq \mathrm{Sp} \leq 19$, as indicated, and the dimensionless force magnitude A is chosen to produce a maximum flagellum amplitude of $0.1L$ in Eq. (2.16) (see Fig. 2.4). The first two rows (a)-(l) compare the time evolution for the linear (Lin) and non-linear (Non) theory. Note that the linear theory fails to predict the flagellar shape for cases (c,i,f,l), and that the pivoting boundary condition is more sensitive to the influence of the non-linear dynamics. The last two rows (m)-(x) illustrate typical symmetry breaking shapes, characterised by an 'S' for clamped boundary conditions (Sp = 19) and a 'C' for pivoting boundary conditions (Sp = 15). Furthermore, all beating patterns are periodic in time, despite their appearance. Figure originally published by Gadêlha et al. [42].

parameter, Sp, corresponding to increasing viscous domination of the dynamics or, alternatively, a higher beating frequency, the symmetry breaking behaviour is particularly enhanced. For clamped head boundary conditions the emergent asymmetrical waveforms are relatively constrained as the tangent vector is also pinned at $s = 0$, whereas asymmetrical bending causes the flagellum to rotate about the point of attachment for the pivoting head boundary condition. We also observe that all flagellar patterns are eventually periodic in time, once transients have decayed, despite the complexity in the dynamics, though the period is greatly increased once symmetry

breaking has occurred.

To delimit the values of the internal shear force wavenumber, k, and sperm-compliance parameter, Sp, simulations were performed for $0 \leq k \leq 10\pi$, $1 \leq \mathrm{Sp} \leq 20$. A measure of the discrepancy between the linear theory predictions for the flagellar waveform, $\mathbf{X}_{\mathrm{L}}(s,t)$, and the non-linear theory predictions, $\mathbf{X}_{\mathrm{N}}(s,t)$, is given by

$$D_{\max} = \max_{s,\,t} |\mathbf{X}_{\mathrm{N}}(s,t) - \mathbf{X}_{\mathrm{L}}(s,t)|.$$

When $D_{\max} = 0$ the agreement is perfect, while if $D_{\max} \approx 0.1$ or less the agreement is observed to be qualitatively reasonable. For example, in plots 2.5 (e) and (c), $D_{\max} = 0.08$ and 0.11 respectively, whereas in plot 2.5 (i) $D_{\max} = 0.47$.

In Fig. 2.6, (a) and (b) $D_{\max}$ is plotted as an interpolated function of Sp and k, with the black contour given by $D_{\max} = 0.1$. The linear theory is increasingly inaccurate as the sperm-compliance parameter, Sp, increases even for moderate internal shear force wavenumbers, k, especially for the pivoting head boundary conditions. In Fig. 2.6, (c) and (d), the linear theory prediction for the global maximum curvature, $\kappa_{\max}$, is plotted as the sperm-compliance, Sp and wavenumber k are varied, with the contour $D_{\max} = 0.1$ once more given by a solid black curve. Clearly, there is a strong positive correlation between the maximum curvature obtained from the linear model and the discrepancy measure, $D_{\max}$ for both boundary conditions, explicitly highlighting that the linear theory becomes inaccurate as its predictions for flagellar curvature increase. In particular once the radius of curvature is less than, approximately, 10% of the flagellar length ($\kappa_{\max} = 10$), the linear theory is observed to be unreliable.

One should note that Fig. 2.6, (b) and (d) exhibit a blank region in the upper left corner. The high flagellar compliance, slowly varying internal shear distribution and flagella hinging characterising this region of parameter space allow a local build up of high curvature and tension, with sudden changes in the force direction. Discretising the non-linear equations produces matrices which are too ill-conditioned for reliable simulation. This region of parameter space will not be considered further.

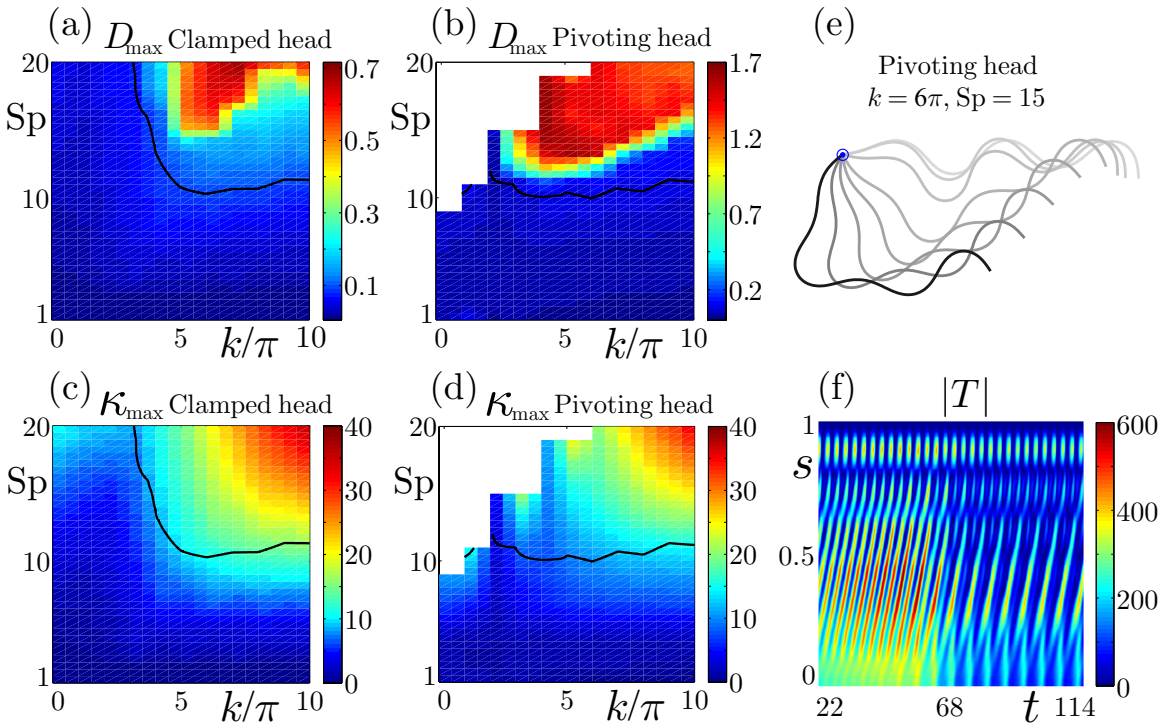

Figure 2.6: The breakdown of linear theory, the symmetry breaking instability and its consequences for the free head swimmer. Plots (a), (b): The discrepancy measure, $D_{\max} = \max_{t,s} |\mathbf{X}_{\mathrm{N}} - \mathbf{X}_{\mathrm{L}}|$, is illustrated for varying internal shear wavenumber k, and sperm-compliance parameter, Sp, in both the pivoting head and clamped head cases. Similarly, in plots (c), (d), the maximum of the linear theory prediction of curvature, $\kappa_{\max}$ is presented. In all these four plots, the solid black contour marks where $D_{\max} = 0.1$, noting that significantly larger values are observed to characterise poor agreement between the linear and non-linear theories. Plots (e) and (f) illustrate the transient features of the symmetry breaking bifurcation to asymmetric waveforms for the pivoting head boundary condition, when $k = 6\pi$ and Sp $= 15$ [case (q) in Fig. 2.5]. Plot (e): Time sequence once the flagellar buckling instability can be readily observed, with waveforms overlaid at equal time intervals with the point of attachment in blue. The initial waveform ($t = 18.18$) is illustrated in light gray and the final waveform ($t = 150.76$) in black, with a progression in darkness with time. Plot (f) is the associated absolute tension $|T|$ as a function of time t and arclength s. Figure originally published by Gadêlha et al. [42].

The symmetry breaking transient dynamics is illustrated in Fig. 2.6, (e) and (f), where we respectively display the flagellar pattern and absolute tension as the buckling instability progresses for the pivoting head boundary conditions with $k = 6\pi$ and Sp $= 15$ [case (q) in Fig. 2.5]. During this instability, a common feature is a large

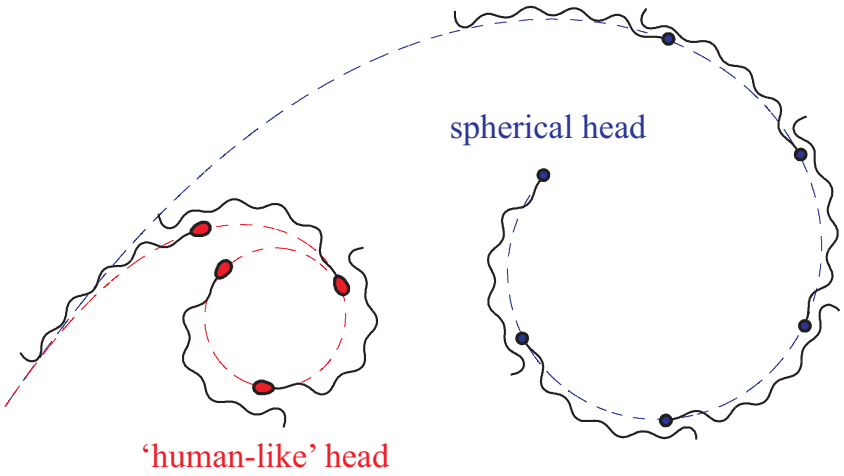

Figure 2.7: The influence of the symmetry breaking instability on the overall trajectory and flagellar beating pattern of the free swimming cell, plotted at equal time intervals. Smoothed trajectories are plotted for two different sperm head geometries: a spherical head (dashed blue) and a 'human-like' head morphology (dashed red), both with the same human-like head volume [119]. Here, the internal shear density is given by Eq. (2.11) with $k = 10\pi$ and $\mathrm{Sp} = 20$, and the dimensionless force magnitude A is 75% of the force amplitude used for the pivoting case when the maximum displacement is $0.1L$ (see Eq. (2.16) and Fig. 2.4). The buckling transition induces an asymmetric waveform that drives swimmers toward permanent circular paths; the swimming direction is inverted if $f \to -f$ in Eq. (2.8). Figure originally published by Gadêlha et al. [42].

absolute tension concentrated towards the sperm cell-flagellum junction at $s = 0$, noting that the tension is zero at the distal flagellum, $s = L$. After reaching a critical value of absolute tension, the beating shape instability is followed by a sudden drop in the absolute tension together with an increase in the period (see Fig. 2.6 (f)). Also, it is noteworthy that the quantity $D_{\max}$, displayed in Fig. 2.6, (a) and (b), or $\kappa_{\max}$ plotted in Fig. 2.6, (c) and (d), can be used as a bifurcation diagram to identify the parameter regimes where the buckling-type instability occurs, since inaccuracies of the linear theory are always observed to be accompanied by this dynamic symmetry breaking behaviour.

2.4.2 Swimming Sperm

We examine the influence of the flagellar buckling instability on swimming sperm. We have considered the effect of two different head morphologies: a 'human-like' sperm head [119] with dimensions $4.5 \times 2.8 \times 1.12\mu$m and a spherical head with diameter 2.40μm so that it has the same volume. The swimming sperm was found to be less sensitive to the flagellar buckling instability, though once both the sperm-compliance, Sp, and the internal shear wavenumber, k, are large, sperm swimming is observed to be profoundly altered by the symmetry breaking mechanism. The transition in behaviour is, however, smooth and drives the sperm towards swimming in circular paths of constant radius. Furthermore, a small (large) sperm head viscous drag leads to larger (smaller) circular paths. The sperm trajectories for both human-like (dashed red) and spherical head (dashed blue), when $k = 10\pi$ and $\mathrm{Sp} = 20$, are illustrated in Fig. 2.7. In addition, the swimming direction in Fig. 2.7 changes from clockwise to counterclockwise if $f \to -f$ in Eq. (2.8), illustrating that overall path direction after buckling is sensitive to the phase of the internal shear forcing.

2.5 Discussion

Although the dynamics of an internally driven filament in viscous fluids has been widely studied, the possible influence of a non-linear buckling instability on the ultimate flagellar patterns has not been explored. Here, we consider the physical principles of this instability in the context of flagellar dynamics, incorporating the influence of the surrounding fluid through resistive-force theory. The structural response of the flagellum is governed by geometrically non-linear filament elasticity theory and the internal forcing is represented via the sliding filament model of eukaryotic flagellar motility. The coupling of these three physical phenomena leads to the emergence of complex flagellar waveforms, which were examined in detail through numerical simulations for a large spectrum of internal shear wavenumber, k, sperm-compliance, Sp,

and different boundary conditions.

While weakly non-linear analyses [55, 94] support the use of geometrically linear elasticity theory in recent models of flagellar dynamics [21, 22, 40, 109], we have demonstrated that linear theory can be unreliable in general. On varying the internal shear wavenumber k and the sperm-compliance, Sp, linear theory yields inaccurate predictions for reasonably large values of Sp and a wide range of wavenumbers k (see Fig. 2.6, (a) and (b)). While the linear model demonstrates a plausible behaviour in this parameter regime [40], the non-linear simulation exposes the higher-order effects and exhibits complex flagellar beating (Fig. 2.5). Physically, it is reasonable to expect an increasing inaccuracy of the linear model for larger values of k and Sp, even with constraints on flagellar waveform amplitude. In particular, higher wavenumbers continuously force the flagellum to increase its curvature locally. With higher sperm-compliance parameters Sp (see Eq. (2.9)), and thus a sufficient viscous resistance to prevent the tendency of elastic forces to reduce this curvature, high tangential forces are induced, which are nominally a second-order contribution [21, 55]. Hence, the validity of the linear theory requires a larger flagellum radius of curvature, observed to be at least 10% of flagellum length, rather than constraints on the amplitude of flagellar deflection [40].

Our main result from this non-linear investigation is that asymmetric flagellar waveforms may arise dynamically, from intrinsically symmetric flagellar dynamics; this is not captured by linear or weakly non-linear theories. Consequently, an asymmetric flagellar waveform can be initiated and maintained without any change in cell signalling or the presence of flagellar heterogeneity. The asymmetric flagellar bending is caused by a common phenomenon in elastic filament dynamics, the buckling instability [13] which is frequently found in passive filaments when subjected to high tangential forces. This mechanism is also manifested in driven flagellar dynamics (Fig. 2.5) though, conversely, it is triggered by the internal shear force via the $f\hat{\mathbf{n}}_s$

contribution in Eq. (2.8). This causes the absolute tension to rise; once beyond a critical value which the flagellum elastic structure cannot support, asymmetric bending is observed (see Fig. 2.6, (e) and (f)). Furthermore, the flagellum is still driven by the same internal shear after buckling, which continuously forces the flagellum to maintain the emerging asymmetric bending pattern: roughly an "S" shape for a fixed head and a "C" shape for both the pivoting head case and the swimming sperm (Fig. 2.5 and Fig. 2.7). This represents a markedly distinct buckling instability from those reported in the literature [13, 15, 63, 131].

This flagellar buckling instability is readily found for large values of the internal shear wavenumber k and the sperm-compliance parameter Sp; it is also apparent for moderate wavenumbers, in particular, for constrained sperm especially when the sperm head is pivoting. While the clamped boundary condition restrains the motion, the free torque condition in the pivoting head simulations allows the sperm to rotate around its fixed point; analogously, the free head swimmer boundary conditions induce waveform asymmetries that drive circular trajectories. Furthermore, the swimming sperm trajectories are sensitive to sperm head morphology. Morphologies may subtlety alter the net viscous drag on the swimming flagellum, in turn altering the tension via the boundary conditions. However, in the context of the emergent behaviour from a tension-driven buckling instability this can have a substantial effect on the emergent waveform, and hence the resulting swimming trajectory (Fig. 2.7). Furthermore, the swimming direction is a non-trivial consequence of the force and torque balance during the bifurcation to asymmetric waveforms and, in particular, exhibits a dependence on the phase of the internal sliding forces.

These results demonstrate that asymmetric flagellar beating does not necessarily require an intrinsic asymmetric forcing mechanism. Thus, observations of circular swimming or flagellar waveform asymmetry are not sufficient to infer the presence of hyperactivation or any other asymmetric physiological regulation or signalling in-

fluencing the internal dynein molecular motors within the flagellum. Similarly, one cannot immediately infer that subtle flagellar structural asymmetries, such as the 5-6 microtubule bridging [99, 112], are dynamically critical and driving symmetry breaking. Moreover, high wavenumbers are commonly exhibited by sperm migrating in high viscosity fluids [120] and circling cells (see Fig. 2.1). The results we have presented indicate that it is physically plausible for this behaviour to be caused by excessive tangential forces on the flagellum due to both internal shear forces and the viscous drag on the sperm cell. Nonetheless, the influences of ultrastructural, histological and physiological complications are currently unexplored. For example, we have not considered the role of tapering in the accessory flagellar structures commonly found in mammalian sperm cells, such as the outer dense fibres. These accessory structures reinforce the flagellum in regions where high tensions are expected, and may also act to prevent the flagellar buckling instability; likewise, subtle structural asymmetries of the sperm flagellum could encourage buckling. Similarly, possible dynein detachment mechanisms at high flagellar curvature, such as the geometric clutch hypothesis [79], may influence the emergent waveform and require exploration. Further work could also account for non-local hydrodynamic effects.

In summary, our formulation is the first to explore the buckling instability of a filament driven by internal shear forces within viscous fluids. It has firstly delimited the validity of geometrically linear elastic filament theory. Secondly, the study has demonstrated the physical plausibility of dynamical symmetry breaking of filaments. Our demonstration that the asymmetric waveforms (see Fig. 2.1) which characterise specialised sperm behaviours, such as hyperactivation or chemotaxis, can also emerge dynamically without recourse to variations in structure or signaling (Figs. 2.5 and 2.7), emphasizes the importance of being alert to this symmetry breaking mechanism when interpreting observations of sperm flagella. These findings are crucial when considering motility at these scales in physiological fluids and their analogues, due to the

fact increased viscosity induces a higher sperm-compliance number, as defined in Eq. (2.9). Furthermore, mathematical models exploring the oscillatory behaviour of cilia and flagella beating should also consider geometrically non-linear dynamics to accommodate the high curvatures observed physiologically.

Chapter 3

Mechanical influence of accessory flagellar structures on the human sperm swimming

3.1 Introduction

The mammalian sperm flagellum differs crucially from simple flagellar axonemes found in nature [11, 38]. In addition to its intricate $9 + 2$ axonemal scaffolding, each of the nine exterior microtubule doublet of the axoneme is attached with nine others outer dense fibres (ODFs), in addition to the exterior fibrous sheath, forming a complex known as $9 + 9 + 2$ [99]. The ODFs are the largest flagellar structural elements, consisting of, highly condensed, modified intermediate cytoskeletal filaments strengthened by disulfide linked keratin proteins [14, 100], that extend and taper throughout the mid-piece, terminating prior to the distal tip of the flagellum. The $9 + 9 + 2$ complex is still surrounded by a fibrous sheath that extends in a tapering fashion from the mid-piece region to the principal piece region, in addition to two longitudinal columns, diametrically opposite, at principal piece [38, 99]. In human sperm cells, the basal portion of the sheath is occupied by a cylindrically arranged mitochondria, which typically covers the first 4μm. The mitochondrial sheath is then continued by a proteinaceous sheath of keratin-like material, namely fibrous sheath, which extends for 50μm. Finally, the whole structure is enveloped within a plasma

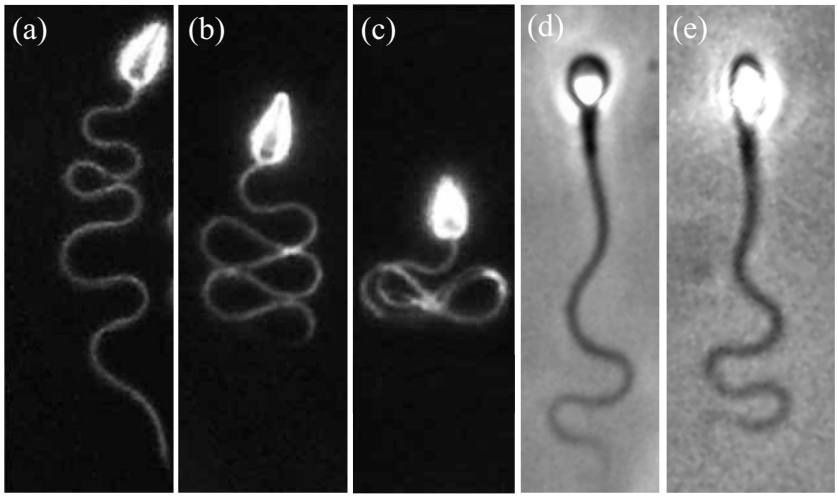

Figure 3.1: Sea urchin sperm (a,b,c) and human spermatozoa (d,e) in a viscous medium, containing 1% (d) and 2% (a,b,c,e) methyl-cellulose, with a nominal viscosity of 1.5 Pa.s in (a), 2 Pa.s in (d), and 4 Pa.s in (b,c,e), according to the molecular mass of the methyl-cellulose. (c) Sea urchin sperm with its head adhered to the coverslip. The flagellum length in (a,b,c) is approximately 42μm, and 50μm in (d,e). Figures (a,b,c) adapted from Wooley & Vernon [143] with permission from Journal of Experimental Biology, and figures (d,e) originally published by Smith, Gaffney, Gadêlha et al. [120] with permission from John Wiley and Sons (2958800134968).

membrane.

Intuitively, one would expect that the additional complexity associated with the mammalian ultrastructural components has a decisive role on the sperm biological function. Since the first macrographs of the mammalian internal architecture, it has been proposed that the accessory complex is necessary to provide the structural and mechanical support to stabilize long flagella observed in most mammalian spermatozoa [14, 38, 81, 86, 99, 100, 110]. The latter is related with the idea that only a reinforced flagellum would be capable of harnessing the power from a long flagella, given the increase on the number of molecular motors [*ibid*]. This is contrast, however, with marine species that fertilize in low-viscosity seawater [143]. The sea urchin sperm flagella, for instance, has an average length comparable with the human sperm flagella, and yet the flagellum is solely composed by the axoneme surrounded by the plasma membrane.

Experimental observations of sea urchin sperm migrating in high viscosity liquids [143], similar to the cervical mucus in the female tract [120], revealed the formation of a flagellar wave compression, Fig. 3.1(a), reaching extreme wave confinement for sperm attached to the coverslip by its head, see Fig. 3.1(c), in addition to curvilinear swimming trajectories. A distinct scenario is found for human sperm cells migrating in high viscosity fluids [120], in Fig. 3.1(b), with the same concentration of methyl-cellulose used by Wooley & Vernon [143] in Figs. 3.1(a,c). In this case, the flagellar wave form is characterised instead by a gradually increasing meander envelope, absence of wave compression, and subsequent decrease of the flagellar curvature [120]. These observations readily establish that mammalian ultrastructural components are critical for the sperm ability to swimming in high-viscosity medium, despite the larger number of motor proteins associated with longer flagella.

Despite the structural significance of the accessory complex on the bend propagation and modulation [43, 120, 143], the role of these ultrastructural components on the swimming behaviour of mammalian spermatozoa have been markedly overlooked in the literature. In the founding theoretical study, Lindemann [81, 86] modified the geometric clutch model [80] to incorporate the effect of accessory structures, by assuming a linear tapering of the elastic stiffness along the arclength, for immobilised sperm cells. While the model predicted a reduction on the maximum flagellar curvature caused by the added stiffness, in addition to a qualitative agreement for bull sperm experiments, no information on the potential advantage of having such reinforcing components could be inferred. Eleven years later, Riedel et al. [109] equally investigated the effects of perturbative structural inhomogeneity, again via a linear decay of the bending rigidity, during a model curve fitting study on the beating shape of steadily bull sperm, by comparing various existing models for the molecular motor coordination [17, 22, 80], at the geometrically linear level. A satisfactory fitting was found for the self-organization model with load dependent detachment rate of

motors [21, 22], when the variation of the elastic stiffness along the flagellum is neglected. As followed, the fitting analysis suggested instead that the gradual tapering of structural components play a minor role in shaping the flagellar waveform, given the model curve fitting was not significantly improved by the tapering effect, in addition to a strong scattering of the extra fit parameters across different cells. This is in contrast, however, with recent estimates from Gaffney et al. [43] for the distribution of hydrodynamic, elastic, and internal sliding bending moments and forces, via geometrically exact calculations from temporal and spatial resolution microscopy of human sperm [43, 120]. By considering an exponential decay of the flagellum stiffness [75, 114], it was found that the internal sliding forces have, approximately, a constant magnitude along the arclength, suggesting a balance between the passive elastic response of the flagellum, due to the tapering of the flagellar ultrastructure, and the density of dynein contraction. Finally, the tapering effect was equally observed to influence the beating pattern of hyperactivated mammalian sperm [101], for an idealised sperm flagellum model, biochemically regulated, and assuming a varying tensile stiffness.

Here, we consider an extension of the elastohydrodynamic formulation presented in Gadêlha et al. [42] to study the role of tapering in the accessory flagellar structures commonly found in mammalian sperm cells, such as the outer dense fibres. By assuming the flagellum elastic stiffness as a monotonically decreasing function of the arclength, we investigate the influence of the accessory structures for a free swimming human sperm. We further investigate the hypothesis raised in Ref. [42], related with the possible prevention of the flagellar buckling instability, consequently circular swimming trajectories, due to stabilizing role of the reinforced structures in regions where high tensions/compression are expected. The equations governing the flagellar dynamics are profoundly changed by several new non-linear terms, which are responsible in driving the cell dynamics in a non-trivial manner, giving a better

insight concerning the possibility of structurally enhanced sperm locomotion in high viscosity fluids.

3.2 Geometrically exact elastohydrodynamic formulation

In order to incorporate the role of tapering in the accessory flagellar structures commonly found in mammalian sperm cells, such as the outer dense fibres, we consider a variation of the sliding filament mechanism [17, 18, 21, 22, 35, 40, 42, 55–57, 109]. In this formalism, the axoneme is represented by a two-dimensional abstraction, where a pair of parallel elastic filaments, depicted by the black curves in Fig. 3.2, slide relative to each other within the beat plane, in response to dynein forces. Each sliding filament is assumed to be homogeneous, inextensible and separated by a constant gap space b, which corresponds to the axoneme diameter. Nevertheless, accessory reinforcing structures, represented by the light blue shading in Fig. 3.2, are paired with each sliding filament, effectively increasing the overall elastic stiffness of the complex. Finally, motor proteins induce active sliding stresses along the axoneme, forcing the filaments, now attached with ultrastructural components, to locally slide with respect to each other, generating flagellar bending. At the sperm head junction, we assume for simplicity that no interfilament shear is permitted owing to structural constraints.

We describe the flagellum position, relative to the laboratory frame of reference, by its neutral line $\mathbf{X}(s,t)$ (see Fig. 3.2), noting that t is time and s denotes the distance along the flagellum with $0 \leq s \leq L$, where L is the filament length. The local flagellum coordinate system is represented as an orthonormal pair with a positive orientation $\{\hat{\boldsymbol{s}}, \hat{\boldsymbol{n}}\}$, where $\hat{\boldsymbol{s}} = \mathbf{X}_s \equiv \partial\mathbf{X}/\partial s$ is the tangent vector and $\hat{\boldsymbol{n}}$ is the vector normal to the flagellum centreline (Fig. 3.2). The flagellar dynamics is inertialess and arises via balancing the viscous drag force per unit length with the internal

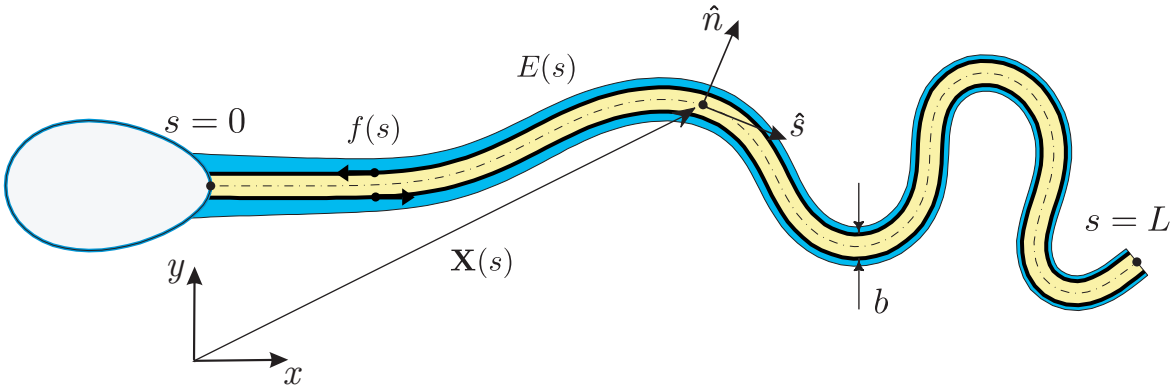

Figure 3.2: A schematic of the sliding filament mechanism modified by the ultrastructural components of mammalian spermatozoa. Relative to a laboratory fixed frame $\{\hat{\mathbf{x}}, \hat{\mathbf{y}}\}$, the vector $\mathbf{X}(s,t)$ describes the position of flagellum neutral line (dashed curve) at time t. The internal shear force $f(s,t)$ is acting tangentially and in opposite directions on each sliding filament (solid black curves) within the axoneme (light yellow shading) with diameter b . The flagellar reinforcing structure (light blue shading), paired with each sliding filament, is captured by an effective elastic stiffness $E(s)$ that monotonically decay along the arclength s.

forces per unit length within the flagellum. We generalise the elastohydrodynamic formulation presented in Ref [42] by incorporating the effect of the ultrastructural components, captured by the effective elastic stiffness $E(s)$ that varies along the arclength s. Nondimensionalising with respect to the length scale L, time scale ω^{-1} and force density E_0/L^3, for a given beating frequency ω and a constant axonemal elastic stiffness E_0, the modified dimensionless elastohydrodynamic equation for a mammalian flagellum reads

$$\begin{aligned} \mathrm{Sp}^4 \mathbf{X}_t = &- \left(e\,\mathbf{X}_{ss}\right)_{ss} - (\gamma - 1)\big(e\,\mathbf{X}_s \cdot \mathbf{X}_{ssss} + 2e_s\,\mathbf{X}_s \cdot \mathbf{X}_{sss}\big)\mathbf{X}_s \\ &+ (T\mathbf{X}_{ss} + \gamma T_s \mathbf{X}_s) + (f_s \hat{\boldsymbol{n}} + \gamma f \hat{\boldsymbol{n}}_s) \end{aligned} \tag{3.1}$$

where the subscript t denotes differentiation with respect to time. The sliding force density within the axoneme is given by $f(s,t)$, $\gamma = \xi_\perp/\xi_\parallel$ is the ratio between the perpendicular, $\xi_\perp$, and parallel, $\xi_\parallel$, fluid dynamic resistance coefficients. The function $e(s)$ represents the flagellar bending stiffness relative to the axoneme stiffness. The

sperm-compliance parameter

$$\mathrm{Sp} = L\left(\frac{\omega\xi_{\perp}}{E_0}\right)^{1/4} \tag{3.2}$$

is dimensionless and characterises the relative importance of elastic forces to viscous drag [140]. The tensile force $T(s,t)$ is related to the Lagrange multiplier for inextensibility, and it is implicitly determined by the constraint $\mathbf{X}_s \cdot \mathbf{X}_s = 1$,

$$\begin{aligned}\gamma T_{ss} - (\mathbf{X}_{ss}\cdot\mathbf{X}_{ss})T = &-3\,e\gamma\,(\mathbf{X}_{sss}\cdot\mathbf{X}_{sss}) - e\,(3\gamma+1)(\mathbf{X}_{ss}\cdot\mathbf{X}_{ssss})\\ &- e_s\,(7\gamma+2)(\mathbf{X}_{ss}\cdot\mathbf{X}_{sss}) - e_{ss}\,(2\gamma+1)(\mathbf{X}_{ss}\cdot\mathbf{X}_{ss})\\ &- (\gamma+1)(\hat{\boldsymbol{n}}_s\cdot\mathbf{X}_s)f_s - \gamma(\hat{\boldsymbol{n}}_{ss}\cdot\mathbf{X}_s)f + \lambda\,\mathrm{Sp}^4(1-\mathbf{X}_s\cdot\mathbf{X}_s).\end{aligned} \tag{3.3}$$

In the absence of structural component, the tapering function $e(s) = 1$, and the governing equations are equivalent to earlier models proposed in [21, 50, 57].

Despite the intrinsic complexity associated with the dynein regulation, recent empirical estimative of the effective sliding moment density [43], resulting from the coupling between the dynein molecular motor activity and the passive cross linking proteins within the axoneme [20, 94], indicate that the observed flagellar waveform of human sperm migrating in high-viscosity fluid is generated by a simple travelling wave of dynein contraction, with a single characteristic frequency, and approximately constant magnitude along the flagellum length. This in-situ observation motivated the use of a simple prescribed travelling wave to model the internal sliding density,

$$f(s,t) = a\,\cos(ks - t), \qquad 0 \le s < 1 \tag{3.4}$$

where a, k are respectively the dimensionless force amplitude and wavenumber. This particular choice of internal sliding force will enable us to isolate effects arising from the flagellar structural tapering. Furthermore, due to the fact that the axoneme lacks structural and motor elements at the very most distal part of the flagellum, [14, 38, 39, 99, 100], the free end is considered to be absent from sliding forces.

3.2.1 Boundary Conditions and numerical methods

The equations governing the flagellar dynamics are complemented by boundary conditions, in which either the movement of the flagellar endpoints is specified or a balance of forces and torques at each end is imposed. In particular, at the distal boundary, $s = 1$, the flagellum is free to move and, therefore, the external forces and torques are zero, i.e.

$$\begin{aligned} 0 = \mathbf{F}_{\text{ext}} &= -e\,\mathbf{X}_{sss} - e_s\,\mathbf{X}_{ss} + T\mathbf{X}_s, \\ 0 = \mathbf{M}_{\text{ext}} \times \mathbf{X}_s &= e\,\mathbf{X}_{ss}. \end{aligned} \tag{3.5}$$

At the proximal end, $s = 0$, the flagellum is driving the sperm head and thus experiences a viscous drag force, $\mathbf{F}_{\text{head}}$, and moment, $\mathbf{M}_{\text{head}}$, given by

$$\begin{pmatrix} \mathbf{F}_{\text{head}} \\ \mathbf{M}_{\text{head}} \end{pmatrix} = \mathcal{L}^4\,\mathcal{R}(r/L, t) \begin{pmatrix} \mathbf{U} \\ \boldsymbol{\Omega} \end{pmatrix}, \tag{3.6}$$

where $\mathcal{L} = L(\eta\omega/E_0)^{1/4}$, and η denotes the fluid viscosity. $\mathcal{R}$ represents the dimensionless grand-resistance matrix for the sperm head, and depends on the head morphology, taken as a 'human-like' sperm head geometry [119], where r denotes the distance between its centre of mass and the sperm junction at $s = 0$. The torque and force balance at $s = 0$ yields the required boundary condition for the flagellum in terms of the motion of the sperm head via a specification of the head velocity field $(\mathbf{U}, \boldsymbol{\Omega})$, via

$$\begin{aligned} \mathbf{F}_{\text{head}} &= e\,\mathbf{X}_{sss} + e_s\,\mathbf{X}_{ss} - f\hat{\boldsymbol{n}} - T\mathbf{X}_s, \\ \mathbf{M}_{\text{head}} \times \mathbf{X}_s &= -e\,\mathbf{X}_{ss} - \hat{\boldsymbol{n}} \int_0^1 f(s')\,\mathrm{d}s'. \end{aligned} \tag{3.7}$$

Numerical solutions of elastohydrodynamic formulation for a free swimming cell, described by the above system Eqs. (3.1)- (3.7), were carried out by employing the numerical scheme devised in Gadêlha et al. [42], which uses a combination of second-order finite differences and second-order implicit time-stepping. Furthermore, the

latter has been validated against analytical and non-linear numerical solutions, in addition to experiments, for an oscillating elastic filament in a viscous fluid [42,144]. In particular, to avoid severe constrains on the time-stepping, the higher-order terms in Eq. (3.1) are treated implicitly, by employing a second-order implicit-explicit method (IMEX) [10]. The spatial discretization is uniform in arclength with N intervals. Second-order divided differences are used to approximate spatial derivatives, in which skew operators are applied at the boundaries. Finally, periodicity is expected from the imposed sliding force in Eq. (3.4), and therefore the time iteration continues until the maximum difference between consecutive solutions, $D_{\max} = \max_s |\mathbf{X}(s,t) - \mathbf{X}(s,t+\mathrm{T})|$, one period apart, is smaller than 5×10^{-4}.

3.2.2 Tapering functions

The dimensionless function $e(s)$ captures the arclength variation of the bending stiffness associated with the tapering of the flagellar ultrastructure. These reinforcing components gradually decrease in radius, but terminate prior to the distal tip of the flagellum, which is solely composed by the axoneme. Here, the tapering function, $e(s)$, measure the flagellar bending stiffness relative to the bending stiffness of the axoneme, $E_0 = 0.9 \times 10^{-21}\,\mathrm{Nm}^2$ [58,97,98], taken from demembranated sperm axonemal flagella of sea urchin *Lytechinus pictus*. Direct measurements of bending stiffness for human sperm flagellum are not available, however estimates can be inferred from rat sperm, given the similarity of the ultrastructural components. Mammalian flagellar structural properties are observed to scale with geometry for a fixed material [11], with the exception of the anomalous bull sperm and guinea pig sperm. Since the cross-sectional area of the human mid-piece outer dense fibre is 1/8 that of the rat [11], the prediction for the bending stiffness of human flagellum yields $E_0 = 4 \times 10^{-21}\,\mathrm{Nm}^2$ in this region, about four times the stiffness of the axoneme. Due to the absence of quantitative studies on the elastic properties of accessory structures in other sections

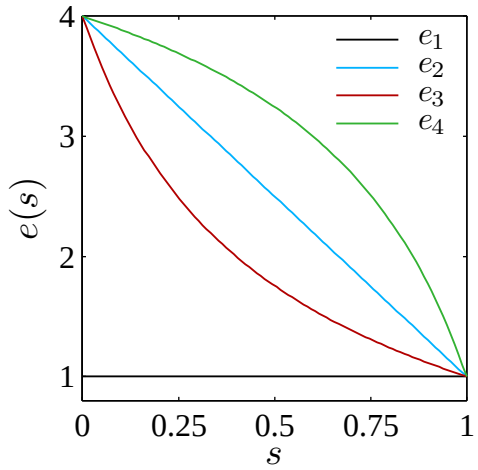

Figure 3.3: Tapering functions: (i) e_1, represent the absence of additional structures, (ii) e_2, linear taper [81,86], (iii) e_3, cotangent tapper, corresponding to the qualitative trend in flagellum stiffness measurements [75, 114], and (iv) inverse cotangent taper, relative to the function e_2.

of the flagellum, we smoothly fitted the upper and lower bound of bending stiffness so that $e(s) \in [1, 4]$. We considered four distinct cases for comparison purpose, illustrated in Fig. 3.3: (i) a constant function e_1, representing the absence of additional structural components found in flagellar axonemes [58, 97, 98], (ii) a linear decaying taper e_2, as utilised in Refs. [81, 86, 109], (ii) a cotangent decaying function e_3, motivated from recent spatially resolved data [75, 114], and therefore the biologically relevant case, and finally (iii) an inverse cotangent decay e_4, representing the mirror image of e_3 relative to the linear function e_1.

3.2.3 Parameter estimation

For human sperm experiments [42, 43, 120], the sperm number may vary from $\mathrm{Sp} = 4$, for low viscosity, watery, in-vitro fertilisation medium, up to $\mathrm{Sp} = 24$, for cervical mucus substitute, assuming a Newtonian behaviour. Estimates for the sliding force density magnitude, a, may be inferred from measurements of the sliding bending moment density [120], extracted from spatial and temporal cinemicroscopy for a swimming cell, or from direct force measurements of molecular motors [111,129].

Indirect measurements of the sliding bending moment density extracted from human sperm indicates a maximum magnitude of 8×10^{-10} N, when the tapering of the structural components is taken into account. If the diameter of the axoneme is assumed to be $b = 200\,\text{nm}$ [114], with a maximum flagellar length of $L = 60\,\mu\text{m}$, the upper limit of the dimensionless force density magnitude yields $a = 3200$. The inferred sliding bending moment density in Ref. [120] is also in agreement with direct measurements of the total force that a dynein motor can generate, which ranges between $2 - 8\,\text{pN}$ per motor domain for, respectively, the inner arm axonemal dynein and cytoplasmic dynein [111,129]. In this context, we may also add the intrinsic contribution from the inter-doublet elastic resistance within the axoneme, observed to be $2\,\text{pN}$ per structural repeat for flagellar axoneme [93], which yields an average resulting sliding force density magnitude of $a = 2400$, if we neglect non-local mechanical effects from the interfilament sliding [84,103]. Here, we will allow the Sperm compliance parameter to vary in the range $\text{Sp} \in [5, 25]$, with a sliding force density magnitude no larger than $a = 2000$.

3.3 Results

Numerical simulations were carried out for a free swimming cell with a 'human-like' sperm head geometry, with dimensions $4.5 \times 2.8 \times 1.12\mu$m, and assuming a fluid dynamic resistance ratio $\gamma = 2$. The parameter regimes considered throughout the study are consistent with typical physical quantities observed in spermatozoa experiments, as discussed in Sec. 3.2.3. We focus our attention on the consequences of a high viscosity medium on the flagellar beating shape, i.e. the high sperm number regime $\text{Sp} = 20 - 25$, although we also display results for Sp as low as 5. Motivated by the observed flagellar waveform in different viscosities [120, 143], we restrict our investigation for even sliding force wave numbers $k = 2\pi$, 4π and 6π. Incidentally, our simulations revealed that, in general, odd wave numbers are not able to generate

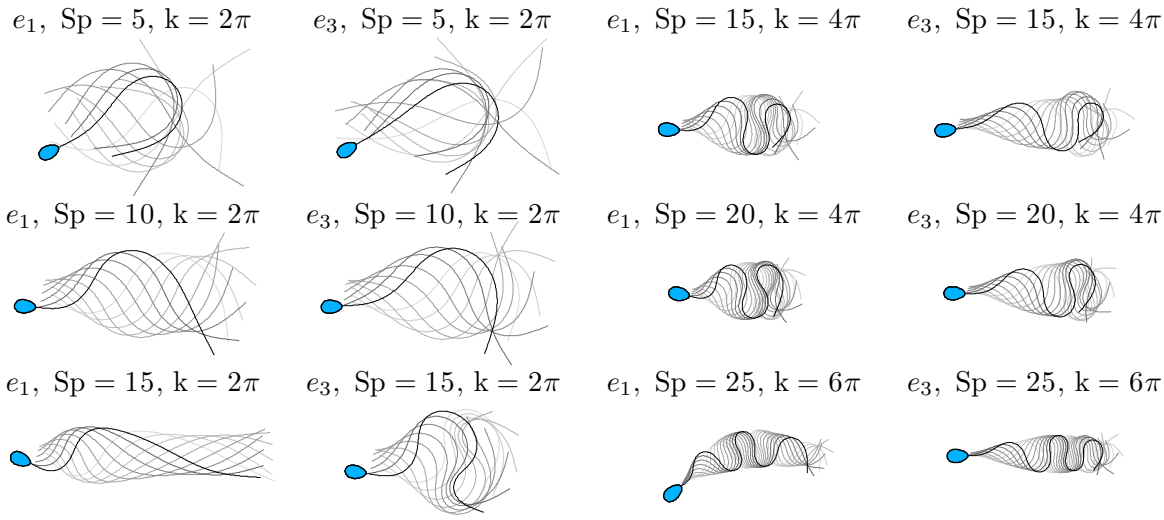

Figure 3.4: Snapshots of the flagellar evolution for the tapering functions e_1 and e_3, and six distinct pairs of wave number and sperm compliance number (Sp, k), as indicated, plotted at equal time intervals over one period (darker curves for later times). The values of force amplitude a, for each row, from top to bottom are, respectively, $a = 2.24, 2.54, 1.96, 2.37$, $a = 2.02, 2.93, 2.04, 2.55$ and $a = 2.54, 3.63, 1.30, 2.21$, nondimensionalised by E_0/ℓ^3, where $\ell = L/\mathrm{Sp}$.

realistic wave patterns [42]. The ability to generate consistent wave amplitude without a significant decay as the waveform progresses depends on the interplay between k and Sp, and can be predicted from the linear analysis [40, 120]. Hence, we focus our investigation on the cases where a noticeable forward motion is achieved as a result of the flagellar beating shape, typically, for corresponding values of k and Sp, i.e. small (large) k with low (high) Sp. Furthermore, the sliding force density magnitude was permitted to gradually increase, within the range of validity, in order to access the entire spectrum of beating patterns for each (Sp, k)-pair considered. For sufficiently large force amplitude, however, flagellar self-intersection occurs, even though the force magnitude is within its validity range. In this case, the numerical simulation is aborted and the upper limit of the force magnitude is updated, and given by the force in which flagellar self-intersection occurs.

We begin our analysis by contrasting the representative beating patterns for both the flagellar axoneme and human sperm flagellum cases, given respectively by the

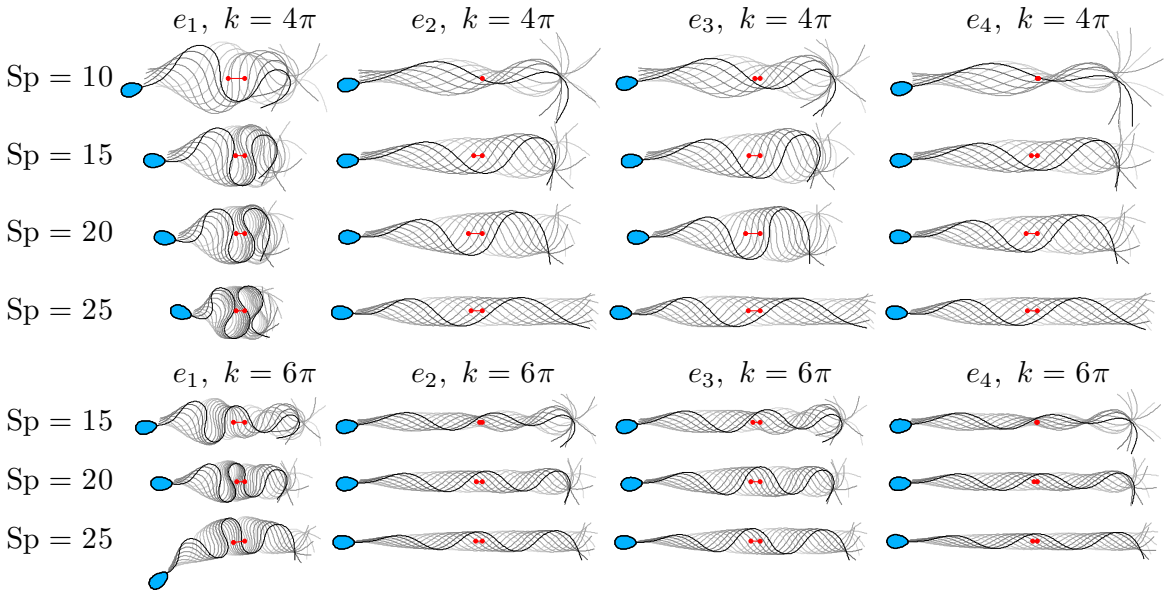

Figure 3.5: Snapshots of the flagellar evolution for the tapering functions $e_1 - e_4$, and seven distinct pairs of wave number and sperm compliance number (Sp, k), as indicated, plotted at equal time intervals over one period (darker curves for later times). The same force amplitude, a, given by the upper limit of the tapering case e_1, is used for the other stiffness functions e_2, e_3 and e_4. The value of a for each row, from top to bottom, is $a = 2.08, 1.96, 2.04, 2.09, 2.22, 1.81, 1.3$, nondimensionalised by E_0/ℓ^3, where $\ell = L/\mathrm{Sp}$. Red markers depict the initial and final position of the flagellum centroid over a period.

tapering functions e_1 and e_3. Fig. 3.4 illustrates the time evolution for six distinct pairs of wave number and sperm compliance number (Sp, k). The flagellar waveform associated with low (Sp, k) is characterised by a large wave amplitude and a significative forward motion, as demonstrated for $(\mathrm{Sp} = 10, k = 2\pi)$. Meandering formation and wave compression are distinctive characteristics of large (Sp, k) in Fig. 3.4. For a large Sp, when the reinforcing flagellar components are absent, extreme wave confinement is observed, in addition to the flagellar buckling instability, which is responsible for driving the cell in a circular trajectory, see the plot $(e_1, \mathrm{Sp} = 25, k = 6\pi)$ in Fig. 3.4. This is in contrast with the human sperm flagellum case, where both flagellar buckling and wave confinement are prevented. Instead, the meandering formation is characterised by a wave envelope that gradually changes with the arclength. For the low sperm compliance parameter cases, the absence of structural components is

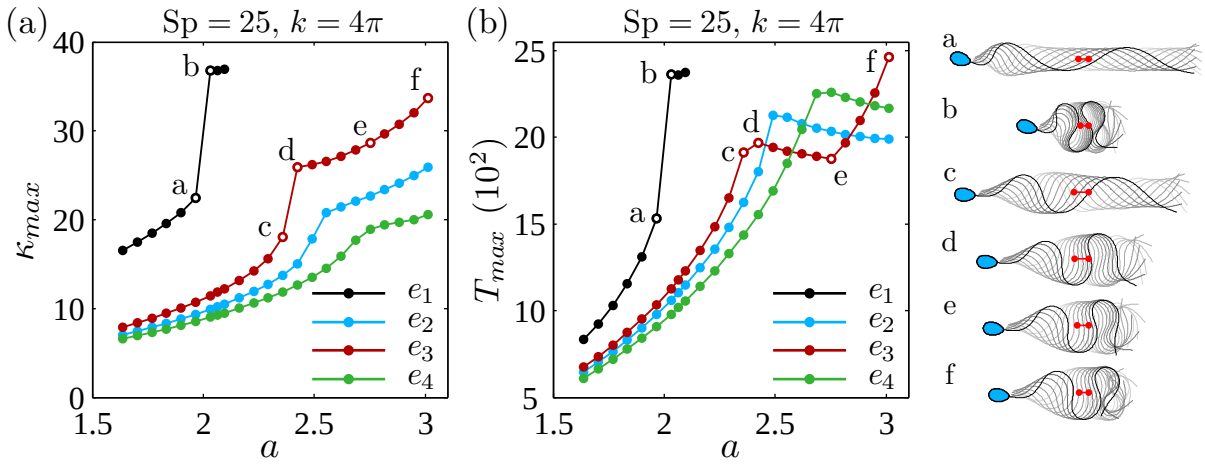

Figure 3.6: The maximum curvature κ_{max} (a) and the maximum absolute tension T_{max} (b), over one period, as a function of the sliding force density magnitude, a, nondimensionalised by E_0/ℓ^3, where $\ell = L/\mathrm{Sp}$. The same points 'a-f' in (a) are depicted in (b), in addition to the associated beating shape, on the right side of (b). Red markers depict the initial and final position of the flagellum centroid over a period.

observed to favour progressive motion.

The stabilising effect of the ultrastructural components is further illustrated in Fig. 3.5, which plots the time evolution of the beating shape for each tapering function e_1, e_2, e_3, e_4 and seven pairs of (Sp, k). In this instance, the same force amplitude, a, given by the upper limit of the tapering case e_1, is used for the other stiffness functions e_2, e_3 and e_4, for each (Sp, k)-pair. The resulting waveform for the tapering functions $e_2 - e_4$ is characterised by the formation of a wave envelope with a gradual change of the wave amplitude with arclength, and followed by a decrease of wave compression, while still maintaining the meander shape. The wave envelope, however, depends on the details of the tapering function: narrow wave envelopes are observed for the tapering cases e_2 e_4, while 'ogive-like' envelopes are associated with the tapering function e_3. The distance travelled per period, depicted by the red markers in Fig. 3.5, is also influenced by the tapering effect. In general, this distance is longer for the tapering function e_3 compared with the tapering cases e_2, e_4 for each (Sp, k)-pair,

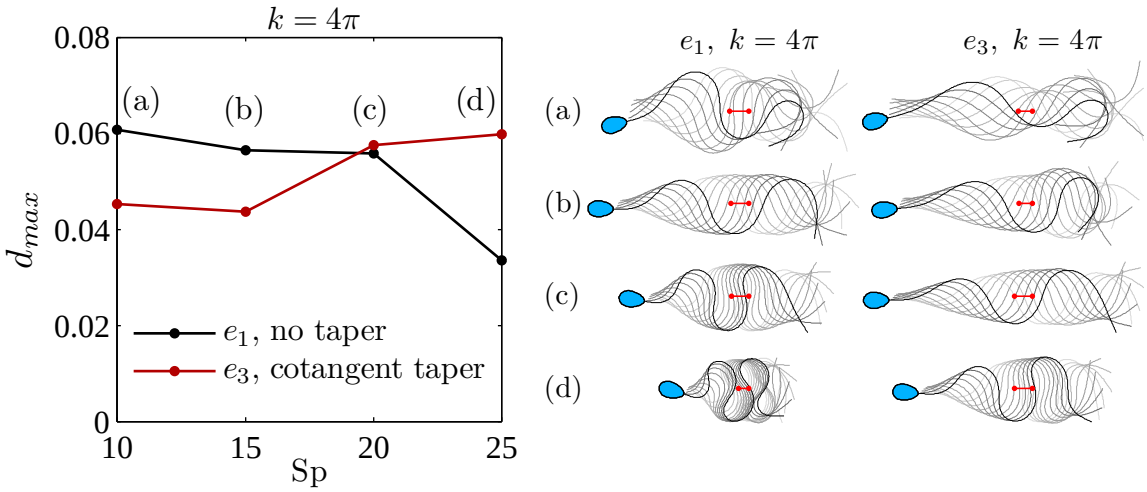

Figure 3.7: The maximum travelled distance of the flagellum, within the allowed range for a, centroid for stiffness functions e_1 and e_3, over one period, as a function of Sp for $k = 4\pi$, with the associated beating shapes to the points (a-d) depicted on the right panel. Red markers depict the initial and final position of the flagellum centroid over a period. The sperm head was omitted for clarity.

with the exception of $(\text{Sp} = 10, k = 4\pi)$ and $(\text{Sp} = 15, k = 6\pi)$. Indeed, for the pairs $(\text{Sp} = 10, k = 4\pi)$ and $(\text{Sp} = 15, k = 6\pi)$, the beating shapes associated with the tapering functions $e_2 - e_4$ are marked by a sharp decay of the wave amplitude in the central flagellum as it progresses. As a consequence of such erratic waveform, the forward motion in virtually absent. This is in contrast with the constant tapering function e_1 that is able to produce a noticeable forward motion for $(\text{Sp} = 10, k = 4\pi)$ and $(\text{Sp} = 15, k = 6\pi)$ in Fig. 3.5.

The maximum curvature, κ_{max}, and maximum absolute tension, T_{max}, over one period, are depicted in Fig. 3.6 for $(\text{Sp} = 25, k = 4\pi)$, as a function of the sliding force magnitude, a. The maximum curvature and tension for tapering function e_1 is characterised by the presence of a sharp transition, depicted by the points 'a' and 'b' in Fig. 3.6. For comparison purpose, the same points 'a' and 'b' from Fig. 3.6(a) are depicted in Fig. 3.6(b), in addition to the associated beating shape, shown on the right side of Fig. 3.6(b). The beating patterns for 'a' and 'b' are separated by a buckling transition: from a spread waveform in 'a' to a large wave confinement in 'b'. A

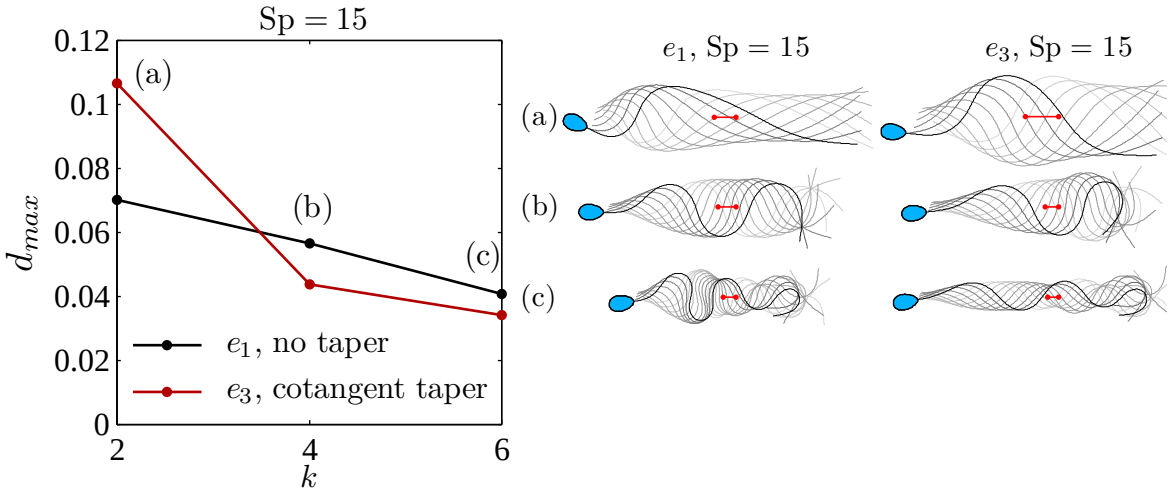

Figure 3.8: The maximum travelled distance of the flagellum centroid, within the allowed range for a, for stiffness functions e_1 and e_3, over one period, as a function of k for Sp = 15, with the associated beating shapes to the points (a-c) depicted on the right panel. Red markers depict the initial and final position of the flagellum centroid over a period. The sperm head was omitted for clarity.

distinct behaviour is found for the tapering functions $e_2 - e_4$, in which the maximum curvature and tension are always lower than the ones observed for the constant tapering function e_1. In this case, while the sharp transition in κ_{max} is gradually decreased in magnitude for the stiffness functions e_3, e_2 and e_4, respectively, in Fig. 3.6(a), no sharp increasing jump in magnitude is detected for T_{max}. Instead, there is the formation of a local maxima, so that T_{max} decreases after the sharp transition, as illustrated by the points 'c' and 'd' Fig. 3.6(b). This sharp transition is also associated with the wave compression buckling instability, but with a lower intensity. This is portrayed by the beating patterns of 'c' and 'd', for the tapering function e_3 in Fig. 3.6. After the buckling transition, the tension maximum, T_{max}, decreases with the sliding force density magnitude between points 'd', 'e' before reverting to an increasing behaviour once more between 'e', 'f'. Despite the sharp transitions in T_{max} between 'd' and 'f', no sharp variation in κ_{max} is present in this region, as equally portrayed by the beating patterns of 'd', 'e' and 'f'. A similar behaviour to e_3 is observed for e_2 and e_4, with the appropriate scaling, as larger values of T_{max} are permitted in these cases.

In order to analyse the effect of the ultrastructural components on the maximum travelled distance, d_{max}, across a wide range of sperm compliance and wave numbers, numerical simulations were performed for both stiffness functions e_1 and e_3, with Sp = 15, 20, 25 and $k = 2\pi$, 4π, 6π. The maximum travelled distance of the flagellum centroid over one period, within the allowed range for a, is plotted in Fig. 3.7 as a function of Sp for $k = 4\pi$, and in Fig. 3.8 as a function of k, for Sp = 15, together with the representative beating pattern for each point depicted. Fig. 3.7 shows a decreasing behaviour of d_{max} for the tapering function e_1 as the sperm number increases. This is in contrast with the stiffness function e_3, which is characterised by a gradual increase of d_{max} with Sp. The overall magnitude of maximum travelled distance for both cases does not exceed $d_{max} \approx 0.06$. The waveform modulation by the sperm number is further demonstrated by the corresponding beating shapes in Fig. 3.7, where the oscillating wave amplitude along the flagellum is switched to a steady wave envelope, followed by a wave compression, with different magnitudes for each stiffness function. Changes on the wave number, on the other hand, are correlated with a reduction on the wave amplitude, for a fixed Sp, as illustrated in Fig. 3.8. This effect is also manifested on the magnitude of d_{max}, which is now a decreasing function of k for both tapering cases, with a more pronounced decay for e_3.

The correlation between the total travelled distance of the flagellum centroid, d, per period and the associated maximum in curvature, κ_{max}, is illustrated in Fig. 3.9 for $e_1 - e_4$ with $k = 4\pi$ and Sp = 10, 15, 20, 25. The total travelled distance for the flagellar axoneme case is characterised by a monotonic increasing behaviour as a function of κ_{max} for Sp = 10 in Fig. 3.9(a), until $\kappa_{max} \approx 22$, where the curve reaches the upper limit in a before self intersection. As Sp increases, in Fig. 3.9(b), the original monotonicity of d is lost, and replaced by non-monotonic behaviour caused by the formation of a local maximum at $\kappa_{max} \approx 15$. The extremum of d varies weakly in magnitude, as well as the corresponding κ_{max} value, as Sp is further augmented in

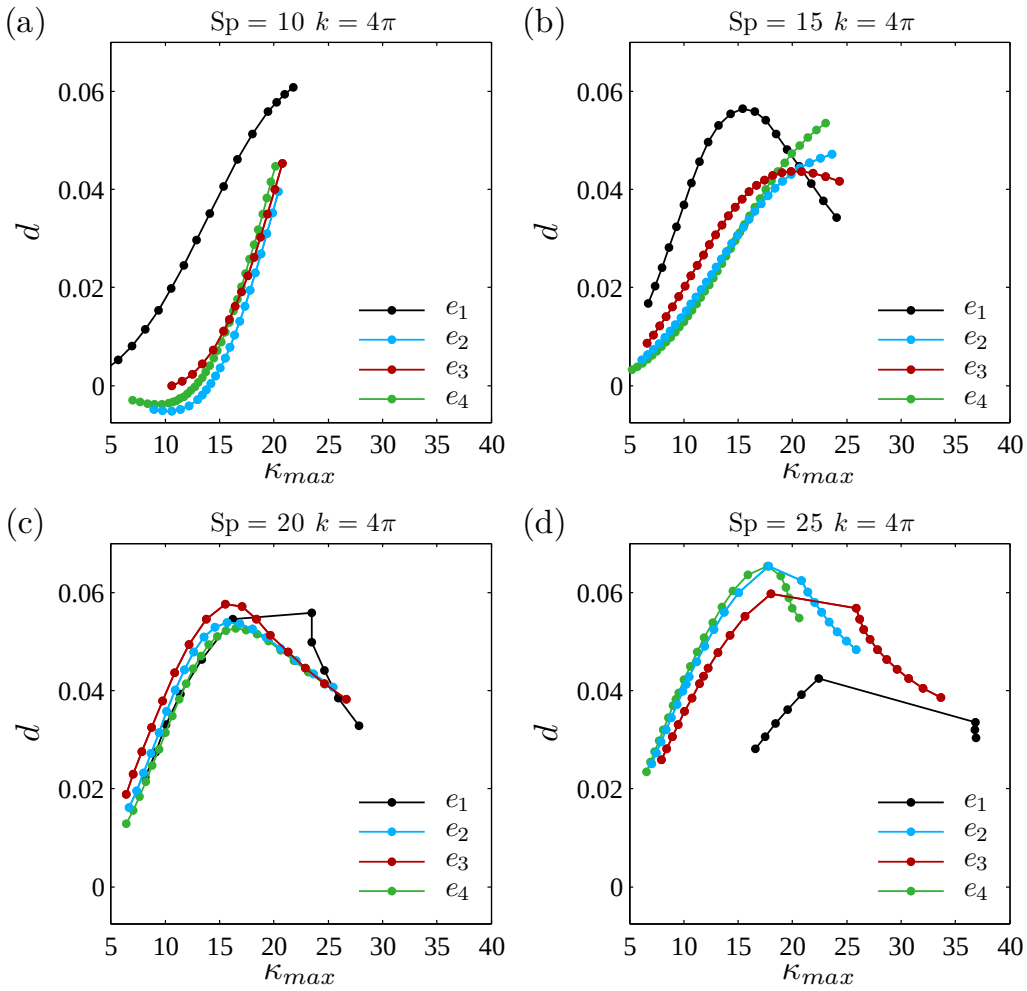

Figure 3.9: The travelled distance of the flagellum centroid d as a function of maximum curvature κ_{max}, over one period, for stiffness functions $e_1 - e_4$, $k = 4\pi$ and Sp = 10, 15, 20, 25, as indicated.

Fig. 3.9(c). Finally, when Sp = 25, the local maximum for e_1 is not only significantly lowered, but also translated to a higher κ_{max}. For both Figs. 3.9(c) and (d), the maximum in d is followed by a jump in curvature, which is associated with the wave confinement buckling depicted in Fig. 3.6. A similar behaviour in respect to the change in monotonicity and the formation of a maximum, as Sp increases, is found for the stiffness function $e_2 - e_4$. However, the location and magnitude of the extremum are modified when compared with e_1. In this case, while a low maximum magnitude occurs for a large κ_{max} in Fig. 3.9(b), the maximum value of d increases in

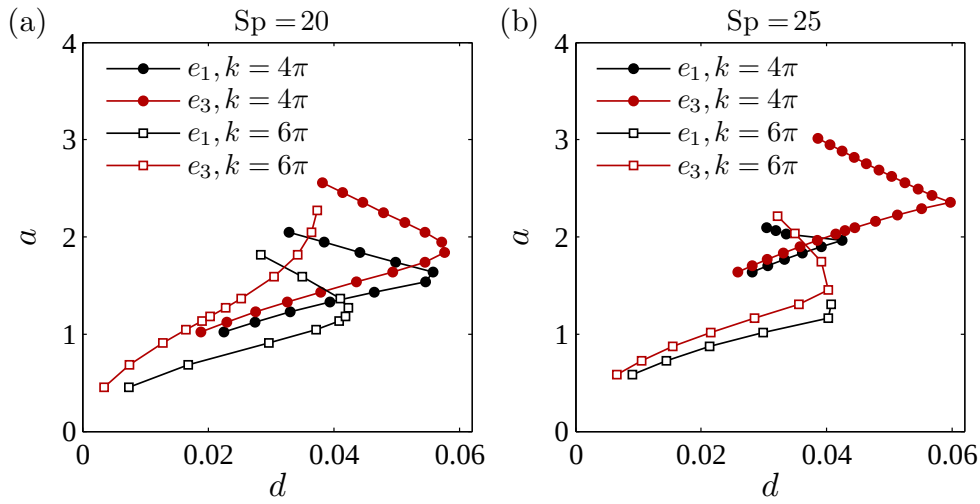

Figure 3.10: The sliding force magnitude, a, nondimensionalised by E_0/ℓ^3, with $\ell = L/\mathrm{Sp}$, as a function of the travelled distance of the flagellum centroid d, over one period, for stiffness functions e_1, e_3, with $k = 4\pi$, 6π and $\mathrm{Sp} = 20$ in (a) and $\mathrm{Sp} = 25$ in (b), as indicated.

magnitude for a continuously lower κ_{max}. As follows, the tapering functions $e_2 - e_4$ induce significant forward motion, with a lower absolute curvature, for a higher sperm compliance number, where the largest values for d are found. This is in contrast with the constant stiffness function e_1, where the largest forward motion is observed to occur at low sperm compliance number, for $\kappa_{max} < 20$.

To further analyse the relation between the cell progression and the sliding force requirement, in Fig. 3.10, the sliding force density amplitude, a, is plotted against the travelled distance d, for stiffness functions e_1 and e_3, for $\mathrm{Sp} = 20$, 25 and $k = 4\pi$, 6π. Fig. 3.10(a) show that, for the case of a constant stiffness, a given displacement d, up to $d \approx 0.04$, requires a smaller force magnitude if $k = 6\pi$, when compared with $k = 4\pi$. In contrast, when the reinforcing components are present, the sliding force magnitude required for the same displacement is larger when $k = 6\pi$. In particular, there is, approximately, a coexistence of two extrema in d associated with $k = 4\pi$ and 6π for $a \approx 1.85$ in Fig. 3.10(a). When Sp is increased, in Fig. 3.10(b), both tapering cases require less sliding force for a higher wave number. However, despite

the low values of a associated with e_1, for $k = 6\pi$, the flagellum is driving the cell in a circular trajectory when $d \approx 0.04$, due to the flagellar buckling instability. On the other hand, if the same sliding force amplitude observed for the maximum distance of (e_1, 4π) in Fig. 3.10(a) is used in Fig. 3.10(b), displacements up to $d \approx 0.04$, without circular swimming, can be obtained if the ultrastructural components are present, by increasing the wave number, even though Sp is considerably larger.

3.4 Discussion

Since the discovery of the flagellar ultrastructural components in mammalian spermatozoa, the scientific community have been debating on the biological function of this accessory complex [14, 38, 81, 86, 99, 100, 110]. Several studies, from electron microscopic to biochemical techniques, have revealed detailed information about the morphology, internal structure and molecular basis of these appendages [14, 38, 86, 99, 100, 110], ultimately unveiling its passive supporting nature. Despite this crucial advance, it is still not clear why the mammalian sperm flagellum is reinforced by this passive elastic complex and, for instance, what were the key competing factors, during evolution, for such specialised structures to emerge. Here, we consider the physical principles of the flagellar ultrastructural components for free swimming spermatozoa in a viscous fluid. The structural response of the sperm flagellum is modified by the addition of reinforcing elastic components that gradually taper along the flagellum length. The fluid-structure interaction is simplified to resistive-force theory level, while keeping the geometrically exact nature of the flagellar elastic structure, as well as taking into account the sperm head contribution. The internal forcing is represented via the sliding filament model of eukaryotic flagellar motility, ultimately responsible for generating complex flagellar waveforms that are examined in detail through numerical simulations.

While the geometrically linear theory [109] supports the idea that gradual taper-

ing of structural components play a minor role in shaping the flagellar waveform, we have demonstrated that these reinforcing flagellar appendages are fundamental for the emerging beating pattern, as well as the resulting swimming behaviour of the spermatozoa. On varying the sperm compliance, Sp, and the sliding force wave number, k, a wide range of beating patterns emerged, from large amplitude waveforms and significative sperm head yawing, for a low (Sp, k)-pair, to the meandering flagellar wave envelope formation, when (Sp, k) is large. In all cases, the flagellar accessory structures acted to considerably reduce the maximum flagellar curvature when compared with the flagellar axoneme, i.e. when the additional elastic components are absent. Such a reduction of flagellar curvature was also reported by the pioneering theoretical work by Lindemann [86].

Our numerical simulations revealed the emergence of a new flagellar buckling instability for flagellar axonemes in the regime of high sperm compliance, illustrated in Fig. 3.5 (e_1, $\mathrm{Sp} = 25, k = 4\pi$), similar to the waveform confinement reported for sea urchin sperm migrating in high viscosity liquid [143] (Fig. 3.1(b)). This wave compression buckling instability is characterised by an extreme wave confinement and formation of symmetric flagellar 'loops' in the limit of self-intersection. Although the buckling instability is commonly found for passive filaments under the action of large tangential forces [13, 15, 131], such a buckling transition is equally observed for sliding filament dynamics of eukaryotic flagella [42]. A crucial difference is, however, that the flagellar buckling instability is generated actively by the internal sliding force in conjunction with the large hydrodynamic friction experienced by the flagellum, for a large sperm compliance number. As the sliding force magnitude increases, the internal flagellar compression rises until a critical value which the flagellar structure cannot withstand, and buckles, in order to minimise the tangential force excess. As a result, the maximum absolute tension is characterised by a sharp transition associated with the increase of sliding force magnitude a, which ultimately induces a jump in

the maximum curvature along the flagellum (Fig. 3.6), causing the associated beating patterns for the points 'a' and 'b' in Fig. 3.6 to change from a spread waveform in 'a' to a large wave confinement in 'b'. In addition to this flagellar compression instability, our numerical simulations confirmed the susceptibility of flagellar axonemes to the symmetry-breaking mechanism, previously reported in Ref. [42], in which asymmetric waveforms drive the sperm cell in circular swimming trajectories, as illustrated in Fig. 3.5 (e_1, Sp $= 25, k = 6\pi$). Comparable asymmetric waveforms were also observed experimentally for sea-urchin sperm swimming in high viscosity medium [143], in the absence of hyperactivation, and illustrated in Fig. 3.1(a).

These results provide strong evidence that asymmetric beating patterns, as in Fig. 3.1(a), and extreme wave confinement, such as in Fig. 3.1(b), observed for sea-urchin flagellar axoneme in high viscosity medium [143], may emerge dynamically, via tension-driven buckling instability due to the large hydrodynamic friction experienced by the flagellum, without recourse to variations in structure or signalling influencing the molecular motors within the flagellum. In this case, the sperm flagellum becomes unable to sustain the high internal tension, ultimately, compromising the sperm migration in a high viscosity medium, and therefore preventing the sole biological function of the spermatozoa. Incidentally, sea-urchin sperm fertilise in low-viscosity seawater, thus avoiding these flagellar elastic instabilities. Internal fertilisers, on the other hand, are required to migrate in high viscosity liquids, and therefore they are susceptible to tension-driven instabilities.

Our main result from this geometrically exact formulation is that the ultrastructural components found in mammalian spermatozoa are essential for sperm migration in high viscosity medium. By reinforcing the flagellum in regions where high tension is expected [42], between the mid- and principal pieces, the flagellar accessory complex is able to prevent two distinct types of flagellar elastic instabilities during migration in high viscosity liquid [120, 143], as shown in Fig. 3.5. The added stiffness of the

ultrastructural complex acts to stabilise the flagellar structure by reducing internal tension (Fig. 3.6), consequently decreases the overall curvature along the flagellum. For a sufficiently large sliding force magnitude, however, the additional structures also act to smooth and reduce the absolute tension, so that the positive jump in T_{max} is suppressed, as illustrated in Fig. 3.6(b). As a result, for an increasing sliding force amplitude, the beating patterns are characterised by a gradual increase of the wave amplitude along the flagellum, with the formation of a wave envelope and the decrease of waveform compression (Figs. 3.5 and 3.6). The shape of the wave envelope, however, depends on the functional form of the ultrastructural tapering, associated with the functions $e_2 - e_4$, where larger cumulative stiffness, given by $\int_0^1 e_i \, \mathrm{ds}$, $i \in \{2, 3, 4\}$, in Fig. 3.3, induces a greater stabilising effect. Moreover, since the stiffness of the flagellum is larger towards mid-piece, the wave compression is highly suppressed in that region [120], as opposed to the end piece, see for instance Fig. 3.1(d,e), which suggests that the average bending stiffness at the flagellum mid-piece may be larger than the stiffness considered in this numerical study, i.e. four times the stiffness of the axoneme; compare for instance Fig. 3.1(d,e) with Figs. 3.4 (e_3, $\mathrm{Sp} = 25, k = 6\pi$) and 3.6(d,e,f). Furthermore, the tapering of the additional flagellar components naturally leads to the concentration of the flagellar motion towards the distal end, as observed empirically [42,120], without recourse to viscoelastic effects from the cervical mucus [40]. Although the structural reinforcing effect is dominant while shaping the waveform, non-linear viscous properties from the fluid change dramatically the forces experienced by the sperm flagellum [43], and may act to favour the concentration of large amplitude bending waves at the end piece region [40].

By preventing excessive flagellar wave compression associated with high curvatures (Fig. 3.6 and 3.9), and consequently flagellar self-intersection due to higher order elastic instabilities for high sperm compliance numbers, the sperm with a structurally reinforced flagellum is able to generate larger progressive velocity, for a given

sliding force wave number k, than the simpler flagellar axoneme (Fig. 3.7). As a result, less absolute curvature is required for the structurally reinforced flagellum in order to achieve locomotion in high sperm number regime, as illustrated in Fig. 3.9(d). Nevertheless, for a given sperm compliance parameter, increasing the sliding force wave number induces a reduction in the flagellar wave amplitude. This in turn causes a reduction on the progressive swimming speed (Fig. 3.8), given that a smaller volume of fluid, or area, for planar beating patterns, is covered by the flagellum during propulsion. Further the smaller flagellar beating frequency observed for high viscosity liquids [120] acts to reduce swimming speeds as viscosity is increased, assuming Newtonian behaviour. As a consequence, the decrease in the maximum cell progression caused by large wave numbers is dominant, and exceed the eventual increase of swimming speed induced by the reinforcing role of ultrastructural components, when Sp is large; compare for instance Figs. 3.7 and 3.8. On the other hand, by increasing the sliding force wave number the required internal force amplitude to achieve locomotion is reduced, for a sufficiently high Sp (Fig. 3.10(b)), which may explain why the observed waveform modulation in increased viscosity [120] switch from low to high wave number. Furthermore, by changing the functional form of the tapering function, the maximum progression per beat changes its maximum across (Sp, k)-parameter space, where the upper limit is constrained by the wave number (Fig. 3.9).

It is also noteworthy that because the sperm compliance number depends on a geometrical factor, given by the flagellum length, long flagella observed in many mammalian spermatozoa, with the largest flagellum about 200 μm long, for Chinese Hamster sperm, can also contribute to a higher sperm compliance parameter, further increasing the sperm susceptibility to flagellar elastic instabilities found in this regime. In this manner, as originally proposed in the literature [14, 38, 81, 86, 99, 100, 110], the addition of structural and mechanical support, such as the outer dense fibres in mammalian flagella, may also act to stabilize the longer flagellum, with a larger

number of molecular motors. Nevertheless, despite the contribution of the flagellum length to a higher sperm compliance, the largest contribution comes from the high viscosity associated with the biological fluid where the mammalian spermatozoa is required to swim, which can easily surpass the figure of hundred times the viscosity of water [43,120], thus inducing a high sperm compliance, even for the shortest flagellum. Furthermore, the relation between an increase of the number of molecular motors and the resulting sliding force is not straightforward. Indeed, the sliding speed of cytoskeletal filaments in gliding assays can remain unchanged after increasing the molecular motor density [15, 125]. Consequently, the stabilising role of the flagellar accessory structures in mammalian sperm is, from a mechanical perspective, the reduction of the impact associated with tension-driven deformations arising from the large viscous friction experienced by mammalian sperm flagellum.

In conclusion, our geometrically exact formulation makes specific predictions on the function of the ultrastructural components found in mammalian spermatozoa, revealing the essential role of these accessory structures for sperm migration in high viscosity medium. By reinforcing the flagellum in regions where high tension is expected [42], the flagellar accessory complex is able to prevent tension-driven elastic instabilities that compromise a core biological function of the cell: the transport of genetic material within highly viscous environments. These results demonstrate that the tapering of structural components plays an important role in shaping the flagellar waveform, further suggesting that the flagellar wave modulation observed empirically [120] may be achieved without recourse to intricate molecular motor regulation [43] via, for example, a constant sliding force amplitude along the flagellum. It can also be hypothesised that the viscosity of the medium where the spermatozoa are naturally required to swim may have acted decisively during the evolutionary process for internal fertilisers, such as human sperm, inducing specialised mutations in order to generate flagellar passive supporting structures to enable the cell to pene-

trate in high viscous fluids. Likewise, the cervical mucus may also have co-evolved in order to select biologically fit spermatozoa, thus ensuring the quality of the internal structure of the cell and, therefore, avoiding genetic diseases related with the flagellum and cilia dysfunction; the so-called 'ciliopathies', which cause in excess of thirty known distinct and severe pathologies for humans [4]. These results also indicate the importance of using high viscosity fluid while screening spermatozoa in the clinical setting [43, 69, 120]. Finally, our numerical investigation showed the possibility of different hydrodynamic optimisation schemes, while designing biologically inspired artificial swimmers, given that the maximum progressive speed depends on an intricate interplay between the fluid viscosity, the internal force density amplitude and wave number, in addition to the functional form of the structural tapering along the axial length.

Chapter 4

Statics and dynamics of planar shearable filaments in viscous fluid: A Cosserat rod approach

4.1 Introduction

The mechanical properties of filamentous polymers play a diverse and complex role in biology. They are responsible for multiple architectural constraints in a broad range of biological structures, ranging from cytoskeletal shape in eukaryotic cells to cellular division and locomotion, via structures such as flagella, cilia and lamellipodia [5]. The biological function of each semiflexible polymer is intrinsically associated with their material properties. In the cytoskeleton of eukaryotic cells, microtubules have typically a flexural rigidity of hundred times more than the other two constituent polymers, hence by resisting compression it is likely that the microtubules support, for instance, cell shape regulation [5, 58] (Fig.4.1). In contrast, the actin and intermediate filaments are known to withstand tension, and may well act as connecting cables within the cellular scaffolding while also assisting in cell shape organization [*ibid*]. Bundles of these filamentous polymers, on the other hand, are commonly formed by an assembly of semiflexible filaments interconnected by crosslinking proteins in an array of intricate three-dimensional arrangements [12, 26, 53, 54, 130], varying from rectangular uniform distribution of filaments, for F-actin bundles, to shell-like struc-

tures as observed in the axoneme within the cilia and flagella, and are ultimately responsible for an intricate mechanical response [60, 64, 70, 84, 103, 130].

A variety of experimental techniques in biology have been employed to extract the mechanical properties of a single filamentous structure, as well as their assembly in bundles, such as thermal fluctuations [45, 60, 102, 134], calibrated flow deformation [30, 134], column-like buckling [29, 67, 71, 84, 93, 97, 98, 103, 122, 126, 130, 133, 136], among others [12, 26, 27, 70, 95, 139, 140]. Despite the intrinsic complexity associated with the internal components and architecture of these flexible slender bodies, Euler-Bernoulli beam theory has been widely used to probe their material quantities [29,30,45,60,67,71,84,95,97,98,103,126,133,134,139,140]. Incidentally, a remarkable controversy has occurred in the literature regarding the flexural stiffness of microtubules with different lengths [60,64,70,71,102,126], where the reported lowest flexural stiffness is associated with microtubules that are few microns long, while higher stiffness is observed for microtubules with lengths of tens of microns [71, 102, 126, 134]. The latter provides strong experimental evidence that microtubules do not behave as simple Euler-Bernoulli rods; nonetheless the similarity between the shape deformation, for instance, in Fig.4.1, with the classical Euler-elastica [8, 41, 73, 128], entails that these observations triggered the unusual hypothesis of a length-dependent flexural stiffness for microtubules, which contradicts the concept of length-independent flexural stiffness for isotropic elastic rods. A similar scenario is also found for bundle of cytoskeletal filaments, in which, once again, the complex mechanical responses cannot be explained by the Euler-Bernoulli theory [12, 26, 27, 84, 103, 130], as for instance the paradoxical counter curvatures that are instigated by the interfilament sliding observed in buckling-like experiments with flagellar axonemes [84, 103]. Indeed, a common feature among all the above biological slender structures is the ability to shear, in addition to bend, under the action of external forces [24, 25, 84, 103]. The shearing deformation is however a consequence of the internal mechanics which causes

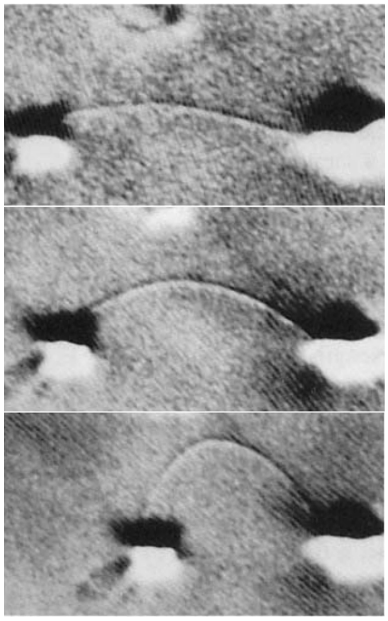

Figure 4.1: Example shape deformation of a single microtubule during buckling experiment [71]. Figure reproduced from Kurachi et al. [71] with permission from John Wiley and Sons (2958780034260).

the elastic bending to couple with shearing displacements, effectively modifying the mechanical response of the structure [12, 26, 71, 84, 93, 102, 103, 126, 130, 130, 134].

A variety of mathematical models have attempted to incorporate the true significance of a low shear modulus on the behaviour of biological slender-bodies [12, 17, 26, 35, 44, 53, 54, 64, 70, 76, 102, 116, 130, 132], including the linear analysis of transversal shear in a single filament [64, 70], composite structure theory [102], orthotropic elastic shell models [76], Timoshenko beam theory [44, 116, 132], and sliding filament models to describe individual polymers and filament bundles [12, 17, 26, 35, 53, 54, 130]. Although these existing works [12, 17, 26, 35, 44, 53, 54, 64, 70, 76, 102, 116, 130, 132] have offered several insights on the importance of shear, for instance, on the length-dependent flexural rigidity of microtubules [44, 64, 70, 76, 102, 116, 132] and the bending stiffness discrepancy between single- and double-stranded DNA [35, 53, 54], the fundamental nature of shearing effects is still a matter of debate, while the relationship between all these different ideas is unclear. In particular, a study accounting for shear-

ing deformations via first principles, in a sufficiently general framework, as well as the influence of geometrical non-linearities, has been largely neglected in the literature.

Thus, in contrast to the vast majority of works on the mechanical behaviour of shearing effects, the exact geometry of deformation is investigated by allowing a very general interaction of deformations in different material directions, by not only accounting for bending, but also shear. Based on the special Cosserat theory for geometrically exact planar deformations of elastic rods [8], we explore both the statics and dynamics of shearable elastic slender-bodies, with a constant axial length, and immersed in a viscous fluid. For the dynamic system, we incorporate shear into the classical hyperdiffusion-type problem of Euler-Bernoulli filaments deforming in inertialess fluids [13, 21, 40, 42, 46, 57, 88, 131, 139–141, 144] . We report the emergence of a novel bending effect instigated by the absence of monotonicity between moments and curvature, in contrast with the Euler-Bernoulli model. For the equilibrium case, we revisit the buckling instability and show that shearing effects can reproduce an apparent dependence of the flexural rigidity with the filament length, as observed experimentally for filaments with a low shear modulus. Furthermore, we analyse the differences between the Cosserat rod theory and the Timoshenko beam theory, by showing that the discrepancy between the two models goes beyond the geometry and, most importantly, they disagree at the material constitutive level. Finally, we show that pure material shearing effects from Cosserat rod theory or, equivalently, the Timoshenko's beam theory are essentially disconnected from the sliding filament induced shear found in filament bundles, such as the axoneme, and therefore they are unable to explain the paradoxical counterbend effect [84, 103].

4.2 Cosserat rod theory

We consider both the statics and dynamics of nonlinearly elastic slender rods immersed in a viscous fluid, undergoing planar deformations in absence of torsion.

The elastic slender-body can bend and shear, in such a way that the axial length is preserved, hence, combining different aspects from inextensible Kirchhoff rods with more general elastic bodies, in which shearability is present. For this purpose, we employ the special Cosserat theory of rods [8, 28].

4.2.1 Geometry of deformation

Consider an elastic slender body $\mathfrak{B}$ embedded in a three-dimensional space defined by an orthonormal fixed frame of reference $\{\boldsymbol{i}, \boldsymbol{j}, \boldsymbol{k}\}$, and subjected to deformations that preserve its $\{\boldsymbol{i}, \boldsymbol{j}\}$-plane symmetry. The reference configuration of the body is taken to be its natural configuration, in which $\mathfrak{B}$ is straight in the rest state. The position of any point of the elastic body $\mathfrak{B}$ lying on the $\{\boldsymbol{i}, \boldsymbol{j}\}$-plane can be described by an arbitrary material curve, also called base curve, typically chosen to lie at the centreline of the body along its axial direction. In the reference configuration, we identify $\boldsymbol{r}^{\circ}(s)$ as the material plane curve, where $s \in [0, L]$ is taken to be the arclength parameter with total axial length L. When the elastic body is deformed to a configuration shown in Fig. 4.2, $\boldsymbol{r}^{\circ}(s)$ is mapped to the material curve $\boldsymbol{r}(s)$, where s is the material parameter and thus not, in general, the arclength. The average orientation of a deformed material cross section at s along the slender body is defined by the director $\hat{\boldsymbol{a}}(s)$, tangent to the cross section (see Fig. 4.2), via

$$\boldsymbol{p}(s, \xi) = \boldsymbol{r}(s) + \xi \hat{\boldsymbol{a}}(s) \tag{4.1}$$

where the thickness parameter $\xi \in [q_{-}(s), q_{+}(s)]$ is bounded by $q_{\pm}(s)$ and defines the region occupied by the body $\mathfrak{B}$. We restrict our attention to slender filaments with a constant diameter d, hence in general the thickness bounding values $q_{\pm}$ are functions of s to account for variations of the vector field $\hat{\boldsymbol{a}}(s)$. We also introduce the director $\hat{\boldsymbol{b}} \equiv -\boldsymbol{k} \times \hat{\boldsymbol{a}}$, as the unit vector normal to the cross section of the slender body $\mathfrak{B}$, also defining the angle θ relative to $\boldsymbol{i}$ at some point along the material curve $\boldsymbol{r}(s)$, as illustrated in Fig. 4.2. The slender body configuration can be decomposed in terms

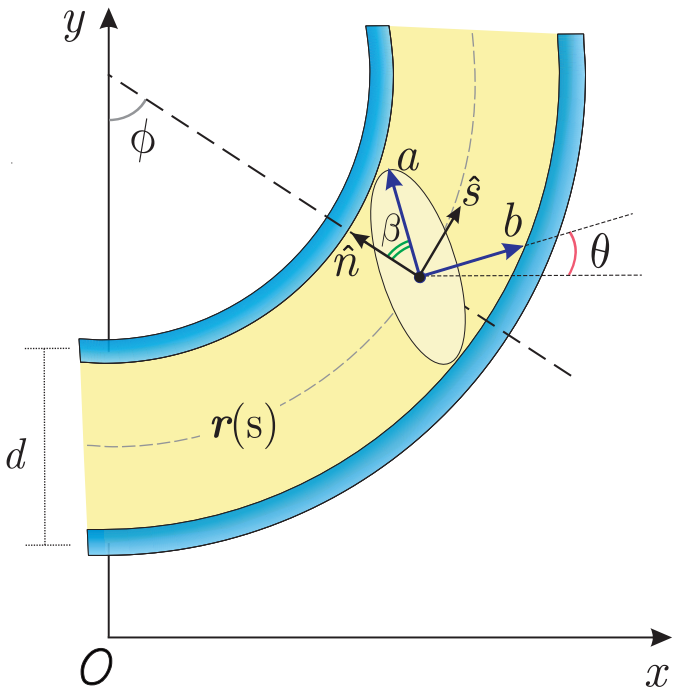

Figure 4.2: Schematic representation of a section of the slender elastic body in a deformed configuration.

of the director basis

$$\boldsymbol{r}_s = \eta \hat{\boldsymbol{a}} + \lambda \hat{\boldsymbol{b}}, \tag{4.2}$$

where the subscript s denotes differentiation with respect to the material coordinate. We take the director basis $\{\hat{\boldsymbol{a}}, \hat{\boldsymbol{b}}\}$ relative to fixed frame of reference as

$$\hat{\boldsymbol{a}} = -\sin\theta \boldsymbol{i} + \cos\theta \boldsymbol{j} \tag{4.3}$$

$$\hat{\boldsymbol{b}} = \cos\theta \boldsymbol{i} + \sin\theta \boldsymbol{j}. \tag{4.4}$$

The functions η, λ, θ_s in Eq. (4.2) are the strain variables responsible for the deformed configuration in Fig. 4.2 and Eq. (4.1). At the natural configuration, they are identified as $\eta^\circ = \theta_s^\circ = 0$ and $\lambda^\circ = 1$, in addition to $\theta^\circ = 0$ so that $\boldsymbol{r}_s^\circ = \hat{\boldsymbol{b}}^\circ = \boldsymbol{i}$. Equation (4.2) is the basis of the special Cosserat rod theory [8], and accounts for bending, stretching and shearing deformations.

It is also convenient to introduce from Fig. 4.2 the shear angle

$$\beta = \arcsin\left(\hat{\boldsymbol{a}} \cdot \frac{\boldsymbol{r}_s}{\|\boldsymbol{r}_s\|}\right), \tag{4.5}$$

thus generalising the curvature of the base curve to

$$\kappa = \frac{\phi_s}{\|\boldsymbol{r}_s\|} = \frac{\theta_s + \beta_s}{\sqrt{\eta^2 + \lambda^2}}, \tag{4.6}$$

given by the derivative of the angle of curvature, $\phi = \theta + \beta$, relative to the physical arclength. Eq. (4.6) accounts for pure bending deformations, related with variations in θ, in addition to changes in curvature that are influenced by the stretch of the base curve relative to the reference configuration, $\|\boldsymbol{r}_s\|$. It becomes clear from Eqs. (4.2)-(4.6) that the strain variable η is in fact related with shearing deformations, while λ is generally linked with the material stretching. If $\eta = 0$ for every configuration of the body, the elastic rod is said to be unshearable, while if $\lambda = 1$ the rod is called inextensible. The Kirchhoff rod theory describe materials that are both inextensible, $\lambda = 1$, and unshearable, $\eta = 0$, and corresponds to a special case of the Cosserat rod theory, where the tangent vector is of unity length and given by $\boldsymbol{r}_s = \hat{\boldsymbol{b}}$, and the material coordinate s coincides with the physical, and preserved, arclength after deformation. It is noteworthy, however, that the single association between the material stretching and the strain variable λ is rather imprecise. Shearing deformations can equally produce variations on the total axial length, causing the rod to shrink or stretch as it deforms. In particular, if $\lambda = 1$ and $\eta \neq 0$, an undeformed fibre along the centreline of the body will not preserve its original length after deformation, as the magnitude of the tangent vector is not unitary $\|\boldsymbol{r}_s\| = \sqrt{\eta^2 + 1}$, and therefore the label "inextensible" is a misnomer. Here we consider shearable and "unstretchable" materials, i.e. shearable materials in which the axial length is preserved after deformation, by letting λ counteract variations in arclength, $\|\boldsymbol{r}_s\| = \sqrt{\eta^2 + \lambda^2} \equiv 1$. Hence, the tangent vector is a function of only two strain variables and reduces to

$$\boldsymbol{r}_s = \sin\beta\,\hat{\boldsymbol{a}} + \cos\beta\,\hat{\boldsymbol{b}}, \tag{4.7}$$

where the parameter s is physical arclength. Furthermore, λ is required to be non-zero and positive throughout the arclength, i.e. $\cos\beta > 0$. This condition accounts for the fact that deformations cannot be so severe that the stretch can be reduced to zero or that the shearing is so intense that the tangent vector $\boldsymbol{r}_s$ would coincide with the director $\hat{\boldsymbol{a}}$ [8].

4.2.2 Balance of forces and torques

The stresses acting at a point s along the slender-body $\mathfrak{B}$ are given by a resultant contact force $\mathbf{N}(s)$ and contact moment $\mathbf{M}(s)$. In the absence of inertial effects, the total balance of *linear* and *angular* momentum simplifies to [8]

$$\mathbf{N}_s + \mathbf{f} = 0 \tag{4.8}$$

$$\mathbf{M}_s + \boldsymbol{r}_s \times \mathbf{N} + \mathbf{l} = 0, \tag{4.9}$$

where the vector field $\mathbf{f}(s)$ and $\mathbf{l}(s)$ are, respectively, the body force and body couple per unit length. The stress-strain relationship of the elastic body $\mathfrak{B}$ is defined by material constitutive relations. We consider the simplest case of hyperelastic homogeneous materials in which the stress is linearly related with the strain

$$\mathbf{N}(s) = G\sin\beta\,\hat{\boldsymbol{a}} + \tau\hat{\boldsymbol{b}} \tag{4.10}$$

$$\mathbf{M}(s) = E\theta_s\boldsymbol{k}, \tag{4.11}$$

where G is the shear modulus and accounts for the material ability to resist shearing forces, and E is the elastic stiffness associated with the restoring bending moment. The function τ, on the other hand, is not defined consitutively. It acts instead as the Lagrange multiplier, implicitly determined by $\boldsymbol{r}_s \cdot \boldsymbol{r}_s = 1$, to preserve the total arclength so that the internal fibres along the slender body will not elongate or shorten after deformation. It is also noteworthy that although pure shearing displacements, and consequently, pure stretching displacements can influence changes in curvature, Eq. (4.6), in the asymptotic limit where the slenderness ratio d/L tends to zero, they

do not exert a flexural bending moment [41]. In other words, Eq. (4.11) isolates the true effects of pure bending, via the strain variable θ_s, from changes in curvature due to the shearing and/or stretching.

4.2.3 Boundary conditions

We will consider slender-bodies governed by natural boundary conditions. We denote a boundary point by $\bar{s} \in \{0, L\}$, as each physical constraint considered here can be applied for both endpoints. In general, we may specify either the position of the slender-body or impose a contact force at endpoints, i.e.

$$\text{(a)} \quad \boldsymbol{r}(\bar{s}) = \boldsymbol{r}_0 \quad \text{or} \quad \text{(b)} \quad \mathbf{N}(\bar{s}) = \mathbf{N}_0 \,. \tag{4.12}$$

For a fixed position, condition (4.12)a, the contact force $\mathbf{N}(\bar{s})$ is not prescribed so that it remains free to accommodate Eq. (4.12)a. Analogously, when the contact force is constrained, Eq. (4.12)b, the position $\boldsymbol{r}(\bar{s})$ is free to vary. Notice, however, that for equilibrium problems the contact force at both ends cannot be prescribed independently, as the resultant contact force on the body must vanish. Similarly, we can prescribe the orientation of $\hat{\boldsymbol{a}}$ for the shearable body or impose a non-zero bending moment at the endpoints so that

$$\text{(a)} \quad \theta(\bar{s}) = \theta_0 \quad \text{or} \quad \text{(b)} \quad \mathbf{M}(\bar{s}) = \mathbf{M}_0 \,, \tag{4.13}$$

respectively, where the constraints (4.13)a and (4.13)b cannot be used concomitantly at the same point $\bar{s}$. If the slender-body is free from external forces and moments at the endpoints,

$$\mathbf{N}(\bar{s}) = 0 \quad \text{and} \quad \mathbf{M}(\bar{s}) = 0 \,. \tag{4.14}$$

A common alternative to boundary condition (4.13)a is to to prescribe the tangent vector by letting

$$\phi(\bar{s}) = \phi_0 \,, \tag{4.15}$$

obtained, for instance, by imbedding a rigid shaft into a groove at the centreline of the body. This condition is equivalent to Eq. (4.13)a for unshearable materials.

Furthermore, there is a class of engineering motivated problems in which it may be desired to constrain not only the position vector $\boldsymbol{r}(\bar{s})$ at the endpoint, but also the amount of shear at this location, by imposing a shear angle β_0. Ultimately, this leads to a further constraint on the contact force $\mathbf{N}(\bar{s})$, requiring the addition of an unknown feedback force and/or a feedback couple in order to satisfy Eqs. (4.12)a,b simultaneously [8, 9]. For this reason, the latter is part of the so called unnatural problems, which are notorious for analytical challenges [8] and even responsible for mechanical instabilities [9]

4.2.4 Kinematics of deformation

The velocity field of the material curve captures the time evolution of the slender-body $\mathfrak{B}$ under deformation, and since the axial length is preserved, this can be readily expressed in terms of the orthonormal Frenet basis $\{\hat{\boldsymbol{s}}, \hat{\boldsymbol{n}}\}$, which denotes, respectively, the tangent ($\hat{\boldsymbol{s}} \equiv \boldsymbol{r}_s$) and normal vectors to the base curve $\boldsymbol{r}(s,t)$, as

$$\boldsymbol{r}_t = V\hat{\boldsymbol{n}} + U\hat{\boldsymbol{s}} \ , \tag{4.16}$$

where subscript t denotes differentiation with respect to time, and V, U are interpreted as the normal and tangential velocities of the elastic body. By using the compatibility condition $\boldsymbol{r}_{st} = \boldsymbol{r}_{ts}$, it is possible to derive the dynamic equations of the material curve that describes the slender-body

$$\phi_t = V_s + \phi_s U \tag{4.17}$$

$$0 = U_s - \phi_s V \ , \tag{4.18}$$

by projecting onto the normal and tangent directions with $\phi = \theta + \beta$. Hence, given the velocity field of the base curve, the time evolution of the elastic rod can be calculated

by integrating Eqs. (4.17) and (4.18) together with

$$\boldsymbol{r}(s,t) = \boldsymbol{r}(0,t) + \int_0^s (\cos\phi \boldsymbol{i} + \sin\phi \boldsymbol{j})\, \mathrm{d}s' \,, \tag{4.19}$$

to reconstruct the rod shape relative to the fixed frame of reference. Note that Eq. (4.19) already accounts for the fact that the axial length of the rod is preserved.

4.3 The dynamics of shearable filaments in a viscous fluid

4.3.1 Geometrically exact formulation

We consider the dynamics of a slender-body $\mathfrak{B}$ immersed in an inertialess viscous medium, characterised by the low Reynolds number hydrodynamics. The slender-body is free from body couples so that $\mathbf{l} = 0$ in Eq. (4.9). The body forces, however, in Eq. (4.8) are non-zero and results from the hydrodynamic drag per unit length, $\mathbf{f}_\mathrm{h}$, experienced by the elastic body. The hydrodynamic coupling is simplified to leading order by employing the resistive-force theory [49], which relates the velocity of the slender-body to the hydrodynamic force exerted on the fluid, via the anisotropic drag coefficient matrix

$$\mathbf{f}_\mathrm{h} = -\left[\xi_\perp \hat{\boldsymbol{n}}\hat{\boldsymbol{n}} + \xi_\parallel \hat{\boldsymbol{s}}\hat{\boldsymbol{s}}\right] \cdot \boldsymbol{r}_t, \tag{4.20}$$

where $\xi_\perp, \xi_\parallel$ represent, respectively, the perpendicular and parallel drag coefficients.

The dynamic equations (4.16)-(4.18), together with Eqs. (4.8)-(4.11) and (4.20) specify the motion of the elastic body in a viscous fluid in terms of θ, β and τ,

$$\begin{aligned} \xi_\perp \phi_t = & -E\left(\theta_{ssss} - \delta\,\phi_s^2\,\theta_{ss}\right) + \phi_{ss}\left(G\sin^2\beta + \tau\cos\beta\right) \\ & + (1+\delta)\phi_s\left(G\sin^2\beta + \tau\cos\beta\right)_s, \end{aligned} \tag{4.21}$$

still subject to boundary conditions. By considering the balance of contact forces and solving Eqs. (4.8), (4.10), (4.16) and (4.20), the inextensibility constraint can be reduced to

$$\delta\left(G\sin^2\beta + \tau\cos\beta\right)_{ss} - \phi_s^2\left(G\sin^2\beta + \tau\cos\beta\right) = -E\phi_s\theta_{sss} - \delta\,E(\phi_s\theta_{ss})_s \tag{4.22}$$

where $\delta \equiv \xi_\perp/\xi_\parallel$. The balance of angular momentum Eq. (4.9) yields to

$$E\theta_{ss} + G\sin\beta\cos\beta - \tau\sin\beta = 0. \tag{4.23}$$

Eq. (4.21) determine the dynamics of θ and β, while Eq. (4.22) specify a second order boundary-value problem for the lagrange multiplier τ. The balance of angular momentum, Eq. (4.23), provides an additional equation for the unknown shearing displacement, and it is characterised by an instantaneous coupling between θ, β and τ. The governing equations (4.21)-(4.23) represent the geometrically exact elastohydrodynamic formulation of a shearable and unstretchable Cosserat elastic filament deforming in a viscous fluid. As reminiscent of elastohydrodynamic formulation for inextensible filaments [42, 57], the system of equations (4.21)-(4.23) is characterised by highly-coupled non-linear partial differential equations with fourth-order derivatives, which are notorious for imposing severe time-stepping constraints in numerical schemes [42, 57, 131]. In addition, notice that for a non-shearable and inextensible material, Eqs. (4.21)-(4.23) are equivalent to the elastohydrodynamics of Kirchhoff filaments in the absence of torsion [42, 57, 131].

4.3.2 The linear theory

For small displacements, the equations of motion (4.21)-(4.23) can be further simplified and allow analytical progress. In this limit, small curvatures constrain the variation of both $\theta, \beta \ll 1$, which results in a partial decoupling of the strain variables. Nondimensionalising with respect to the length scale L and time scale $L^4\xi_\perp/E$, the *dimensionless* linear theory of shearable and unstretchable filament moving in a Stokes fluid reads

$$\theta_t - \nu\theta_{sst} + \theta_{ssss} = 0 \tag{4.24}$$

$$\beta + \nu\theta_{ss} = 0 \ , \tag{4.25}$$

where the stretching τ only contributes to higher orders of deformation. The shear-compliance parameter

$$\nu = \frac{E}{GL^2} \tag{4.26}$$

is a dimensionless geometrical quantity and characterises the relative importance between pure bending and pure shearing forces. In the limiting case where shear compliance is absent, $G \to \infty$, and therefore $\nu \to 0$ and $\beta \to 0$, leading to the so called "hyperdiffusion" equation

$$\gamma_t + \gamma_{ssss} = 0, \tag{4.27}$$

where γ is the tangent angle relative to the fixed frame of reference. Eq. (4.27) describes the elastohydrodynamics of a passive Euler-Bernoulli filament in a viscous fluid and have been widely studied both mathematically [46, 47, 88, 140, 141] and experimentally [140, 144]. The latter represents the traditional dynamics of a non-shearable material where changes in curvature are only associated with the body flexure. Clearly, Eqs. (4.24), (4.25) generalise the usual dynamics of passive filaments Eq. (4.27) by incorporating the effect of shear. The effect of shear is simply regulated by the shear-compliance parameter ν so that shear is absent when $\nu = 0$, but becomes increasingly important as ν increases. In particular, the shear parameter ν is bounded by a critical value ν_c in which $\cos\beta > 0$ still holds, and therefore $\nu \in [0, \nu_c]$.

In the following sections, we study the effect of shear for two experimentally motivated systems: (a) The relaxation of an initially bent shearable filament in a viscous fluid, in the absence of external forces and torques. (b) The propulsive dynamics of a periodically actuated shearable filament via an angular oscillation at $s = 0$.

4.3.3 Relaxation of shearable filaments

We consider the transient dynamics of a shearable slender-body, initially deformed, relaxing in a viscous fluid by employing standard spectral techniques to evaluate the exact solutions of Eqs. (4.24), (4.25). We begin by multiplying Eq. (4.24) by

an arbitrary function $S_c(s)$, where c denotes an unknown parameter rather than a derivative, and integrate over domain of s [140],

$$\int_0^1 S_c\,\theta_t\,\mathrm{d}s = -\int_0^1 S_c\,\theta_{ssss}\,\mathrm{d}s + \nu\int_0^1 S_c\,\theta_{sst}\,\mathrm{d}s. \tag{4.28}$$

Six surface terms, from a total of twelve boundary terms resulting from Eq. (4.28), can be eliminated by imposing boundary conditions. We firstly consider the situation where the slender-body is completely free from external forces and torques at the endpoints $s = 0, 1$, Eq. (4.14), requiring $\theta_s|_{s=0,1} = \theta_{ss}|_{s=0,1} = 0$. The remaining surface terms in Eq. (4.28) are equally eliminated by choosing the function S_c to inherit the conditions imposed on θ at the boundary points. Additionally, if we choose S_c to satisfy

$$\partial_s^4 S_c = c^4\left[1 - \nu\partial_s^2\right] S_c, \tag{4.29}$$

and define $\bar{\theta}_c \equiv \int_0^1 (S_c - \nu\,\partial_s^2 S_c)\,\theta\,\mathrm{d}s$, the equation of motion can be further simplified, hence leading to the solution

$$\bar{\theta}_c(t) = \bar{\theta}_c(0)\,e^{-c^4 t}. \tag{4.30}$$

The spatial dependence, however, imbedded in $S_c(s)$ still need to be determined from Eq. (4.29). This is done by considering a linear combination of the Fourier basis with hyperbolic trigonometric functions,

$$S_c(s) = r_1\cosh(q_1 s) + r_2\sinh(q_1 s) + r_3\cos(q_2 s) + r_4\sin(q_2 s) \tag{4.31}$$

where Eq. (4.31) is the general solution of Eq. (4.29) and

$$q_l = c\sqrt{\frac{(-1)^l\nu c^2}{2} + \sqrt{1 + \left(\frac{\nu c^2}{2}\right)^2}},\ \text{for } l = 1, 2. \tag{4.32}$$

The coefficients $\{r_i\}$ and permitted wave numbers c are specified by boundary conditions, cf. Appendix B. Because of the format of the eigenfunctions (4.31), the

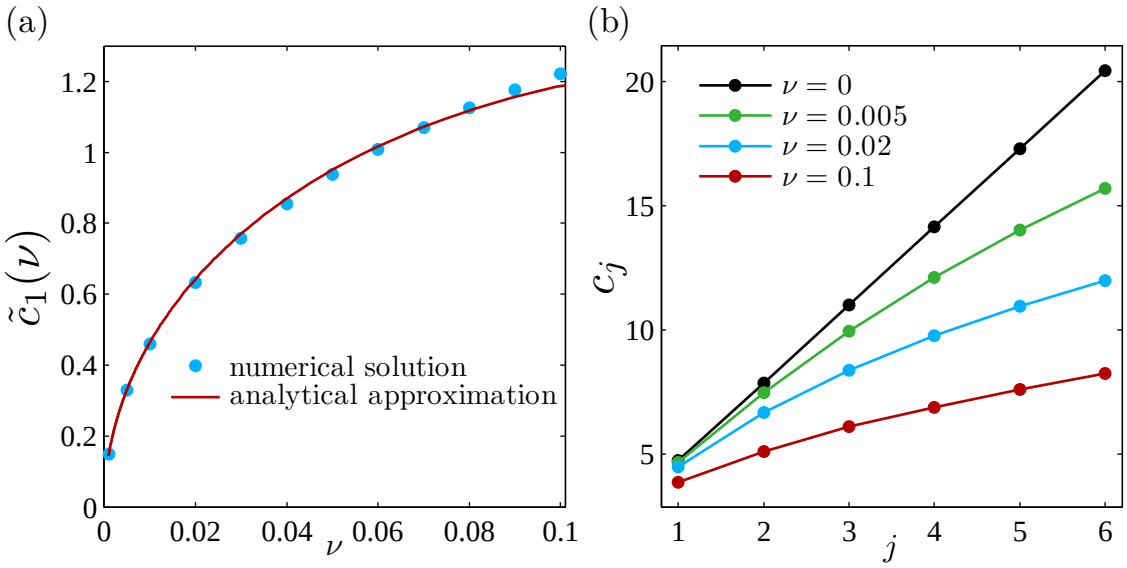

Figure 4.3: The permitted wave number c for the free ends boundary condition: (a) Comparison between the analytical approximation of the first mode coefficient $\tilde{c}_1$, from Eq. (4.34), with the numerical solution of transcendental equation (4.33), when rescaled $E\xi_\perp/G$. (b) First six roots calculated numerically from Eq. (4.33) for three distinct values of shear number

relaxation coefficients c are roots of transcendental solvability conditions. For the free ends case this condition can be simplified to

$$1 - \cos q_2 \cosh q_1 = \left(\frac{\nu\, c^2}{2}\right) \sin q_2 \sinh q_1, \tag{4.33}$$

where the $\{r_i\}$'s are given by Eq. (B.3); different boundary conditions inserted in Eq. (4.31) lead to a distinct a family of eigenfunctions and transcendental solvability condition, see Appendix B. If we instead rescaled time by $E\xi_\perp/G$ in Eq. (4.33), the first root of solvability condition can be approximated by

$$\tilde{c}_1 \simeq 4.7435\,\sqrt{\nu} - 9.8915\,\nu^{3/2}. \tag{4.34}$$

A comparison between this expression and the numerical solution of the rescaled solvability condition is provided in Fig. 4.3(a), while the first six roots from Eq. (4.33), evaluated numerically, are shown in Fig. 4.3(b), for three distinct values of shear number. The normalised eigenfunctions and associated shape solution are portrayed

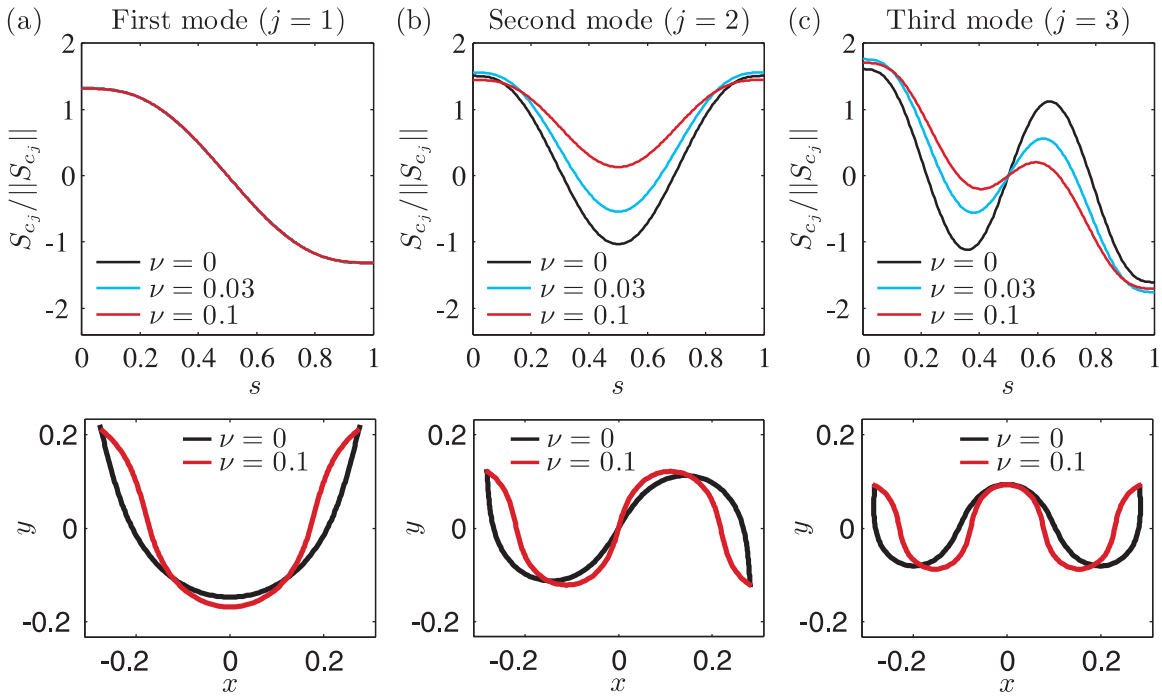

Figure 4.4: The effect of shear on the normalised eigenfunctions and associated shape solution for the free first three roots of the transcendental condition (4.33). Note that in (a) the eigenfunctions are overlaid.

in Fig. 4.4 for the first three modes. Finally, we complete the formulation by relating the initial configuration of the slender-body with later-time solutions via

$$\theta(s,t) = \int_0^1 g(s,s',t)\,\theta(s',0)\,\mathrm{d}s', \tag{4.35}$$

where

$$g(s,s',t) = \sum_j S_{c_j}(s) S_{c_j}(s')\, e^{-{c_j}^4 t} \tag{4.36}$$

is the Green's function. The shape solution relative to the laboratory frame of reference can evaluated from Eqs. (4.19), (4.25), whereas the directors are given by Eq. (4.3). Furthermore, because the equations of motion were linearised by considering a small angle approximation, the exact solution (4.35) is equally valid for large displacements, as long as the curvature do not exceed $\mathcal{O}(\tau)$.

We now turn our attention to the consequences of the material shearability on the transient dynamics. Fig. 4.3(b) shows how the relaxation coefficient of each mode is

altered, by a decrease in its magnitude as shear compliance increases, when compared with non-shearable materials (black curve in Fig. 4.3(b)). In particular, the roots of the solvability condition when shearability is present are not evenly spaced over the domain of c, which results in a non-linear growth of c with the wave number. Despite the fact that the root of the dominant mode appears to have a modest variation with ν in Fig. 4.3(b), this is sufficient to induce significant differences on the relaxation time, as the solution in Eq. (4.35) decays with time constant $\mathcal{T}_1 = 1/c_1^4$. A similar behaviour is also found for the spatial part of the solution. The eigenfunctions of the first mode, displayed in Fig. 4.4(a), for the shearable and non-shearable cases are overlaid, since the eigenfunctions depend on trigonometric function of c, and c is only slightly modified by the shear compliance, Fig. 4.3(b). Nevertheless, because the configuration of the centreline depends upon the angle of curvature, which is equally influenced by shearing deformations $\phi = \theta - \nu\theta_{ss}$, the resulting shape differs substantially from non-shearable filaments (black curve at the associated shape solution in Fig. 4.4(a)). Now, shearing displacements along the slender-body are responsible for large-scale deformations, forcing the neutral line near the boundaries to bend in opposition to the imposed curvature for a given wave number, Fig. 4.4. It is noteworthy that the dominant mode for pure bending deformations still behaves like a non-shearable and inextensible filament, effectively separating bending and shearing effects. Incidentally, both pure bending and shearing deformations decay with the same effective, and larger, time constant $\mathcal{T}_j$, when compared with non-shearable filaments, thus indicating that shearability weakens the stiffness potential of the elastic body.

Beyond the initial transient, the overall shape of filament is well approximated by a single mode. Without lost of generality we focus on the relaxation dynamics of the dominant mode. We assume the right end of the slender-body is always free from external forces and torques, so that Eq. (4.14) applies at $s = 1$. At the left end, we considered five distinct conditions, summarised in Table 4.1. With the exception

of boundary condition (i) in Table 4.1, the filament position at $s = 0$ is constrained for boundary conditions (ii)-(v). The pinned condition in (ii) is a similar case to condition (i), where the left end is absent of external torque, so that the tangent vector is free to rotate around the point of attachment. Conditions (iii) and (iv) explore the degree of freedom introduced by the shearability of the material, where not only the orientation of the director $\hat{\boldsymbol{a}}$ can be constrained, as in case (iii) in Table 4.1, but also the tangent vector of the centreline, as with case (iv) in Table 4.1. In contrast with the natural conditions (i)-(iv), the boundary condition (v) reflects an unnatural problem (cf. Sec. 4.2.3). In this case, the contact force is constrained to vanish, in addition to the position vector restriction, by welding, for instance, an outer rigid clamp that encloses the tip of the left end, so that no shear deformation is permitted at this point.

Table 4.1: Boundary conditions for the relaxation of a shearable filament.

Boundary Condition	Constraints at $s = 0$
(i) Free force and torque condition	$\theta_{ss} = 0$ & $\theta_s = 0$
(ii) Pinned condition	$\theta_s = 0$ & $\theta_{sss} = 0$
(iii) Clamped shear condition	$\theta = 0$ & $\theta_{sss} = 0$
(iv) Clamped tangent condition	$\phi = 0$ & $\theta_{sss} = 0$
(v) Welded base condition	$\theta_{ss} = 0$ & $\theta_{sss} = 0$

The time sequence of the relaxation dynamics for each case in Table 4.1 is depicted in Figs. 4.5, 4.6 and 4.7. The shape solution and pure shearing deformations, represented by a deforming mesh, in addition to the shear angle, or alternatively the distribution of contact forces, indicated by the overlaid colour plot, are portrayed; a downward translation for each subsequent time was introduced to facilitate the visualisation. The most evident feature in Figs. 4.5 - 4.7 is the simultaneous hyperdiffusive relaxation of bending and shear deformations. Now, both the curvature and the shear angle decay towards the reference configuration by effectively diffusing the reference state of the strain variables, $\theta^\circ = \beta^\circ = 0$, throughout the arclength.

Fig. 4.5(a) exemplifies this dissipative dynamics for the free ends condition, where $\beta^\circ = 0$ diffuses symmetrically from each of the three initial locations with zero-shear (light green region at the left, middle and right of the filament). Note that the light green regions in Figs. 4.5 - 4.7 indicate where the contact forces are absent. This explains for instance the nonexistence of shear at the endpoints in Fig. 4.5(a). In this case, however, the lack of shear displacement at the filament midpoint results from a change of the shear orientation at this point to satisfy the symmetry imposed by the boundary conditions, Fig. 4.5(a). Incidentally, the midpoint is also the location of highest curvature. Indeed, condition (i) is characterised by a reversed monotonicity between curvature and shear, i.e. large shearing displacements are observed at a low curvature locations. In general, the expected monotonicity between moments and curvature, from the traditional Euler model, is lost due to the material shearing, as the bending moment depends on β_s, see Figs. 4.5 - 4.7. The curvature, instead, is marked by a sudden sign change towards the free ends. Certainly, because no external forces or torques are imposed at these points, shearing moments are able to counteract the imposed initial curvature so that the total length is preserved. The appearance of opposing curvatures, namely counterbend effect, toward the free end in Figs. 4.5, 4.6 and 4.7 is therefore a genuine manifestation of the coupling between flexure and shear while implicitly satisfying the axial length constraint, Eq. (4.7).

Figs. 4.5(b), 4.6 and 4.7 demonstrate the sensitivity of the solution to different boundary conditions, as usually found in elastohydrodynamic problems. In particular, conditions (ii)-(v) are characterised by an asymmetric distribution of flexure and shear. A common constraint is however the fixed position of the left end, which implicitly defines the contact forces at this point. In this case the pinned condition induces a negative shear orientation 4.5(b), reminiscent of case (i). A different scenario is found when external moments are applied at the left end, Fig. 4.6. By prescribing the orientation of $\hat{\boldsymbol{a}}$ in Fig. 4.6(a), shear deformation is free to modify the orientation

of the tangent vector so that less bending occurs when compared with condition (iv) in Fig. 4.6(b), where the tangent vector is fixed, instead causing the shear orientation to vary in order to accommodate this constraint. An even more distinct picture is depicted in Fig 4.7 for the unnatural condition (v). In this case, a non-zero shear displacement is induced by the position constraint, however the orientation of the director $\hat{\boldsymbol{a}}$ varies in such a way that the contact forces vanish at this point, via the action of a feedback couple, which ultimately results in the rotation of tangent vector.

4.3.3.1 Summary

The relaxation dynamics of a shearable filament in a viscous fluid revealed distinctive behaviours associated with the material shear in the following ways:

1. The material shearability causes a reduction on the relaxation coefficient, when compared with non-shearable filaments, which is now corrected by shearing deformations. This has two important consequences on the filament dynamics: (i) Shearable filaments under thermal fluctuation will take a longer time for the shape to change, and therefore longer times are required while considering imaging samples between successive shapes to be independent, as required to guarantee a statistical significance [45]. (ii) A lower relaxation coefficient indicates that shearability is causing a reduction on the effective stiffness of the material, as a longer time is required to reach the undeformed configuration.

2. The modified hyper-diffusion system is characterised by a simultaneous diffusion of both bending and shearing deformations. Even though the associated eigenfunction shows little or no variation, to changes on the material shear, the shape solution is governed by a generalised angle of curvature, which is modified by shear. The shape deformation is characterised by a reversed monotonicity between bending moment and shear, which is further responsible for the formation of a novel bending behaviour, namely the counterbend effect. These

opposing curvatures are found near boundaries where the filament is free from external forces, and therefore no shearing deformation is permitted. In order to satisfy this constraint, the shearing deformations generate moments that act in opposition to the imposed curvature, thus inducing a change in the sign of the curvature.

3. Finally, the analytical formulation allows a simple implementation of the model to extract bulk material parameters from experiments with relaxing shearable filaments.

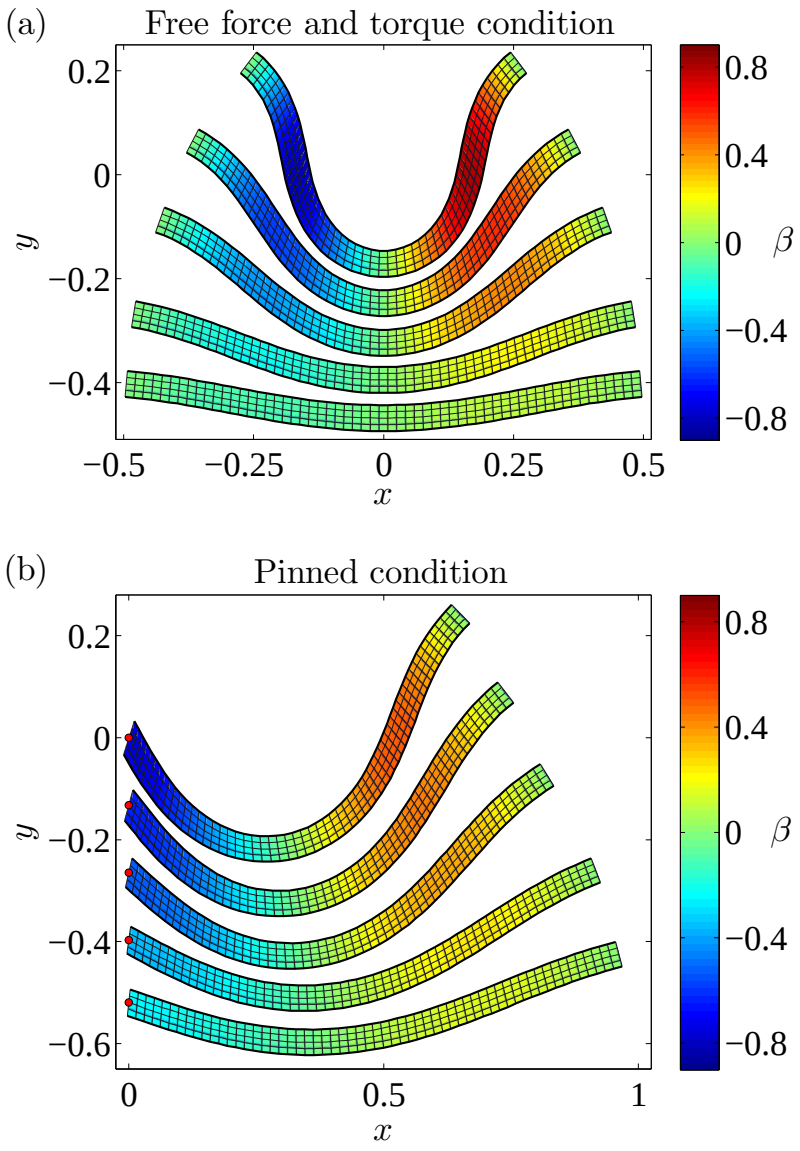

Figure 4.5: Snapshots of the time evolution for the dominant mode of a shearable slender-body relaxing in a viscous fluid for $\nu = 0.1$ and the boundary conditions (i) and (ii) from Table 4.1, as indicated. Pure shearing deformations are represented by the internal deforming mesh, where the overlaid surface plot indicates the shear angle $\beta(s)$ along the arclength. The time sequence plotted from top to bottom in (a) and (b) are, respectively, $t/10^{-3} = 0, 1.5, 3, 6, 9$, $t/10^{-3} = 0, 1.4, 3.2, 6.8, 10.4$. Notice that the slender-body diameter was exacerbated to improve visualisation, in addition to a downward translation for each subsequent time. The red markers in (b) denote the pinned point.

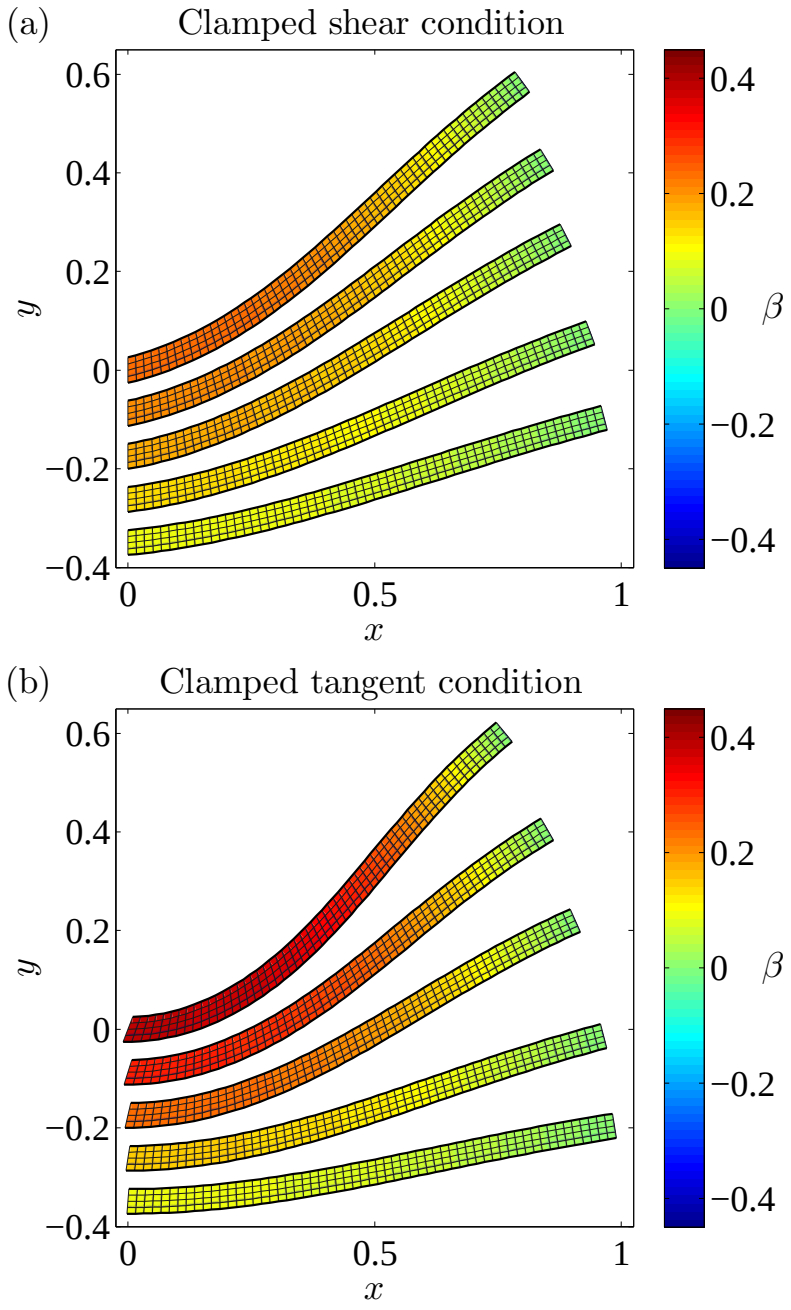

Figure 4.6: Snapshots of the time evolution for the dominant mode of a shearable slender-body relaxing in a viscous fluid for $\nu = 0.1$ and the boundary conditions (iii) and (iv) from Table 4.1, as indicated. Pure shearing deformations are represented by the internal deforming mesh, where the overlaid surface plot indicates the shear angle $\beta(s)$ along the arclength. The time sequence plotted from top to bottom in both (a) and (b) is $t/10^{-3} = 0, 17.6, 35.6, 71.6, 107.6$. Notice that the slender-body diameter was exacerbated to improve visualisation, in addition to a downward translation for each subsequent time.

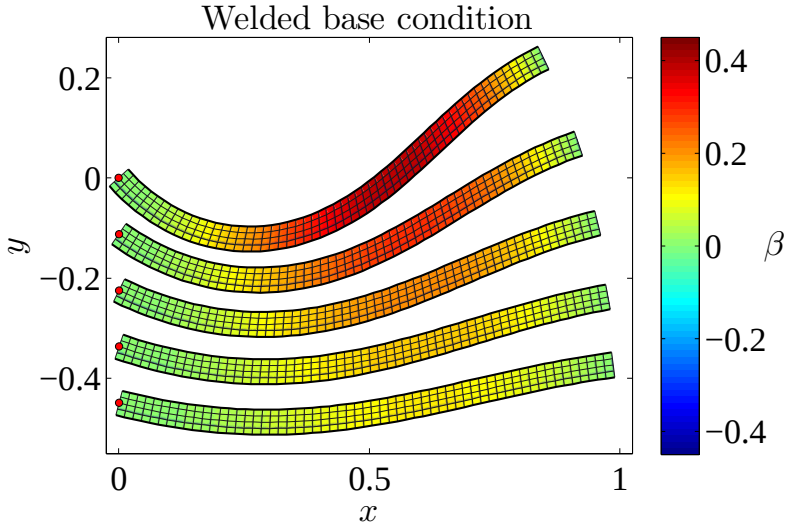

Figure 4.7: Snapshots of the time evolution for the dominant mode of a shearable slender-body relaxing in a viscous fluid for $\nu = 0.1$ and the boundary condition (v) from Table 4.1. Pure shearing deformations are represented by the internal deforming mesh, where the overlaid surface plot indicates the shear angle $\beta(s)$ along the arclength. The plotted time sequence from top to bottom is $t/10^{-3} = 0, 4.2, 8.4, 12.6, 16.2$. Notice that the slender-body diameter was exacerbated to improve visualisation, in addition to a downward translation for each subsequent time. The red marker denote the fixed position at $s = 0$.

4.3.4 Propulsive dynamics of shearable filaments

We now consider the propulsive dynamics of a periodically actuated shearable filament in a viscous fluid, via an angular oscillation of the left end

$$\phi(0,t) = \phi_0 \cos \omega t, \tag{4.37}$$

with a frequency ω and amplitude ϕ_0. Since the forcing is harmonic, we assume that there is only one frequency of motion for the filament, so that

$$\theta(s,t) = \phi_0 \, \mathrm{Re}\left\{ S(s)\, e^{-it} \right\}, \tag{4.38}$$

where time was rescaled by $1/\omega$ and Re denotes the real part of the argument. The function $S(s)$ satisfies the differential equation $S_{ssss} - i\,\mathrm{Sp}^4\,(S - \nu\, S_{ss}) = 0$, the solution to which is

$$S(s) = \sum_{j=1}^{4} r_j \, e^{\mathrm{m}_j s}, \tag{4.39}$$

where the m_j's are the four roots of

$$\mathrm{m}_j^4 - i\,\mathrm{Sp}^4(1 - \nu\,\mathrm{m}_j^2) = 0. \tag{4.40}$$

The new geometrical dimensionless parameter

$$\mathrm{Sp} = L\left(\frac{\omega \xi_\perp}{E}\right)^{1/4} \tag{4.41}$$

is referred as the sperm compliance number and captures the relative contribution between pure bending and viscous forces. The four coefficients r_j are determined by the imposed boundary conditions. The left end consists of an oscillating pivoting arm, with a fixed hinged point, while the right end is kept free from external forces and torques, i.e

$$\begin{bmatrix} 1-\nu\,\mathrm{m}_1^2 & 1-\nu\,\mathrm{m}_2^2 & 1-\nu\,\mathrm{m}_1^2 & 1-\nu\,\mathrm{m}_2^2 \\ \mathrm{m}_1^3 & \mathrm{m}_2^3 & -\mathrm{m}_1^3 & -\mathrm{m}_2^3 \\ \mathrm{m}_1\, e^{\mathrm{m}_1} & \mathrm{m}_2\, e^{\mathrm{m}_2} & -\mathrm{m}_1\, e^{-\mathrm{m}_1} & -\mathrm{m}_2\, e^{-\mathrm{m}_2} \\ \mathrm{m}_1^2\, e^{\mathrm{m}_1} & \mathrm{m}_2^2\, e^{\mathrm{m}_2} & \mathrm{m}_1^2\, e^{-\mathrm{m}_1} & \mathrm{m}_2^2\, e^{-\mathrm{m}_2} \end{bmatrix} \begin{bmatrix} r_1 \\ r_2 \\ r_3 \\ r_4 \end{bmatrix} = \begin{bmatrix} 1 \\ 0 \\ 0 \\ 0 \end{bmatrix}, \tag{4.42}$$

where $\mathrm{m}_3 = -\mathrm{m}_1$ and $\mathrm{m}_4 = -\mathrm{m}_2$ from Eq. (4.40). Since no pair of $\{\mathrm{m}_1 \dots \mathrm{m}_4\}$ are complex conjugates, the exponentials in Eq. (4.39) always induce travelling waves.

Representative solutions of increasing Sp are depicted in Fig. 4.8 for the shearable and non-shearable cases. As expected from an Euler elastica within a viscous fluid, small sperm compliance number dynamics corresponds to a stiff filament, while larger sperm compliance numbers are associated with increasing filament flexibility [88]. Shearing deformations, however, modify how the elastic slender-body reacts to body forces, such as viscous friction. In this case, the shearing magnitude equally depends on the ratio between pure bending and viscous forces, as Sp regulates the overall magnitude of curvature. As a result, significant changes in the shapes of the beating patterns are observed when compared with the non-shearable case $\nu = 0$. More precisely, the material shear tends to deform the free end of the filament in opposition to the imposed curvature, thus diminishing the influence of the pivoting actuation while propagating bending waves along the arclength. Fig. 4.9 further demonstrates the shear induced dissipative dynamics as the pivoting arm oscillates. The prescribed angular actuation is now divided in bending and shearing deformations. In particular, due to the necessary contact forces at the pivoting point, the induced shear at this point, when combined with the counterbend curvatures towards the free end, tends to suppress bending deformations by effectively decreasing the bending penetration length of an Euler filament $\ell = L/\mathrm{Sp}$.

In order to quantify the effect of the material shearing on the propulsive dynamics, we evaluated the total propulsive force averaged over time, by integrating the force exerted by the slender-body on the fluid, Eq. (4.20), in the x direction,

$$\langle \mathrm{F_p} \rangle = \left\langle \boldsymbol{i} \cdot \int_s^1 \mathbf{f}_\mathrm{h}(s')\, \mathrm{d}s' \right\rangle = \mathrm{Sp}^4\, \Upsilon_x[\boldsymbol{r}], \tag{4.43}$$

where lengths were rescaled by $\ell = L/\mathrm{Sp}$, and $\langle ... \rangle$ indicates the time average over one period. Eq. (4.43) is geometrically exact, given by the resistive force theory, and only depends on the geometry of deformation. The latter reflects the fact that in iner-

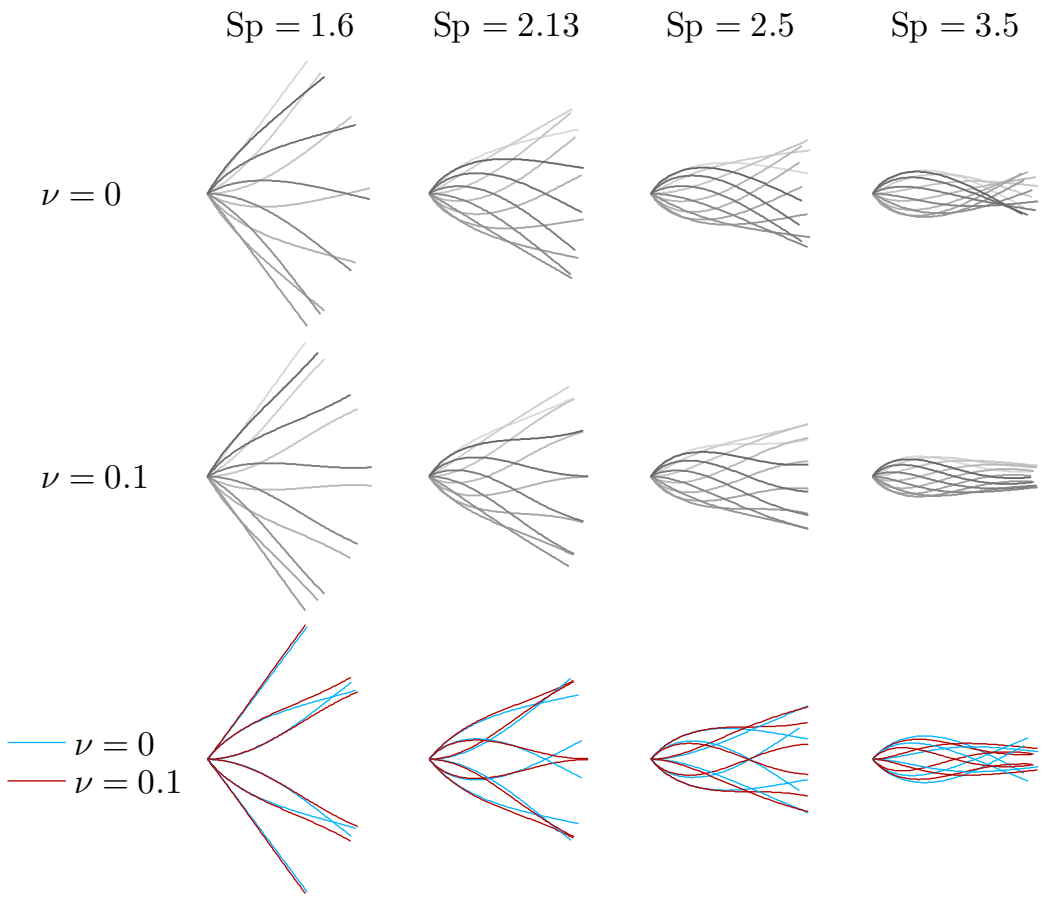

Figure 4.8: Snapshots of the time evolution of a shearable and non-shearable filaments with an oscillating pivoting arm over a period, plotted at equal time intervals (darker curves for later times), with an amplitude $\phi_0 = \pi/3$. The first and second rows depict the non-shearable and shearable cases, respectively, for four distinct values of Sp. The third row overlay both shearable and non-shearable solutions for comparison, as indicated.

tialess fluids the net motion finds its origin mostly in geometry rather than dynamics. The scaling function $\Upsilon_x[\boldsymbol{r}]$, calculated from the linear theory, is plotted in Fig. 4.10(a) as a function of Sp for distinct values of ν. In general, when the sperm compliance number is small, no net force is produced, as expected from a pivoting stiff filament. This is also in agreement with the Purcell's scallop theorem, i.e. no time-reversible motion can produce a net displacement in low Reynolds number regime. As Sp increases, for the non-shearable case (black curve in Fig. 4.10), the flexibility breaks the time-reversibility symmetry leading to a net propulsion. However, the induced bend-

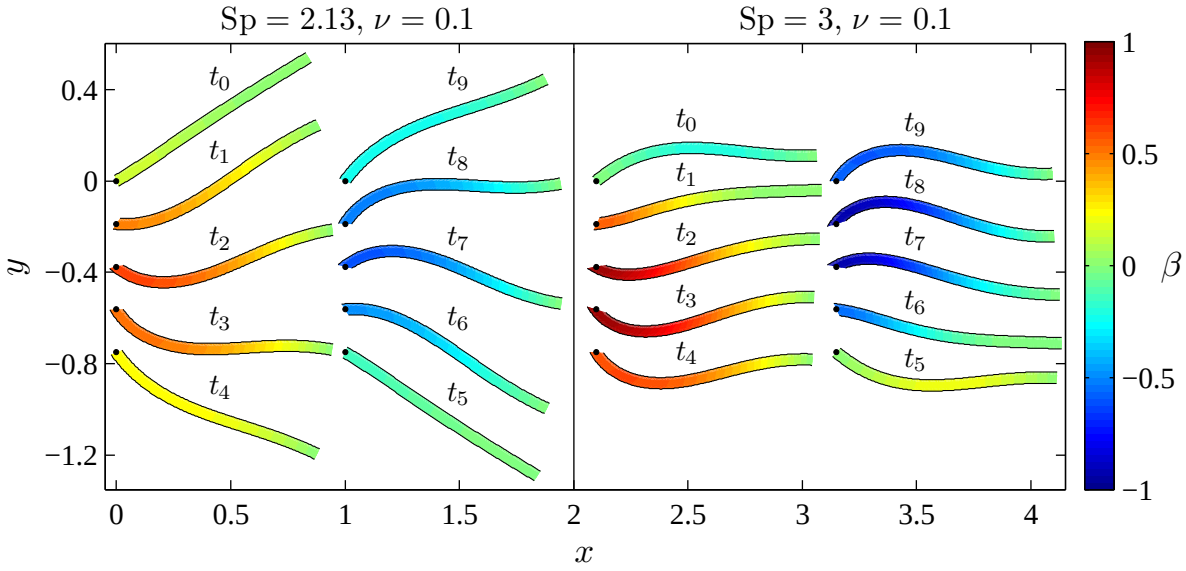

Figure 4.9: Snapshots of the time evolution of a shearable filament with an oscillating pivoting arm, plotted at the same time interval, 0.2π, with an amplitude $\phi_0 = \pi/3$ and two values of Sp. The shear angle $\beta(s)$ along the arclength is represented by the overlaid surface, and indicates pure shearing deformations. The black marker show the pivoting point.

ing waves tend to decay more rapidly when the the filament is very flexible, which explains the appearance of an optimal value for $\mathrm{Sp}_{\max} \approx 2.13$ where $\Upsilon_x[\boldsymbol{r}]$ reaches a maximum. For a sufficiently large sperm compliance number, typically $\mathrm{Sp} > 7$, the prescribed actuation decays so rapidly that most of the filament stay undeformed, with the exception of the oscillating arm. In this limit, the hydrodynamic scaling function is characterised by a plateau, as the propulsive force is solely produced by the tangential viscous drag, Fig. 4.10(a). A distinct scenario is found when shear deformations are present. It is clear that the material shearability tends to decrease the overall propulsive force when compared with the non-shearable case. In particular, shear deformations tend to lower the maximum of $\Upsilon_x[\boldsymbol{r}]$, while preserving a similar optimal $\mathrm{Sp}_{\max}$. Additionally, shearability causes the hydrodynamic scaling function $\Upsilon_x[\boldsymbol{r}]$ to monotonically decrease after reaching the optimal value. Indeed, as presented in Fig. 4.9, the filament shearing induces the free end to deform in opposition to the imposed curvature by the pivoting arm. In turn, this lead to an increase of

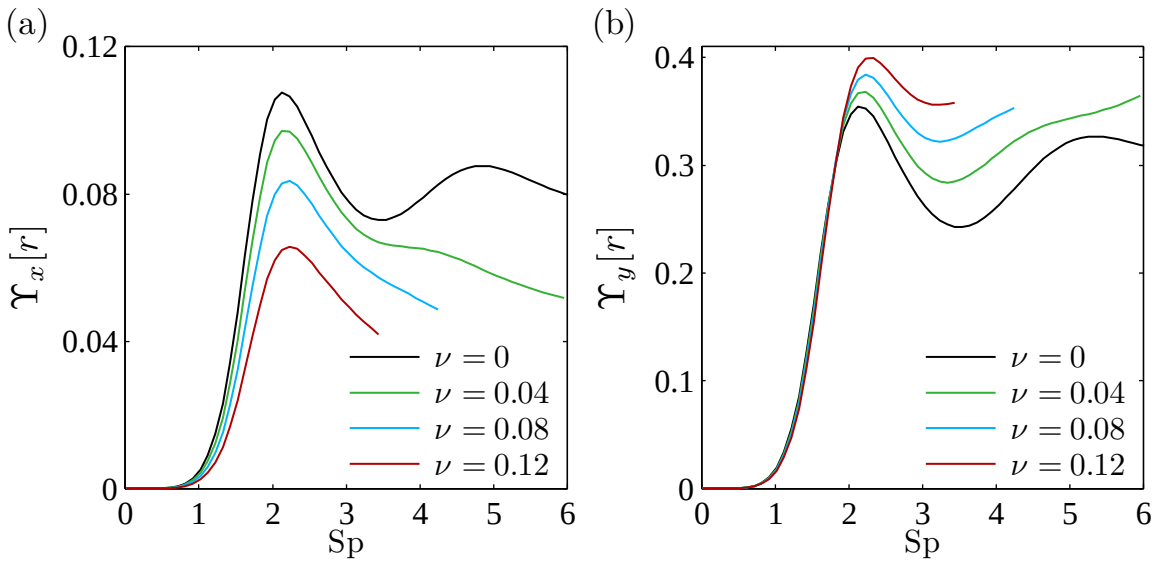

Figure 4.10: (a) Scaling function $\Upsilon_x[\boldsymbol{r}]$ of the dimensionless propulsive force, averaged over one period, Eq. (4.43), as a function of Sp for four values of shear number ν and amplitude of oscillation $\phi_0 = \pi/3$. (b) Scaling function $\Upsilon_y[\boldsymbol{r}]$ of the dimensionless hydrodynamic force in the y direction, averaged between $\phi(0) = \phi_0$ and $\phi(0) = 0$. Note that for the shearable case, when $\nu > 0$, there exist a critical sperm compliance number Sp^* where the curve terminates, so that if $\mathrm{Sp} > \mathrm{Sp}^*$ the condition $\cos\beta > 0$ is not satisfied.

the hydrodynamic force normal to the slender-body in the y direction, which culminates in less force in the swimming direction. This effect is also demonstrated in Fig. 4.10(b), which plots the scaling function $\Upsilon_y[\boldsymbol{r}]$ of the hydrodynamical force in the y direction, averaged between $\phi(0) = \phi_0$ and $\phi(0) = 0$ instead. Moreover, because shear deformations are intensified as Sp is increased, the pivoting actuation tends to induce larger shearing displacements, as well as bending dissipation, hence causing the propulsive force to decay monotonically beyond $\mathrm{Sp}_{\mathrm{max}}$ in Fig. 4.10(a). Finally, although shearable filaments have a poor performance regarding the net propulsive force for swimming purposes, Fig. 4.10(a), they are good candidates for driving fluid laterally, such as in cilia arrays, given the increased hydrodynamic driving force in the y direction associated with shearable filaments and the counterbend effect, see Fig. 4.10(b). It is also noteworthy that the curves for non-zero shear compliance ter-

minates at a given critical value Sp^*, where the condition $\cos\beta > 0$ is still satisfied.

4.3.4.1 Summary

The classical elastohydrodynamic problem for angularly actuated filaments, first solved by Machin [88] in 1958, was revisited for the case of a shearable filament. In this instance, the system is governed not only by the ratio between viscous and elastic forces, but also the relative importance of pure bending and shearing resistance. The material shearability effectively modifies the bending wave propagation along the filament, as not only waves of curvature are transmitted to distant parts of the filament, but also shearing deformations. Furthermore, due to the susceptibility of shearable filaments to the formation of counter-curvatures towards the free end, the resulting propulsive force was considerably reduced because of the material shearability. Nevertheless, as the free end of the filament tends to deform in opposition to the imposed bending angle, by the pivoting arm, a larger volume of fluid is driven in the perpendicular direction to the wave propagation, exemplifying the potential of using shearable filaments to induce flows perpendicular to the propulsive direction.

4.4 The equilibrium of shearable filaments

4.4.1 The shearable Euler-elastica

We now focus our study on the behaviour of a shearable and unstretchable slender-body at equilibrium. In this case, the deformed state induced by an external load is a static configuration. We consider an external load, $\mathbf{F}_{\mathrm{ext}} = -\mathrm{Q}\,(\cos\alpha\,\boldsymbol{i} + \sin\alpha\,\boldsymbol{j})$, acting at the right end of the slender-body, while reaction forces at the left end ensure a zero resultant force. Additionally, the elastic body is free from external torque and body-forces. Hence, the contact force is only balanced by the external load, $\mathbf{N}(s) = -\mathbf{F}_{\mathrm{ext}}$ on $]0,1]$. Note that at $s = 0$, we replace the stress-resultant with the corresponding limit from the forced point, so that the closed interval $[0,1]$ can be

considered. Thus, the static configuration is governed by the balance of moments and contact forces, in the direction of $\hat{\boldsymbol{a}}$. We nondimensionalise with respect to the length scale L, while forces are rescaled by E/L^2, yielding the dimensionless geometrically exact equilibrium equations

$$\theta_{ss} + Q \sin(\theta - \alpha + \beta) = 0, \tag{4.44}$$

$$\sin\beta - \nu\, Q \sin(\theta - \alpha) = 0, \tag{4.45}$$

where $\nu = E/GL^2$ as in the previous section. In the limit where $\nu \to 0$, Eqs. (4.44) and (4.45) describe the classical Euler-elastica with terminal loading. The analytical solution for the governing equations (4.44), (4.45) can be written in terms of an elliptic function defined as

$$s = \int_{\theta_0}^{\theta(s)} \left\{ {\theta_0}_s^2 - 2Q\, \left[\Gamma(s) - \Gamma(0)\right] \right\}^{-\frac{1}{2}} \mathrm{d}\bar{\theta}, \tag{4.46}$$

where the shape solution for each coordinate is calculated from $\boldsymbol{r} = \int_0^s (\cos\phi\boldsymbol{i} + \sin\phi\boldsymbol{j})\,\mathrm{d}s'$. The function $\Gamma(s)$ defines the $M-\theta$ phase-portrait landscape,

$$\theta_s^2 = {\theta_0}_s^2 - 2Q\, \left[\Gamma(s) - \Gamma(0)\right], \tag{4.47}$$

and is given by

$$\Gamma(s) = \frac{1}{4}\Bigg\{ \nu\, Q \cos(2(\theta-\alpha)) - 2\cos(\theta-\alpha)\sqrt{1-\nu^2\, Q^2 \sin^2(\theta-\alpha)} \\ + \frac{2(\nu^2\, Q^2 - 1)}{\nu\, Q} \ln\left[\sqrt{2}\nu\, Q\cos(\theta-\alpha) + \sqrt{2 - 2\nu^2\, Q^2 \sin^2(\theta-\alpha)} \right] \Bigg\}. \tag{4.48}$$

In Eqs. (4.47) and (4.46), $\theta_0 \equiv \theta(0)$ is an unknown parameter to be determined by imposing the boundary conditions, $\theta_s(0) = \theta_s(1) = 0$. Now, the singular points of the $M-\theta$ phase-portrait are generalised for the shearable case by $\sin(\theta - \alpha + \beta) = 0$, i.e.

$$(\theta - \alpha) + \sin^{-1}(\nu\, Q \sin(\theta - \alpha)) = k\pi,$$

where k is an integer. In the limit of small deformations, both $\theta, \beta \ll 1$, the critical axial load ($\alpha = 0$), immediately before the buckling bifurcation point, is given by

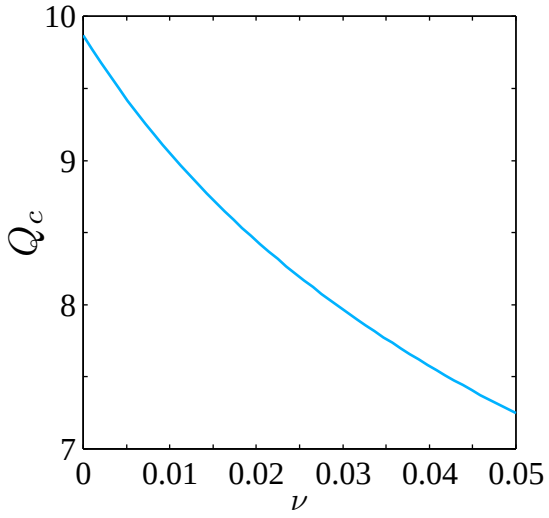

Figure 4.11: Critical buckling load Q_c as a function of ν for the fundamental mode, from Eq. (4.49).

the eigenvalues of linearised system derived from Eqs. (4.44), (4.45), modified by the material shear as

$$Q_c = \frac{1}{2\nu}\left(\sqrt{1+4\nu\, n^2\pi^2}-1\right), \tag{4.49}$$

where $n > 0$ is an integer, eigenvalue corresponding to $n = 0$ is zero, and this represents the extreme case of the column being compressed to a single point. The classical Euler-buckling load, $P_e = n^2\pi^2$, is recovered from Q_c in Eq. (4.49) when $\nu \to 0$. The critical load in Eq. (4.49) is a monotonic decreasing function of ν for any buckling mode n, as depicted in Fig. 4.11 for $n = 1$. For a shear compliance of 0.05, Q_c is approximately 25% smaller than the Euler-buckling load, with even more significant changes for higher modes, Eq. (4.49), see for example the bifurcation diagram in Fig. 4.12(a). If we rescale forces by a test Euler load $P_0 = (n^2\pi^2 E)/L_0^2$ instead, for a reference length L_0, Eq. (4.49) reveals its length dependence

$$\left(\frac{Q_c\,\mathcal{L}^2}{P_0}\right) = \frac{\mathcal{L}^2}{\mu}\left(\sqrt{1+\frac{4\mu}{\mathcal{L}^2}}-1\right), \tag{4.50}$$

where $\mu = \nu\, n^2\pi^2$ and $\mathcal{L} = L/L_0$ is a dimensionless length. For an Euler-Bernoulli filament, the ratio in Eq. (4.50) is unitary for any $\mathcal{L}$. However, for a non-zero material

shear, the buckling load depends on the dimensionless length $\mathcal{L}$, so that the effective elastic rigidity, E_f, based on the Euler-Bernoulli theory for a shearable filament would appear to depend on the overall length. In particular, Eq. (4.50) predicts a low (large) buckling load for short (long) filament, also in agreement with the reported 'length-dependent' flexural rigidity for microtubules [60, 64, 70, 71, 102, 126].

In order to solve numerically Eqs. (4.44)-(4.48), we consider the filament near the bifurcation point, where the small amplitude approximation can be applied. The initial guess for the boundary value problem is provided by the the eigenfunctions of the linearised system, for each mode, while an iterative shooting method is used to satisfy the conditions at boundaries, via 'bvp4c' Matlab function. The continuation method is employed to resolve each branch of the bifurcation diagram by slowly increasing the external load Q.

Numerical solutions for Eqs. (4.44)-(4.48) are depicted in Fig. 4.12 for the first ($n = 1$) and second ($n = 2$) modes of deformation, in the presence and absence of material shear. The load-displacement curves in Fig. 4.12(a) further demonstrates the weakening effect of the material shearability (red curves), characterised by a decrease on the maximum load that the elastic body can sustain without buckling, demonstrated in Eq. (4.49), in addition to an increasing sensitivity to small variations of the external load Q. A contrast between the shape solution for the shearable and non-shearable cases are depicted in Fig. 4.12(b), for each point of the bifurcation diagram, Fig. 4.12(a), indicated by the red and blue markers, i.e. for the same horizontal displacement of the end point relative to its reference underformed position, $d = x^{\circ}(1) - x(1)$. Despite the increased sensitivity of shearable filaments to the external load, the shape solution of the centreline, for equal displacements d, show minor differences when compared with the classical Euler elastica, mostly found for large displacements and $n = 1$, while no substantial changes are observed for the second mode; note that the blue and red curves are overlaid in Fig. 4.12(b) for $n =$

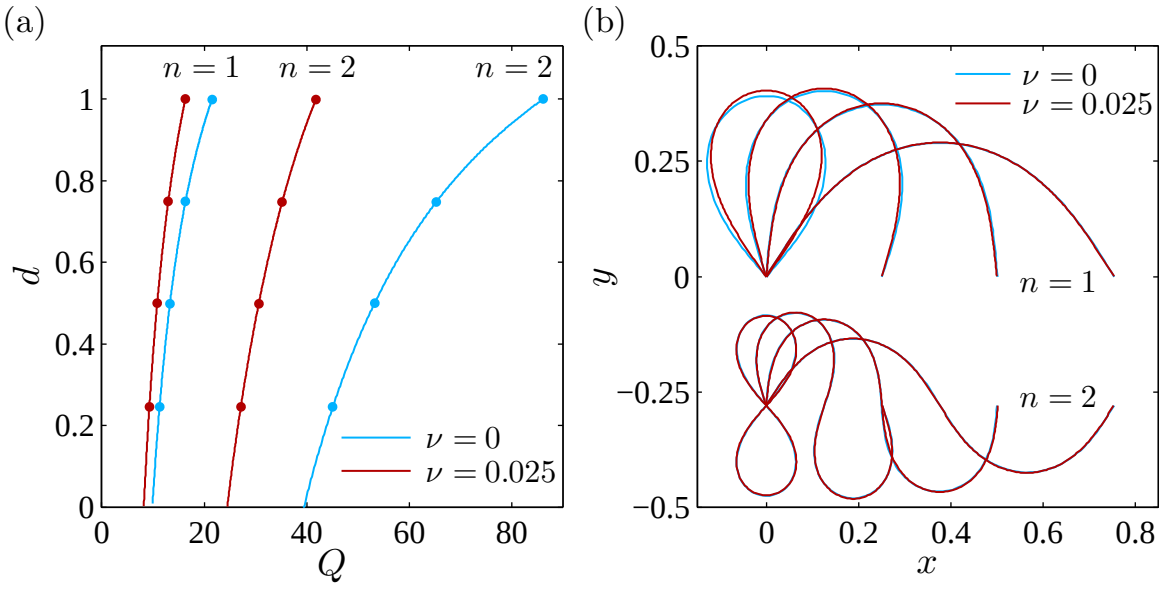

Figure 4.12: Post-buckled configuration of externally loaded shearable filaments in the axial direction ($\alpha = 0$): (a) Load-displacement curves for the first and second modes, in the presence and absence of shear, as a function of the external load Q, where d denotes the horizontal distance between the end point of the post-buckled configuration relative to its undeformed reference state, i.e. $d = x^{\circ}(1) - x(1)$. (b) Shape solution of the slender-body centreline for each point indicated in the bifurcation diagram (a) by the red and blue markers, for the shearable and non-shearable cases respectively and $d = 0.25, 0.5, 0.75, 1$.

2. Nonetheless, large shearing displacements are generated as the filament deforms. Fig. 4.13 portraits the shearing behaviour of an increasing load Q for the first and second modes of deformation. The external load and its reaction at the left end induce large amounts for shearing displacements towards the actuation points. The distribution of shear along the slender-body also depends on mode imposed curvature while satisfying the force balance: odd modes present a shear distribution at the first half of the filament equal to the negative of the other half, whilst even modes exhibit a self-similar shear distribution for each half.

The deformed configuration is characterised by an inverse relation between shear and curvature, where the highest curvature is found at the arclength with minimal shear displacement. In this case, although the bending moment is not a function of curvature, the shear distribution scales, approximately, with pure bending due to

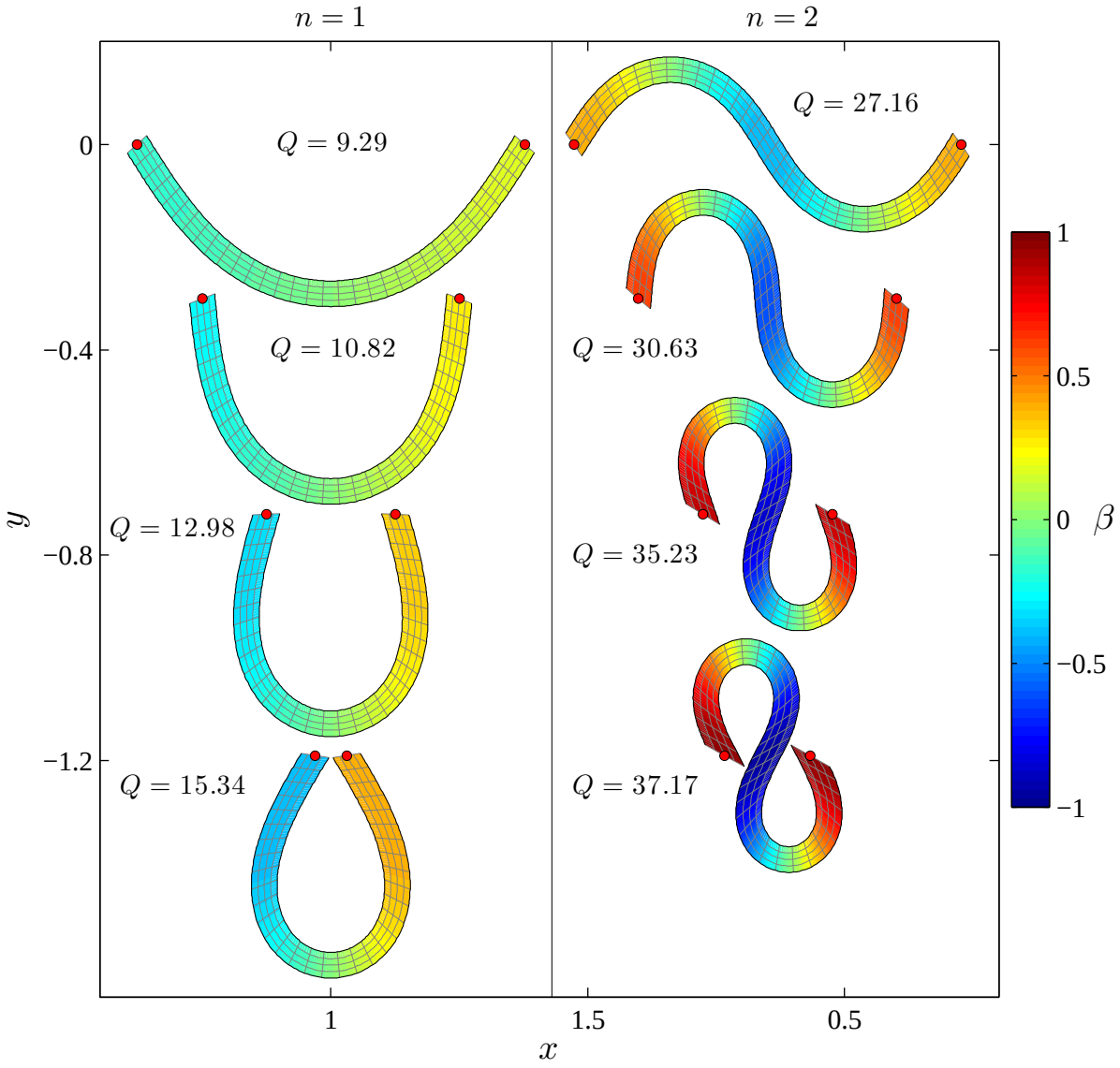

Figure 4.13: Post-buckled shear deformations of externally loaded shearable filament in the axial direction ($\alpha = 0$), for the first and second modes and four distinct values of Q, as indicated. Pure shearing deformations are represented by the internal deforming mesh, where the overlaid surface plot indicates the shear angle $\beta(s)$ along the arclength. Notice that the slender-body diameter was exacerbated to improve visualisation. The red markers denote the pinned and actuation points, respectively at $s = 0$ and $s = 1$.

the imposed external force, so that the rate of change in shear along the arclength is also function of θ_s. This suppresses, for instance, any form of counter curvature from shear induced moments, in contrast with shearable filaments with free ends sub-

jected to body forces, Fig. 4.5(a). Furthermore, because νQ is in general one order of magnitude smaller than θ_s, the shear induced curvature only marginally increases the centreline curvature, as shown in Fig. 4.12(b), providing an apparent monotonicity between moments and curvature, as observed for the classical Euler elastica. As follows, for higher modes of deformation, the shearing contribution for the overall curvature becomes increasingly negligible, despite the fact that large shear deformations are taking place, see Fig. 4.13. As a result, the Euler elastica model provide a good approximation for the filament centreline, but with large errors associated with the shear contribution on the necessary load to hold the actuation point at distance d. The equilibrium system therefore unveils the sensitivity of the material shearing to external contact forces while inducing bending moments that are, or not, strong enough to modify the curvature, via the coupling between bending and shear.

In the experimental setting, shearable and unstretchable slender-bodies can be mistakenly identified as a simpler Euler-Bernoulli filament, given the resemblance between the shape of centreline and the preserved length after deformation, Fig. 4.12(b). This fact is even more aggravated when combined with imaging difficulties while resolving small scales, typically on the order of microns for biological polymers, so that nuances in shearing deformation occurring in-situ are easily lost. Nevertheless, load-displacement experiments provide sufficient information to characterise both the elastic stiffness and the shear modulus via curve fitting Eqs. (4.44)-(4.48), as shearable filaments react differently to the external force, with significant differences for large displacements d. Certainly, the precision while probing the material parameters is improved if in addition to the deformed configuration, independent shear measurements are provided during the model fitting. At the micro-scale, this can be obtained, for instance, by attaching micro-beads along the length of the elastic body to act as markers for shear displacements occurring at the surface of the body, and relative to the reference configuration.

4.4.1.1 Summary

The generalised Euler-elastica equations to describe post-buckled configurations of shearable filaments, forced at the endpoints, were derived. By solving the full boundary value problem, geometrically exact solutions for the two modes of deformation, namely bending and shear, were found for filaments free from external torques at the boundaries. Upon linearization of the system, the critical buckling load, corrected by shearing effects, revealed a reduction in magnitude for low shear modulus when compared with the Euler-buckling load, in addition to a further dependence of critical load on the dimensionless axial length of the filament, which is not captured by the Euler-Bernoulli theory. The bifurcation diagram, accounting for geometrically non-linear deformations, confirmed the reduction on the load requirement to displace the actuation point. Each branch mode, associated with the shearable case, presented similar load-displacement functional behaviour to non-shearable filaments, for equivalent modes. Comparison between shape solutions of shearable and non-shearable filaments, at the same actuation point, revealed only minor changes on the configuration of the filament centreline. Nevertheless, large-scale shearing deformations, induced by the external actuation, were observed along the filament length. Furthermore, these results demonstrate that pure material shearing effects can reproduce the dependence of the bending stiffness with the axial length observed in shearable filaments, such as microtubules [71], as well as the similarity between the resulting post-buckled configuration of shearable filaments and the classical Euler-elastica, equally reported for microtubules [71] (Fig.4.1). Hence, care must be taken while differentiating shearable from Euler-Bernoulli filaments in the experimental setting.

4.4.2 Parallel with Timoshenko beam theory

A natural question at this point is related with how a more general approach provided by the Cosserat rod theory [8, 28] compares with the widely used model in

structural engineering given by Timoshenko beam theory [128]. In order to elucidate this question one need to understand the fundamental basis of the Timoshenko beam theory, which can be traced back to Engesser [32, 128] who generalised the classical elastica theory in 1889 to account for shearing forces in the geometrically linear regime. In the 1950's, Haringx proposed a modified Engesser theory to explain the observed buckling behaviour of helical springs [51, 52, 128]. Thereafter, mechanical engineers diverged to the Haringx school, while structural engineers continued to follow the Engesser school, and for the past 60 years they have been debating on the so called Engesser-Haringx discord [108,145]. In this context, the work from Cosserat & Cosserat [28] have been largely neglected in the engineering community, even though it was first published in 1909, in french. It is also worth noting the term "Timoshenko beam theory", used in the literature, refers in fact to the geometrically linear regime of an an isotropic elastic material governed by Engesser theory.

The main difference between the two engineering schools is related to the way by which the total internal stresses are acting in an arbitrary cross section of the rod. The Engesser school [32], also known as the Timoshenko approach, assumes that the resultant contact forces are acting in the direction of the rod axis and the direction orthogonal to the rod axis [32,108,128,145], and therefore all vector fields are decomposed in the Frenet basis, Fig. 4.2. The Haringx's approach, on the other hand, considers that the resultant contact forces are acting on the convected direction of the sheared cross section and in the direction normal to the sheared cross section [32,108, 128, 145]. In other words, the Haringx's formulation decomposes the total stresses similarly to the directors basis used in the Cosserat rod theory, Fig. 4.2. Indeed, in the geometrically linear limit, the buckling load provided by the Cosserat's approach, in Eq. (4.50), is identical to the modified Timoshenko bulking load given by Haringx's formulation, pg. 135 in Ref. [128].

The discrepancy between the Engesser and Haringx school, and consequently the

Cosserat rod theory, is solely related to the way that the resultant contact forces are decomposed. As in the Cosserat Rod Theory, the Timoshenko's formulation considers homogeneous elastic materials in which the stress is linearly related with the strain, at the Frenet basis. Because the above transformation does not change the bending moment vector field, the balance of moments simply results in Eq. (4.44), rewritten below for convenience. Nevertheless, at equilibrium, the total contact forces are balanced by the external load, $-\mathrm{Q}\boldsymbol{i}$, taken to be acting at the left end of the rod, in the horizontal direction for simplicity, so that

$$\theta_{ss} + Q \sin(\theta + \beta) = 0, \tag{4.51}$$

$$\sin\beta - \nu\, Q \sin(\theta + \beta) = 0, \tag{4.52}$$

where we used the same nondimensionalisation from Eq. (4.44). The above system of equations provide the corrections for the Timoshenko theory associated with the exact geometry of deformation, and is valid for the elastic buckling of Timoshenko rods. The Timoshenko's equations [32, 44, 116, 128, 132] are simply obtained by linearising Eqs. (4.51), (4.52). By rescaling dimensional quantities as in Eq. (4.50), the Timoshenko critical load is simply given by

$$\left(\frac{Q_T\,\mathcal{L}^2}{P_0}\right) = \left(1 + \frac{\mu}{\mathcal{L}^2}\right)^{-1}, \tag{4.53}$$

with $\mu = \nu\, n^2\pi^2$. The result in Eq. (4.53) goes back to 1891, when was first obtained by Engesser [32,128]. In the limit when the material shear is absent, the critical load from the Timoshenko theory, Eq. (4.53), tends to the Euler buckling load, as with Eq. (4.50). In addition, Eq. (4.53) also captures the length-dependence of the buckling load associated with non-zero shearing effects [44, 116, 128, 132]. Nonetheless, for an infinitely short filament, or equivalently, an infinitely stiff filament, the Timoshenko buckling load Q_T/P_0 in Eq. (4.53) is characterised by a paradoxical upper limit, which only depends on the modified shear number μ^{-1} [108, 128]. In other words, the buckling load approaches the shear stiffness as the filament gets very short. A

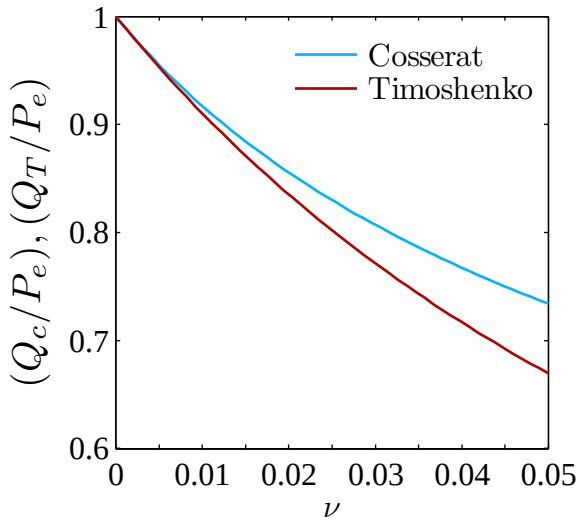

Figure 4.14: Comparison between critical buckling load from the Cosserat rod theory Q_c and Timoshenko beam theory Q_T, relative to the Euler-Bernoulli critical load Pe, as a function of ν for the fundamental mode in Eqs. (4.49), (4.53).

different scenario, however, is observed for the buckling of materials with a low shear modulus, revealing that the upper limit for the critical buckling load, μ^{-1}, can be surpassed [51, 52, 108, 128, 145]. In contrast to the above paradoxical upper limit, the Cosserat rod theory predicts an increasingly large buckling load, $Q_c/P_0 = \mathcal{L}^{-1}\mu^{-1/2}$, when $\mathcal{L} \to 0$ in Eq. (4.50). Finally, in Fig.4.14 we contrast the predicted Timoshenko buckling load, with the Cosserat theory, or equivalently, the Haringx' formulation. For filaments with $\nu \simeq 0$, the difference between the two models is negligible. However, as the shear modulus decreases the discrepancy becomes apparent. According to Timoshenko & Gere [128], the "modified" theory, referring to Haringx' formulation, "may be more accurate" when the effect of shear "is unusually large, as in the buckling of helical springs [51, 52], although Eq. (4.53) is more on the safe side".

We continue our analysis by inferring an equivalence between Cosserat's and Timoshenko's formulations. This is done by contrasting the stress resultant from the Cosserat rod theory, decomposed in the Frenet basis, with the Timoshenko constitu-

tive relations,

$$\nu_T = \nu_C \cos\beta + Q\cos\theta, \tag{4.54}$$

where the subscripts T and C denote, respectively, the Timoshenko and Cosserat shear compliance. It becomes evident from Eq. (4.54) that the Timoshenko theory is using in fact different constitutive laws for the material, despite the initial assumption of the linearity between stress and strain, by effectively coupling, instead, bending and shearing deformations at the constitutive level. As a result, the discrepancy between the two theories goes beyond the geometrical nonlinearities, as significative differences are observed already at the linear approximation, $\nu_T \approx \nu_C + Q$. In this case, if $\nu \equiv \nu_T$ in Eqs. (4.53), (4.52), the Timoshenko beam theory becomes identical to the geometrically linear Cosserat theory. Thus, in principle, the difference between the two approaches is absent provided the correct shear number is used. Nevertheless, since ν_C regulates pure shearing deformations of the material, captured by the director $\hat{\boldsymbol{a}}$ in the Cosserat formulation, equivalence with the Timoshenko theory, from Eq. (4.54), requires that shear number ν_T is not simply a property of the elastic body, but also depends on the axial external force acting on the body. The latter, in particular, is behind many fundamental issues associated the Timoshenko theory [44, 51, 52, 108, 116, 128, 128, 132, 145], such as the paradoxical upper limit of the buckling load in shearable filaments, and has motivated a number of studies with the objective to correct the Timoshenko theory in different applications [33, 44, 87, 90, 128, 132, 135].

It is clear from the above analysis that the Cosserat theory provides a sufficiently general framework that can describe both the Timoshenko's and Heringx's formulation, given the appropriate constitutive laws. In particular, it was shown that the Heringx's formulation is equivalent to the Cosserat approach for linear constitutive relations between the stress and strain. Likewise, Timoshenko theory is characterised, in the director space, by a modified constitutive relation that couples the external

force with bending deformation at the geometrically nonlinear level. Deciding the relevance between the two schools depends on the material properties itself. From first principles, for a linearly elastic shearable material, it seems unnatural that the constitutive relations depend on the external force. Of course, different kind of materials may present the above Timoshenko constitutive relation, for instance, in sandwich and composite beams where the outside wall is intrinsically connected with the internal shearing. It is important, however, to note that finding the correct constitutive laws via phenomenological observation is a challenging process, which is only aggravated by the possibility of non-uniqueness of constitutive laws while solving the inverse problem [8] for a given data set, without mention intrinsic noise fluctuations. Given the complexity of each biological filamentous structure found in nature, it is seems appropriate to conduct a first analysis on the material properties by employing simple constitutive laws, such as a linear stress-strain relaxation, within a general framework, by using the Cosserat Theory, and built complexity from this initial basis according to the system.

4.4.3 Shearable filaments vs. sliding filament induced shear in filament bundles

The interfilament shear, passive or active, is the cornerstone of prevailing models for the axoneme and other slender filament bundles. These bundles of filamentous polymers are characterised not only by a small slenderness ratio, but also a very low effective shear modulus, so that large sliding displacements may occur. Despite the similarities with the framework developed here for shearable slender bodies, crosslinked filament bundles are fundamentally different from the pure shearing mechanics offered by the Cosserat Rod Theory, or Timoshenko's beam theory, for linearly elastic materials. To give some consideration on the differences, consider a simple shearable material with a linear stress-strain relationship. The bending moment is proportional to pure bending deformation, while the contact forces scale with shearing displace-

ments. Thus, the strain variables are local in nature, despite the geometrical coupling between bending and shearing effects. As follows from these constitutive relations, shearing deformations are nonexistent if no contact forces are imposed in the event of, for instance, a free force condition at the filament end. In this case, no further bending moments originating from shearing deformations can be transmitted non-locally elsewhere along the slender material, a fact that is inconsistent with the experimental observations of counterbend phenomenon [84, 103]. In contrast, filament bundles are characterised by non-local 'shearing' effects. Each filament is interconnected by elastic links that are able to transmit sliding displacements to distal parts of the bundle. The elastic crosslinking is, therefore, responsible for generating a distribution of moments along the bundle, triggered by the sliding displacement relative to each filament. For that reason, the sliding filament induced shear in filament bundles, and the shearable slender-bodies, as in pure material shear, are fundamentally different, and therefore the use of the term 'shear', interchangeably, for pure material shear and sliding filament shear, should be avoided, or alternatively clearly stated. The nature and consequences of the interfilament shear in filament bundles will be further explored in Chapter 5.

4.5 Discussion

Although the dynamics and statics of biological filaments have been widely studied, the influence of pure shearing deformations for materials with a low shear modulus have been not explored. The framework presented here generalises the structural response of a single filament by employing the special Cosserat rod theory to account for the exact geometry of planar deformations and its interaction with the material flexure and shear. The mechanical material response is governed by linear stress-strain constitutive relations for shearable rods with preserved length. In this context, we considered both the equilibrium of post-buckled configurations and the dynamics of

shearable filaments deforming in a viscous fluid, while the influence of the surrounding fluid was obtained via the Gray & Hancock local drag theory. We performed a linear analysis for the relaxation and propulsive dynamics of shearable filaments. The post-buckling equilibrium state was solved with the exact geometry of deformation.

Our linear results for the generalised hyper-diffusion equation indicate an increase in the relaxation time, when compared with a nonshearable filament, due to the additional diffusion of shearing displacements. Likewise, the propulsive dynamics of oscillating filaments is characterised by a diminution on the hydrodynamic propulsive force, followed by a growth in the driving force perpendicular to the actuation. Moreover, the intricate interplay between the strain variables is manifested via an unusual inversion of the monotonicity between bending moment and curvature, ultimately leading to the emergence of a novel counterbend effect for shearable filaments.

The geometrically exact formulation revealed a marginal difference between the post-buckled configurations of a shearable filament and the classical Euler-elastica, for the same deformed position of the actuation point. This is regardless of large shearing deformations along the filament that are induced by the external load. The material shearability also introduces an inherent length dependence on the critical load required to deform the filament, while reducing the effective material stiffness. As a result, post-buckled configuration are obtained with lower external actuation, demonstrating in this way the 'weakening' effect of shear on the filament ability to resist compression. Incidentally, buckling experiments with microtubules revealed a remarkable similarity of the deformed shape with Euler-elastica solutions, in addition to the paradoxical length-dependent bending stiffness [64, 70, 71, 76, 102]. Indeed, microtubules are characterised by a low shear modulus and therefore the constituent protofilaments are susceptible to shearing effects [*ibid*].

By contrasting the geometrically exact formulation presented here, for pure shearable materials, with the Timoshenko beam theory, we have demonstrated that the

Timoshenko school, commonly used in the engineering setting, is fundamentally different form the pure shearing mechanics considered by the Cosserat approach, as they differ on the constitutive level. Although both models incorporate shearing effects, they do not describe the same local shearing deformations, and therefore care must be taken while employing these theories. After 50 years of controversy between different Timoshenko schools, we have shown that the Cosserat approach is sufficiently general to describe the existing shear theories, via the implementation of the relevant constitutive equation. The Cosserat theory further provides a common framework for a systematic comparison, although largely neglected in the literature. Finally, we have demonstrated that pure shearing mechanics is essentially different from the cross-linking interfilament shearing in filament bundles, such as the axoneme; these observations have motivated the investigation in Chapter 5.

Chapter 5

The role of axonemal cross-link passive elements and the counterbend phenomenon

5.1 Introduction

Flagella and cilia are ubiquitous in nature as a means of motility and critical for diverse phenomena such as sperm migration in reproduction and the virulence of devastating parasitic pathogens such as the trypanosomatids. Their inner core, namely the axoneme, consists of a remarkable phylogenetically conserved cytoskeletal structure, typically composed by $9 + 2$ microtubules arranged cylindrically and interconnected by radial spokes and nexin bridges, which spans along the centreline by combining over than 250 constituent proteins. Nonetheless, this complex structure is far from being a passive component, as dynein motor proteins deeply embedded within the axonemal scaffolding attach and detach to outer adjacent microtubules, inducing a relative shearing force to, constructively, deform the overall structure in a harmonic, and rather gracious, self-organized undulatory motion. Despite this ubiquity and importance, the details of how each active and passive components within the axonemal scaffolding, sharing different mechanical properties, sizes and functions, are orchestrated to generate bending waves is far from fully understood, while the elastic material contribution from the intricate three-dimensional architecture plays

a crucial role and is generally unknown. At the same time the small scales involved repress the use of well-known mechanical experiments from engineering science. How to even investigate the molecular motor oscillations from detailed flagellar waveform information, with scarce information about the resulting bulk material properties of such complex cytoskeletal scaffolding or how they respond to applied forces, is yet to be fully understood.

Several empirical studies investigated the mechanical response of flagellar cytoskeletal elements across species [29, 30, 45, 60, 67, 71, 84, 95, 97, 98, 103, 126, 133, 134, 139, 140], ranging from indirect bending stiffness measurements of a single microtubule [29, 30, 45, 60, 67, 71, 126, 133, 134], and sperm flagellum [84, 97, 98, 103], to direct measurement of inter-doublet elasticity in *Chlamydomona* axonemes [93]. In the founding study, Okuno at al. [97, 98] employed the three point flexural test by using a force calibrated microprobe to deform the sea-urchin sperm flagellum and measure its resulting bending stiffness, after disabling molecular motors of demembranated flagella by inhibiting dynein ATPase through a solution of vanadate, in the presence and absence of ATP. The continuous addition of ATP acted to modify the physiological state of the flagellum causing the dynein crossbridges to switch from rigor to a relaxed state, whereas the resulting flexural rigidity of flagellum in an ATP-free solution were about ten times higher than the ones treated with ATP. It is noteworthy, however, that the bending stiffness measurements reported in [97, 98] considered the flagellum as an Euler-Bernoulli elastic rod.

Despite the important influence of the elastic cross-linking proteins on the effective bending rigidity of the flagellum [97, 98], large-scale structural effects were not revealed until recent years by Lindemann [84] while investigating the material properties of rat sperm flagellum, and providing for the first time an empirical demonstration of counterbend phenomenon, as illustrated in Fig. 5.1(a). This apparent paradoxical effect took place when the proximal region of a passive flagellum, treated with vana-

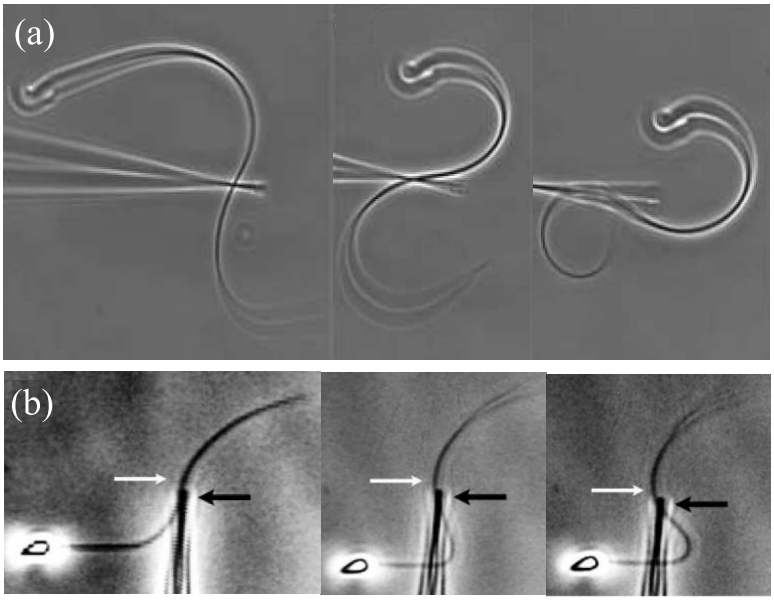

Figure 5.1: Overview of the counterbend phenomenon during buckling experiments of: (a) rat sperm flagellum [84] and (b) sea urchin sperm flagellum [103]. Figure reproduced from Lindemann et al. [84] and Pelle et al. [103], with permission from Elsevier (2958780544029) and John Wiley and Sons (2958780742312), respectively.

date and ATP to avoid rigor, was forced to bend via the actuation of a microprobe, causing the remainder of the flagellum distal to the probe to deform in the direction opposite to the imposed bend (Fig. 5.1(a)). However, since the sperm flagellum in mammals is reinforced by additional ultrastructural components [38, 39], such as the outer dense fibres, in addition to axonemal scaffolding itself, it was not entirely clear which structural interaction was fundamental for instigating the counterbend effect. Nevertheless, Lindemann and co-workers [103] demonstrated the existence of counterbend deformations in sea-urchin sperm flagellum few years later, as depicted in Fig. 5.1(b). The crucial difference, in this case, is that the sea-urchin sperm flagellum is solely composed by the axoneme and the cell membrane, hence establishing the counterbend phenomenon as a non-local, large-scale signature of the existing axonemal cross-linking proteins [103]. From the mechanical standpoint, it is no surprise that complex filament bundles, such as the axoneme, do not behave as slender Euler-Bernoulli rods. Even though each constituent filament may be treated as an in-

extensible Euler-Bernoulli filament, they are coupled together by resilient connectors which are intrinsically responsible for the interfilament shear during flexural deformations, further exposing the inadequacy of the Euler-Bernoulli theory to describe this system [97, 98].

Brokaw first considered the microtubule sliding mechanism in modelling flagellar locomotion [17, 18] by incorporating active, passive, and even viscous, axonemal sliding resistances. Based on Brokaw's sliding filament idea, Hines & Blum [57] derived, few years later, the geometrically non-linear elastohydrodynamic formulation for the sperm flagellum, by also including a passive shearing resistance. Incidentally, the physical principles behind the sidling filament mechanism were also incorporated by Everaers [35], in what appears to be an independent study, via the 'railway track' model to describe the discrepancies between the bending rigidity of single- and double-stranded polymers, due to the interfilament shear. Thereafter, several experimental and theoretical investigations considered some form of active sliding filament mechanics [17, 18, 35, 57] to describe the dynamics of the flagellar bend propagation [21, 22, 40, 42, 43, 55, 56, 79, 109].

Even though the interdoublet active shear is a well-known mechanism behind the generation of flagellar bending waves since the discovery of the axoneme [112], theoretical studies on the resulting material response from the passive cross-linking proteins, in the absence of dynein oscillations, was markedly overlooked in the literature. Pelle et. al [103] first attempted to simulate the axonemal static shapes observed in their experiments, but the computer model was based on a dynamical description of the sperm flagellum [19], which required the specification of ad-hoc shear moments in one side of the axoneme, for quiescent shapes, and high viscous resistance to restrain the movement or rotation of the proximal end, ultimately culminating in unrealistic behaviour when the force applied by the probe was not constrained to be perpendicular to the flagellum [103]. Apart from this initial effort, no rigorous mathematical

demonstration has been shown to date of counterbend effect, while studies on the static, post-buckled configurations of the axoneme, induced by external forces, are still lacking in the literature.

In a general perspective, the axonemal scaffolding is nothing more than a canonical example of a highly organized class of filament bundles [12, 26, 53, 54, 130], as it is basically composed by an assembly of semiflexible strands interconnected by elastic links. In this analogy, one would expect a similar counterbend behaviour if a filament bundle other than the axoneme is forced to bend via a micromanipulator. However, despite the number of experimental and theoretical studies on the dynamics and statics of filament bundles [12, 26, 53, 54, 130], the counterbend phenomenon was not reported elsewhere in the literature. This fact suggests other aspects could well be playing an important role during manifestation of this rather unique phenomenon. For instance, at the proximal end of the sperm flagellum, the axoneme is compliantly attached to the sperm head in the centriole, at the connecting piece region [38, 39]. This anchoring structure offers an additional sliding resistance at the basal end, whilst its significance is found to affect directly the pacemaking and bending initiation of the sperm flagellum. Previous studies on the mechanical aspects of flagellar axonemes [84, 103] have not dealt with the inherent influence of the basal compliance on the bulk material properties of the overall structure. In addition, the intrinsic nature of the interfilament shear makes any empirical measurements of the material parameters extremely difficult, as the bending stiffness is not only highly coupled with the elastic cross-link resistance, but also with a possible compliance at basal end.

Thus, in contrast with the vast majority of works on the sliding filament mechanics and filament bundles, we investigate role of elastic cross-link passive elements and the counterbend phenomenon via a geometrically exact two-dimensional representation of the axoneme. This requires an intricate interaction among pure elastic bending moments, the interfilament compliant base and intrinsic sliding moments resulting from

the passive interfilament shear resistance, in addition to the external load acting at a generic point along the axonemal length. An explicit mathematical demonstration of the counterbend effect as a generic property of the axoneme, or any cross-linked filament bundle, is provided. The counterbend shapes solutions are readily accessed in its geometrically exact form by solving a generalised Euler-elastica problem, subjected to non-trivial boundary conditions modified by the non-local sliding moments. Furthermore, the counterbend solution is given by a simple, geometrically exact formulae that may be applied for axoneme buckling experiments in order to measure the relevant material parameters, namely the pure bending stiffness, the interfilament sliding resistance and the basal compliance.

5.2 Geometrically exact formulation

Crosslinked bundle of filaments are found with an array of intricate three-dimensional arrangements [12, 26, 53, 54, 130], varying from rectangular uniform distribution of filaments, for F-actin bundles, to shell-like structures as observed in the axoneme. The geometrical distribution of filaments plays an important role on the mechanical properties [54] and dynamical aspects [56] of the bundle. Nevertheless, despite the complexity behind its geometry, filament bundles often undergo planar deformation during buckling experiments [12,26,53,54,84,103,130], while the equivalence between the faithful three-dimensional description with its corresponding plane projection, in the case of an axoneme [56], also supports the use of a simpler two-dimensional representation of the filament bundle when considering planar deformations [55,56]. Here, we will focus our attention on deformations constrained to the plane, while proposing a planar mathematical representation of the axoneme, as a generic filament bundle, and hence the terms axoneme and filament bundle will be used interchangeably thereafter.

5.2.1 Geometry of deformation

We consider the axoneme as a filament bundle composed of a pair of parallel elastic slender rods, as illustrated in Fig. 5.2(a), embedded in a three-dimensional space defined by an orthonormal fixed frame of reference $\{\boldsymbol{i}, \boldsymbol{j}, \boldsymbol{k}\}$, and subjected to geometrically nonlinear deformations that preserve its $\{\boldsymbol{i}, \boldsymbol{j}\}$-plane symmetry. Each filament is assumed to be an extensible, unshearable hyperelastic material in which the bending moment is linearly related with the curvature and characterised by the same young modulus E. The filaments are separated by a constant gap spacing b, also referred to as the bundle diameter, so that $b/L << 1$ when compared with the total length L. The position of each filament can, therefore, be described in terms of an arbitrary material curve $\boldsymbol{r}(s)$, chosen to lie on the centreline of the bundle (Fig. 5.2(a)),

$$\boldsymbol{r}_{\pm}(s) = \boldsymbol{r}(s) \pm \frac{b}{2}\hat{\mathbf{n}}(s), \tag{5.1}$$

with the orientation of the cross section at distance s along its length defined by the normal vector to the centreline, $\hat{\mathbf{n}} = -\sin\phi\,\boldsymbol{i} + \cos\phi\,\boldsymbol{j}$, where $\phi = \phi(s)$ is the angle between the tangent vector, $\hat{\mathbf{s}} \equiv \boldsymbol{r}_s = \partial\boldsymbol{r}/\partial s$, and the $\boldsymbol{i}$ direction. In Equation (5.1), the subscripts $+$ and $-$ refers to the top and bottom filaments respectively, see Fig. 5.2(a).

5.2.2 Elastic crosslinking mechanics

The geometrical constraint given by the constant diameter of the bundle, together with the filament inextensibility, force the top and bottom filaments to travel different distances, as a railway track, that scales with the curvature of the centreline, inducing an arclength mismatch [17, 18, 35, 57], as sketched in Fig. 5.2(a),

$$\Delta(s) = \Delta_0 + b(\phi(s) - \phi_0), \tag{5.2}$$

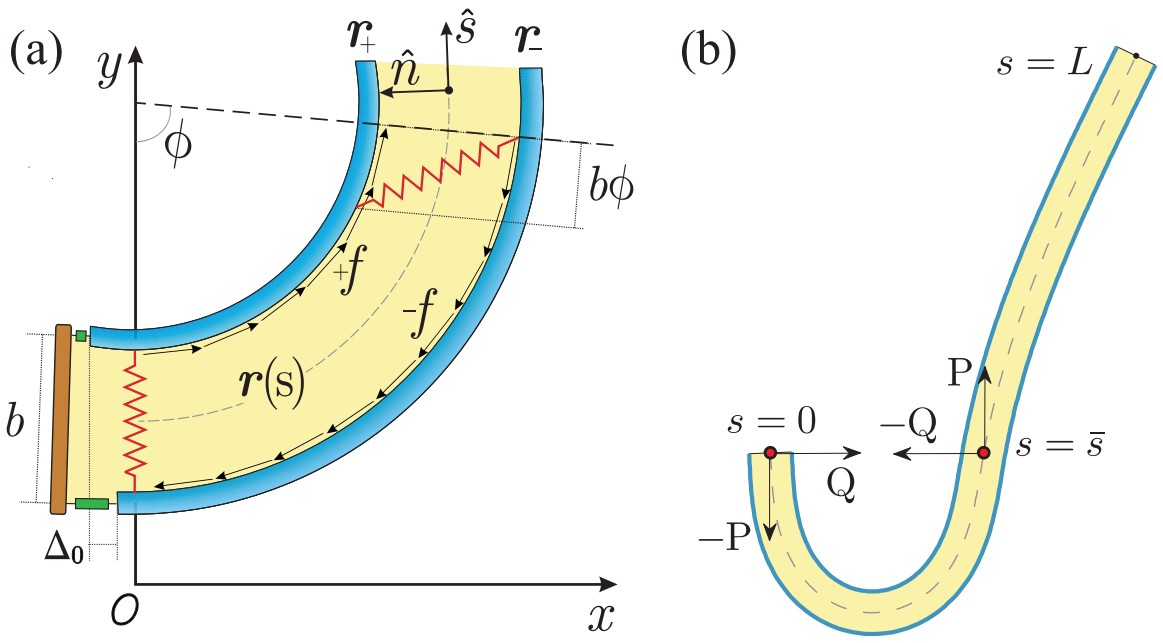

Figure 5.2: (a) Two-dimensional representation of the axoneme and the sliding filament mechanism. (b) The static configuration of the filament bundle under the action of external forces Q and P acting at a generic point along the axial length, and the associated reactions required at the pinned basal end.

where Δ_0 accounts for any possible arclength incongruity between the filament pair at $s = 0$ due to the basal compliance, and ϕ_0 is the centreline angle at the base of the bundle (Fig. 5.2(a)). Since the filament pair is coupled by discretely located interlayer elastic connectors between points of identical contour length, the arclength mismatch Δ between the filaments locally induces opposing tangential forces distributed along each filament (Fig. 5.2(a)) generating, ultimately, non-local effects that may dominate deformations at large length-scales. The interlayer elastic links are regarded as continuous, so that each sliding filament is compressed or extended by a tangential force density, $\mathbf{f}_\pm = \pm f\,\hat{\mathbf{s}}$, that acts to resist shear displacements within the bundle. The nature of the passive sliding force per unit length $f(s)$, however, depends on the constitutive relations of the elastic links and, in general, is a function of the strain Δ. In this proof of principle study, the passive sliding force density is assumed be

linearly related to the sliding,

$$f(s) = -K\Delta, \tag{5.3}$$

with a constant elastic slip resistance K. At the basal end of the bundle, however, the possibility of anchoring between the filament pair is accounted for by allowing a non-zero basal resilience that resists any sliding displacement induced by the total interfilament shear force at this point (Fig. 5.2(a))

$$\xi\Delta_0 - \int_0^L f \mathrm{d}s' = 0, \tag{5.4}$$

where the basal sliding resistance is considered to behave as Hookean material with a spring constant ξ. The limiting case where the filament bundle is welded at the base, $\xi \to \infty$ and no basal sliding displacement occurs, $\Delta_0 = 0$, while $\xi = 0$ correspond to an isotropic filament bundle, as it is equally free to slide at both ends with $\int_0^L \Delta \mathrm{d}s = 0$.

5.2.3 Balance of forces and torques

The stresses acting on the filament bundle are given by a resultant contact force $\mathbf{N}(s)$ and contact moment $\mathbf{M}(s)$. At the equilibrium, the buckled state induced by an external load is a static configuration, and the total balance of *linear* and *angular* momentum simplifies to

$$\mathbf{N}_s = 0 \tag{5.5}$$

$$\mathbf{M}_s + \hat{\mathbf{s}} \times \mathbf{N} = 0. \tag{5.6}$$

The internal sliding forces $\mathbf{f}_\pm$ do not contribute to the total contact forces of the filament bundle. Nevertheless, the elastic sliding resistance between the filaments are capable to generate a non-zero couple distribution that contributes to the total internal moment of the bundle $\mathbf{M}(s) = \mathrm{M}\,\boldsymbol{k}$, given by

$$\mathrm{M}(s) = E_b\,\phi_s - b\int_s^L f\,\mathrm{d}s', \tag{5.7}$$

where we have approximated $\phi_{s\pm} \approx \phi_s$, as we only consider bundles of filaments with $b/L << 1$. The combined elastic stiffness of the filament pair is represented by $E_b = EI_+ + EI_-$, where I_+ and I_- are the principal moments of inertia of top and bottom filaments, respectively, relative to the centre of gravity of the bundle.

We allow a general external load, $\mathbf{F}_{\text{ext}} = -\mathrm{Q}\,\boldsymbol{i} + \mathrm{P}\,\boldsymbol{j}$, to act at an arbitrary point $\bar{s}$ along the centreline, as illustrated in Fig. 5.2(b), effectively dividing the filament bundle in two regions: the *active* bent region $[0, \bar{s}]$, constrained by the external load and reaction forces at the basal end, $s = 0$, and the *passive* region $[\bar{s}, L]$, characterised by the absence of external forces or torques. The filament pair is free from body-forces and the total contact force, at the active region, is only balanced by the external load and given by a constant vector $\mathbf{N}(s) = \mathbf{F}_{\text{ext}}$ on $]0, \bar{s}]$. At $s = 0$, we replace the stress-resultant with the corresponding limit from the forced point, so that we can consider the above system on the closed interval $[0, \bar{s}]$ (Fig. 5.2(b)). At the passive region $[\bar{s}, L]$, however, the total contact force vanishes. We nondimensionalise with respect to the length scale L, while forces are rescaled by E_b/L^2. The *dimensionless* geometrically exact equilibrium equations for the centreline of the filament bundle is given by the balance of moments and contact forces, and yields

$$\phi_{ss} + \gamma\mu \int_0^1 (\phi - \phi_0)\,\mathrm{d}s' - \mu(\phi - \phi_0) + Q\sin\phi + P\cos\phi = 0, \qquad 0 \le s \le \bar{s} \tag{5.8}$$

$$\phi_{ss} + \gamma\mu \int_0^1 (\phi - \phi_0)\,\mathrm{d}s' - \mu(\phi - \phi_0) = 0, \qquad \bar{s} \le s \le 1 \tag{5.9}$$

where the dimensionless quantity

$$\mu = L^2 \left(\frac{b^2 K}{E_b}\right) \tag{5.10}$$

represents the sliding resistance parameter, and measures the relative importance of the bundle effective elastic rigidity compared to the crosslink elastic resistance. The basal compliance number is referred as

$$\gamma = \frac{KL}{KL + \xi}, \tag{5.11}$$

and determines the ratio between the compliant anchoring and passive sliding forces at the base, where $\gamma = 1$ and $\gamma = 0$ corresponds to zero basal resistance and rigid anchoring (welded base), respectively, so that $0 \leq \gamma \leq 1$. When the bundle is terminally loaded and no sliding displacements are permitted, both μ and γ vanish, and Eqs. (5.8) and (5.9) describe the classical Euler-elastica [8, 34, 73].

5.2.4 Boundary conditions

The governing equations (5.8),(5.9) together with boundary conditions, in which either the angle of the endpoints is specified or a balance of torques is imposed, define a second order boundary value problem that, in general, may still be subjected additional parameter constraints. Inspired by typical laboratory examples, the distal boundary, $s = 1$, is considered to be absent of external moments

$$\phi_s(1) = 0, \tag{5.12}$$

while the basal end, $s = 0$, is assumed to be (i) pinned, corresponding to a free pivoting case

$$\phi_s(0) + (1 - \gamma)\,\mu \int_0^1 (\phi - \phi_0)\,\mathrm{d}s' = 0, \tag{5.13}$$

or (ii) clamped, in which no rotation is allowed about the point of attachment and therefore the tangent vector is fixed

$$\phi(0) = \phi_0 = 0. \tag{5.14}$$

Furthermore, the external load induces a discontinuity on the contact forces across $s = \bar{s}$ that, ultimately, leads to a jump in ϕ_{ss}, so that the resulting solution $\phi(s)$ is only once-differentiable. In this case, however, the curvature ϕ_s is a continuous function, as the moment acting on element at $s = \bar{s}$ must balance those on the adjacent element, providing the matching condition between the active and passive regions, which are also considered to be free from external moments,

$$\phi_s(\bar{s}) - \gamma\mu(1 - \bar{s}) \int_0^1 (\phi - \phi_0)\,\mathrm{d}s' + \mu \int_{\bar{s}}^1 (\phi - \phi_0)\,\mathrm{d}s' = 0. \tag{5.15}$$

Finally, the system is completed by either prescribing an external load Q, P, referred as a traction (soft or dead-load) problem [41, 128], or by imposing displacement constraints at the actuation point, $s = \bar{s}$,

$$\boldsymbol{r}(\bar{s}) = \int_0^{\bar{s}} (\cos\phi, \sin\phi)\, \mathrm{d}s' = \boldsymbol{r}_d\,, \tag{5.16}$$

so that the axial and transversal loads are implicitly determined by the prescribed coordinate position $\boldsymbol{r}_d = (x_d, y_d)$, corresponding to the displacement (hard) boundary problem [41, 128]. The integration interval in Eq. (5.16) is replaced by the full range $[0, 1]$ when the terminal loading case is considered, corresponding to the forced buckling of the whole structure. In the absence of external forces, the filament bundle assumes a fully straight configuration, considered to lie horizontally relative to the frame of reference.

5.2.5 Exact solution for the passive region

The system of Eqs. (5.8)-(5.16) can be further simplified by solving Eq. (5.9) analytically, for a given angle $\phi(\bar{s})$ at the actuation point, and together with boundary conditions (5.12), (5.15). The solution of the passive region is unique and simply yields

$$\begin{aligned}\phi(s) = \left(\phi(\bar{s}) - \phi_0 - \gamma \int_0^1 (\phi - \phi_0)\, \mathrm{d}s'\right) \left[\frac{e^{s\sqrt{\mu}} + e^{(2-s)\sqrt{\mu}}}{e^{\bar{s}\sqrt{\mu}} + e^{(2-\bar{s})\sqrt{\mu}}}\right] \\ + \phi_0 + \gamma \int_0^1 (\phi - \phi_0)\, \mathrm{d}s', \quad \bar{s} \leq s \leq 1,\end{aligned} \tag{5.17}$$

which conveniently depends on the important parameters of the problem, in addition to a strong dependence on the active bent region $[0, \bar{s}]$ through non-local effects related with the compliance at the base and the interlayer shear. The solution (5.17) automatically satisfy the free momentum conditions at the boundaries, and throughout the passive section of the bundle, as the lack of external forces and torques in that region causes the elastic bending moment to uniquely balance the torque due to the internal resistance to sliding. In the following, deformations found in the passive region are a direct consequence of competing effects on the internal torque, acting to

completely compensate the total internal moment (5.7) in $\bar{s} \leq s \leq 1$. Nevertheless, despite its relatively simple analytical formulae, the solution (5.17) still requires an iterative implementation as the compliant base has direct coupling to the passive part of the bundle itself $[\bar{s}, 1]$. Furthermore, the Eq. (5.17) is a geometrically non-linear exact solution for deformations of the passive region, and can be readily utilized to extract empirical material quantities via curve fitting with the observed deformations from microscope imaging, as will be exemplified later in this chapter.

In a previous study, Pelle at al. [103] considered a simplified scenario for the bending moments acting at the passive region during curve fitting routines, by neglecting non-local effects of the basal compliance on the passive section, as well as the intrinsic coupling between the passive and the active regions; given by Eq. (6) in Ref. [103], which corresponds to $\gamma = 0$ and $\phi_0 = 0$ in Eq. (5.9), after appropriate nondimensionalization. Moreover, the analytical solution presented in [103] was only subjected to the free torque boundary condition at $s = 1$, causing the solution to depend on one unknown constant, multiplying the eigenfunction. The solution was then complemented, in an ad-hoc manner, by adding a further constant to correct the angle reference point during the curve fitting with experiments [103]. As a consequence, the final expression, Eq. (10) in Ref. [103], is not a formal solution of the original boundary value problem, Eq. (6) in Ref. [103], and depends on two unknown constants that are disconnected from the biophysical quantities of system, while the repercussions of using an incomplete solution during curve fitting with empirical counterbend data are not known. In fact, these ad-hoc constants included by [103] are well defined quantities of the problem, as demonstrated by the above formalism, Eq. (5.17).

5.2.6 Numerical methods

Numerical solutions for the active region $[0, \bar{s}]$ of the filament bundle were performed in Matlab (Mathworks) by employing the 'bvp4c' Matlab function, a robust

solver for boundary value problems involving ordinary differential equations [115], in conjunction with standard iterative shooting methods while imposing the integral conditions Eqs. (5.13), (5.15) and (5.16). Numerical solutions were found with a relative accuracy of 0.0001%. Due to the intrinsic coupling between the active and passive regions, the analytical solution Eq. (5.17) was used to avoid numerical instabilities and save computational time during the numerical solution of the full boundary value problem Eqs. (5.8)-(5.16). A uniform spatial discretization was used with N intervals of arclength. The numerical solution of both active and passive regions were found simultaneously while satisfying boundary and matching conditions by slowly varying the relevant parameters of the system in a continuous manner, a method also known as continuation. This is particularly important while searching for eigenfunctions with a specific eigenmode in boundary value problems with infinitely many solutions, as required for good initial guesses to start the iterative scheme. Here, we focused on the solutions corresponding to the fundamental mode only, due to the experimental relevance, and therefore the solution and stability of higher modes will not be discussed.

5.2.7 Parameter estimation from flagellar axoneme experiments

We will mostly focus our dimensional analysis on the typical physical quantities found in experimental models of flagellar axonemes, commonly extracted from sea urchin sperm and *Chlamydomonas* due to the absence of accessory structures in their flagellum. In demembranated sperm flagella of sea urchin *Lytechinus Pictus*, in the presence of ATP and vanadate, the flexural rigidity is $E_b = 0.9 \times 10^{-21}\,\mathrm{Nm}^2$ [58,97,98], while the inter-doublet elastic resistance from demembranated flagellar axonemes of *Chlamydomonas*, equally in the presence of ATP, yields an estimate spring constant of $2.0 \times 10^{-3}\,\mathrm{N/m}$ for $1\,\mu$m of axoneme [93]. If the diameter of the axoneme is assumed to be $b = 185\,\mathrm{nm}$ with a total length of $L = 35\,\mu\mathrm{m}$, as typically found in sea urchin

flagellar axoneme [103], the dimensionless sliding resistance parameter is $\mu \approx 93$, from Eq. (5.10), reaching values as high as $\mu \approx 150$ for an increment of only $10\,\mu$m in the total length, due to its sensitivity to the length scale. In addition, a good correspondence with the above estimative of the sliding resistance number is found when we consider, instead, direct measurements of the relative ratio between the bending rigidity and the interfilament sliding resistance, estimated to be $b^2K/E_b = 0.03 - 0.08/\mu\text{m}^2$ for demembranated sea urchin flagellar axoneme [103], which results in a slip resistance number varying from $\mu \approx 36$ to $\mu \approx 98$. Surprisingly, similar estimatives for μ can also be derived from bull sperm flagellum data [109], despite its additional structural elements, such as outer dense fibres and fibrous sheath. Indirect calculations via model curve fitting of extracted flagellar bending waves, from live bull sperm swimming in watery medium, gives a consensus of $E_b = 1.7 \times 10^{-21}\,\text{Nm}^2$, and a sliding resistance of $-1580\,\text{N/m}^2$ and $-93.6 \times 10^{-3}\,\text{N/m}$ for the basal compliance [109]. The details of the negative signs appearing on the estimated sliding resistance and basal compliance are explained by specific model assumptions in Ref. [109]. However if we consider the absolute value of their estimates, together with the dimensional parameters utilized in Ref. [109] for the model curve fitting, that is $L = 58.3\,\mu$m and $b = 185\,$nm, the resulting dimensionless sliding resistance and basal compliance number reads, respectively, $\mu \approx 108$ and $\gamma \approx 0.5$.

Intrinsic uncertainties from model simplifications are, however, present for each of the experimental measurements discussed above. Flexural experiments to extract the axonemal bending rigidity categorically neglected the mechanical influence of the passive crosslinking proteins [58, 97, 98], while the possible mechanical effect of a compliant base was not taken into account for measurements of the axonemal inter-doublet elasticity [93] or during direct evaluation of the relative ratio between K and E_b [103], in addition to the likelihood of fluctuations related with the parameter fitting procedure to estimate K/E_b from a mathematically incomplete solution in Ref. [103],

as discussed in Sec. 5.2.5. Furthermore, it is not clear what are the consequences, as well as the limitations, while fitting dimensional parameters from large amplitude bending waves via linear mathematical models and, therefore, restricted to small deflections [109]. The latter additionally considered no tapering of the additional structural elements found in bull sperm flagella, such as outer dense fibres and fibrous sheath that gradually tapers down to the axoneme diameter at the end piece [38, 39, 43], by assuming a constant bending rigidity along the flagellum length with diameter given by the axoneme, instead, during the parameter fitting routine. In this case, the flagellum bending rigidity is not only expected to be stiffer than the axonemes of sea urchin flagella but also a monotonically decreasing function of the arclength s; variation in the flagellum diameter is also present.

Here we will consider the sliding resistance parameter varying from $\mu = 0$ to $\mu = 100$, and a basal compliance number bounded in $0 \leq \gamma \leq 1$, as detailed in Sec. 5.2.3. This parameter range is sufficient to scrutinize the mechanical effects instigated by the sliding crosslinking resistance and the basal compliance in a general setting, while studying a physiologically relevant parameter regime. Nevertheless, intrinsic uncertainties are present in each experimental measurement discussed above [93, 97, 98, 103, 109] due, not only to inherent experimental noise but, and most importantly, due to model simplifications while extracting empirical quantities.

5.3 The counterbend phenomenon

Numerical solutions were carried by considering external forces acting at the middle point of the filament bundle, $\bar{s} = 0.5$, while keeping its basal end at the origin of the reference frame. The external load was implicitly determined by imposing displacement constraints at the actuation point, $\boldsymbol{r}_d = (x_d, y_d)$, such that $y_d = 0$ in Eq. (5.16). We considered horizontal displacements of the actuation point $\bar{s}$ by

varying the displacement parameter

$$d = x_d^0 - x_d \,, \tag{5.18}$$

defined as the horizontal distance between the actuation point of a post-buckled configuration, x_d, relative to its undeformed reference state, x_d^0, in discrete increments within the range $0 \leq d \leq 0.5$. Furthermore, we investigate the mechanical influence of the sliding resistance and its combined role with the basal compliance for both pinned and clamped base conditions in a wide range of physiologically relevant parameters, $0 \leq \mu \leq 100$ and $0 \leq \gamma \leq 1$. We stress that values we take for our dimensionless parameters are consistent with typical physical quantities extracted from experimental models of flagellar axonemes [58, 93, 97, 98, 103, 109], as detailed in Sec. 5.2.7.

5.3.1 Pivoting base condition

In this section we investigate the consequences of the internal crosslinking resistance in filament bundles with a pivoting base. The pivoting boundary condition is particularly important in our study as it offers a 'natural' condition in which the system is free from rigid constraints on the torque at the boundaries, and therefore it cannot intrinsically induce any form of asymmetric deformations due to the symmetric boundary conditions. We focus on three basic questions: (i) is the crosslinking mechanics sufficient to generate opposing curvatures in filament bundles, such as observed empirically? (ii) how additional sliding resistance at the base modifies the overall mechanics of the bundle, as commonly found in flagellar axonemes? and finally (iii) how the interfilament resistance is distributed along the bundle, and in what way does it change for different material parameters?

We begin by portraying in Fig. 5.3 numerical solutions of post-buckled configurations of filament bundles for fifteen different pairs of (μ, γ), with $5 \leq \mu \leq 70$ and $0 \leq \gamma \leq 1$, and four distinct positions of the actuation point d, which is indicated by a grayscale gradient in Fig. 5.3. The most evident feature in Fig. 5.3 is the

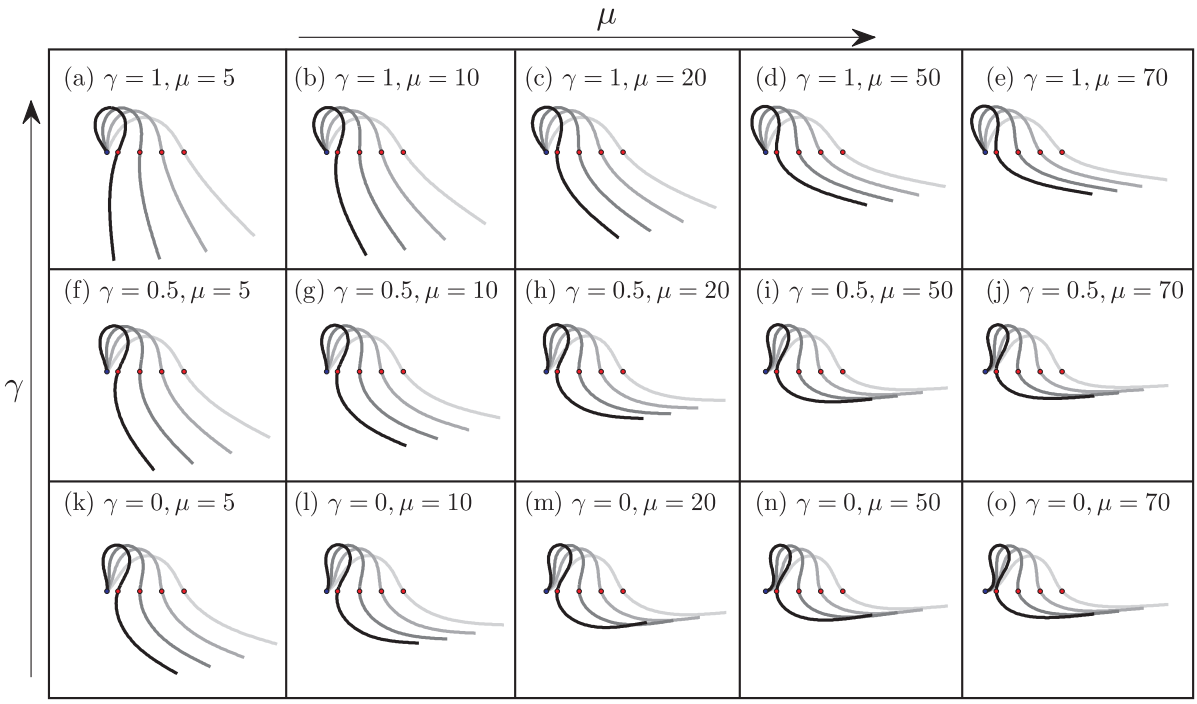

Figure 5.3: Post-buckling deformations of pinned filament bundles at the base (blue marker) for $5 \leq \mu \leq 70$ and $0 \leq \gamma \leq 1$, as indicated, and four distinct positions of the actuation point (red marker), plotted at equal intervals varying from 0.09 to 0.39 (with darker curves used for larger d, given by Eq. (5.18)).

emergence of opposing curvatures beyond the actuation point (red markers). The magnitude of these counterbend curvatures, however, depends upon details of the elastic sliding resistance, basal compliance and imposed bending of the active region $0 \leq s \leq \bar{s}$. The counterbend effect increases as the active region progressively deform with increments in d for any pair (μ, γ), but also for larger values of μ for a fixed (γ, d). The sensitivity of the counterbend effect to the sliding resistance parameter is regulated by the basal compliance. Imposing additional sliding resistance at $s = 0$ induces a faster increase of the counterbend curvature with increments in μ, as illustrated by the plots with $\gamma = 0$, see Figs. 5.3(k-o), and with higher values of γ, e.g. Figs. 5.3(a-e). Furthermore, because of the combined behaviour of μ and γ while determining the counterbend effect, it is possible to find deformations with similar features for reasonably distant points in parameter space (μ, γ), as for example in Figs. 5.3(h,l). Finally, in addition to the counter-curvatures developed beyond the

actuation point, asymmetric post-buckling deformations are also found at the active region $0 \leq s \leq \bar{s}$, between the pinned and actuated points in Fig. 5.3. These asymmetric solutions are equally modulated by details of γ and become apparent as μ increases, see Figs. 5.3(e,j,o). When $\gamma = 1$, an overall 'U' shape is formed at the active region, which is "rotated" on the counterclockwise direction while pinned at both $s = 0$ and $s = \bar{s}$, as μ increases (Figs. 5.3(a-e)). The opposing scenario is found when γ decreases, transforming the slightly rotated 'U' shape of the active region, when $\gamma = 1$, into a 'loop' shape characterized once again by a counter-curvature, but in this instance at the proximity of the basal end. Such sudden change in curvature near to the pinned point is exacerbated for $\gamma = 0$ and higher values of μ, as shown in Fig. 5.3(o).

The elastic crosslinking resistance is able to induce mechanical responses that appear to be somewhat conflicting: while the interfilament resistance instigates, posterior to the buckling of the proximal region, large-scale counter-distortions at the distal region, it equally reinforces the overall structure so that higher load is needed to achieve the buckling itself. Fig. 5.4 illustrates how the applied load, required to horizontally displace the actuation point, and the counterbend effect, characterised by the counter-curvature developed at the actuation point $\bar{s}$, are modified by the triplet (μ, γ, d). In particular, due to symmetry properties of the pinned boundary condition, only the axial external load Q is required for deformations imposed by Eq. (5.18). For larger values of the sliding resistance μ, the load-displacement curves, depicted in Fig. 5.4(a), show an increase on the maximum load that the filament bundle can sustain without buckling, referred as the critical load, regardless of γ. The basal sliding resistance, on the other hand, has the tendency to decrease the critical load as the basal end becomes more compliant (dashed curves). Nevertheless, the typical monotonic increasing behaviour of the bifurcation parameter Q with the displacement d, found for Euler-Bernoulli filaments (solid black curve in

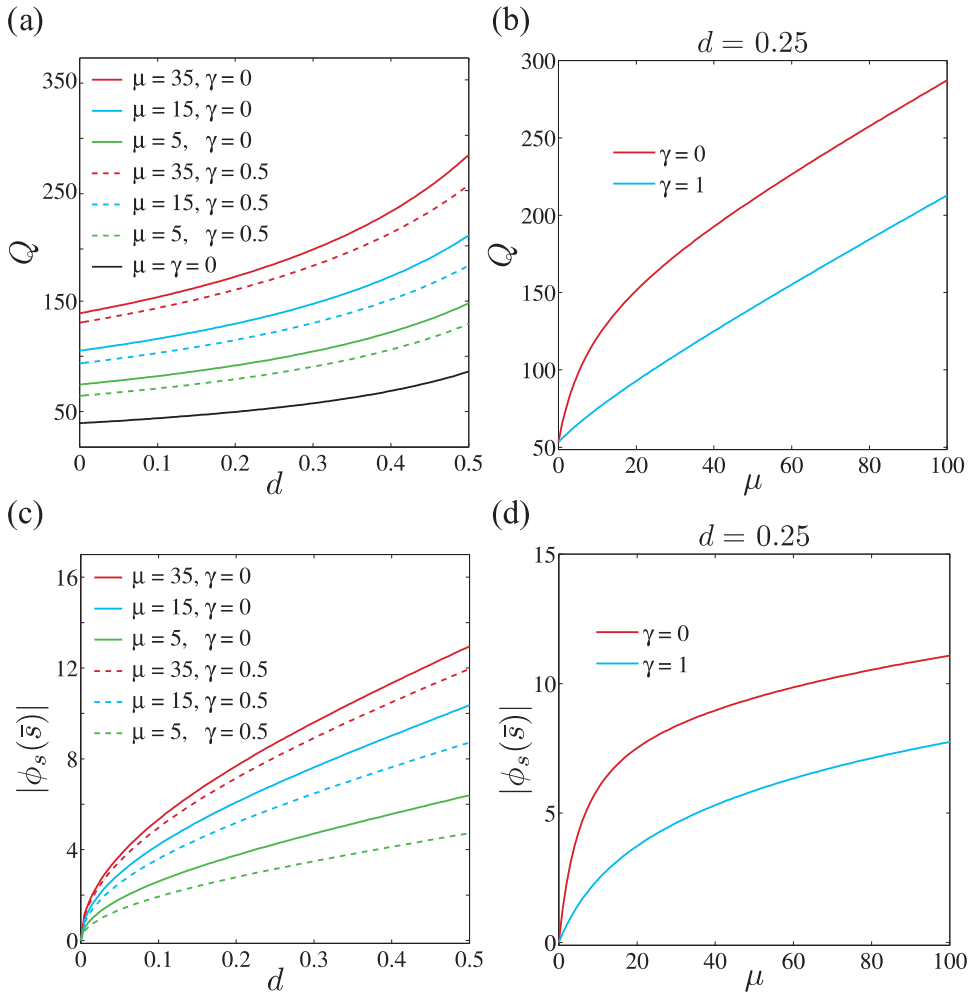

Figure 5.4: The external load Q and the absolute curvature, measured at the actuation point, $|\phi_s(\bar{s})|$ as a function of the displacement d, in (a,c), and as a function the sliding resistance parameter μ, in (b,d). Due to symmetries related to the pinned boundary condition, no vertical forces are required for horizontal deformations, Eq. (5.18), and therefore $P = 0$ for any parameter (μ, γ, d). It is also noteworthy that the counter-curvature of the actuation point $|\phi_s(\bar{s})|$, found to be the maximum curvature developed at the passive region, is a convenient manner to measure of the magnitude of the counterbend effect in the parameter space.

Fig. 5.4(a)), is equally observed for filament bundles with non-zero sliding resistance. The reinforcing behaviour of the interfilament resistance is further demonstrated in Fig. 5.4(b), which plots the applied load necessary to hold the bundle at a fixed position ($d = 0.25$) as a function of μ for two values of γ. The added strength from the elastic sliding resistance results in a faster growth of Q when the basal filaments are welded together (red curve in Fig. 5.4(b)). In this case, the external load almost

doubles, $Q \approx 106$, for a relatively low sliding resistance, $\mu \approx 7$, when compared to the required force to deform an ordinary Euler-Bernoulli beam ($Q_{\mathrm{EB}} \approx 53$ for $d = 0.25$ and $\bar{s} = 0.5$), whilst μ raises to approximately 28 for the same applied force, when no basal sliding resistance is present, blue curve in Fig. 5.4(b). An important consequence, however, of the combined influence of the basal compliance and the interfilament sliding resistance is the existence of filament bundles, with distinct values of (μ, γ), that share the same buckling load Q for a given displacement d. Thus, load-displacement measurements, commonly extracted from empirical flexural tests, are not sufficient to fully determine the pair (μ, γ) for a crosslinked filament bundle with a pinned base, as the external force Q and displacement d do not uniquely identify its material quantities (Figs. 5.4(a,b)). One should also note that the resemblance between the load-displacement curves of generic filament bundles (coloured curves) with the Euler-Bernoulli case (black curve), in Fig. 5.4(a), introduces further difficulty while differentiating, empirically, ordinary elastic rods from crosslinked filament bundles. Hence, such correspondence might explain why experimental investigation, prior to the discovery of the counterbend phenomenon [84], failed to access the true significance of the crosslinking mechanics - often interpreted as higher, and effective, bending stiffness instead [58].

The magnitude of the counterbend effect can be captured by tracking the counter-curvature formed at the distal region. For simplicity, the maximum counter-curvature, found to be at the actuation point $\bar{s}$, is plotted in Figs. 5.4(c,d) against, respectively, the displacement d and the sliding resistance μ. As one would expect, the bifurcation diagram in Figs. 5.4(c,d) shares analogous features to the ones displayed in Figs. 5.4(a,b), as similarly to the external load Q, $|\phi_s(\bar{s})|$ is also a bifurcation parameter of the system. Nevertheless, Figs. 5.4(c,d) exhibit a slow increase of the counterbend magnitude when compared to the behaviour of the external load Q for the same parameters used in Figs. 5.4(a,b). The maximum counter-curvature grows

as the displacement d, or applied load Q, increases, with a pronounced growth for larger values of μ and lower values of γ, in agreement with Fig. 5.3. Figs. 5.4(c,d) also outline the counterbend phenomenon and its sensitivity to different quantities in the (μ, γ, d)-parameter space.

In order to differentiate post-buckled deformations that require the same external load Q to displace the actuation point a distance d, we analysed the sensitivity of each solution to the sliding resistance and basal compliance along contour lines of Q across the (μ, γ)-parameter space for $d = 0.25$, depicted in Fig. 5.5(a). We measured the discrepancy in the relative angle between solutions along each Q_i contour, defined by the curve in which the external load Q has a constant value Q_i. To compare with solutions for $\gamma = 0$ at $(\bar{\mu}_0, \bar{\gamma}_0 = 0)$ and $(\bar{\mu}, \bar{\gamma})$ on the same Q_i contour, define

$$D_{\max} = \max_{s} \left\| (\phi - \phi_0)_{(\bar{\mu}_0, \bar{\gamma}_0)}|_{Q=Q_i} - (\phi - \phi_0)_{(\bar{\mu}, \bar{\gamma})}|_{Q=Q_i} \right\| . \tag{5.19}$$

When $D_{\max} = 0$ the solutions are identical, while if $D_{\max} \leq 0.1$ the agreement is observed to be qualitatively reasonable. Hence the region below the purple solid contour in Fig. 5.5(a), which marks where $D_{\max} = 0.1$, depicts the domain where the solutions along each contour lines $\Gamma_{Q_i}(\bar{\mu}, \bar{\gamma})$, with equal values of Q and d, are found to present very small changes. The latter is exemplified in Fig. 5.5(b), which plots three distinct solutions along the contour line $Q = 200$ for $D_{\max} \leq 0.1$. Although the counterbend phenomenon is influenced by the combined effect of μ and γ, it is clear that variations of the basal compliance may have little effect on the overall shape depending on the domain of interest in the (μ, γ)-space, considering that in the region where $D_{\max} \leq 0.1$, the Q_i contours depend very weakly on μ as shown, for instance, at the contour $Q = 200$, in which μ increases from 75 (black circle) to only 77 (red circle) in Fig. 5.5(a). The basal compliance has virtually no effect when μ is small, typically $0 > \mu \geq 3$. This scenario is rapidly changed as μ increases (see purple curve in Fig. 5.5(a)), but not for all permitted values of γ. Such weak sensitivity to variations in γ is found across filament bundles that are rigidly anchored at the base

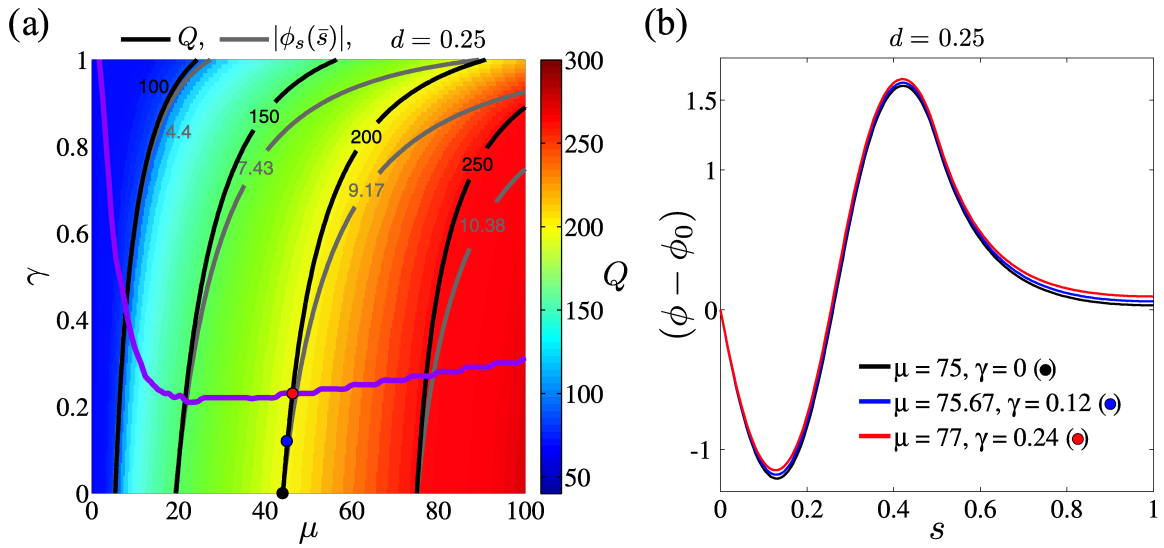

Figure 5.5: Sensitivity of post-buckled deformations, with equal values of actuation force Q, to the basal compliance and sliding resistance; analogous contour are plotted for the maximum counter-curvature $|\phi_s(\bar{s})|$: (a) Colour plot of the external load, Q, as a function of (μ, γ), necessary to hold a filament bundle at a distance $d = 0.25$ of the actuation point. Black curves depict contour lines of Q , while grey curves depict the contour lines of $|\phi_s(\bar{s})|$ as indicated. The purple solid curve marks where $D_{\max} = 0.1$ in Eq. (5.19), so that the region below the purple curve delimits the region where $D_{\max} < 0.1$ (see text for more details). (b) Plots of the relative angle to the base for three distinct solutions along the isoline $Q = 200$, for $D_{\max} \leq 0.1$, depicted by the coloured circles shown in (a).

$(\gamma = 0)$, when $\xi \to \infty$ in Eq. (5.11), and bundles with a large basal sliding resistance $(\gamma \approx 0.25)$.

For comparison purpose, Fig. 5.5(a) additionally includes the contours of the maximum counter-curvature, $|\phi_s(\bar{s})|$, depicted as a grey solid curves, for the same values of μ at the interception between $\gamma = 0$ and the contour lines of Q in black. Apart from the region to the left of $\mu \approx 15$ and below $\gamma \approx 0.25$, no strong correlation is found between Q and $|\phi_s(\bar{s})|$, indicating that the curvature at the actuation point can be used to distinguish solutions with the same actuation force, but only for both $\mu > 15$ and $\gamma > 0.25$. Improved precision, however, is obtained if the overall deflected shape, in addition to the actuation force, is taken into account instead, while characterising the (μ, γ)-material properties from, for example, flexural experiments. Even when the

system is weakly influenced by γ, it is possible to identify the material parameters of such filament bundles by obtaining, alternatively, a range of values for the basal compliance.

We now turn our attention to the consequences of the interfilament sliding resistance on the internal mechanics of filament bundles. Fig. 5.6 portrays the typical behaviour of the angle, relative to the base, curvature and bending moments against the arclength, as the horizontal displacement d gradually increases (darker curves are used for larger d)). The relative angle, depicted in Figs. 5.6(a,d), has a non-monotonic behaviour characterised by the formation of a peak in the vicinity of the actuation point (black marker), which increases in magnitude as the active region progressively deforms. Within the passive region, the relative angle does not follow the same growth, and decays with different intensities. The external load, on the other hand, introduces a jump in ϕ_{ss}, so that the solution $\phi(s)$ is only once-differentiable, despite the smooth appearance in Figs. 5.6(a,d). The curvature plots, depicted by the solid curves in Figs. 5.6(b,e), show even more clearly the effect of the external actuation. As the curvature reaches its maximum at the active region, it is rapidly followed by a decay until a break point at $\bar{s}$, where the function ϕ_s is not differentiable, but still continuous. The break point marks the maximum of the counter-curvature developed at the distal region, relative to the imposed curvature at $0 \leq s \leq \bar{s}$, and it gradually relaxes to zero at the end of the filament bundle.

To further understand the behaviour above, it is necessary to analyse how the interfilament sliding moment M_μ, defined by $M = \phi_s + M_\mu$ from Eq. (5.7), is distributed along the bundle, represented by dashed lines in Figs. 5.6(b,e). As the active region gradually deforms with increments in d, it also forces the internal crosslinks to stretch while resisting the external load, which causes the sliding moment M_μ to increase in this region. The distal part of the bundle is, however, completely free from external forces and torques, so that the total moment M adds to zero, forcing M to

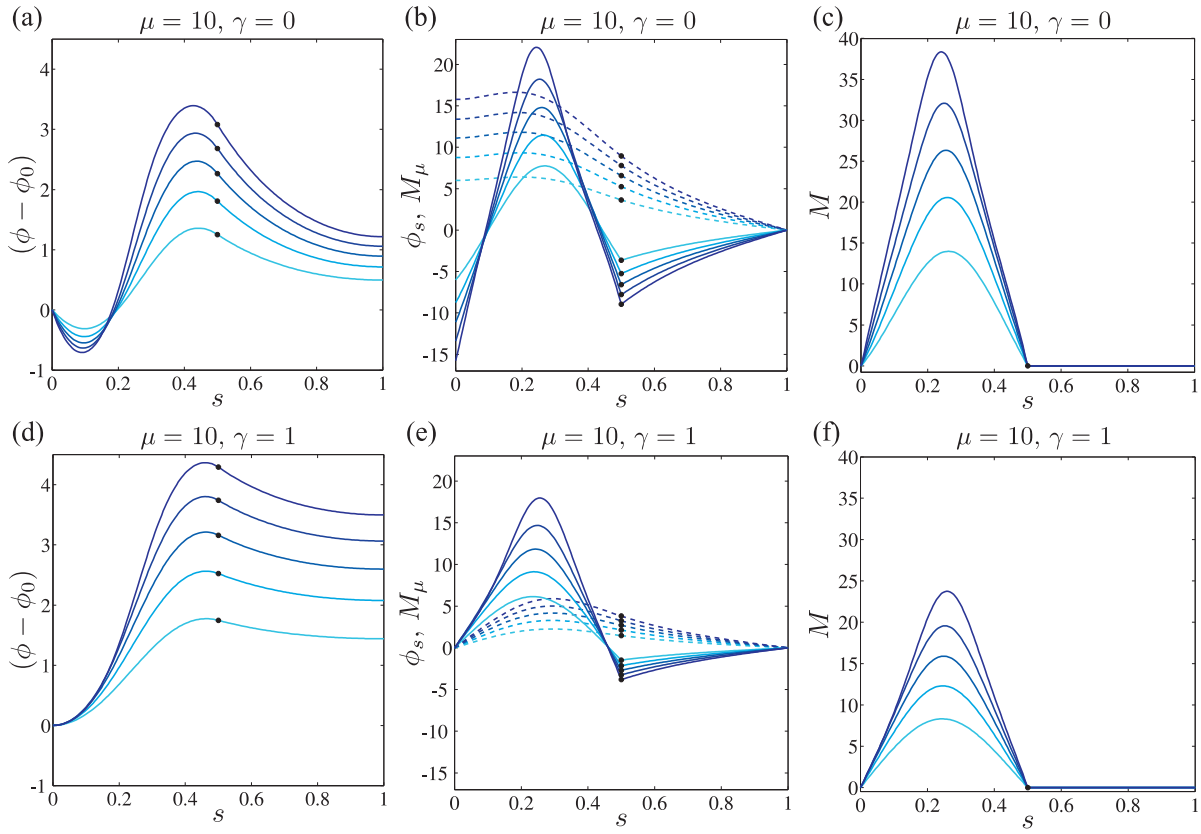

Figure 5.6: The angle relative to the base (a,d), curvature (solid curves in (b,e)), interfilament sliding moment M_μ (dashed curves in (b,e)) and the total bending moment M as a function of arclength, for $\mu = 10$, in the presence ($\gamma = 0$), and absence ($\gamma = 1$) of additional sliding constraints at the base, and five distinct horizontal displacements d, varying from 0.1 to 0.5 with equal intervals (darker curves are used for larger d). Black markers show the actuation point $\bar{s}$. The interfilament sliding moment M_μ is defined in dimensionless units by $M = \phi_s + M_\mu$ from Eq. (5.7).

vanish very rapidly as it approaches the actuation point $\bar{s}$, due to the pinned boundary condition at this point, see Figs. 5.6(c,f). In order to do so, the filament bundle deforms in opposition to the stored moment originated from the interfilament sliding resistance of the active portion (Figs. 5.6(b,e)), thus generating the characteristic counter-curvature beyond the actuation point.

In other words, the counterbend phenomenon can be viewed as a structural side effect of the interfilament sliding resistance. By adding internal elastic links, further moments M_μ can be generated, in addition to ϕ_s, acting to constructively resist the imposed bending at the active portion (Figs. 5.6(b,e)). In turn, the overall structure

is reinforced and a higher load is needed to achieve buckling (Fig. 5.4). Nevertheless, once the critical load is exceeded and the bundle finally buckles, the internal sliding moment M_μ has no other alternative than to also increase with the imposed deformation. At the passive region, which is torque and force-free, the stored internal sliding moment, instead of suppressing deformations, favours the formation of counter-deflections that gradually decay along the arclength (see Figs. 5.6(d,e,f)).

The role of the basal compliance while modifying the internal distribution of moments is also demonstrated in Fig. 5.6. When the sliding filaments are anchored at the base ($\gamma = 0$), a non-zero interfilament sliding moment M_μ is accumulated at the vicinity of the basal end, contributing later to a larger counter-deflection of the passive region, see Fig. 5.6(b) and 5.7(a). Nevertheless, due to the pinned boundary condition Eq. (5.13) at $s = 0$, the stored additional moments from the basal sliding resistance instigate a counter-deflection near the basal end, so that the balance of the total bending moment is satisfied at this point. As a consequence, the relative angle in Fig. 5.6(a) exhibits a minimum near the pinned point, which is followed by a non-zero opposing curvature in Fig. 5.6(b). In contrast, when the basal end is free from additional sliding resistance ($\gamma = 1$), the filament bundle is isotropic, i.e. $\int_0^1 \Delta \mathrm{d}s = 0$, and no interfilament sliding moment is generated at $s = 0$, causing the curvature to vanish at this point, Eq. (5.13).

To investigate the correlation between the interfilament sliding and the actual distortion of the filament bundle, in Fig. 5.7 we plot a model abstraction of the elastic crosslinking between the sliding filaments, for three different horizontal displacements d. We consider the two cases depicted in Figs. 5.3(b,l) for $\mu = 10$: (i) when the filaments within the bundle are rigidly anchored at the base, $\gamma = 0$, so that no sliding is allowed at $s = 0$ (welded bundle), and (ii) when the filaments at the base are free from any additional sliding resistance, $\gamma = 1$. The graphical representation of the sliding displacement $\Delta(s)$ in Fig. 5.7 demonstrates a non-trivial coupling between

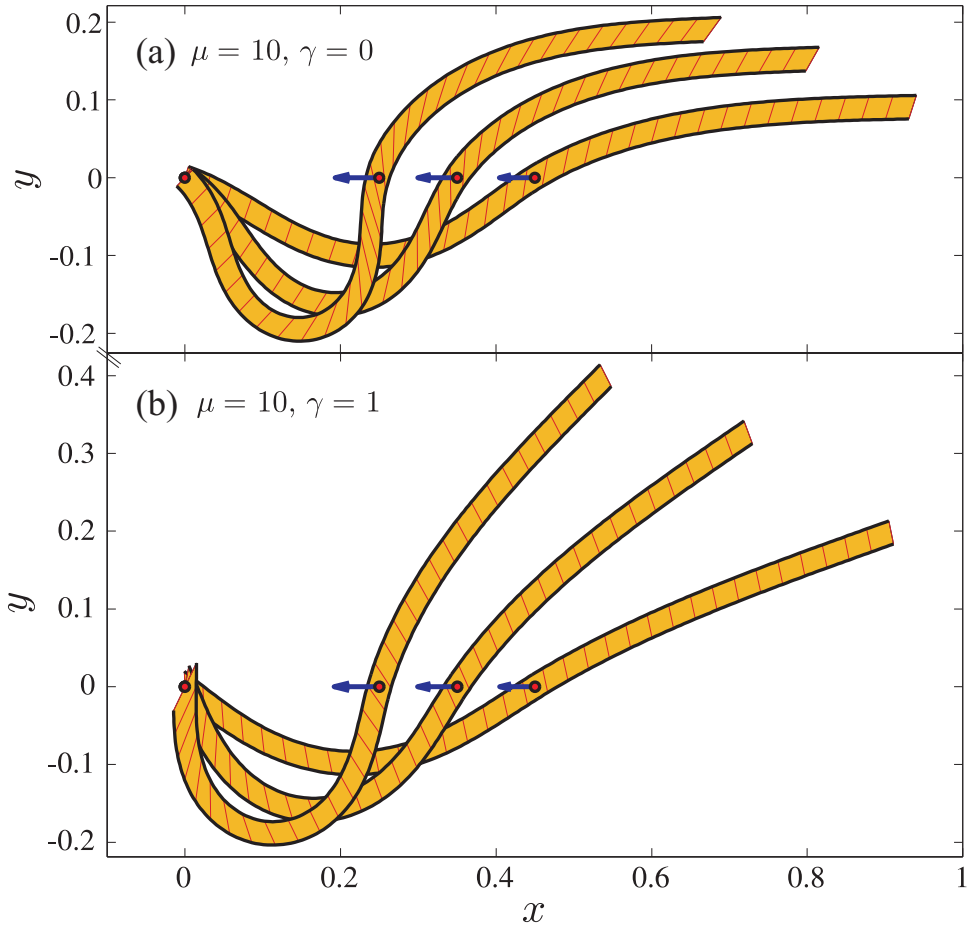

Figure 5.7: Illustrative representation of the sliding displacement $\Delta(s)$ during post-buckling deformations of pinned filament bundles for three distinct positions of the actuation point $d = 0.05, 0.15, 0.25$, Eq. (5.18), and two different basal constraints: (a) rigidly anchored filaments at $s = 0$ (welded bundle) and (b) free from additional basal sliding resistance. Blue arrows correspond to the total imposed force at the actuation point necessary to hold the filament bundle at a given displacement d found to be, respectively, $Q = 96.97, 107.50, 121.07$ for $\gamma = 0$ and $Q = 58.81, 65.80, 74.96$ for $\gamma = 1$, while $P = 0$ for all cases. Reaction forces at the pinned base are omitted for clarity. Note that the transversal red lines showing the crosslinkage between the filaments are a model abstraction, and represent the deviation angle, $\beta = \arcsin(\Delta/\sqrt{\Delta^2 + b^2})$, from the normal vector $\hat{\mathbf{n}}$ along the centreline of the filament bundle.

bending deformation and the sliding-filament distribution. In particular, when $\gamma = 0$ in Fig. 5.7(a), Δ_0 also vanishes, forcing a large sliding displacement towards the actuation point. Beyond $s = \bar{s}$, the amount of sliding relaxes in magnitude, although not rapidly enough to completely vanish at the end of the bundle. The opposite scenario is depicted in Fig. 5.7(b) for $\gamma = 1$, as the maximum of the absolute sliding

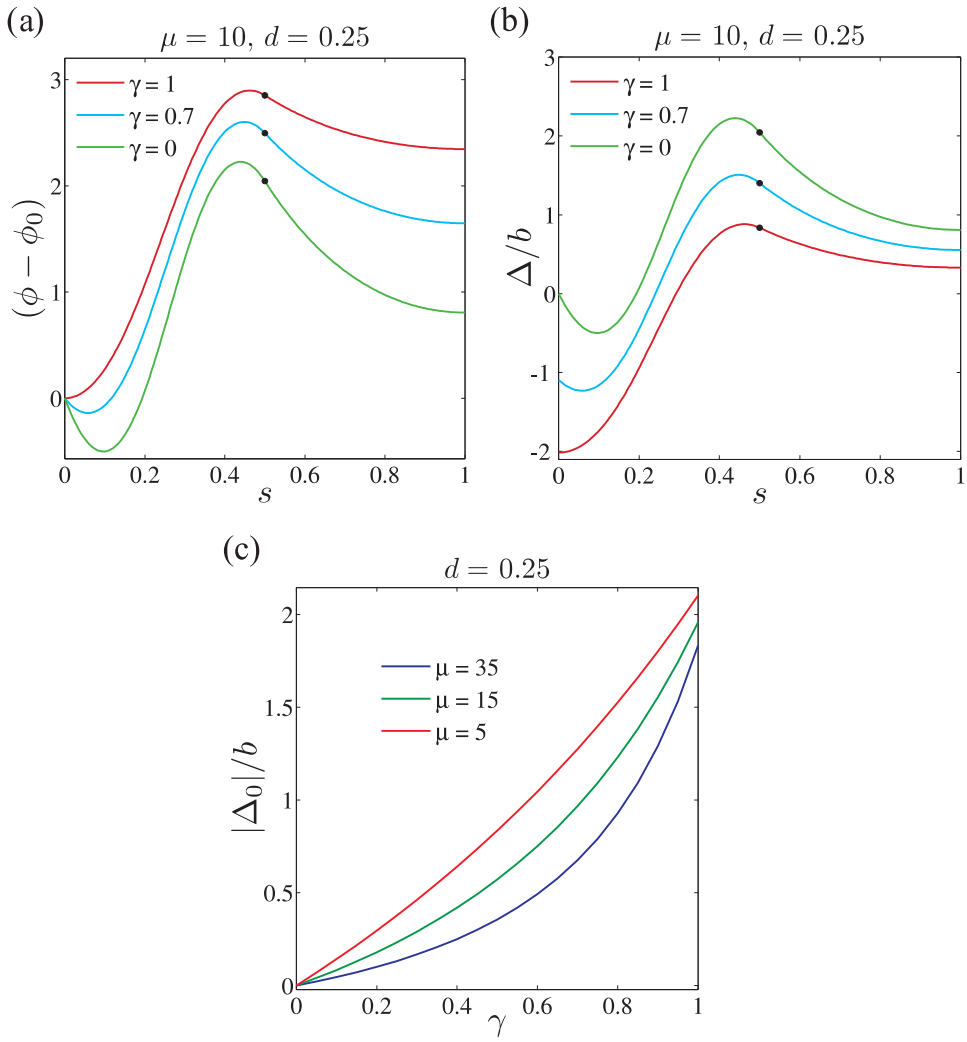

Figure 5.8: The angle relative to the base (a) and sliding displacement relative to the bundle diameter (b) as a function of arclength, for $\mu = 10$, a fixed displacement $d = 0.25$, and three distinct values of sliding resistance $\gamma \in [0, 1]$, as indicated by the colour label. Black markers in (a,b) show the actuation point $\bar{s}$. The basal sliding displacement relative to the bundle diameter is depicted in (c) as a function of the basal compliance γ and three distinct values of sliding resistance $\mu \in [5, 35]$.

displacement is shifted towards the pinned point, forcing $|\Delta_0|$ to increase. In this case, the addition of elastic sliding resistance at the base modifies the magnitude of the applied force, necessary to hold the bundle at a distance d, by almost 40% when compared with the welded base condition, i.e. $\gamma = 0$.

Fig. 5.8(a,b), on the other hand, depicts the relative angle and the sliding displacement as a function of s, for fixed μ and three values of γ, including the two cases

from Fig. 5.7. Similarly to Fig. 5.7, Fig. 5.8(a) demonstrates how the additional basal sliding resistance encourages the formation of counter-curvatures at both passive and active regions. The sliding displacement, however, presents a shift on the overall magnitude towards the negative axis as $\gamma \to 1$, so that the sliding force distribution satisfies $\int_0^1 \Delta \mathrm{d}s = 0$ when $\gamma = 1$, which in turn allows larger displacements at the base. It is also noteworthy that when $\gamma = 0$, $\Delta/b = (\phi - \phi_0)$, and therefore the green curve in both Figs. 5.8(a) and (b) are identical. Furthermore, the increasing behaviour of the basal sliding displacement is depicted in Fig. 5.8(c); reaching values as high as two times the diameter of the bundle, as the basal sliding resistance gradually decreases. Nevertheless, the overall magnitude of the basal sliding displacement decreases with μ, as the sliding resistance restrains filament sliding: compare for instance the colour curves in Fig. 5.8(c). In other words, Figs. 5.7 and 5.8 exemplify how the crosslinking mechanics modify, non-locally, the distribution of sliding displacement and, consequently, sliding forces (Eq. (5.3)), i.e. the amount of stretching of the internal links, as the bundle is deformed.

Finally, we show in Fig. 5.9 the typical changes of the relative angle to the base, and associated curvature, as function of s, for variations in μ with $\gamma = 0, 1$. As expected from Euler-Bernoulli theory, no counter-curvature is observed when $\mu = 0$ (black curves). But similarly to d in Fig. 5.6, increments of μ induce an increasingly large counter-curvature at the passive region, although equally regulated by the basal sliding resistance. When $\gamma = 1$ the plateau, observed at the passive part for $\mu = 0$ in Fig. 5.9(c), is nearly conserved for $\mu > 0$, with the introduction of a peak near the actuation point, whilst the active part is only slightly modified. Fig. 5.9(a), on the other hand, exhibits the formation a global maximum and minimum, further exposing the lack of accuracy if the Euler-Bernoulli theory is used instead. Nonetheless, the Euler-Bernoulli theory is still able to provide a reasonable guess if $\gamma = 1$, but still limited to the active region (Fig. 5.9(c)). Moreover, large values of μ are associated

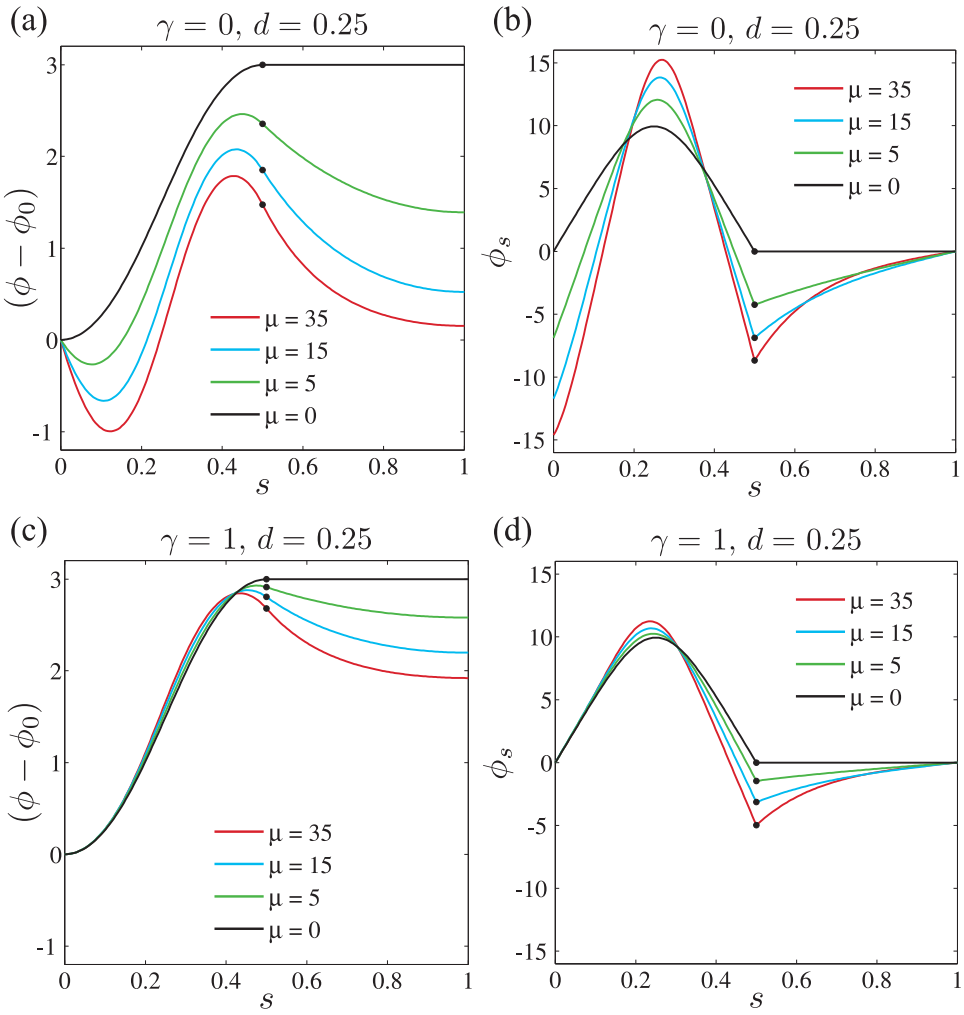

Figure 5.9: The angle relative to the base (a,c) and curvature (b,d) as a function of arclength, for $d = 0.25$, in the presence ($\gamma = 0$), and absence ($\gamma = 1$) of additional sliding constraints at the base, and four distinct values of sliding resistance $\mu \in [0, 35]$, indicated by the colour label. Black markers show the actuation point $\bar{s}$. It is also noteworthy that the black curves represent the relative angle and curvature for an Euler-Bernoulli beam, and they are identical in both (a,c) and (b,d), respectively, as if $\mu = 0$, $\gamma = 0$ by definition.

with a rapid rate of decay of the absolute counter-curvature beyond the actuation point, with faster decays for $\gamma = 0$ (Fig. 5.9(b,d)).

5.3.1.1 Directional polarity of the counterbend effect

Euler-Bernoulli filaments are known to preserve symmetry during deformations if subjected to identical conditions at the boundaries. A pinned filament at the middle

point along the arclength, and externally forced at left end ($s = 0$) towards the hinged point, will deform in the exact same way of a filament actuated, instead, at terminal end ($s = 1$) that moves towards $\bar{s}$, up to a reflection relative to the middle point. This symmetry property is equally shared by isotropic filament bundles, characterised by an uniform distribution of elastic crosslinks along its length and absence of additional sliding resistance at the base ($\gamma = 1$). Hence, the addition of basal sliding resistance introduces an intrinsic asymmetry between the proximal and end pieces of the filament bundle. The consequences of such intrinsic asymmetry can be further explored by considering the above symmetrically opposite system, in which the external force, $\mathbf{F}_{\text{ext}} = -\mathrm{Q}\,\boldsymbol{i} + \mathrm{P}\,\boldsymbol{j}$, acts at the terminal end instead, $s = 1$, while its reaction is located at pinned point $s = \bar{s}$, effectively transforming the intervals $[0, \bar{s}]$ and $[\bar{s}, 1]$ into a passive and active region, respectively. The resulting governing equations are identical to Eqs. (5.8),(5.9), with the appropriate change of the arclength interval. In this case, the solution for the passive region simply reads

$$\phi(s) = \phi_0 + [\,\gamma + \gamma\cosh(s\sqrt{\mu}) - (1-\gamma)\sqrt{\mu}\,\sinh(s\sqrt{\mu})\,]\int_0^1 (\phi - \phi_0)\,\mathrm{d}s', \qquad 0 \leq s \leq \bar{s}, \tag{5.20}$$

after imposing free torque condition at both the base and the pinned point, $s = \bar{s}$. Eq. (5.20) is then complemented by the numerical solution of the active part, $[\bar{s}, 1]$, by employing the numerical scheme discussed in Sec. 5.2.6, with the adequate arclength interval.

A graphical representation of the sliding displacement is shown in Fig. 5.10 for three distinct post-buckled configurations, with equivalent displacements to the ones found in Fig. 5.7, when the sliding filaments at the basal end are rigidly anchored. For comparison purposes, Fig. 5.10 also depicts, as red dashed curves, the centreline for the case of an isotropic filament bundle, i.e. $\gamma = 1$, for the same sliding resistance, $\mu = 10$. Although the filament bundle is still susceptible to the counterbend effect in this configuration, the overall magnitude is suppressed in such a way that the bundle

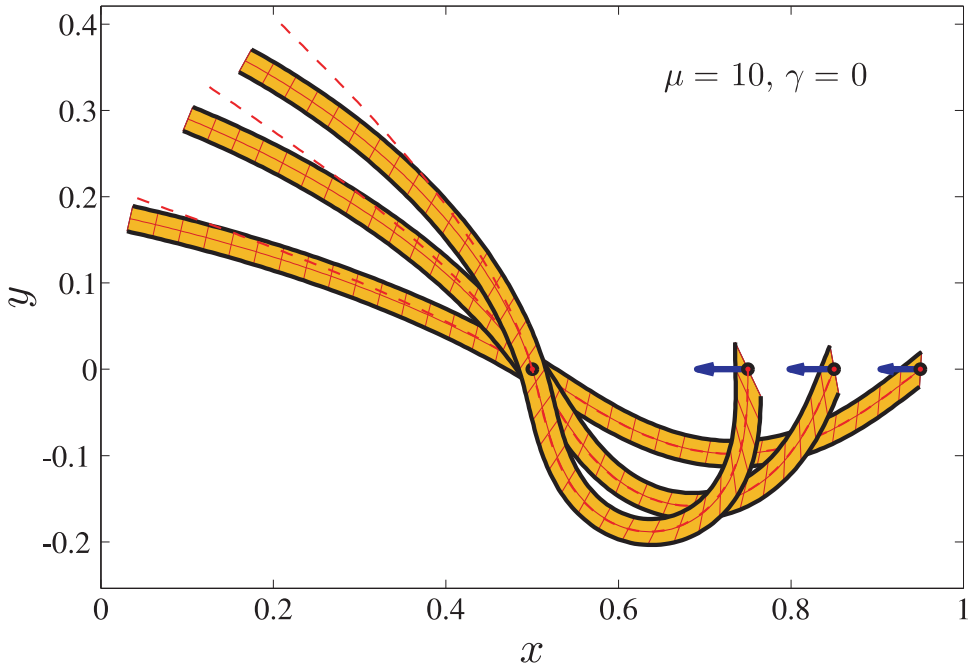

Figure 5.10: Filament bundle externally actuated at $s = 1$, pinned at $\bar{s} = 0.5$ and free from external forces and torques at the basal end ($s = 0$). Illustrative representation of $\Delta(s)$ for three distinct horizontal displacements relative to the undeformed reference state, equivalent to $d = 0.05, 0.15, 0.25$, Eq. (5.18), in Fig. 5.7. Dashed red curves represent the centreline of filament bundles for $\gamma = 1$. Blue arrows correspond to the total imposed force at the actuation point necessary to hold the bundle at a given displacement d found to be, respectively, $Q = 59.45, 66.50, 75.76$ for $\gamma = 0$ and $Q = 58.81, 65.80, 74.96$ for $\gamma = 1$, while $P = 0$ for all cases. Reaction forces at the pinned point $\bar{s}$ are omitted for clarity. Note that the transversal red lines showing the crosslinkage between the filaments are a model abstraction, and represent the deviation angle, $\beta = \arcsin(\Delta/\sqrt{\Delta^2 + b^2})$, from the normal vector $\hat{\mathbf{n}}$ along the centreline of the filament bundle.

with $\gamma = 0$ only exhibited a small deviation from the isotropic case (red curves). In this instance, the force magnitude, required to displace of d the actuated point $s = 1$ in Fig. 5.10, only showed a minor increase. Most of the relative filament sliding occurs at the deformed section of the bundle, similarly to the case shown in Fig. 5.7(b), as at $s = 1$ the filament bundle is free from additional sliding resistance. Consequently, the sliding displacement decays rapidly before transmitting to distant parts along the arclength, thus causing a decrease in the magnitude of the counter curvature.

Although symmetric conditions are imposed at the boundaries, the addition of

basal sliding resistance introduces a directional polarity on the counterbend phenomenon, depending on what section of the bundle, relative to the base, is actively deformed, effectively breaking the symmetry of the system. In particular, the importance of the basal anchor in the transmission of sliding displacements and the directional polarity were also reported by Pelle et. al. [103], during the manipulation of a sea-urchin sperm flagellum that was fortuitously stuck to the glass in only a short mid-flagellar section. Isotropic bundles, on the other hand, are able to preserve symmetry properties, as demonstrated in Fig. 5.10; in particular the red dashed curves are identical to the solutions displayed in Fig. 5.7(b), after appropriate reflection relative to y axis and a translation in the x axis.

5.3.2 Clamped base condition

In this section we study the consequences of clamping the filament bundle at the base while externally actuated at $\bar{s}$. For a general discussion on the counterbend phenomenon, the reader is directed to the Sec. 5.3.1, as this will be omitted in the present section.

We begin by displaying, in Fig. 5.11, post-buckled configuration for four distinct horizontal displacements across fifteen points in the (μ, γ)-parameter space. The numerical solutions reveal that the counterbend effect at the passive region is equally present when the basal end is clamped, and similarly to the pinned boundary condition in Sec. 5.3.1, the counter-curvature depends upon the interplay between the sliding resistance and basal compliance, in addition to the horizontal displacement d. Fig. 5.11 shows the counterbend magnitude increasing with d regardless of μ and γ. This is further demonstrated in Fig.5.12(a,b,d,e), in which the angle relative to the base and curvature, as function of the arclength, are plotted as d increases. The rate of increase, however, is regulated by the (μ, γ)-pair, which ultimately leads to the lost of monotonicity as γ tends to 1 in Fig. 5.15(c), which plots the maximum counter-

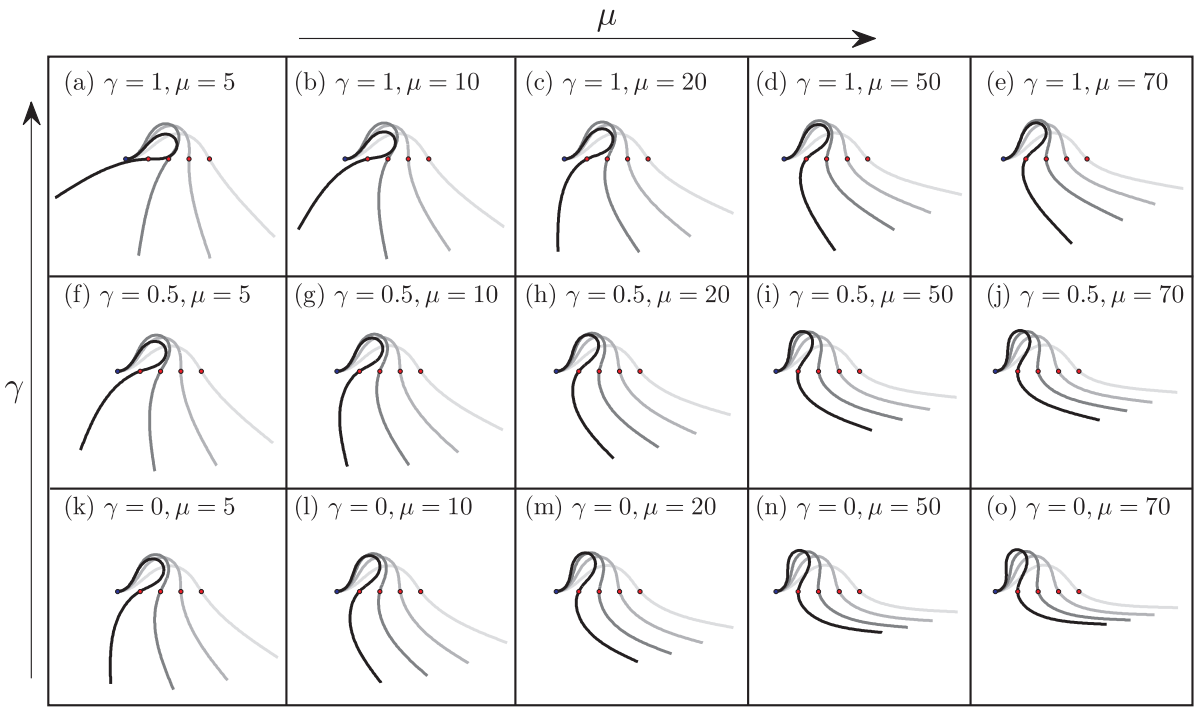

Figure 5.11: Post-buckling deformations of clamped filament bundles at the base (blue marker) for $5 \leq \mu \leq 70$ and $0 \leq \gamma \leq 1$, as indicated, and four distinct positions of the actuation point (red marker), plotted at equal intervals varying from 0.09 to 0.39 (with darker curves used for larger d, given by Eq. (5.18)).

curvature of the passive region as a function of d for six different (μ, γ) parameters. Analogously, Figs. 5.11, 5.15(d) and 5.13 demonstrate how the counterbend effect is intensified for a larger sliding resistance μ. Nevertheless, the lack of compliance at the base tends to decrease, in magnitude, the counter-curvature found at the passive region, exemplified by Figs. 5.11, 5.15(d), 5.18 and 5.17(a). In general, the fundamental effects induced by the crosslinking mechanics remained unchanged for the clamped boundary condition.

The numerical solutions also revealed the presence of counter-curvatures near the basal end in Fig. 5.11, i.e when the curvature changes in sign. However, in contrast with the pinned case in Sec. 5.3.1, the near base counterbend is present for any (μ, γ)-pair in Fig. 5.11, in addition to the simpler Euler-Bernoulli case in Fig. 5.13, as depicted by the black solid curves. Indeed, the near base counter-curvature is a

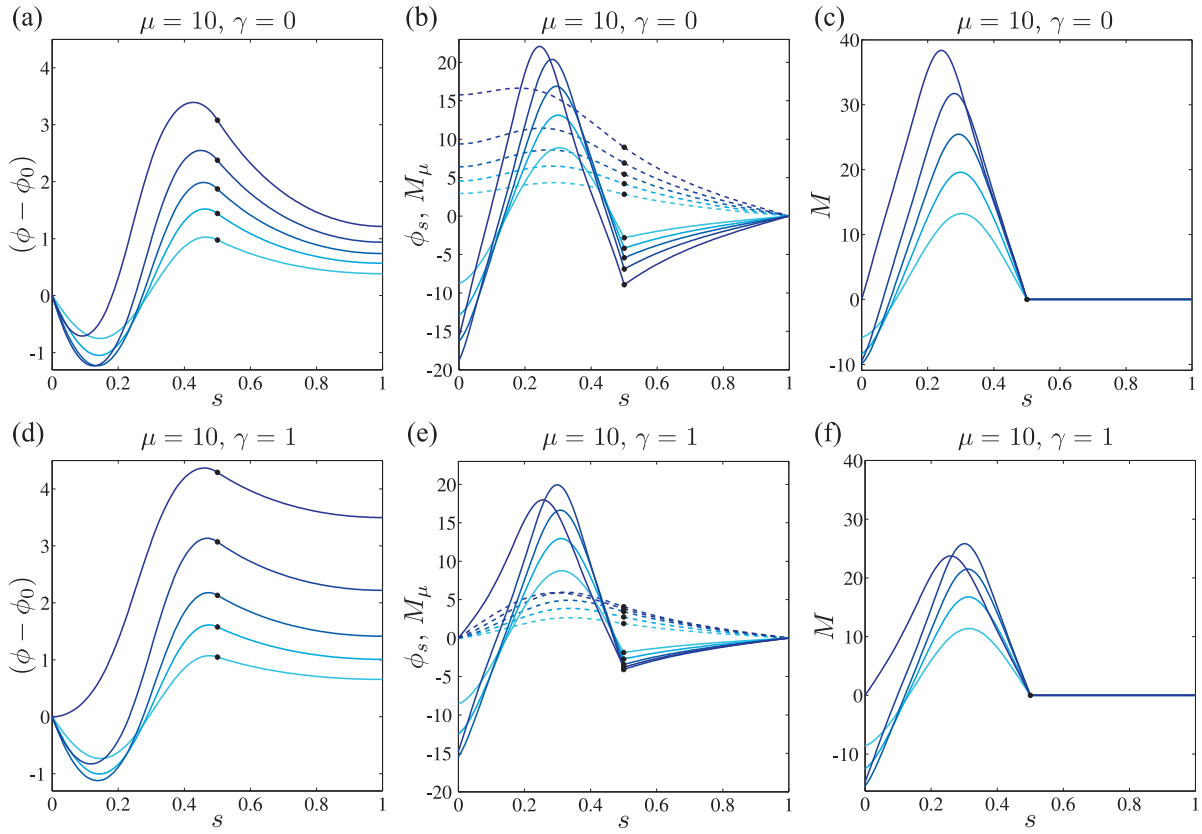

Figure 5.12: The angle relative to the base (a,d), curvature (solid curves in (b,e)), interfilament sliding moment M_μ (dashed curves in (b,e)) and the total bending moment M as a function of arclength, for $\mu = 10$, in the presence ($\gamma = 0$), and absence ($\gamma = 1$) of additional sliding constraints at the base, and five distinct horizontal displacements d, varying from 0.1 to 0.5 with equal intervals (darker curves are used for larger d). Black markers show the actuation point $\bar{s}$. The interfilament sliding moment M_μ is defined in dimensionless units by $M = \phi_s + M_\mu$ from Eq. (5.7).

sole result of the clamped boundary condition, as the base is constrained to lie in the horizontal direction during actuation. This induces, in turn, an overall rotation of the shape around $\bar{s}$ due to the torque-free condition at the actuation point. This rotation is ultimately responsible for a decrease of the near base counterbend as the actuation point approaches the base, after an initial increase with the displacement d, see Fig. 5.12(a,b,d,e) (darker curves are used for larger d). Fig. 5.13, on the other hand, shows how the near base counter-curvature increases with the interfilament sliding resistance μ, regardless of γ. This is in contrast with the pinned case in Fig. 5.9, in which the near base counterbend depends on the basal compliance. Hence,

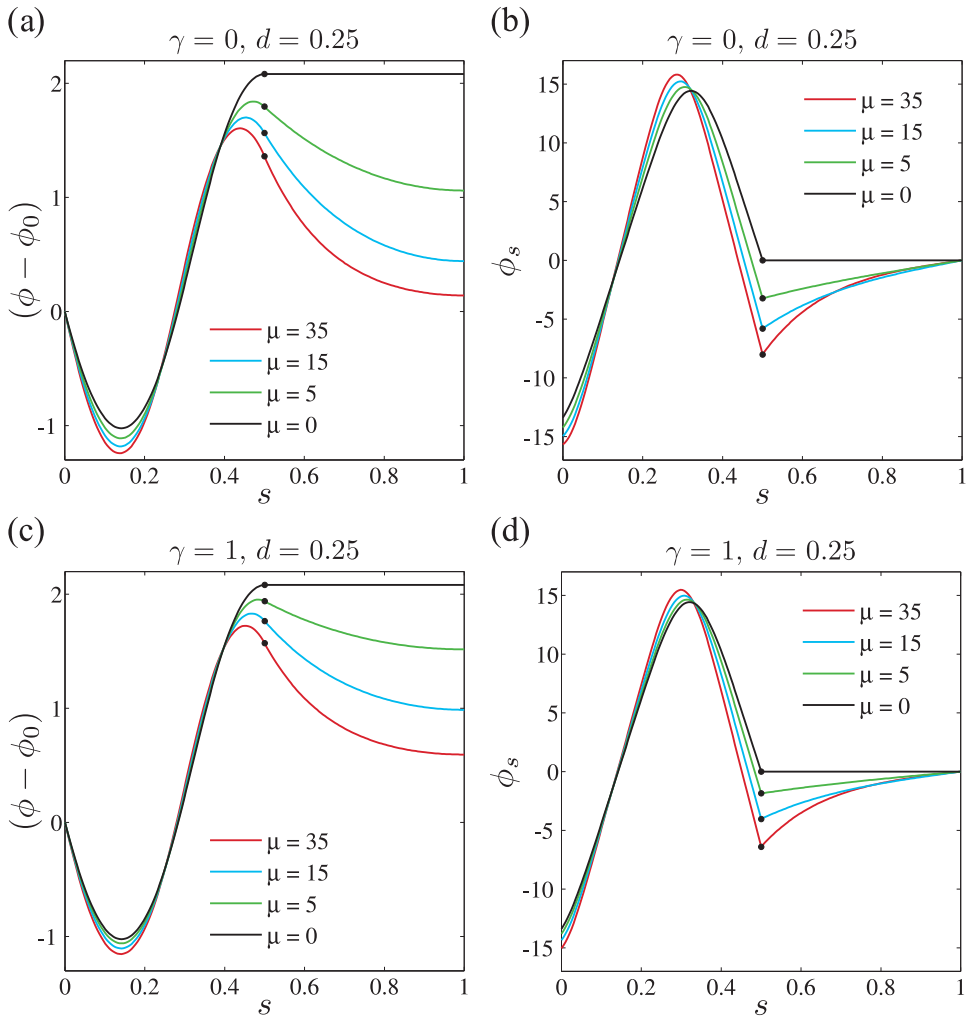

Figure 5.13: The angle relative to the base (a,c) and curvature (b,d) as a function of arclength, for $d = 0.25$, in the presence ($\gamma = 0$), and absence ($\gamma = 1$) of additional sliding constraints at the base, and four distinct values of sliding resistance $\mu \in [0, 35]$, indicated by the colour label. Black markers show the actuation point $\bar{s}$. It is also noteworthy that the black curves represent the relative angle and curvature for an Euler-Bernoulli beam, and they are identical in both (a,c) and (b,d), respectively, as if $\mu = 0$, $\gamma = 0$ by definition.

the near base counterbend is a deformation signature of rigid constraints at the base: either the sliding filaments are rigidly anchored at the base ($\gamma = 0$) or the base is simply clamped. A constructive superposition is found when both constraints are present, leading to a larger near base counter-curvature, Fig. 5.13(a,b). It is also noteworthy that the arclength position where the curvature changes in sign tends to remain unchanged for the clamped constraint, Fig. 5.13(b,d), while the opposite was

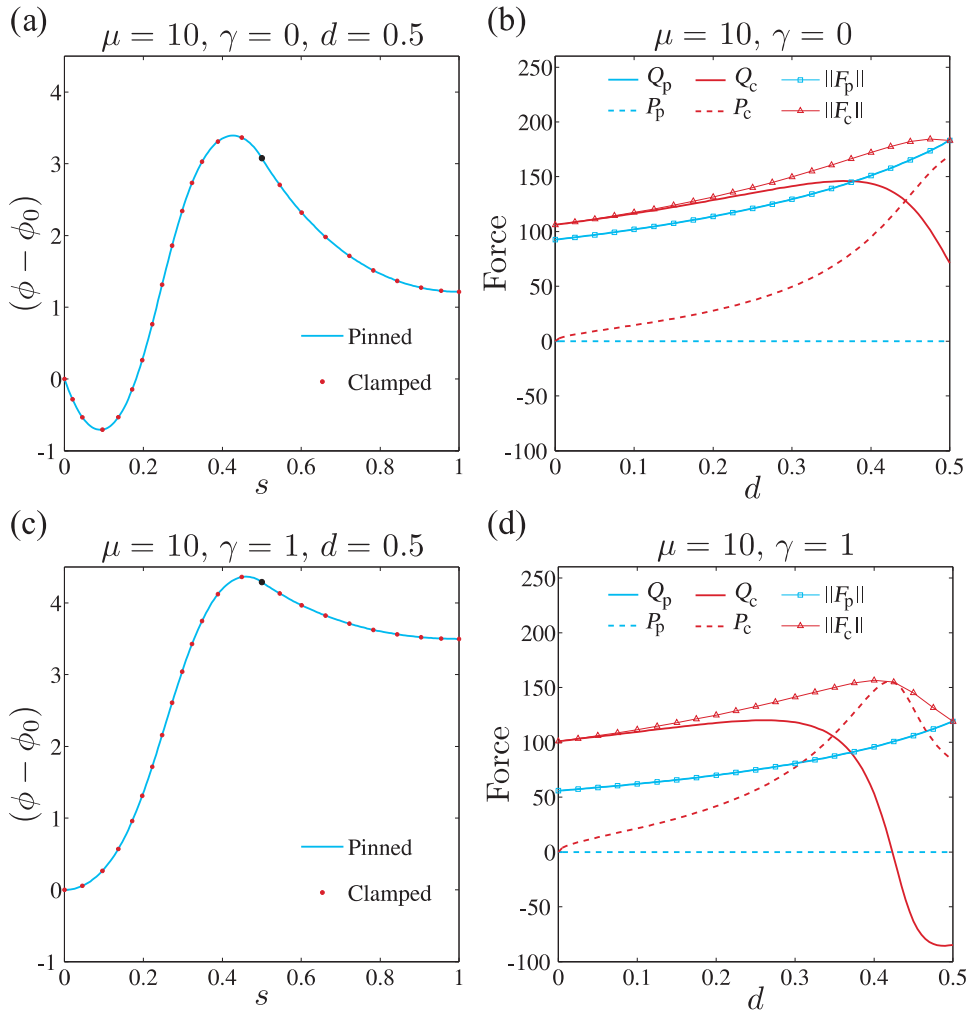

Figure 5.14: Comparison between the pinned and clamped boundary conditions when the actuation point $\bar{s}$ reaches the basal end, in the presence ($\gamma = 0$), and absence ($\gamma = 1$) of additional sliding constraints at the base. (a,c) Show the angle relative to the base as a function of arclength, for $\mu = 10$ and $d = 0.25$. (b,d) Plots the horizontal force, Q, the vertical force, P, and total force magnitude, $||\mathrm{F}|| = \sqrt{Q^2 + P^2}$, as function of d for both clamped and pinned boundary conditions, indicated by the subscript c and p in the figure label, respectively. Black markers in (a,c) show the actuation point $\bar{s}$, while $||\mathrm{F}_p|| = Q_p$ in (b,d), as $P_p = 0$ for any d. It is noteworthy that when $d = 0.5$ not only the solutions for both clamped and pinned cases are identical in (a,c), but also $||\mathrm{F}_p|| = ||\mathrm{F}_c||$.

observed for the pinned boundary condition, Fig. 5.9(b).

Fig. 5.12 further demonstrates how the internal mechanics is modified by the clamped boundary condition at $s = 0$. It plots the curvature, the total bending moment and the interfilament sliding moment M_μ, defined by $M = \phi_s + M_\mu$ from

Eq. (5.7), as a function of s for various (μ, γ, d) triplets. Now, because of the torque constraint at the base, the total internal moment does not vanish at $s = 0$, as it is required to balance the appropriate external moment so that $\phi_0 = 0$. In general, the sliding moments tends to offset the pure elastic moments, ϕ_s, since M_μ increases with the imposed deformation of the active region. This, in turn, induces the curvature near the base, and beyond the actuation point, to switch sign in order to match the external torque at $s = 0$, and balance the stored sliding moment M_μ at the passive section. Similar behaviour was observed for the pinned case in Fig. 5.6, the only difference being that $M(0) = 0$.

One should note, however, that when the actuation point coincides with the basal end, i.e $d = 0.5$, no external torque is required at the base to ensure $\phi_0 = 0$ (darker curves in Fig. 5.12(c,f)), as the stored bending moment at this point is dissipated through the free torque condition at the actuation point, via a rotation around $\bar{s}$. As a consequence, the solutions for the clamped and pinned boundary conditions, shown in Fig. 5.14(a,c), are identical when $d = 0.5$, after rotating, for instance, the pinned solution of $-\phi_0$ around base. Such rotation can only be achieved via additional forces in the vertical direction, not present when the bundle is pinned ($P = 0$), so that the total force magnitude $\sqrt{Q^2 + P^2}$ is conserved. Indeed, the total external force required to hold the actuation point at $d = 0.5$ for the clamped condition is equal to the one required by the pinned case, although the horizontal and vertical forces from the clamped and pinned conditions are not correlated. This fact is demonstrated in Fig. 5.14(b,d), which shows how the horizontal and vertical forces vary with d, so that the total force coincides at $d = 0.5$. In other words, the clamped boundary condition assume a hybrid state, when $d = 0.5$, which satisfies simultaneously the clamped and the pinned boundary condition at $s = 0$. Also note that the latter is general, and equally applies for Euler-Bernoulli beams.

The bifurcation diagram depicted in Fig. 5.15(a,b) demonstrates another funda-

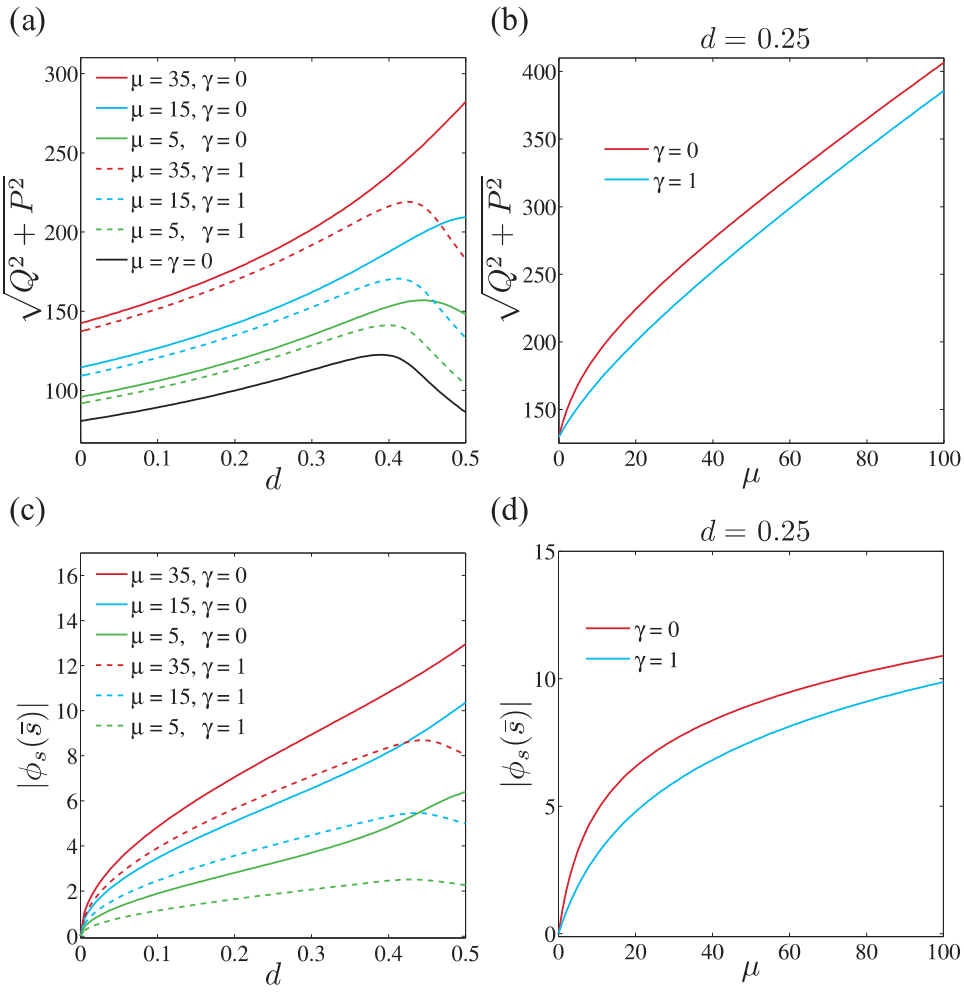

Figure 5.15: The total external load, $\sqrt{Q^2 + P^2}$, and the absolute curvature, measured at the actuation point, $|\phi_s(\bar{s})|$ as a function of the displacement d, in (a,c), and as a function the sliding resistance parameter μ, in (b,d). It is also noteworthy that the counter-curvature of the actuation point $|\phi_s(\bar{s})|$, found to be the maximum curvature developed at the passive region, is a convenient manner to measure of the magnitude of the counterbend effect in the parameter space.

mental aspect from the crosslinking mechanics: the increase of the actuation force, in magnitude, as either μ increases or γ decreases. The internal links in association with a large resistance to sliding at the base reinforce the overall structure of the bundle so that higher load is required to achieve buckling. Nevertheless, the clamped case is less sensitive to variations in γ, at $0 \leq d \leq 0.35$, as shown in Fig. 5.15(a) (note that the dashed curves in Fig. 5.15(a) are for $\gamma = 0$, and not 0.5 as in Fig. 5.4(a)). Furthermore, while the modulus of the actuation force, as a function of d, inherits the

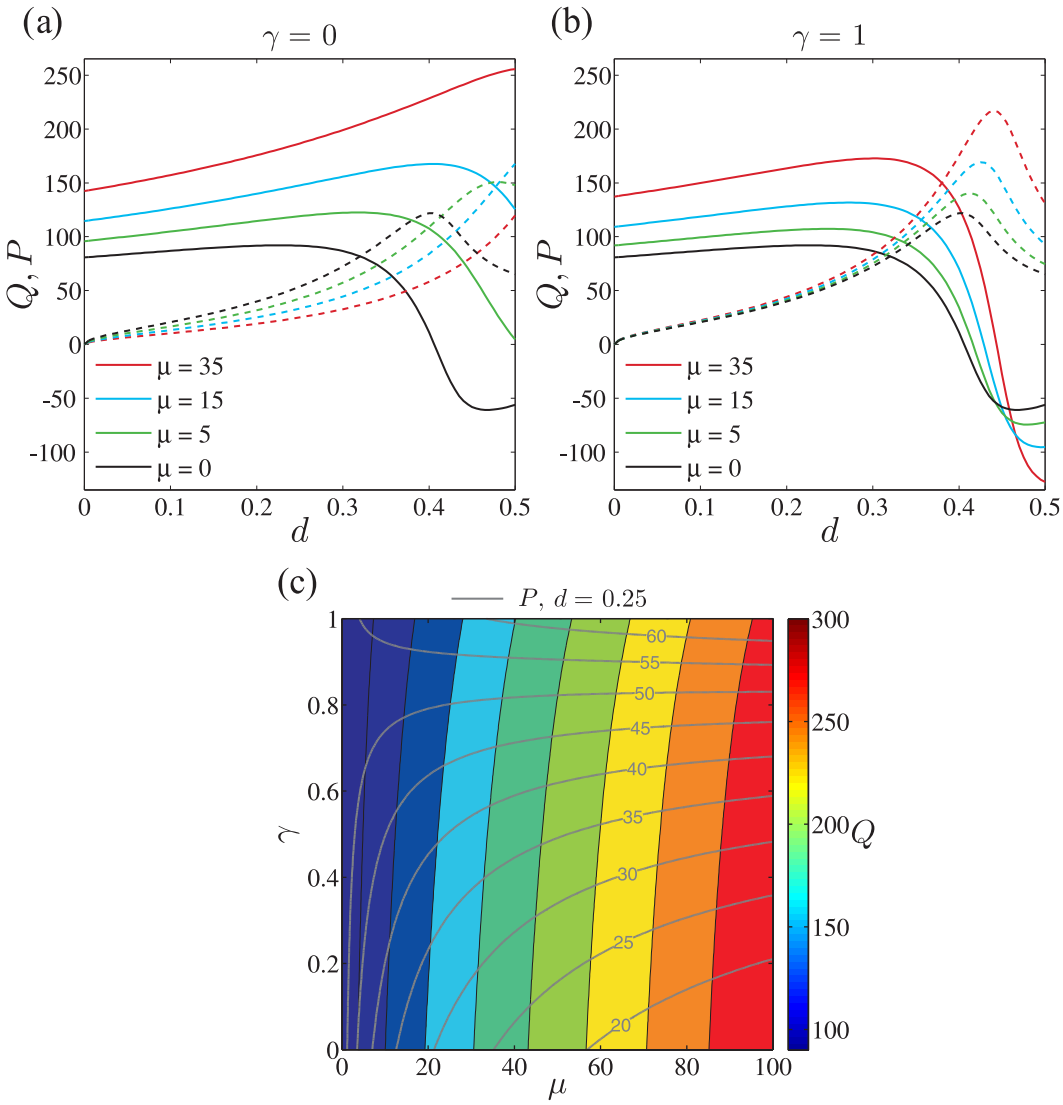

Figure 5.16: Sensitivity of post-buckled deformations to the basal compliance and sliding resistance: (a,b) The horizontal external load Q (continuous curves) and vertical external load P (dashed curves) as a function of d for four distinct values of μ. The black curves (solid and dashed) in (a,b) represent the Euler-Bernoulli case, and they are identical in both (a,b). (c) Colour plot of the external load, Q, as a function of (μ, γ), necessary to hold a filament bundle at a distance $d = 0.25$ of the actuation point. Black curves depict contour lines of Q, while grey curves depict the contour lines of P, as indicated. Note that the isolines of Q and P generate a mesh in (μ, γ)-space.

observed behaviour of simpler Euler-Bernoulli filaments (black curve in Fig. 5.15(a)), the extra sliding resistance at the base gradually drifts the maximum of $\sqrt{Q^2 + P^2}$ towards lager values of d, as μ increases. This fact is even more clearly depicted

by Figs. 5.16(a,b), which show the behaviour of each individual force, horizontal (continuous curves) and vertical (dashed curves), for the same parameters used in Fig. 5.15(a). In particular, while in Fig. 5.16(b) both horizontal and vertical loads increase, in magnitude, with d, preserving the Euler-Bernoulli behaviour (black curves), Fig. 5.16(a), on the other side, shows an intricate change in behaviour, diverging from the Euler-Bernoulli case. In this instance, Q can even admit larger values than P, for example, at $d = 0.5$ in Fig. 5.16(a), though this is not possible for $\gamma = 1$. The resulting interplay between the horizontal and vertical load is even more clearly demonstrated in Fig. 5.16(c), which show the antagonistic behaviour between the contours of Q and P in the (μ, γ)-parameter space, which ultimately favours the formation of a mesh-like pattern. The contour lines of Q tend to vary more rapidly with γ, while the opposite is found for P, expect for the region where μ is very small. Now, solutions that require the same resulting external load to displace the actuation point of d, that previously could not be distinguished in the parameter space from bifurcation diagrams, such as Figs. 5.4(a) and 5.15(a), can be differentiated by following the contours of Q and P simultaneously. An even higher precision while differentiating solutions in the parameter space is achieved by considering that the (Q, P)-landscape is also modified by d, Figs. 5.16(a,b). As a result, by clamping one end of the filament bundle, which is easily implemented in micro-scale experiments by attaching, for instance, the sperm head to the substrate, entails the accuracy of material parameters extracted from load-displacement experiments is increased.

Finally, we close this section by analysing the combined effect of clamped boundary condition and the basal compliance. As discussed earlier, the near base counterbend is naturally induced by external moments that are generated by the clamped constraint. The latter is equally responsible for geometrically restricting the total amount of sliding displacement permitted at the base, which in turn causes the overall shape at the active section to change weakly with the internal material properties, Figs. 5.13(a)

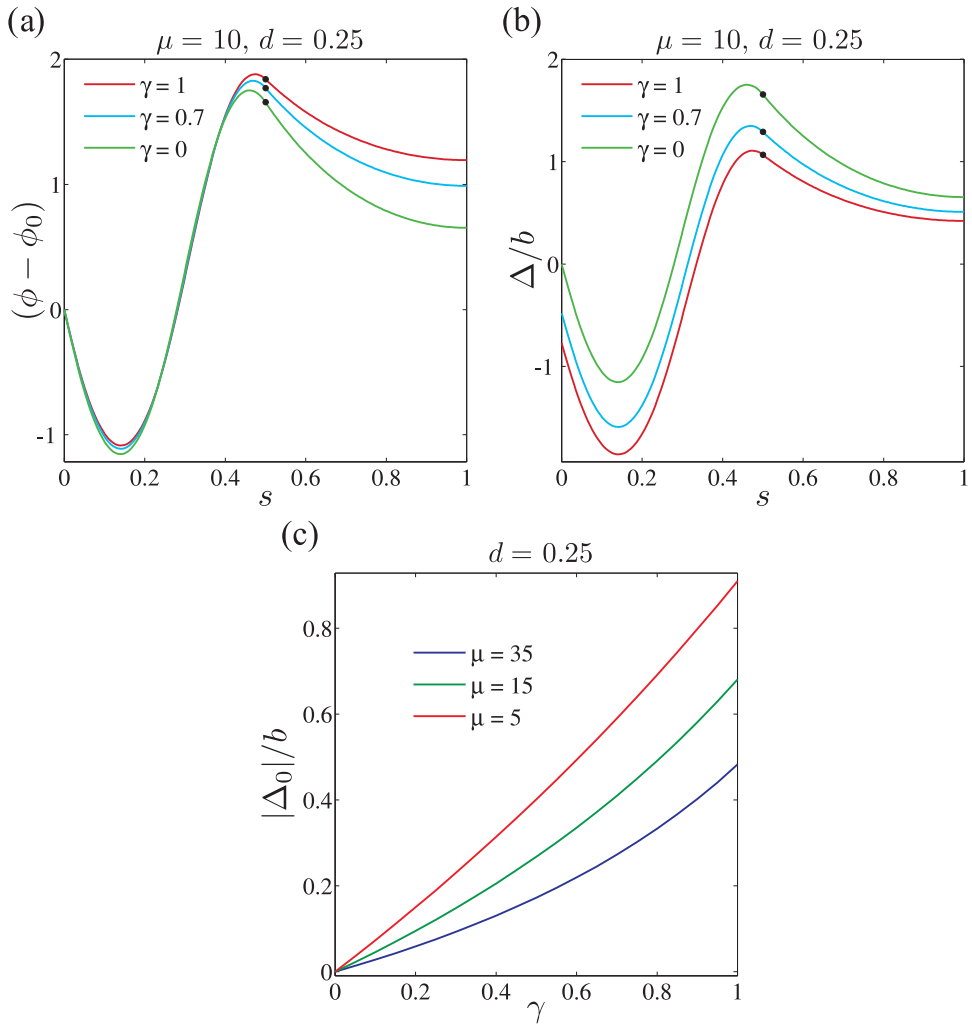

Figure 5.17: The angle relative to the base (a) and sliding displacement relative to the bundle diameter (b) as a function of arclength, for $\mu = 10$, a fixed displacement $d = 0.25$, and three distinct values of sliding resistance $\gamma \in [0, 1]$, as indicated by the colour label. Black markers in (a,b) show the actuation point $\bar{s}$. The basal sliding displacement relative to the bundle diameter is depicted in (c) as a function of the basal compliance γ and three distinct values of sliding resistance $\mu \in [5, 35]$.

and 5.18. Fig. 5.13(c) demonstrates even more clearly the restrictive effect of the clamped condition on the basal sliding displacement which is now, typically, smaller than the bundle diameter. Similarly to the hinged case in Fig. 5.9, the magnitude of sliding displacement increases for larger values of basal sliding resistance, however the near base behaviour is conserved for all values of γ when the base is clamped, see Fig. 5.13(b,d). As a result, large deformations due to variations of the basal

compliance are mostly observed in the passive section, characterised by an increase of the counterbend magnitude, as depicted in Figs. 5.17(a) and 5.18. In other words, the clamped boundary condition successfully isolates the resulting effect from the internal crosslinking mechanics to the passive region only.

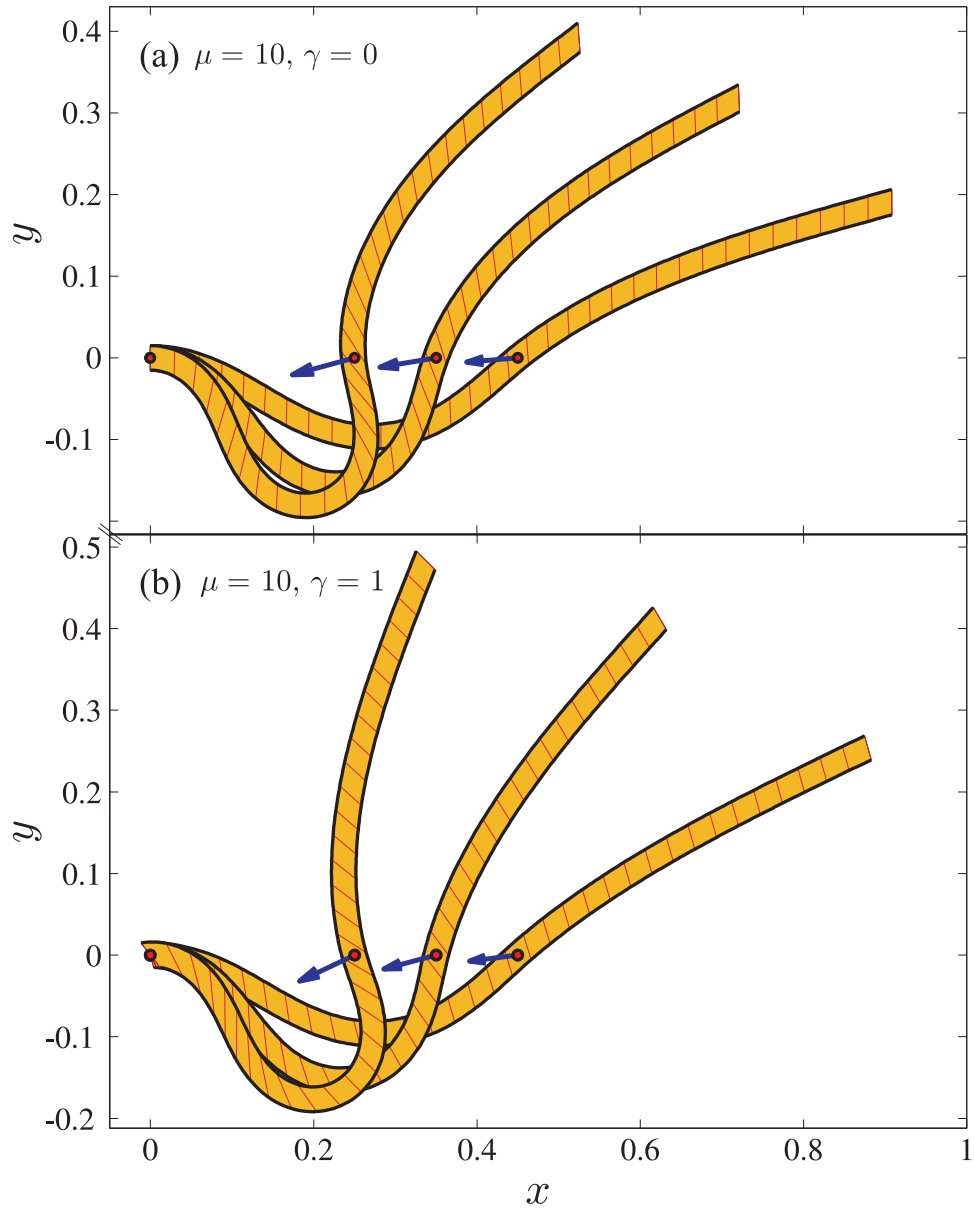

Figure 5.18: Illustrative representation of the sliding displacement $\Delta(s)$ during post-buckling deformations of clamped filament bundles for three distinct positions of the actuation point $d = 0.05, 0.15, 0.25$, Eq. (5.18), and two different basal constraints: (a) rigidly anchored filaments at $s = 0$ (welded bundle) and (b) free from additional basal sliding resistance. Blue arrows correspond to the total imposed force at the actuation point necessary to hold the filament bundle at a given displacement d found to be, respectively, $\sqrt{Q^2 + P^2} = 111.45, 124.08, 140.15$ for $\gamma = 0$ and $\sqrt{Q^2 + P^2} = 106.08, 117.9, 132.67$ for $\gamma = 1$. Reaction forces at the pinned base are omitted for clarity. Note that the transversal red lines showing the crosslinkage between the filaments are a model abstraction, and represent the deviation angle, $\beta = \arcsin(\Delta/\sqrt{\Delta^2 + b^2})$, from the normal vector $\hat{\mathbf{n}}$ along the centreline of the filament bundle.

5.4 Extracting material parameters: an example result

In this section, we provide an example result for measurements of material parameters from counterbend experiments by employing the formulation developed here. The geometrically non-linear analytical solution of the passive region, given by Eq. (5.17), was used to estimate both μ and γ via model curve fitting. In this example, we considered existing data reported by Pelle et. al [103], where the flagellum configuration was captured, as illustrated by the white curves in Figs. 5.19, 5.20 and 5.21. Least squares fitting of the captured angle relative to the base, $(\phi - \phi_0)$, with the analytical formulae for the configuration of the passive region, Eq. (5.17), provided estimates for both μ and γ.

Fig. 5.19 shows the captured flagellum (white curves), and associated relative angle to the base (blue curves), for a sequence of increasing probe actuation (a-c). As the imposed deformation induced by the microprobe increases, the curvature of the distal flagellum beyond the actuation point also increases, in agreement with model predictions discussed in the last section; compare for instance Fig. 5.19 with Fig 5.12(a,d). Nevertheless, the first half of the active region $[0, \bar{s}]$ of the flagellum configuration is characterised by the absence of deformations, demonstrated by a flat plateau near the basal end of the captured $(\phi - \phi_0)$. This straight configuration indicates that the flagellum is not only clamped at the base, via the anchoring of the sperm head, but also that the flagellum is attached to the substrate in this region. This is fact is further exemplified by Fig. 5.21(a), which for a similar probe actuation, a larger near base flagellar distortion is generated, when compared with Fig. 5.19. As a result, the estimated values for both μ and γ are very low for Fig. 5.19, varying from $\mu \approx 16$ to $\mu \approx 19$, while γ was zero in all cases, despite the excellent match between Eq. (5.17) and the captured data. Indeed, $\gamma = 0$ indicates that the microtubules are prevented from sliding at the base. In this case, however, the lack of basal sliding is

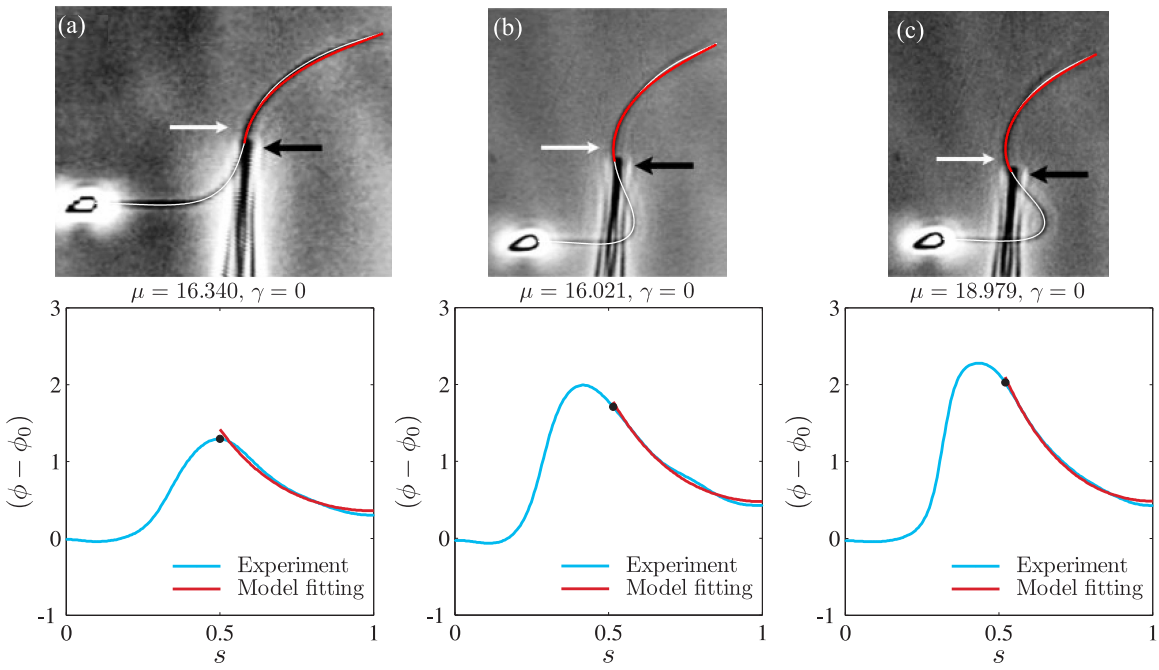

Figure 5.19: Model curve fitting with existing experiment by Pelle et. al [103]. Microscope imaging for an increasing probe actuation is depicted in the first row, in sequence (a-c). For each panel (a-c) the captured flagellar profile is indicated in white (first row), and the resulting angle relative to the base (blue curves) are plotted as a function of the arclength (second row). The red curves in both rows show the model curve fitting result from the analytical solution of the passive region, given by Eq. (5.17), from where the values of μ and γ are extracted, as indicated. The black markers in the second row depicts the probe actuation point. The counter-curvature (white arrows) and the direction of probe movement (black arrows) are indicated in the micrographs. Microscope images adapted from Pelle et al. [103] with permission from John Wiley and Sons (2958780742312).

caused by the attachment between the demembranated flagellum and the substrate, as the adhesive contact forces prevent the interfilament sliding at the point or section of contact on the sperm flagellum.

To further demonstrate the flagellum-substrate adhesion near the basal end, we contrast the observed deformation with the geometrically exact formulation in Fig. 5.20, by evaluating numerical solutions for the values of (μ, γ) extracted from the curve fitting routine above. Fig. 5.20 reveals discrepancies between the model prediction and the flagellar configuration towards the first half of the active region $[0, \bar{s}]$, as the clamped condition is only imposed at the basal end, as opposed to a whole flagellar

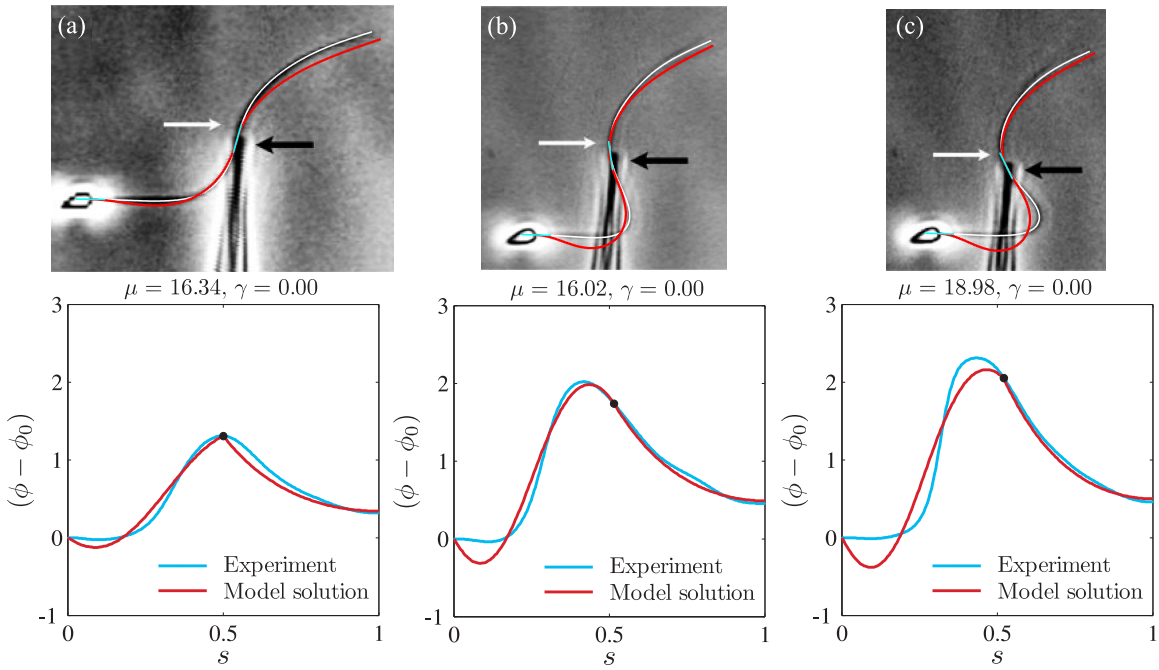

Figure 5.20: Parallel between the geometrically exact formulation and existing experiment by Pelle et. al [103]. Microscope imaging for an increasing probe actuation is depicted in the first row, in sequence (a-c). For each panel (a-c) the captured flagellar profile is indicated in white (first row), and the resulting angle relative to the base (blue curves) are plotted as a function of the arclength below (second row). The red curves in both rows show the geometrically non-linear solutions for the values of μ and γ, as indicated, that were extracted via curve fitting the analytical solution of the passive region, Eq. (5.17), with the captured shape. Numerical solutions where evaluated by imposing the bending angle at the basal end ($s = 0$) and at the actuation point ($s = \bar{s}$) from the captured flagellar profile, indicated by the tangent lines (cyan) overlaid in the microscope snapshots. The black markers in the second row depicts the probe actuation point. The counter-curvature (white arrows) and the direction of probe movement (black arrows) are indicated in the micrographs. Microscope images adapted from Pelle et al. [103] with permission from John Wiley and Sons (2958780742312).

section. Note that small changes in $(\phi - \phi_0)$ results in large differences in the associated shape solution. Furthermore, despite the bias introduced by flagellum-substrate adhesion forces, the geometrically non-linear formulation has a reasonable qualitative agreement with the captured relative angle $(\phi - \phi_0)$ from experiment.

The opposite scenario is depicted in Fig. 5.21, where the near base section of the flagellum is relatively free from the substrate attachment. As a result, the estimated

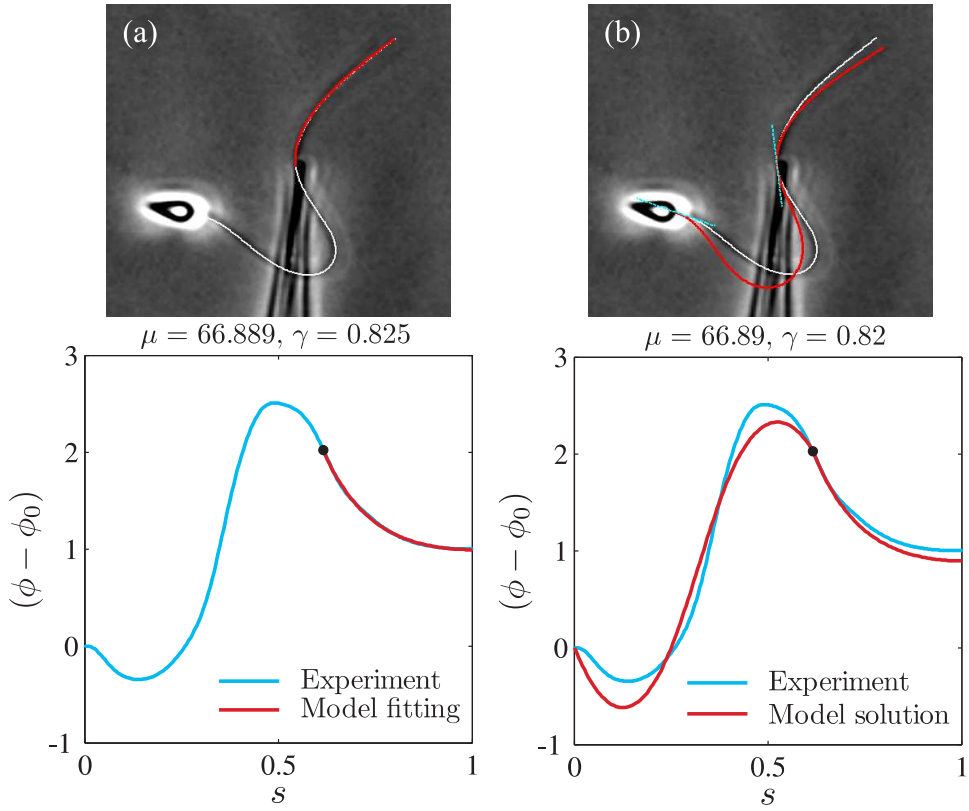

Figure 5.21: Model curve fitting (a) and parallel between the geometrically exact formulation and existing experiment (b) by Pelle et. al [103]. For each panel (a,b) the captured flagellar profile is indicated in white (first row), and the resulting angle relative to the base (blue curves) are plotted as a function of the arclength below (second row). The red curves in (a) for both rows show the model curve fitting result from the analytical solution of the passive region, given by Eq. (5.17), from where the values of μ and γ are extracted, as indicated. The red curves in (b) for both rows show the geometrically non-linear solutions for the values of μ and γ, as indicated, that were extracted via model curve fitting, Eq. (5.17), with the captured shape. Numerical solutions in (b) where evaluated by imposing the bending angle at the basal end ($s = 0$) and at the actuation point ($s = \bar{s}$) from the captured flagellar profile, indicated by the tangent lines (cyan) overlaid in the microscope snapshots. The black markers in the second row depicts the probe actuation point. Microscope images adapted from Pelle et al. [103] with permission from John Wiley and Sons (2958780742312).

values for the material parameters via model curve fitting are markedly different from the cases depicted in Fig. 5.19, with $\mu \approx 67$ and $\gamma \approx 0.8$, see Fig. 5.21 (a). Furthermore, the model comparison in Fig. 5.21 (b) demonstrates a good agreement between the shape solution from the geometrically non-linear formulation and observed flag-

ellar deformation. It is noteworthy, however, that a good match was obtained via the model curve fitting for all cases discussed here. This results from the fact that the analytical formulae in Eq. (5.17) depends on the shape of the active region, which was provided by the captured flagellum, further validating in this way the physical principles incorporated by the filament bundle elastica formulation presented here.

In summary, we have exemplified how geometrically non-linear filament bundle elastica model may be readily applied to extract bulk material properties from filament bundles, such as the axoneme. However, because of the sensitivity of the solutions to the action of additional contact forces and different conditions at the boundaries, care must be taken during experimental investigation to fully isolate the elastic structure from other sources of forces and torques.

5.5 Discussion

Recent empirical studies revealed the structural importance of the elastic cross-link elements while developing the flagellar counterbend phenomenon [84, 103]. This apparent paradoxical effect takes place when a passive flagellar axoneme, simply obtained by disabling the dynein molecular motors, is forced under the action of an external load. Because the axonemal structure is composed of $9 + 2$ microtubules, arranged cylindrically, and each microtubule is interconnected by radial spokes and nexin links, it is no surprise that the resulting elastic structure do not behave as a simple Euler-Bernoulli filament. Instead, the axoneme generates an intrinsic moment along its length, due to the mismatch length of each microtubule under imposed flexure, capable of deforming the structure in opposition to the point force, thus inducing a counterbend curvature. Even though the counterbend phenomenon can be conceptually understood from the prevailing sliding doublet model of axoneme mechanics [84, 103], no rigorous mathematical demonstration has been shown to date of counterbend effect, while the static, post-buckled configurations of the axoneme,

induced by external forces, is still lacking in the literature.

Thus, in contrast to the vast majority of studies on the material properties of filament bundles, we considered the structural effect of the passive link proteins that are found in the axoneme via first principles. We developed a simple and effective mathematical model based on the sliding-filament mechanism, widely used for the dynamics of flagella and cross-linked filament bundles, to elucidate the static scenario of the counterbend phenomenon. We provided an explicit mathematical description of the counterbend as a generic property of the axoneme, or any cross-linked filament bundle. The intricate counterbend shapes were readily accessed in its geometrically exact form by solving the filament bundle elastica problem, modified by the intrinsic moments originated from the elastic cross-linked structure, and subjected to non-trivial boundary conditions related to such internal moments. Furthermore, we have demonstrated the key role of the basal compliance while regulating the overall sliding displacement along the bundle, including the counterbend directional polarity effect, that was also reported during counterbend experiments [103]. A further understanding concerning the differences between the elastic cross-links response and pure shear material resistance has also been provided, as the counterbend complex behaviour cannot be captured by pure shear mechanics, usually found in Timoshenko's beam theory or Cosserat Rod Theory for shearable filaments. Therefore, such cross-linked filament bundles, cannot be treated a priori as simple Euler-Bernoulli or shearable filaments.

For the usual buckling experiment, our model requires three fitting parameters, which become very challenging to extract from the usual experiment of considering buckling loads at the end points. Instead, by employing the counterbend type procedure it is possible to evaluate the basal compliance and the interfilament shearing independently. The force, on the other hand, is solely determined by the position of the basal and forced point, which gives a measure of the elastic bending.

A good comparison was found between the filament bundle elastica model and existing experiments by Pelle et. al [103]. We have shown that the discrepancy between the model and the captured flagellum deformation is related with adhesive forces between the flagellum and the substrate that are not taken into account in the theoretical formulation. We have shown that the adhesive contact forces for a demembranated flagellar axoneme near surfaces introduce a systematic deviation of the predicted configuration from observation. Adhesive contact forces on the sperm flagellum prevent the interfilament sliding at the point or section of contact, thus introducing a bias on the measurements of the bulk material parameters, via a stiffer cross-linking elastic resilience, when curve fitting the captured flagellum deformation. After accounting for such difficulties, the simplicity of the analytical solution nonetheless entails that this formalism can be readily applied, without requiring laborious computer implementation or simulation. Finally, we have demonstrated how sensitive the solutions are when considering different boundary conditions, so that care must be taken in considering how the cell body mechanically behaves when interpreting experimental data.

The large scale counterbend deformation is a manifestation of the key structural role of the internal elastic links on the overall mechanical response of flagellar axonemes. We therefore expect that counter-curvatures may equally play an important role during bending wave generation in flagellar axonemes, in the dynamical setting. By inducing a coherent sliding displacement in one section of the flagellum length, the other section would be induced to deform in opposition, effectively forcing a non-local waveform without the necessary need of complex chemical regulation. In this way, the axonemal scaffolding may intrinsically assist the regulation of dynein self-oscillations within the sperm flagellum by inducing a non-local coupling.

Chapter 6

Conclusions and future work

6.1 Summary

In this thesis, theoretical and experimental investigations have been conducted for spermatozoa locomotion and the propulsive waveform which emerges from the balance between an internally-generated bending moment and both the flagellar elastic resistance and viscous drag forces, in addition to the study of the material properties associated with the axonemal cross-linked structures and pure shearing deformations in elastic filaments.

We successfully constructed a simple biomathematical model for the human sperm movement in Chapter 2. Our mathematical model takes into account the sperm cell and its interaction with surrounding medium, coupling several force-generating mechanisms with the geometrically non-linear response of the flagellum structure. We have demonstrated that when the surrounding fluid is viscous enough, the sperm flagellum may buckle, leading to profound changes in both the waveforms and the swimming cell trajectories. For a wide range of physiologically relevant parameters, the non-linear model predicts that flagellar compression by the internal forces initiates an effective buckling behaviour, leading to a symmetry breaking bifurcation which causes complicated changes in the waveform and swimming trajectory, as well as the breakdown of the linear theory. The emergent waveform also induces curved swimming in an otherwise symmetric system, with the swimming trajectory being sensitive to head

shape - no signalling or asymmetric forces are required. This asymmetry is sufficient to trap swimming cells in a circular loop, exemplifying how flagellar elastic instabilities may affect the cell behaviour. These results also emphasise that, in general, one cannot infer the presence of asymmetric molecular forces within the flagellum from observations of a bias in swimming direction, such as circular swimming.

In Chapter 3, we generalised the elastohydrodynamic formulation presented in Chapter 2 to consider the influence of the tapering ultrastructure of the mammalian sperm flagellum. As a result, the equations governing flagellar dynamics are profoundly changed by several new non-linear terms, which are responsible for driving the cell dynamics in a non-trivial manner. We have shown that these ultrastructural components are essential for sperm migration in high viscosity medium. By reinforcing the flagellum in regions where high tension is expected, between the mid- and principal pieces, the flagellar accessory complex is able to prevent tension-driven elastic instabilities that compromise the biological function of the spermatozoa. Furthermore, our results demonstrate that the tapering of structural components plays an important role in shaping the flagellar waveform, further suggesting that the flagellar wave modulation observed empirically, with the formation of a wave envelope that gradually increase its amplitude along the flagellum length, is achieved without recourse to intricate molecular motor regulation via, instead, a travelling wave of sliding bending moment along the flagellum.

In Chapter 4, we turned our attention to the significance of a low shear modulus on the behaviour of biological slender-bodies. The exact geometry of deformation was investigated by allowing a interaction of deformations in different material directions, by not only accounting for flexure, but also shearing deformations. In this instance, we employed the special Cosserat theory for planar deformations of geometrically non-linear elastic slender-bodies. In turn, this permitted the generalisation of the classical hyperdiffusion-type problem of Euler-Bernoulli filaments deforming in

inertialess fluids for filaments with a low shear modulus. We reported the emergence of a novel bending effect due to the absence of monotonicity between moments and curvature. Furthermore, we have shown that shearing effects are responsible for an apparent dependance of the flexural rigidity with the filament length, as observed experimentally for microtubules. The differences between the Cosserat rod theory and the Timoshenko beam theory were also provided. In particular, we have demonstrated that the discrepancy between the two models goes beyond the geometrical nature and, as they disagree at the material constitutive level. Finally, we showed that pure material shearing effects from Cosserat Rod Theory or the, equivalently, the Timoshenko's beam theory are essentially disconnected from the sliding filament induced shear found in filament bundles, such as the axoneme, and therefore they are unable to explain the paradoxical counterbend effect.

Motivated by the results presented in Chapter 4, we considered, in Chapter 5, the physical principles of the structural effects associated with the passive cross-link proteins in flagellar axonemes. We developed a simple and effective mathematical model based on the sliding-filament mechanism, to elucidate the static scenario of the counterbend phenomenon. Hence, we provided an explicit mathematical demonstration of the counterbend phenomenon as a generic property of the axoneme, or any cross-linked filament bundle. The intricate counterbend shapes were readily accessed in its geometrically exact form by solving the well-known elastica problem, corrected by intrinsic moments originated from the elastic cross-linked structure, and subjected to non-trivial boundary conditions modified by such internal moments. Using a simple analytical formula for the geometrically exact counterbend shape, we exemplify a model application to measure material properties from the developed counterbend deformation during load-displacement experiments of flagellar axonemes, and other cross-linked filament bundle.

6.2 Future work

6.2.1 Some important questions

The investigation presented in this DPhil work lays the groundwork for further complementary studies, which could be addressed by extending and improving methodologies developed in this thesis. Although some important phenomena associated with the spermatozoa motility and the mechanical properties of the sperm flagella, and its constituent elements, were elucidated, it also raises many important questions, exemplifying the fruitful prospects in different research directions, for example:

- How are the molecular motors within the sperm flagellum regulated in order to generate self-organised oscillations and how they respond to viscous drag in order to modulate the beating pattern accordingly?

- How can sperm swim at nearly equal speeds in media of dramatically different viscosities? Is there any mechanism that can ameliorate the otherwise enormous upregulation of dynein forces that are required? What can we deduce about the forces and energetics of sperm swimming and what does this tell us about the internal force generating mechanism?

- How does viscosity affect sperm boundary accumulation, since the flagellar waveform itself is dramatically changed according to the properties of the surrounding medium? How is the flagellar beat modulated close to a surface and does this influence boundary accumulation?

6.2.2 Outlook

A natural generalisation of the biomathematical model for the human sperm movement developed in Chapters 2 and 3 is to replace the resistive force theory by the

slender-body theory, which will improve the accuracy of the hydrodynamic modelling, and allow us to consider surface effects. This will allow us to predict changes in flagellar beat patterns when the cell approaches a surface in the absence of mechanotransduction. In this case, the flexible sperm structure will interact with the surface and the surrounding fluid, enabling an assessment of how mechanics influences the phenomenon of sperm boundary accumulation; by comparison with experiments, this may also reveal whether mechanotransduction is a key aspect of boundary accumulation. Moreover, in addition to the accurate implementation of non-local hydrodynamic effects, further generalisation of the sperm flagellum elastic structure can be achieved by considering the geometrically exact three-dimensional deformations of the flagellum. This can be done by incorporating, for instance, not only bending deformations, but also the effect of torsion and the three-dimensional sliding forcing mechanism.

In Chapter 4, we have considered the static scenario of a simple filament bundle, consisting of two inextensible and unshearable filaments. An important extension of this system would be to consider geometrically exact deformations associated with the three-dimensional axonemal structure, by considering a cylindrical arrangement of filaments interconnected by elastic links, so that not only bending deformations and filament sliding is allowed, but also torsion. Furthermore, due to large shearing effects associated with microtubules, we expect that shearing deformations will also play an important role in filament bundles composed of shearable microtubules, such as the axoneme itself. In this case, the sliding filament model proposed in Chapter 5 can be easily modified in order to consider a bundle of shearable filaments. Additionally, our sliding filament model can also be modified to include the influence from ultrastructural components of mammalian sperm flagellum, so that it could be appropriately applied to explore the material parameters of the mammalian flagellum via buckling experiments.

During the introductory Chapter, we have shown how the sperm cells are highly specialised: each different part, namely the head, midpiece, principal piece and the end piece, exhibits an intricate complexity in its internal architecture, and the functional significance is still not entirely understood. Throughout the evolutionary process, these cells were subjected to high levels of competition within males, and it is believed that the current cell configuration is a result of an evolutionary race [7, 16, 72, 89, 121]. Although the biological design is a result of various conflicting demands within cell competition, from a mathematical perspective, such high level of cell specialisation motivates the study of swimming optimisation through computational simulations and subsequent comparison with biological observations. By using the present elastohydrodynamic formulation, we can determine the optimal internal sliding force required to maximise the swimming efficiency, which can be defined as the ratio of the work required to move over the distance d at an average speed U, to the total work exerted by the swimmer against viscosity. In turn, this will allow us to address the effects of viscosity on the resulting optimal active bending moment, and further contrast between the beat pattern arising from the optimal internal molecular forcing and experimental observations.

Future work also include the test of competing hypotheses for the internal self-organized molecular motor oscillations in human sperm flagella by validating model predictions against characteristic flagellar waveforms in fluids of different viscosities. This is working towards the construction of multiscale virtual sperm motility models incorporating a understanding of dynein regulation and thus the mechanical modulation of the flagellar waveform.

These fundamental developments in the microbiomechanics of sperm motility will be used to explore many facets of sperm behaviour in the female reproductive tract. For example, in cervical crypts, what kinematical features of the flagellar waveform encourage trapping or escape and how will these translate to sperm flagella behaviours

in diagnostic settings. One can also explore sperm rheotaxis, i.e. an alignment of swimming direction with a surrounding flow, assessing whether it is important in sperm navigation whether due to uterine peristalsis or oviductal cilia. Further generalizations will allow us to consider progression within the convoluted elastic folds of the oviducts and predict if hyperactivation (changes in waveform) coupled with boundary interactions encourage sperm escape from the epithelial surface to swim throughout the fallopian tube, reducing the prospect of missing the egg.

Further extensive theoretical and computational work is required to consider the sperm microenvironment. Models of sperm motility are typically limited to Newtonian fluidics, though very recent investigations have considered viscoelastic media in simple settings. In this case, it is possible to extend models for sperm swimming in media with a viscoelastic response, for example simple representations of mucus, or media with a purely linear elastic response, possibly with enzyme lysis, modelling penetration of the zona pellucida which is a glycoprotein coat surrounding the egg. Modelling progression within linearly viscoelastic and elastic media can be developed by generalising [118], although more general media will require selectively combining the algorithms within commercial packages with bespoke codes.

Appendix A

Supporting information: human sperm observation

A.1 Internal shear density as a travelling wave

The internal elastic and viscous forces are balanced at any point along the flagellum and, after non-dimensionalisation, the viscous forces acting on the flagellum between arclength s and the end of the flagellum can be written as

$$\mathbf{F}_{\text{vis}} = -\text{Sp}^4 \int_s^1 \left[\left(\hat{\mathbf{n}}\hat{\mathbf{n}} + \frac{1}{\gamma}\hat{\mathbf{s}}\hat{\mathbf{s}} \right) \mathbf{X}_t \right] \text{ds}'. \tag{A.1}$$

Using a non-dimensional version of Eq. (2.6) and (A.1), we have that the non-dimensional internal shear density $f(s,t)$ is given by

$$f(s,t) = \left(\frac{L}{b} \right) \left[\mathbf{X}_{sss} - \mathbf{F}_{\text{vis}} \right] \cdot \hat{\mathbf{n}}. \tag{A.2}$$

where L/b is the ratio of flagellum length to axoneme diameter. Thus given $\mathbf{X}(s,t)$ from imaging experiments of swimming spermatozoa [120] moving in a fixed plane, one may deduce estimates for the combined internal shear from the dynein molecular motor activity and the passive cross linking proteins within the flagellum. In particular, travelling waves of deflection are observed to periodically propagate down the flagellum of swimming human sperm [120]. Under such circumstances f is simply the sum of a third derivative of travelling waves plus the spatial integral of a temporal derivative of travelling waves, Eq. (A.2). Hence $f(s,t)$ is in the form of travelling

waves propagating down the flagellum given estimates of $\mathbf{X}(s,t)$ from recent human sperm experiments [120].

A.2 Material and methods: human sperm imaging

Human spermatozoa were obtained by masturbation, after 2-4 days abstinence, from normozoospermic research donors with informed consent at the Centre for Human Reproductive Science, Birmingham Women's NHS Foundation Trust. The penetration medium was made from Earle's Balanced Salt Solution (041-94189H, Gibco-BRL, Paisley, UK), 0.45% human serum albumin to prevent cell adhesion to glass surfaces (BioProducts Laboratory, Elstree, UK) and 2% methylcellulose mucus substitute (MC400, Sigma-Aldrich, Poole, UK). The migrating cell population were selected for imaging by using a borosilicate capillary tube (VITROTUBES, 2540, Composite Metal Services, Ilkley, UK) loaded with the penetration medium through capillary action. After sealing one end of the tube with CRISTASEAL (Hawksley, Sussex, UK, #01503-00), the other end was immersed into a BEEM capsule (G360-2, size 00, Agar Scientific, Stansted, UK), containing 200 μl of raw semen, and followed by 30 min incubation at 37°C in 6% CO_2. Cells were imaged at $\sim$2 cm migration distance into the capillary tube, with an Olympus (BX-50) microscope, 20$\times$ positive phase contrast lens and a Hamamatsu Photonics C9300 CCD camera at 50 Hz. The cell tracking analysis was performed with Image Pro Plus (Media-Cybernetics) and MATLAB (Mathworks). A detailed description of the apparatus for phase contrast microscopy, as well as the experimental setup for human sperm migration in capillary tubes, filled with methylcellulose mucus substitute, has been presented in [120].

Appendix B

Eigenfunctions $S_c(s)$ and associated transcendental solvability conditions

The general solution of Eq. (4.29) is given by a linear combination of hyperbolic and trigonometric functions

$$S_c(s) = r_1 \cosh(q_1 s) + r_2 \sinh(q_1 s) + r_3 \cos(q_2 s) + r_4 \sin(q_2 s), \tag{B.1}$$

where

$$q_l = c\sqrt{\frac{(-1)^l \nu c^2}{2} + \sqrt{1 + \left(\frac{\nu c^2}{2}\right)^2}}, \text{ for } l = 1, 2. \tag{B.2}$$

The coefficients $\{r_i\}$ and permitted wave numbers c are specified by boundary conditions. We considered the right end of the slender-body to be always free from external forces and torques, so that Eq. (4.14) applies at $s = 1$, and five distinct conditions at the left end:

(a) free force and torque condition, Eq. (4.14): $\theta_s|_{s=0} = \theta_{ss}|_{s=0} = 0$,

(b) pinned condition, Eqs. (4.12)a, (4.13)b: $\theta_s|_{s=0} = \theta_{sss}|_{s=0} = 0$,

(c) clamped shear condition, Eqs. (4.12)a, (4.13)a: $\theta|_{s=0} = \theta_{sss}|_{s=0} = 0$,

(d) clamped tangent condition, Eqs. (4.12)a, (4.15): $(\theta - \nu\theta_{ss})|_{s=0} = \theta_{sss}|_{s=0} = 0$,

(e) welded base condition, Eqs. (4.12)a,b: $\theta_{ss}|_{s=0} = \theta_{sss}|_{s=0} = 0$.

We list the unnormalised eigenfunctions coefficients and the associated solvability

conditions for each case above, respectively:

(a)

$$
\begin{aligned}
r_1 &= q_2^2(\cos q_2 - \cosh q_1) \\
r_2 &= q_2(-q_1 \sin q_2 + q_2 \sinh q_1) \\
r_3 &= q_1^2(\cos q_2 - \cosh q_1) \\
r_4 &= q_1(q_1 \sin q_2 - q_2 \sinh q_1) \\
1 &- \cos q_2 \cosh q_1 - \left(\frac{\nu\, c^2}{2}\right) \sin q_2 \sinh q_1 = 0
\end{aligned}
\tag{B.3}
$$

(b)

$$
\begin{aligned}
r_1 &= q_2(q_2 - q_2 \cos q_2 \cosh q_1 + q_1 \sin q_2 \sinh q_1) \\
r_2 &= q_2(-q_1 \cosh q_1 \sin q_2 + q_2 \cos q_2 \sinh q_1) \\
r_3 &= q_1(-q_1 + q_1 \cos q_2 \cosh q_1 + q_2 \sin q_2 \sinh q_1) \\
r_4 &= q_1(q_1 \cosh q_1 \sin q_2 - q_2 \cos q_2 \sinh q_1) \\
q_1 &\cosh q_1 \sin q_2 - q_2 \cos q_2 \sinh q_1 = 0
\end{aligned}
\tag{B.4}
$$

(c)

$$
\begin{aligned}
r_1 &= -c^2 \left(q_1^2 \cos q_2 + q_2^2 \cosh q_1\right) \\
r_2 &= q_2^3(q_2 \sin q_2 + q_1 \sinh q_1) \\
r_3 &= c^2 \left(q_1^2 \cos q_2 + q_2^2 \cosh q_1\right) \\
r_4 &= q_1^3(q_2 \sin q_2 + q_1 \sinh q_1) \\
(q_1^4 + q_2^4) &\cos q_2 \cosh q_1 - \nu\, c^6 \sin q_2 \sinh q_1 + 2c^4 = 0
\end{aligned}
\tag{B.5}
$$

(d)

$$
\begin{aligned}
r_1 &= c^2\left(1+q_2^2 u\right)\left(q_1^2\cos q_2 + q_2^2\cosh q_1\right)\\
r_2 &= q_2^3\left(q_2\left(-1+q_1^2 u\right)\sin q_2 - q_1\left(1+q_2^2 u\right)\sinh q_1\right)\\
r_3 &= c^2\left(-1+q_1^2 u\right)\left(q_1^2\cos q_2 + q_2^2\cosh q_1\right)\\
r_4 &= q_1^3\left(q_2\left(-1+q_1^2 u\right)\sin q_2 - q_1\left(1+q_2^2 u\right)\sinh q_1\right)\\
&(q_1^4+q_2^4-\nu^2\,c^8)\cos q_2\cosh q_1 + \nu\,c^6\sin q_2\sinh q_1 + c^4(2+\nu^2\,c^4) = 0 \qquad \text{(B.6)}
\end{aligned}
$$

(e)

$$
\begin{aligned}
r_1 &= c^4\cos q_2 + q_2^4\cosh q_1\\
r_2 &= q_2^3(q_1\sin q_2 - q_2\sinh q_1)\\
r_3 &= q_1^4\cos q_2 + c^4\cosh q_1\\
r_4 &= q_1^3(q_1\sin q_2 - q_2\sinh q_1)\\
&\nu\,c^2(\cos q_2\cosh q_1 - 1) - 2\sin q_2\sinh q_1 = 0 \qquad \text{(B.7)}
\end{aligned}
$$

Bibliography

[1] Human fertilization embriology authority, www.hfea.gov.uk.

[2] World Health Organization, WHO Laboratory Manual for the Examination of Human Semen and Sperm Cervical Mucus Interaction, 4th Ed. Cambridge University Press, Cambridge (1999).

[3] D. J. Acheson. *Elementary Fluid Dynamics*. Oxford University Press, 1990.

[4] M. Adams, U M Smith, C V Logan, and C A Johnson. Recent advances in the molecular pathology, cell biology and genetics of ciliopathies. *Journal of Medical Genetics*, **45**(5):257–267, May 2008.

[5] B. Alberts. *Molecular Biology of the Cell*. Garland Science, New York, 2002.

[6] A . G. Andersen, T. K. Jensen, E. Carlsen, N. Jorgensen, A.M. Andersson, T. Krarup, N. Keiding, and N. E. Skakkebaek. High frequency of suboptimal semen quality in an unselected population of young men. *Human Reproduction*, **15**:366 372, 2000.

[7] M.J. Anderson, J. Nyholt, and A.F. Dixson. Sperm competition and the evolution of sperm midpiece volume in mammals. *J. Zool.*, **267**:135142, 2005.

[8] SS Antman. *Nonlinear Problems of Elasticity*, **107** of *Applied Mathematical Sciences*. Springer, 2005.

[9] S.S. Antman and M.Lanza de Cristoforis. Peculiar instabilities due to the clamping of shearable rods. *International Journal of Non-Linear Mechanics*, **32**(1):31–54, January 1997.

[10] U. M. Ascher, S. J. Ruuth, and B. T. R. Wetton. Implicit-explicit methods for time-dependent partial differential equations. *SIAM J. Numerical Analysis*, **32**:797–823, 1995.

[11] J. M. Baltz, P. O.Williams, and R. A. Cone. Dense fibers protect mammalian sperm against damage. *Biol. Reprod.*, **43**:485–491, 1990.

[12] M. Bathe, C. Heussinger, M.A.E. Claessens, A. R. Bausch, and E. Frey. Cytoskeletal bundle mechanics. *Biophysical Journal*, **94**(8):2955–2964, April 2008.

[13] L. E. Becker and M. J. Shelley. Instability of elastic filaments in shear flow yields first-normal-stress differences. *Phys. Rev. Lett.*, **87**:198301–198304, 2001.

[14] J. M Bedford and H. I Calvin. Changes in -s-s- linked structures of the sperm tail during epididymal maturation, with comparative observations in sub-mammalian species. *Journal of Experimental Zoology*, **187**(2):181–203, February 1974.

[15] L. Bourdieu, T. Duke, M. B. Elowitz, D. A. Winkelmann, S. Leibler, and A. Libchaber. Spiral defects in motility assays: A measure of motor protein force. *Phys. Rev. Lett.*, **75**:176–179, 1995.

[16] J.V. Briskie and R. Montgomerie. Sperm size and sperm competition in birds. *Proc. R. Soc. London, Ser. B*, **247(1319)**:8995, 1992.

[17] C. J. Brokaw. Bend propagation by a sliding filament model for flagella. *J. Exp. Biol.*, **55**(2):289–304, 1971.

[18] C. J. Brokaw. Molecular mechanism for oscillation in flagella and muscle. *Proc. Natl. Acad. Sci.*, **72**:3102–3106, 1975.

[19] C. J. Brokaw. Computer simulation of flagellar movement VIII: coordination of dynein by local curvature control can generate helical bending waves. *Cell Motility and the Cytoskeleton*, **53**(2):103–124, October 2002.

[20] C. J. Brokaw. Thinking about flagellar oscillations. *Cell. Mot. Cytoskel.*, **66(8)**:425–436, 2009.

[21] S. Camalet and F. Jülicher. Generic aspects of axonemal beating. *New J. Phys.*, **2**:24.1–24.23, 2000.

[22] S. Camalet, F. Jülicher, and J. Prost. Self-organized beating and swimming of internally driven filaments. *Phys. Rev. Lett.*, **82**:1590–1593, 1999.

[23] Stephen Childress. *Mechanics of swimming and flying*. Cambridge University Press, 1981.

[24] D. Chretien, H. Flyvbjerg, and S.D. Fuller. Limited flexibility of the inter-protofilament bonds in microtubules assembled from pure tubulin. *European Biophysics Journal*, **27**(5):490–500, 1998.

[25] D. Chretien and S. D. Fuller. Microtubules switch occasionally into unfavorable configurations during elongation. *Journal of Molecular Biology*, **298**(4):663–676, May 2000.

[26] M. A. E. Claessens, M. Bathe, E. Frey, and A. R. Bausch. Actin-binding proteins sensitively mediate f-actin bundle stiffness. *Nature Materials*, **5**(9):748–753, August 2006.

[27] M. M. A. E. Claessens, C. Semmrich, L. Ramos, and A. R. Bausch. Helical twist controls the thickness of f-actin bundles. *Proceedings of the National Academy of Sciences*, **105**(26):8819–8822, 2008.

[28] E. Cosserat and F. Cosserat. Theorie des corps deformables. *Paris*, 1909.

[29] M. Dogterom and B. Yurke. Measurement of the Force-Velocity relation for growing microtubules. *Science*, **278**(5339):856–860, October 1997.

[30] R B Dye, S P Fink, and R C Williams. Taxol-Induced flexibility of microtubules and its reversal by MAP-2 and tau. *Journal of Biological Chemistry*, **268**(10):6847–6850, April 1993.

[31] M. Eisenbach. *Chemotaxis*. Imperial College Press, 2004.

[32] F. Engesser and D.K.G. Stabe. Zentr. *Bauverwaltung 11 (1891), S*, **483**, 1891.

[33] A. C. Eringen. On differential equations of nonlocal elasticity and solutions of screw dislocation and surface waves. *Journal of Applied Physics*, **54**(9):4703–4710, September 1983.

[34] L. Euler. *Methodus inveniendi lineas curvas maximi minimive proprietate gaudentes, sive solutio problematis isoperimetrici lattissimo sensu accepti*. chapter Additamentum 1, eulerarchive.org E065, 1744.

[35] R. Everaers, R. Bundschuh, and K. Kremer. Fluctuations and stiffness of double-stranded polymers: railway-track model. *EPL (Europhysics Letters)*, **29**:263, 1995.

[36] R. Everaers, F. Julicher, A. Ajdari, and A. C. Maggs. Dynamic fluctuations of semiflexible filaments. *Physical Review Letters*, **82**(18):3717–3720, May 1999.

[37] L. J. Fauci and R. Dillon. Biofluidmechanics of reproduction. *Annu. Rev. Fluid Mech.*, **38**:371, 2006.

[38] D. W. Fawcett. The mammalian spermatozoon. *Developmental Biology*, **44**:394–436, 1975.

[39] D. W. Fawcett, W. Bloom, and E. Raviola. *A Textbook of Histology*. Chapman & Hall, June 1994.

[40] H. C. Fu, C. W. Wolgemuth, and T. R. Powers. Beating patterns of filaments in viscoelastic fluids. *Phys. Rev. E*, **78**:041913–041925, 2008.

[41] Y. C. Fung and P. Tong. *Classical and computational solid mechanics*. Word Scientific, 2001.

[42] H. Gadêlha, E. A. Gaffney, D. J. Smith, and J. C. Kirkman-Brown. Nonlinear instability in flagellar dynamics: a novel modulation mechanism in sperm migration? *J. Roy. Soc. Int.*, **7**:1689–1697, 2010.

[43] E. A. Gaffney, H. Gadêlha, D. J. Smith, J.R. Blake, and J. C. Kirkman-Brown. Mammalian sperm motility: Observation and theory. *Annual Review of Fluid Mechanics*, 2011.

[44] Y. Gao and F.M. Lei. Small scale effects on the mechanical behaviors of protein microtubules based on the nonlocal elasticity theory. *Biochemical and Biophysical Research Communications*, **387**(3):467–471, September 2009.

[45] F. Gittes, B. Mickey, J. Nettleton, and J. Howard. Flexural rigidity of microtubules and actin filaments measured from thermal fluctuations in shape. *The Journal of cell biology*, **120**(4):923, 1993.

[46] R. E. Goldstein and S. A. Langer. Nonlinear dynamics of stiff polymers. *Phys. Rev. Lett.*, **75**:1094–1097, 1995.

[47] R. E. Goldstein, T. R. Powers, and C. H. Wiggins. Viscous nonlinear dynamics of twist and writhe. *Phys. Rev. Lett.*, **80**:5232–5235, 1998.

[48] S. F. Goldstein. Asymmetric waveforms in echinoderm sperm flagella. *J Exp Biol*, **71**:157–170, 1977.

[49] J. Gray and G. J. Hancock. The propulsion of sea-urchin spermatozoa. *J. Exp. Biol.*, **32**:802–814, 1955.

[50] S. Gueron and N. Liron. Simulations of three-dimensional ciliary beats and cilia interactions. *Biophys. J.*, **65**(1):499 – 507, 1993.

[51] JA Haringx. On the buckling and lateral rigidity of helical springs. *Proc. Konink. Ned. Akad. Wet*, **45**(533):142, 1942.

[52] J.A. Haringx. *On highly compressible helical springs and rubber rods, and their application for vibration-free mountings.* 1950.

[53] C. Heussinger, M. Bathe, and E. Frey. Statistical mechanics of semiflexible bundles of wormlike polymer chains. *Physical Review Letters*, **99**(4):048101, July 2007.

[54] C. Heussinger, F. Schüller, and E. Frey. Statics and dynamics of the wormlike bundle model. *Phys. Rev. E*, **81**(2):021904, Feb 2010.

[55] A. Hilfinger, A. K. Chattopadhyay, and F. Jülicher. Nonlinear dynamics of cilia and flagella. *Phys. Rev. E*, **79**:051918–051925, 2009.

[56] A. Hilfinger and F. Jülicher. The chirality of ciliary beats. *Phys. Biol.*, **5**:016003–016015, 2008.

[57] M. Hines and J. Blum. Bend propagation in flagella. i. derivation of equations of motion and their simulation. *Biophys. J.*, **23(1)**:41–57, 1978.

[58] J. Howard. *Mechanics of motor proteins and the cytoskeleton.* Sinauer Associates Sunderland, MA, 2001.

[59] M. G. Hull, C.M. Glazener, N.J. Kelly, D.I. Conway, P.A. Foster, R.A. Hinton, C. Coulson, P.A. Lambert, E. M. Watt, and K. M. Desai. Population study of causes, treatment, and outcome of infertility. *British Medical Journal*, **291**:1693, 1985.

[60] M. E. Janson and M. Dogterom. A bending mode analysis for growing microtubules: Evidence for a Velocity-Dependent rigidity. *Biophysical Journal*, **87**(4):2723–2736, October 2004.

[61] R. E. Johnson. An improved slender-body theory for stokes flow. *J. Fluid Mech.*, **99**:411–431, 1980.

[62] R.E. Johnson and C.J. Brokaw. Flagellar hydrodynamics. a comparison between resistive-force theory and slender-body theory. *Biophys. J.*, **25**:113–127, 1979.

[63] V. Kantsler and R. E. Goldstein. Fluctuations, dynamics, and the Stretch-Coil transition of single actin filaments in extensional flows. *Physical Review Letters*, **108**(3):038103, January 2012.

[64] S. Kasas, A. Kis, B. M. Riederer, L. Forro, G. Dietler, and S. Catsicas. Mechanical properties of microtubules explored using the finite elements method. *ChemPhysChem*, **5**(2):252–257, February 2004.

[65] D. F. Katz, E. Drobnis, and J. W. Overstreet. Factors regulating mammalian sperm migration through the female reproductive tract and oocyte vestments. *Gamete Research*, **22**:443–469, 1989.

[66] J. B. Keller and S. I. Rubinow. Slender-body theory for slow viscous flow. *Journal of Fluid Mechanics Digital Archive*, **75**(04):705–714, 1976.

[67] M. Kikumoto, M. Kurachi, V. Tosa, and H. Tashiro. Flexural rigidity of individual microtubules measured by a buckling force with optical traps. *Biophysical Journal*, **90**(5):1687–1696, March 2006.

[68] M. Kinukawa, M. Nagata, and F. Aoki. Changes in flagellar bending during the course of hyperactivation in hamster spermatozoa. *Reproduction*, **125**:43–51, 2003.

[69] J. C Kirkman-Brown and D. J Smith. Sperm motility: Is viscosity fundamental to progress? *Molecular Human Reproduction*, **17**(8):539–544, August 2011.

[70] A. Kis, S. Kasas, B. Babic, A. J. Kulik, W. Benoit, G. A. D. Briggs, C. Schonenberger, S. Catsicas, and L. Forro. Nanomechanics of microtubules. *Physical Review Letters*, **89**(24):248101, November 2002.

[71] M. Kurachi, M. Hoshi, and H. Tashiro. Buckling of a single microtubule by optical trapping forces: Direct measurement of microtubule rigidity. *Cell Motility and the Cytoskeleton*, **30**(3):221–228, January 1995.

[72] C.W. LaMunyon and S. Ward. Evolution of sperm size in nematodes: sperm competition favours larger sperm. *Proc. R. Soc. London, Ser. B*, **266**:263267, 1999.

[73] L D Landau, L. P. Pitaevskii, E.M. Lifshitz, and A. M. Kosevich. *Theory of Elasticity*. Butterworth-Heinemann, 3rd edition, January 1986.

[74] L. Lefievre, K Bedu-Addo, S. J. Conner, G. S. M. Machado-Oliveira, Y. Chen, J. C. Kirkman-Brown, M. A. Afnan, S. J. Publicover, W. C. L. Ford, and C. L. R. Barratt. Counting sperm does not add up any more: time for a new equation? *Reproduction*, **133**:675, 2007.

[75] K. A. Lesich, D. W. Pelle, and C. B. Lindemann. Insights into the mechanism of ADP action on flagellar motility derived from studies on bull sperm. *Biophysical Journal*, **95**(1):472–482, July 2008.

[76] C. Li, C.Q. Ru, and A. Mioduchowski. Length-dependence of flexural rigidity as a result of anisotropic elastic properties of microtubules. *Biochemical and Biophysical Research Communications*, **349**(3):1145–1150, October 2006.

[77] J. Lighthill. *Mathematical Biofluiddynamics*. Society for Industrial and Applied Mathematics, 1975.

[78] J. Lighthill. Flagellar hydrodynamics. *The John von Neumann Lecture, 1975 SIAM Rev*, **18**:161–230, 1976.

[79] C. Lindemann and K. Kanous. "geometric clutch" hypothesis of axonemal function: key issues and testable predictions. *Cell. Mot. Cytoskel.*, **31**:1, 1995.

[80] C. B. Lindemann. A model of flagellar and ciliary functioning which uses the forces transverse to the axoneme as the regulator of dynein activation. *Cell Motility and the Cytoskeleton*, **29**(2):141–154, January 1994.

[81] C. B Lindemann. Functional significance of the outer dense fibers of mammalian sperm examined by computer simulations with the geometric clutch model. *Cell Motility and the Cytoskeleton*, **34**(4):258–270, January 1996.

[82] C. B. Lindemann. Testing the geometric clutch hypothesis. *Biology of the Cell*, **96**:681–690, 2004.

[83] C. B. Lindemann and K. A. Lesich. Flagellar and ciliary beating: the proven and the possible. *J Cell Sci*, **123**(4):519–528, 2010.

[84] C. B. Lindemann, J. A. Macauley, and K. A. Lesich. The counterbend phenomenon in dynein-disabled rat sperm flagella and what it reveals about the interdoublet elasticity. *Biophys. J.*, **89**:1165–1174, 2005.

[85] C. B. Lindemann, A. Orlando, and K. S. Kanous. The flagellar beat of rat sperm is organized by the interaction of two functionally distinct populations of dynein bridges with a stable central axonemal partition. *J. Cell Sci.*, **102**:249–260, 1992.

[86] C. B. Lindemann, W. G. Rudd, and R. Rikmenspoel. The stiffness of the flagella of impaled bull sperm. *Biophysical Journal*, **13**(5):437–448, May 1973.

[87] H.M. Ma, X.-L. Gao, and J.N. Reddy. A microstructure-dependent timoshenko beam model based on a modified couple stress theory. *Journal of the Mechanics and Physics of Solids*, **56**(12):3379–3391, December 2008.

[88] K. E. Machin. Wave propagation along flagella. *J. Exp. Biol.*, **35**:796–806, 1958.

[89] A. F. Malo, M. Gomendio, J. Garde, B. Lang-Lenton, A. J. Soler, and E. R.S Roldan. Sperm design and sperm function. *Biology Letters*, **2**(2):246–249, 2006.

[90] I. Mechab, A. Tounsi, M.A. Benatta, and E.A. Adda bedia. Deformation of short composite beam using refined theories. *Journal of Mathematical Analysis and Applications*, **346**(2):468–479, October 2008.

[91] N. J. De Mestre and W. B. Russel. Low reynolds number translation of a slender cylinder near a plane wall. *Journal of Engineering Mathematics*, **9(2)**:81–91, 1975.

[92] R. L. Miller and C. J. Brokaw. Chemotactic turning behaviour of tubularia spermatozoa. *J. Exp. Biol.*, **52(3)**:699–706, 1970.

[93] I. Minoura, T. Yagi, and R. Kamiya. Direct measurement of inter-doublet elasticity in flagellar axonemes. *Cell structure and function*, **24**(1):27–33, 1999.

[94] T. J. Mitchison and H. M. Mitchison. Cell biology: How cilia beat. *Nature*, **463**:308–309, 2010.

[95] D. J. Needleman, M. A. Ojeda-Lopez, U. Raviv, K. Ewert, J. B. Jones, H. P. Miller, L. Wilson, and C. R. Safinya. Synchrotron x-ray diffraction study of microtubules buckling and bundling under osmotic stress: A probe of interprotofilament interactions. *Physical Review Letters*, **93**(19):198104, November 2004.

[96] M.G. Nielsen and E.C. Raff. The best of all worlds or the best possible world? developmental constraint in the evolution of beta-tubulin and the sperm tail axoneme. *Evolution & Development*, **4(4)**:303, 2002.

[97] M. Okuno. Inhibition and relaxation of sea urchin sperm flagella by vanadate. *The Journal of Cell Biology*, **85**(3):712, 1980.

[98] M. Okuno and Y. Hiramoto. Direct measurements of the stiffness of echinoderm sperm flagella. *Journal of Experimental Biology*, **79**(1):235, 1979.

[99] G. E. Olson and R. W. Linck. Observations of the structural components of flagellar axonemes and central pair microtubules from rat sperm. *J. Ultrastruct. Res.*, **61**(1):21–43, 1977.

[100] G. E. Olson and D. W. Sammons. Structural chemistry of outer dense fibers of rat sperm. *Biology of Reproduction*, **22**(2):319–332, March 1980.

[101] S. D. Olson, S. S. Suarez, and L. J. Fauci. Coupling biochemistry and hydrodynamics captures hyperactivated sperm motility in a simple flagellar model. *Journal of Theoretical Biology*, **283**(1):203–216, August 2011.

[102] F. Pampaloni, G. Lattanzi, A. Jonas, T. Surrey, E. Frey, and E. L. Florin. Thermal fluctuations of grafted microtubules provide evidence of a Length-Dependent persistence length. *Proceedings of the National Academy of Sciences*, **103**(27):10248–10253, July 2006.

[103] D. W. Pelle, C. J Brokaw, K. A Lesich, and C. B Lindemann. Mechanical properties of the passive sea urchin sperm flagellum. *Cell Motil Cytoskeleton*, **66**(9):721–735, 2009.

[104] C. S. Peskin. The immersed boundary method. *Acta Numerica*, **11**(1):479–517, 2002.

[105] M. E. Pettitt, B. A. A. Orme, J. R. Blake, and B. S. C. Leadbeater. The hydrodynamics of filter feeding in choanoflagellates. *Europ. J. Protistol.*, **38**:313–332, 2009.

[106] C. Pozrikidis. *Boundary integral and singularity methods for linearized viscous flow*. Cambridge University Press, 1992.

[107] E.M. Purcell. Life at low reynolds number. *Am. J. Phys.*, **45**:3, 1977.

[108] E. Reissner. Some remarks on the problem of column buckling. *Archive of Applied Mechanics*, **52**(1):115119, 1982.

[109] I. H. Riedel-Kruse, A. Hilfinger, J. Howard, and F. Jülicher. How molecular motors shape the flagellar beat. *HFSP*, **1**:192–208, 2007.

[110] R. Rikmenspoel. The tail movement of bull spermatozoa: Observations and model calculations. *Biophysical Journal*, **5**(4):365–392, July 1965.

[111] H. Sakakibara, H. Kojima, Y. Sakai, E. Katayama, and K. Oiwa. Inner-arm dynein c of chlamydomonas flagella is a single-headed processive motor. *Nature*, **400**(6744):586–590, August 1999.

[112] P. Satir. Studies on cilia: Ii examination of the distal region of the ciliary shaft and the role of the filaments in motility. *J. Cell Biol.*, **26(3)**:805, 1965.

[113] P. Satir. Studies on cilia : Iii. further studies on the cilium tip and a 'sliding filament' model of ciliary motility. *J. Cell Biol.*, **39**:77, 1968.

[114] K. A. Schmitz-Lesich and C. B. Lindemann. Direct measurement of the passive stiffness of rat sperm and implications to the mechanism of the calcium response. *Cell Motility and the Cytoskeleton*, **59**(3):169–179, 2004.

[115] L.F. Shampine, I. Gladwell, and S. Thompson. *Solving ODEs with MATLAB*. Cambridge University Press, 2003.

[116] Y.J. Shi, W.L. Guo, and C.Q. Ru. Relevance of timoshenko-beam model to microtubules of low shear modulus. *Physica E: Low-dimensional Systems and Nanostructures*, **41**(2):213–219, December 2008.

[117] P. Skjetne, R. F. Ross, and D. J. Klingenberg. Simulation of single fiber dynamics. *The Journal of Chemical Physics*, **107**(6):2108–2121, 1997.

[118] D. J Smith, E. A Gaffney, and J. R Blake. Mathematical modelling of Cilia-Driven transport of biological fluids. *Proceedings of the Royal Society A: Mathematical, Physical and Engineering Science*, **465**(2108):2417–2439, August 2009.

[119] D. J. Smith, E. A. Gaffney, J. R. Blake, and J. C. Kirkman-Brown. Human sperm accumulation near surfaces: a simulation study. *J. Fluid Mech.*, **621**:289–320, 2009.

[120] D. J. Smith, E. A. Gaffney, H. Gadêlha, N. Kapur, and J. C. Kirkman-Brown. Bend propagation in the flagella of migrating human sperm, and its modulation by viscosity. *Cell. Motil. Cytoskel.*, **66**:220–236, 2009.

[121] R. R. Snook. Sperm in competition: not playing by the numbers. *Trends in Ecology & Evolution*, **20**(1):46 – 53, 2005.

[122] C. Spoon and W. Grant. Biomechanics of hair cell kinocilia: Experimental measurement of kinocilium shaft stiffness and base rotational stiffness with EulerBernoulli and timoshenko beam analysis. *Journal of Experimental Biology*, **214**(5):862–870, March 2011.

[123] S. Suarez. How do sperm get to the egg? bioengineering expertise needed! *Journal of Experimental Mechanics*, **0014-4851**:1–8, 2009.

[124] S. S. Suarez and H. C. Ho. Hyperactivated motility in sperm. *Reprod Dom Anim*, **38**:119–124, 2003.

[125] Y. Sumino, K. H. Nagai, Y. Shitaka, D. Tanaka, K. Yoshikawa, H. Chate, and K. Oiwa. Large-scale vortex lattice emerging from collectively moving microtubules. *Nature*, **483**(7390):448–452, March 2012.

[126] T. Takasone, S. Juodkazis, Y. Kawagishi, A. Yamaguchi, S. Matsuo, H. Sakakibara, H. Nakayama, and H. Misawa. Flexural rigidity of a single microtubule. *Japanese Journal of Applied Physics*, **41**:3015–3019, 2002.

[127] A. Templeton, C. Fraser, and B. Thompson. The epidemiology of infertility in aberdeen. *British Medical Journal*, **301**:148, 1990.

[128] S.P. Timoshenko and J.M. Gere. *Theory of elastic stability*. McGraw-Hill, New York, 1961.

[129] S. Toba, T. M Watanabe, L. Yamaguchi-Okimoto, Y. Y. Toyoshima, and H. Higuchi. Overlapping Hand-Over-Hand mechanism of single molecular motility of cytoplasmic dynein. *Proceedings of the National Academy of Sciences*, **103**(15):5741–5745, April 2006.

[130] J.A. Tolomeo and M.C. Holley. Mechanics of microtubule bundles in pillar cells from the inner ear. *Biophysical Journal*, **73**(4):2241–2247, October 1997.

[131] A. K. Tornberg and M. J. Shelley. Simulating the dynamics and interactions of flexible fibers in stokes flows. *J. Comput. Phys.*, **196**:8–40, 2004.

[132] A. Tounsi, H. Heireche, H. Benhassaini, and M. Missouri. Vibration and length-dependent flexural rigidity of protein microtubules using higher order shear deformation theory. *Journal of Theoretical Biology*, **266**(2):250–255, September 2010.

[133] J. van Mameren, K. C. Vermeulen, F. Gittes, and C. F. Schmidt. Leveraging single protein polymers to measure flexural rigidity. *J. Phys. Chem. B*, **113**(12):3837–3844, 2009.

[134] P. Venier, A.C. Maggs, M.-F. Carlier, and D. Pantaloni. Analysis of microtubule rigidity using hydrodynamic flow and thermal fluctuations. *Journal of Biological Chemistry*, **269**(18):13353–13360, 1994.

[135] C M Wang, Y Y Zhang, Sai Sudha Ramesh, and S Kitipornchai. Buckling analysis of micro- and nano-rods/tubes based on nonlocal timoshenko beam theory. *Journal of Physics D: Applied Physics*, **39**(17):3904–3909, September 2006.

[136] N. Wang, K. Naruse, D. Stamenovic, J. J Fredberg, S. M Mijailovich, I. M. Tolic-Norrelykke, T. Polte, R. Mannix, and D. E. Ingber. Mechanical behavior in living cells consistent with the tensegrity model. *Proceedings of the National Academy of Sciences*, **98**(14):7765–7770, July 2001.

[137] G. E. Ward, C. J. Brokaw, D. L. Garbers, , and V. D. Vacquier. Chemotaxis of arbacia punctulata spermatozoa to resact, a peptide from the egg jelly layer. *J. Cell Biol.*, **101(6)**:2324–2329, 1985.

[138] Z. U. A. Warsi. *Fluid Dynamics: theoretical and computational approaches.* CRC press, 1998.

[139] C. H. Wiggins and R. E. Goldstein. Flexive and propulsive dynamics of elastica at low reynolds number. *Phys. Rev. Lett.*, **80**:3879, 1998.

[140] C. H. Wiggins, D. Riveline, A. Ott, and R. E. Goldstein. Trapping and wiggling: elastohydrodynamics of driven microfilaments. *Biophys. J.*, **74**:1043–1060, 1998.

[141] C. W. Wolgemuth, T. R. Powers., and R. E. Goldstein. Twirling and whirling: Viscous dynamics of rotating elastic filaments. *Phys. Rev. Lett.*, **84**:1623–1626, 2000.

[142] D. M. Woolley. Motility of spermatozoa at surfaces. *Reproduction*, **126**:259–270, 2003.

[143] D. M Woolley and G. G Vernon. A study of helical and planar waves on sea urchin sperm flagella, with a theory of how they are generated. *Journal of Experimental Biology*, **204**(7):1333–1345, April 2001.

[144] T. S. Yu, , E. Lauga, and A. E. Hosoi. Experimental investigations of elastic tail propulsion at low reynolds number. *Phys. Fluids*, **18**:0917011–0917014, 2006.

[145] H. Ziegler. Arguments for and against engesser's buckling formulas. *Archive of Applied Mechanics*, **52**(1):105–113, 1982.